

PASSIVE CONTROL OF COMBUSTION NOISE AND THERMO-ACOUSTIC  
INSTABILITY WITH POROUS INERT MEDIA

by

ZACHARY A. SMITH

AJAY K. AGRAWAL, COMMITTEE CHAIR  
JOHN BAKER  
ALAN M. LANE  
ROBERT P. TAYLOR

A THESIS

Submitted in partial fulfillment of the requirements  
for the degree of Master of Science  
in the Department of Mechanical Engineering  
in the Graduate School of  
The University of Alabama

TUSCALOOSA, ALABAMA

2011

Copyright Zachary A. Smith 2011  
ALL RIGHTS RESERVED

## ABSTRACT

Combustion noise and thermo-acoustic instability present a major area of concern for many industrial combustion applications, especially those operating under lean-premixed (LPM) conditions. While LPM combustion reduces thermal NO<sub>x</sub> by allowing operation at reduced flame temperatures, LPM flames are particularly susceptible to combustion noise and instability. While combustion noise and thermo-acoustic instability are distinctly different phenomena; both originate from the same source – unsteady heat release in a turbulent flow field. Instabilities are self-excited and arise when energy from combustion is added to the system faster than energy is dissipated by heat transfer.

In a typical swirl-stabilized combustor, flame is stabilized downstream of the dump plane and is sustained by central and corner recirculation zones. The present study combines porous inert media (PIM) assisted combustion with swirl-stabilized combustion to alter the combustor flow field in an advantageous manner. A ring-shaped PIM insert is placed directly at the dump plane to eliminate zones of intense turbulent fluctuations, thereby mitigating combustion noise at the source. With PIM, a central flame is confined within the annular void of the insert while a small portion of reactants flow through the PIM and stabilize on the downstream surface. Additionally, the porous insert provides acoustic damping and passive attenuation of pressure waves. This study is a preliminary step towards implementing the technique at elevated operating pressures, and eventually, liquid fuel combustors. Atmospheric combustion tests are conducted for a variety operating conditions to determine effectiveness of PIM to reduce combustion noise and instability. Parameters varied include air preheat temperature, air flow

rate, equivalence ratio, and swirler axial location. Experiments are conducted with a high swirl angle, as opposed to previous experiments which used a lower swirl angle. For most conditions, PIM is shown to reduce total sound pressure level (SPL) in cases where instability is not intense. For all cases where instability is the dominant component of total SPL, PIM is extremely effective in eliminating instability. In these cases, total SPL is reduced by as much as 30 dB with PIM combustion. Furthermore, experiments show that no significant pressure drop penalty is incurred with porous media.

## DEDICATION

This thesis is dedicated to my late grandmother, Betty Smith, who fought a courageous battle with pancreatic cancer. She was one of the finest people I have ever known and will always be remembered kindly by those who knew her.

## LIST OF ABBREVIATIONS AND SYMBOLS

|                  |                                  |
|------------------|----------------------------------|
| 2D               | Two-dimensional                  |
| AF               | Air to fuel ratio                |
| AF <sub>st</sub> | Stoichiometric air to fuel ratio |
| B                | Bias uncertainty                 |
| CFD              | Computational fluid dynamics     |
| CFM              | Cubic feet per minute            |
| CH <sub>4</sub>  | Methane                          |
| CNG              | Compressed natural gas           |
| CO               | Carbon monoxide                  |
| CO <sub>2</sub>  | Carbon dioxide                   |
| dB               | Decibel                          |
| H <sub>2</sub> O | Water                            |
| HfC              | Hafnium carbide                  |
| ID               | Inside Diameter                  |
| IRZ              | Inner recirculation zone         |
| LNPM             | Liters normal per minute         |
| LPM              | Lean pre-mixed                   |
| N <sub>2</sub>   | Diatomic nitrogen                |

|                    |   |
|--------------------|---|
| NO <sub>x</sub>    | Nitrous oxides                                  |
| NPT                | National pipe thread                            |
| O <sub>2</sub>     | Diatomic oxygen                                 |
| ORZ                | Outer recirculation zone                        |
| P                  | Random uncertainty                              |
| PIM                | Porous inert media                              |
| ppcm               | Pores per centimeter                            |
| ppi                | Pores per inch                                  |
| Q                  | Air flow rate                                   |
| R                  | Swirler effective radius                        |
| R <sub>i</sub>     | Swirler radius                                  |
| R <sub>c</sub>     | Swirler center body radius                      |
| RNG                | Renormalization group                           |
| S                  | Swirl number                                    |
| SiC                | Silicon carbide                                 |
| SLPM               | Standard liters per minute                      |
| SPL                | Sound pressure level                            |
| T <sub>inlet</sub> | Air inlet temperature                           |
| α                  | Swirler vane angle                              |
| ΔP                 | Pressure differential                           |
| μ                  | Total uncertainty                               |
| μ <sub>f</sub>     | Viscosity of flowing gas                        |
| μ <sub>std</sub>   | Viscosity of flowing gas at standard conditions |

|                     |                                |
|---------------------|--------------------------------|
| $\varphi$           | Equivalence ratio              |
| $\rho$              | Density                        |
| $\rho_{\text{std}}$ | Density at standard conditions |

## ACKNOWLEDGMENTS

I would like to take the opportunity to show my sincere gratitude towards each person who contributed towards the completion of this thesis.

First of all, I would like to thank my graduate advisor, Dr. Ajay K. Agrawal, for his unconditional support and assistance during my time as a graduate student at The University of Alabama. His technical guidance and forward initiative were always delivered with the utmost patience and professionalism. Dr. Agrawal's guidance has allowed me to progress as both an engineer and a person, for which I will always be grateful.

I would like to thank both the Office of Naval Research as well as ULTRAMET Corporation for providing funding for the research contained within this thesis

I would also like to extend my most sincere appreciation to the members of my committee, Dr. Alan M. Lane, Dr. John Baker and Dr. Robert P. Taylor. I am thankful to have had the privilege of learning from these upstanding professors throughout my academic career.

Next, I would like to express thanks to all the graduate students in Dr. Agrawal's research group whom I have had the pleasure of working with. Ben, Dan, Heena, Lulin, Pankaj, Tanisha, Troy, and Yonas were always helpful and supportive to the fullest extent. I would like to give special thanks to Daniel, who I worked closely with during the initial stages of my research. As a senior graduate student, Daniel's leadership and direction was largely responsible for the successful implementation of our high pressure combustion test facility. His graduate research also provided the foundation for the technique examined in this thesis. I would also like to express my immense appreciation for the contributions of Justin and Joseph towards the work

contained in this thesis. Completion of this investigation was only possible with their unconditional support and assistance. Finally, I want to convey enormous gratitude to my parents for their constant support and encouragement throughout my entire career at The University of Alabama.

## CONTENTS

|   |      |
|---|------|
| ABSTRACT .....                          | ii   |
| DEDICATION .....                        | iv   |
| LIST OF ABBREVIATIONS AND SYMBOLS ..... | v    |
| ACKNOWLEDGMENTS .....                   | vii  |
| LIST OF TABLES .....                    | xii  |
| LIST OF FIGURES .....                   | xiii |
| 1. INTRODUCTION .....                   | 1    |
| 1.1. Background .....                   | 1    |
| 1.2. Previous Research .....            | 2    |
| 1.3. Objectives of Present Study .....  | 13   |
| 2. EXPERIMENTAL APPROACH .....          | 22   |
| 2.1. Overview .....                     | 22   |
| 2.2. Air Supply System .....            | 23   |
| 2.3. Fuel Supply System .....           | 26   |
| 2.4. Exhaust System .....               | 27   |
| 2.5. Experimental Apparatus .....       | 28   |
| 2.5.1. Inlet Pipe Section.....          | 28   |
| 2.5.2. Combustion Chamber.....          | 29   |

|   |    |
|---|----|
| 2.5.3. Inlet Swirler.....   | 30 |
| 2.5.4. Pressure Throttle Valve.....   | 32 |
| 2.5.5. Ignition System.....   | 32 |
| 2.6. Instrumentation and Data Acquisition.....  | 33 |
| 2.6.1. Flow Measurement.....  | 33 |
| 2.6.2. Pressure and Temperature Measurement.....  | 35 |
| 2.6.3. Noise Measurement.....   | 36 |
| 2.6.4. Emissions Sampling.....  | 38 |
| 2.6.5. Data Acquisition System.....   | 38 |
| 2.7. Operating Procedure.....   | 40 |
| 2.7.1. Preliminary Tasks.....   | 40 |
| 2.7.2. Air Flow.....  | 41 |
| 2.7.3. Fuel Flow and Ignition.....  | 41 |
| 2.7.4. System Operation.....  | 42 |
| 2.7.5. System Shutdown.....   | 43 |
| 3. REDUCTION OF COMBUSTION NOISE AND ACOUSTIC INSTABILITIES WITH<br>POROUS INERT MEDIA..... | 72 |
| 3.1. Overview.....  | 72 |
| 3.2. Experimental Procedure.....  | 73 |
| 3.3. Results and Discussion.....  | 76 |
| 3.3.1. Effect of Microphone Location.....   | 77 |
| 3.3.2. Reduction in Combustion Noise.....   | 78 |
| 3.3.3. Elimination of Thermo-acoustic Instability.....                                      | 81 |
| 3.3.4. CO and NO <sub>x</sub> Emissions.....  | 81 |

|   |     |
|---|-----|
| 3.3.5. Pressure Drop.....   | 83  |
| 3.3.6. Effect of Air Flow Rate .....  | 84  |
| 3.3.7. Effect of Preheat Temperature.....   | 85  |
| 3.3.8. Effect of Equivalence Ratio.....   | 87  |
| 3.3.9. Effect of Swirler Location.....  | 88  |
| 3.3.10. Endurance Testing.....  | 89  |
| 4. CONCLUSIONS AND RECOMMENDATIONS .....  | 178 |
| 4.1. Conclusions .....  | 178 |
| 4.2. Recommendations .....  | 180 |
| REFERENCES .....  | 182 |
| APPENDIX A – DETAILED DRAWINGS OF COMBUSTOR.....  | 185 |
| APPENDIX B – CALCULATION OF SWIRL NUMBER FOR FLOW SWIRLER .....                             | 196 |
| APPENDIX C – CALCULATION OF AIR FLOW RATE, EQUIVALENCE RATIO,<br>AND REYNOLDS NUMBER .....  | 198 |
| APPENDIX D – SOUND PRESSURE LEVEL CALCULATION M-SCRIPT .....                                | 203 |
| APPENDIX E – SAMPLE CALCULATIONS OF O <sub>2</sub> AND CO <sub>2</sub> CONCENTRATIONS ..... | 217 |
| APPENDIX F – UNCERTAINTY ANALYSIS .....   | 219 |

## LIST OF TABLES

|     |   |     |
|-----|---|-----|
| 1.1 | Effect of pore density on total SPL reduction, Q = 300 SLPM ..... | 9   |
| 1.2 | Effect of PIM geometry on total SPL reduction, Q = 300 SLPM.....  | 9   |
| 1.3 | Summary of sound pressure levels for Q = 1020 SLPM.....           | 12  |
| 1.4 | Summary of Sound Pressure Levels for Q = 1400 SLPM .....          | 13  |
| 2.1 | Air supply system components.....                                 | 25  |
| 2.2 | Fuel supply system components.....                                | 28  |
| 2.3 | Instrumentation used for flow measurement.....                    | 35  |
| 3.1 | Characteristics of PIM.....                                       | 75  |
| 3.2 | Microphone position and corresponding SPL.....                    | 78  |
| 3.3 | Comparison of SPL without and with porous media.....              | 80  |
| C.1 | Reynolds number of reactant flow inside premixer pipe.....        | 201 |
| F.1 | Random sample measurements for air and fuel flow rates.....       | 220 |

## LIST OF FIGURES

|     |   |    |
|-----|---|----|
| 1.1 | Schematic diagram of swirl-stabilization process .....  | 15 |
| 1.2 | Porous insert located inside a swirl-stabilized combustor .....   | 16 |
| 1.3 | Velocity vectors for reacting flow where $\phi = 0.58$ (a) Without PIM (b) With PIM .....   | 17 |
| 1.4 | Schematic diagram of PIM configurations .....   | 18 |
| 1.5 | Photographic images (a) PIM insert (b) Combustor without PIM<br>(c) Combustor with PIM .....  | 19 |
| 1.6 | Flame images, (a) With PIM interior combustion (b) With PIM surface combustion ...  | 20 |
| 1.7 | Schematic diagrams of PIM assisted combustion, (a) Interior combustion<br>(b) Surface combustion .....  | 20 |
| 1.8 | Transverse emissions profiles (a) CO at $Q = 300$ SLPM, $\phi = 0.8$ , $T_{inlet} = 100$ °C<br>(b) NO <sub>x</sub> at $Q = 300$ SLPM, $\phi = 0.8$ , $T_{inlet} = 100$ °C (c) CO at $Q = 600$ SLPM,<br>$\phi = 0.8$ , $T_{inlet} = 120$ °C (d) NO <sub>x</sub> at $Q = 600$ SLPM, $\phi = 0.8$ , $T_{inlet} = 120$ °C ..... | 21 |
| 2.1 | General schematic of high pressure combustion laboratory .....  | 44 |
| 2.2 | Layout of air flow control system .....   | 45 |
| 2.3 | Top view layout of high pressure combustion laboratory .....  | 46 |
| 2.4 | Side view layout of high pressure combustion laboratory .....   | 47 |
| 2.5 | Electric air heater (a) Photographic image (b) Schematic diagram .....  | 48 |
| 2.6 | Outdoor fuel station .....  | 49 |
| 2.7 | Layout of fuel flow control system .....  | 50 |

|      |   |    |
|------|---|----|
| 2.8  | Photographic image (front view) of exhaust system .....                 | 51 |
| 2.9  | Side view of layout for exhaust system .....                            | 52 |
| 2.10 | Overhead view of layout for exhaust system .....                        | 53 |
| 2.11 | Back view of layout for exhaust system .....                            | 54 |
| 2.12 | Schematic of assembled experimental apparatus .....                     | 55 |
| 2.13 | Exploded view of experimental apparatus .....                           | 56 |
| 2.14 | Photographic image of experimental apparatus .....                      | 57 |
| 2.15 | Photographic image of experimental apparatus .....                      | 58 |
| 2.16 | Photographic image of experimental apparatus .....                      | 59 |
| 2.17 | Photographic image of swirler .....                                     | 60 |
| 2.18 | Detailed drawing of swirler .....                                       | 61 |
| 2.19 | Exploded schematic of variable swirler mechanism .....                  | 62 |
| 2.20 | Schematic diagram of swirler mechanism mounted inside inlet pipe .....  | 63 |
| 2.21 | Photographic image of pressure throttle valve .....                     | 64 |
| 2.22 | Schematic of pressure throttle valve .....                              | 65 |
| 2.23 | Photographic image of ignition probe .....                              | 66 |
| 2.24 | Photographic image of electrode gap .....                               | 66 |
| 2.25 | Schematic layout of flow control system .....                           | 67 |
| 2.26 | Emissions sampling probe .....  | 68 |
| 2.27 | Layout of NI CompactRIO data acquisition system .....                   | 69 |
| 2.28 | LabVIEW flow measurement front panel as displayed on operator PC .....  | 70 |
| 2.29 | LabVIEW noise measurement front panel as displayed on operator PC ..... | 71 |
| 3.1  | Schematic of experimental setup .....                                   | 91 |

|      |  |     |
|------|--|-----|
| 3.2  | Schematic of holding mechanism for quartz tube .....   | 92  |
| 3.3  | Drawing of porous inserts (a) PIM #1, (b) PIM #2, (c) PIM #3 .....   | 93  |
| 3.4  | SPL per 1/3 octave band for microphone location test .....   | 94  |
| 3.5  | Pressure oscillations over a 5 second range for selected case<br>in which instability is dominant, $T_{inlet} = 21^{\circ}\text{C}$ , $Q = 600$ SLPM, $\phi = 0.70$ .....  | 95  |
| 3.6  | SPL per 1/3 octave band for selected case in which<br>instability is dominant, $T_{inlet} = 21^{\circ}\text{C}$ , $Q = 600$ SLPM, $\phi = 0.70$ .....  | 96  |
| 3.7  | Photographic images showing an increase in flame length with porous media<br>(a) Flame photograph without PIM, (b) Flame photograph with PIM .....   | 97  |
| 3.8  | Adiabatic flame temperature for methane-air combustion with reactant<br>inlet temperatures of $T_{inlet} = 21^{\circ}\text{C}$ , $T_{inlet} = 130^{\circ}\text{C}$ , and $T_{inlet} = 260^{\circ}\text{C}$ ..... | 98  |
| 3.9  | Results for $T_{inlet} = 21^{\circ}\text{C}$ , $Q = 300$ SLPM, $\phi = 0.60$<br>(a) Flame photograph without PIM, (b) Flame photograph with PIM,<br>(c) Pressure drop measurements with and without PIM .....    | 99  |
| 3.10 | Results for $T_{inlet} = 21^{\circ}\text{C}$ , $Q = 300$ SLPM, $\phi = 0.60$ (a) SPL per 1/3 octave band,<br>(b) Spectral power, (c) NOx emissions, (d) CO emissions .....                                       | 100 |
| 3.11 | Results for $T_{inlet} = 21^{\circ}\text{C}$ , $Q = 300$ SLPM, $\phi = 0.65$<br>(a) Flame photograph without PIM, (b) Flame photograph with PIM,<br>(c) Pressure drop measurements with and without PIM .....    | 101 |
| 3.12 | Results for $T_{inlet} = 21^{\circ}\text{C}$ , $Q = 300$ SLPM, $\phi = 0.65$ (a) SPL per 1/3 octave band,<br>(b) Spectral power, (c) NOx emissions, (d) CO emissions .....                                       | 102 |
| 3.13 | Results for $T_{inlet} = 21^{\circ}\text{C}$ , $Q = 300$ SLPM, $\phi = 0.70$<br>(a) Flame photograph without PIM, (b) Flame photograph with PIM,<br>(c) Pressure drop measurements with and without PIM .....    | 103 |
| 3.14 | Results for $T_{inlet} = 21^{\circ}\text{C}$ , $Q = 300$ SLPM, $\phi = 0.70$ (a) SPL per 1/3 octave band,<br>(b) Spectral power, (c) NOx emissions, (d) CO emissions .....                                       | 104 |
| 3.15 | Results for $T_{inlet} = 21^{\circ}\text{C}$ , $Q = 300$ SLPM, $\phi = 0.75$<br>(a) Flame photograph without PIM, (b) Flame photograph with PIM,<br>(c) Pressure drop measurements with and without PIM .....    | 105 |
| 3.16 | Results for $T_{inlet} = 21^{\circ}\text{C}$ , $Q = 300$ SLPM, $\phi = 0.75$ (a) SPL per 1/3 octave band,<br>(b) Spectral power, (c) NOx emissions, (d) CO emissions .....                                       | 106 |

|      |   |     |
|------|---|-----|
| 3.17 | Results for $T_{inlet} = 21^{\circ}\text{C}$ , $Q = 600$ SLPM, $\phi = 0.60$<br>(a) Flame photograph without PIM, (b) Flame photograph with PIM,<br>(c) Pressure drop measurements with and without PIM ..... | 107 |
| 3.18 | Results for $T_{inlet} = 21^{\circ}\text{C}$ , $Q = 600$ SLPM, $\phi = 0.60$ (a) SPL per 1/3 octave band,<br>(b) Spectral power, (c) NO <sub>x</sub> emissions, (d) CO emissions .....                        | 108 |
| 3.19 | Results for $T_{inlet} = 21^{\circ}\text{C}$ , $Q = 600$ SLPM, $\phi = 0.65$<br>(a) Flame photograph without PIM, (b) Flame photograph with PIM,<br>(c) Pressure drop measurements with and without PIM ..... | 109 |
| 3.20 | Results for $T_{inlet} = 21^{\circ}\text{C}$ , $Q = 600$ SLPM, $\phi = 0.65$ (a) SPL per 1/3 octave band,<br>(b) Spectral power, (c) NO <sub>x</sub> emissions, (d) CO emissions .....                        | 110 |
| 3.21 | Results for $T_{inlet} = 21^{\circ}\text{C}$ , $Q = 600$ SLPM, $\phi = 0.70$<br>(a) Flame photograph without PIM, (b) Flame photograph with PIM,<br>(c) Pressure drop measurements with and without PIM ..... | 111 |
| 3.22 | Results for $T_{inlet} = 21^{\circ}\text{C}$ , $Q = 600$ SLPM, $\phi = 0.70$ (a) SPL per 1/3 octave band,<br>(b) Spectral power, (c) NO <sub>x</sub> emissions, (d) CO emissions .....                        | 112 |
| 3.23 | Results for $T_{inlet} = 21^{\circ}\text{C}$ , $Q = 600$ SLPM, $\phi = 0.75$<br>(a) Flame photograph without PIM, (b) Flame photograph with PIM,<br>(c) Pressure drop measurements with and without PIM ..... | 113 |
| 3.24 | Results for $T_{inlet} = 21^{\circ}\text{C}$ , $Q = 600$ SLPM, $\phi = 0.75$ (a) SPL per 1/3 octave band,<br>(b) Spectral power, (c) NO <sub>x</sub> emissions, (d) CO emissions .....                        | 114 |
| 3.25 | Results for $T_{inlet} = 21^{\circ}\text{C}$ , $Q = 900$ SLPM, $\phi = 0.60$<br>(a) Flame photograph without PIM, (b) Flame photograph with PIM,<br>(c) Pressure drop measurements with and without PIM ..... | 115 |
| 3.26 | Results for $T_{inlet} = 21^{\circ}\text{C}$ , $Q = 900$ SLPM, $\phi = 0.60$ (a) SPL per 1/3 octave band,<br>(b) Spectral power, (c) NO <sub>x</sub> emissions, (d) CO emissions .....                        | 116 |
| 3.27 | Results for $T_{inlet} = 21^{\circ}\text{C}$ , $Q = 900$ SLPM, $\phi = 0.65$<br>(a) Flame photograph without PIM, (b) Flame photograph with PIM,<br>(c) Pressure drop measurements with and without PIM ..... | 117 |
| 3.28 | Results for $T_{inlet} = 21^{\circ}\text{C}$ , $Q = 900$ SLPM, $\phi = 0.65$ (a) SPL per 1/3 octave band,<br>(b) Spectral power, (c) NO <sub>x</sub> emissions, (d) CO emissions .....                        | 118 |
| 3.29 | Results for $T_{inlet} = 21^{\circ}\text{C}$ , $Q = 900$ SLPM, $\phi = 0.70$<br>(a) Flame photograph without PIM, (b) Flame photograph with PIM,<br>(c) Pressure drop measurements with and without PIM ..... | 119 |

|      |   |     |
|------|---|-----|
| 3.30 | Results for $T_{\text{inlet}} = 21^{\circ}\text{C}$ , $Q = 900$ SLPM, $\phi = 0.70$ (a) SPL per 1/3 octave band, (b) Spectral power, (c) NO <sub>x</sub> emissions, (d) CO emissions .....                            | 120 |
| 3.31 | Results for $T_{\text{inlet}} = 21^{\circ}\text{C}$ , $Q = 900$ SLPM, $\phi = 0.75$<br>(a) Flame photograph without PIM, (b) Flame photograph with PIM,<br>(c) Pressure drop measurements with and without PIM .....  | 121 |
| 3.32 | Results for $T_{\text{inlet}} = 21^{\circ}\text{C}$ , $Q = 900$ SLPM, $\phi = 0.75$ (a) SPL per 1/3 octave band,<br>(b) Spectral power, (c) NO <sub>x</sub> emissions, (d) CO emissions .....                         | 122 |
| 3.33 | Results for $T_{\text{inlet}} = 130^{\circ}\text{C}$ , $Q = 300$ SLPM, $\phi = 0.60$<br>(a) Flame photograph without PIM, (b) Flame photograph with PIM,<br>(c) Pressure drop measurements with and without PIM ..... | 123 |
| 3.34 | Results for $T_{\text{inlet}} = 130^{\circ}\text{C}$ , $Q = 300$ SLPM, $\phi = 0.60$ (a) SPL per 1/3 octave band,<br>(b) Spectral power, (c) NO <sub>x</sub> emissions, (d) CO emissions .....                        | 124 |
| 3.35 | Results for $T_{\text{inlet}} = 130^{\circ}\text{C}$ , $Q = 300$ SLPM, $\phi = 0.65$<br>(a) Flame photograph without PIM, (b) Flame photograph with PIM,<br>(c) Pressure drop measurements with and without PIM ..... | 125 |
| 3.36 | Results for $T_{\text{inlet}} = 130^{\circ}\text{C}$ , $Q = 300$ SLPM, $\phi = 0.65$ (a) SPL per 1/3 octave band,<br>(b) Spectral power, (c) NO <sub>x</sub> emissions, (d) CO emissions .....                        | 126 |
| 3.37 | Results for $T_{\text{inlet}} = 130^{\circ}\text{C}$ , $Q = 300$ SLPM, $\phi = 0.70$<br>(a) Flame photograph without PIM, (b) Flame photograph with PIM,<br>(c) Pressure drop measurements with and without PIM ..... | 127 |
| 3.38 | Results for $T_{\text{inlet}} = 130^{\circ}\text{C}$ , $Q = 300$ SLPM, $\phi = 0.70$ (a) SPL per 1/3 octave band,<br>(b) Spectral power, (c) NO <sub>x</sub> emissions, (d) CO emissions .....                        | 128 |
| 3.39 | Results for $T_{\text{inlet}} = 130^{\circ}\text{C}$ , $Q = 300$ SLPM, $\phi = 0.75$<br>(a) Flame photograph without PIM, (b) Flame photograph with PIM,<br>(c) Pressure drop measurements with and without PIM ..... | 129 |
| 3.40 | Results for $T_{\text{inlet}} = 130^{\circ}\text{C}$ , $Q = 300$ SLPM, $\phi = 0.75$ (a) SPL per 1/3 octave band,<br>(b) Spectral power, (c) NO <sub>x</sub> emissions, (d) CO emissions .....                        | 130 |
| 3.41 | Results for $T_{\text{inlet}} = 130^{\circ}\text{C}$ , $Q = 600$ SLPM, $\phi = 0.60$<br>(a) Flame photograph without PIM, (b) Flame photograph with PIM,<br>(c) Pressure drop measurements with and without PIM ..... | 131 |
| 3.42 | Results for $T_{\text{inlet}} = 130^{\circ}\text{C}$ , $Q = 600$ SLPM, $\phi = 0.60$ (a) SPL per 1/3 octave band,<br>(b) Spectral power, (c) NO <sub>x</sub> emissions, (d) CO emissions .....                        | 132 |

|      |   |     |
|------|---|-----|
| 3.43 | Results for $T_{\text{inlet}} = 130^{\circ}\text{C}$ , $Q = 600$ SLPM, $\phi = 0.65$<br>(a) Flame photograph without PIM, (b) Flame photograph with PIM,<br>(c) Pressure drop measurements with and without PIM ..... | 133 |
| 3.44 | Results for $T_{\text{inlet}} = 130^{\circ}\text{C}$ , $Q = 600$ SLPM, $\phi = 0.65$ (a) SPL per 1/3 octave band,<br>(b) Spectral power, (c) NO <sub>x</sub> emissions, (d) CO emissions .....                        | 134 |
| 3.45 | Results for $T_{\text{inlet}} = 130^{\circ}\text{C}$ , $Q = 600$ SLPM, $\phi = 0.70$<br>(a) Flame photograph without PIM, (b) Flame photograph with PIM,<br>(c) Pressure drop measurements with and without PIM ..... | 135 |
| 3.46 | Results for $T_{\text{inlet}} = 130^{\circ}\text{C}$ , $Q = 600$ SLPM, $\phi = 0.70$ (a) SPL per 1/3 octave band,<br>(b) Spectral power, (c) NO <sub>x</sub> emissions, (d) CO emissions .....                        | 136 |
| 3.47 | Results for $T_{\text{inlet}} = 130^{\circ}\text{C}$ , $Q = 600$ SLPM, $\phi = 0.75$<br>(a) Flame photograph without PIM, (b) Flame photograph with PIM,<br>(c) Pressure drop measurements with and without PIM ..... | 137 |
| 3.48 | Results for $T_{\text{inlet}} = 130^{\circ}\text{C}$ , $Q = 600$ SLPM, $\phi = 0.75$ (a) SPL per 1/3 octave band,<br>(b) Spectral power, (c) NO <sub>x</sub> emissions, (d) CO emissions .....                        | 138 |
| 3.49 | Results for $T_{\text{inlet}} = 130^{\circ}\text{C}$ , $Q = 900$ SLPM, $\phi = 0.60$<br>(a) Flame photograph without PIM, (b) Flame photograph with PIM .....   | 139 |
| 3.50 | Results for $T_{\text{inlet}} = 130^{\circ}\text{C}$ , $Q = 900$ SLPM, $\phi = 0.60$ (a) SPL per 1/3 octave band,<br>(b) Spectral power, (c) NO <sub>x</sub> emissions, (d) CO emissions .....                        | 140 |
| 3.51 | Results for $T_{\text{inlet}} = 130^{\circ}\text{C}$ , $Q = 900$ SLPM, $\phi = 0.65$<br>(a) Flame photograph without PIM, (b) Flame photograph with PIM .....   | 141 |
| 3.52 | Results for $T_{\text{inlet}} = 130^{\circ}\text{C}$ , $Q = 900$ SLPM, $\phi = 0.65$ (a) SPL per 1/3 octave band,<br>(b) Spectral power, (c) NO <sub>x</sub> emissions, (d) CO emissions .....                        | 142 |
| 3.53 | Results for $T_{\text{inlet}} = 130^{\circ}\text{C}$ , $Q = 900$ SLPM, $\phi = 0.70$<br>(a) Flame photograph without PIM, (b) Flame photograph with PIM .....   | 143 |
| 3.54 | Results for $T_{\text{inlet}} = 130^{\circ}\text{C}$ , $Q = 900$ SLPM, $\phi = 0.70$ (a) SPL per 1/3 octave band,<br>(b) Spectral power, (c) NO <sub>x</sub> emissions, (d) CO emissions .....                        | 144 |
| 3.55 | Results for $T_{\text{inlet}} = 130^{\circ}\text{C}$ , $Q = 900$ SLPM, $\phi = 0.75$<br>(a) Flame photograph without PIM, (b) Flame photograph with PIM .....   | 145 |
| 3.56 | Results for $T_{\text{inlet}} = 130^{\circ}\text{C}$ , $Q = 900$ SLPM, $\phi = 0.75$ (a) SPL per 1/3 octave band,<br>(b) Spectral power, (c) NO <sub>x</sub> emissions, (d) CO emissions .....                        | 146 |

|      |   |     |
|------|---|-----|
| 3.57 | Results for $T_{inlet} = 260^{\circ}C$ , $Q = 300$ SLPM, $\phi = 0.60$<br>(a) Flame photograph without PIM, (b) Flame photograph with PIM,<br>(c) Pressure drop measurements with and without PIM ..... | 147 |
| 3.58 | Results for $T_{inlet} = 260^{\circ}C$ , $Q = 300$ SLPM, $\phi = 0.60$ (a) SPL per 1/3 octave band,<br>(b) Spectral power, (c) NOx emissions, (d) CO emissions .....                                    | 148 |
| 3.59 | Results for $T_{inlet} = 260^{\circ}C$ , $Q = 300$ SLPM, $\phi = 0.65$<br>(a) Flame photograph without PIM, (b) Flame photograph with PIM,<br>(c) Pressure drop measurements with and without PIM ..... | 149 |
| 3.60 | Results for $T_{inlet} = 260^{\circ}C$ , $Q = 300$ SLPM, $\phi = 0.65$ (a) SPL per 1/3 octave band,<br>(b) Spectral power, (c) NOx emissions, (d) CO emissions .....                                    | 150 |
| 3.61 | Results for $T_{inlet} = 260^{\circ}C$ , $Q = 300$ SLPM, $\phi = 0.70$<br>(a) Flame photograph without PIM, (b) Flame photograph with PIM,<br>(c) Pressure drop measurements with and without PIM ..... | 151 |
| 3.62 | Results for $T_{inlet} = 260^{\circ}C$ , $Q = 300$ SLPM, $\phi = 0.70$ (a) SPL per 1/3 octave band,<br>(b) Spectral power, (c) NOx emissions, (d) CO emissions .....                                    | 152 |
| 3.63 | Results for $T_{inlet} = 260^{\circ}C$ , $Q = 300$ SLPM, $\phi = 0.75$<br>(a) Flame photograph without PIM, (b) Flame photograph with PIM,<br>(c) Pressure drop measurements with and without PIM ..... | 153 |
| 3.64 | Results for $T_{inlet} = 260^{\circ}C$ , $Q = 300$ SLPM, $\phi = 0.75$ (a) SPL per 1/3 octave band,<br>(b) Spectral power, (c) NOx emissions, (d) CO emissions .....                                    | 154 |
| 3.65 | Results for $T_{inlet} = 260^{\circ}C$ , $Q = 600$ SLPM, $\phi = 0.60$<br>(a) Flame photograph without PIM, (b) Flame photograph with PIM,<br>(c) Pressure drop measurements with and without PIM ..... | 155 |
| 3.66 | Results for $T_{inlet} = 260^{\circ}C$ , $Q = 600$ SLPM, $\phi = 0.60$ (a) SPL per 1/3 octave band,<br>(b) Spectral power, (c) NOx emissions, (d) CO emissions .....                                    | 156 |
| 3.67 | Results for $T_{inlet} = 260^{\circ}C$ , $Q = 600$ SLPM, $\phi = 0.65$<br>(a) Flame photograph without PIM, (b) Flame photograph with PIM,<br>(c) Pressure drop measurements with and without PIM ..... | 157 |
| 3.68 | Results for $T_{inlet} = 260^{\circ}C$ , $Q = 600$ SLPM, $\phi = 0.65$ (a) SPL per 1/3 octave band,<br>(b) Spectral power, (c) NOx emissions, (d) CO emissions .....                                    | 158 |
| 3.69 | Results for $T_{inlet} = 260^{\circ}C$ , $Q = 600$ SLPM, $\phi = 0.70$<br>(a) Flame photograph without PIM, (b) Flame photograph with PIM,<br>(c) Pressure drop measurements with and without PIM ..... | 159 |

|      |  |     |
|------|--|-----|
| 3.70 | Results for $T_{inlet} = 260^{\circ}\text{C}$ , $Q = 600$ SLPM, $\phi = 0.70$ (a) SPL per 1/3 octave band, (b) Spectral power, (c) NO <sub>x</sub> emissions, (d) CO emissions .....   | 160 |
| 3.71 | Results for $T_{inlet} = 260^{\circ}\text{C}$ , $Q = 600$ SLPM, $\phi = 0.75$<br>(a) Flame photograph without PIM, (b) Flame photograph with PIM,<br>(c) Pressure drop measurements with and without PIM .....   | 161 |
| 3.72 | Results for $T_{inlet} = 260^{\circ}\text{C}$ , $Q = 600$ SLPM, $\phi = 0.75$ (a) SPL per 1/3 octave band, (b) Spectral power, (c) NO <sub>x</sub> emissions, (d) CO emissions .....   | 162 |
| 3.73 | Results for flush mounted swirler, $T_{inlet} = 21^{\circ}\text{C}$ , $Q = 600$ SLPM, $\phi = 0.60$<br>(a) Flame photograph without PIM, (b) Flame photograph with PIM,<br>(c) SPL per 1/3 octave band, (d) Spectral power .....                                   | 163 |
| 3.74 | Results for flush mounted swirler, $T_{inlet} = 21^{\circ}\text{C}$ , $Q = 600$ SLPM, $\phi = 0.65$<br>(a) Flame photograph without PIM, (b) Flame photograph with PIM,<br>(c) SPL per 1/3 octave band, (d) Spectral power .....                                   | 164 |
| 3.75 | Results for flush mounted swirler, $T_{inlet} = 21^{\circ}\text{C}$ , $Q = 600$ SLPM, $\phi = 0.70$<br>(a) Flame photograph without PIM, (b) Flame photograph with PIM,<br>(c) SPL per 1/3 octave band, (d) Spectral power .....                                   | 165 |
| 3.76 | Results for flush mounted swirler, $T_{inlet} = 21^{\circ}\text{C}$ , $Q = 600$ SLPM, $\phi = 0.75$<br>(a) Flame photograph without PIM, (b) Flame photograph with PIM,<br>(c) SPL per 1/3 octave band, (d) Spectral power .....                                   | 166 |
| 3.77 | Results for recessed swirler, $T_{inlet} = 21^{\circ}\text{C}$ , $Q = 600$ SLPM, $\phi = 0.60$<br>(a) Flame photograph without PIM, (b) Flame photograph with PIM,<br>(c) SPL per 1/3 octave band, (d) Spectral power .....  | 167 |
| 3.78 | Results for recessed swirler, $T_{inlet} = 21^{\circ}\text{C}$ , $Q = 600$ SLPM, $\phi = 0.65$<br>(a) Flame photograph without PIM, (b) Flame photograph with PIM,<br>(c) SPL per 1/3 octave band, (d) Spectral power .....  | 168 |
| 3.79 | Results for recessed swirler, $T_{inlet} = 21^{\circ}\text{C}$ , $Q = 600$ SLPM, $\phi = 0.70$<br>(a) Flame photograph without PIM, (b) Flame photograph with PIM,<br>(c) SPL per 1/3 octave band, (d) Spectral power .....  | 169 |
| 3.80 | Results for recessed swirler, $T_{inlet} = 21^{\circ}\text{C}$ , $Q = 600$ SLPM, $\phi = 0.75$<br>(a) Flame photograph without PIM, (b) Flame photograph with PIM,<br>(c) SPL per 1/3 octave band, (d) Spectral power .....  | 170 |
| 3.81 | Flame photographs from endurance test, $T_{inlet} = 21^{\circ}\text{C}$ , $Q = 600$ SLPM, $\phi = 0.70$<br>(a) Baseline case without PIM (b) Immediately after ignition with PIM<br>(c) 5 hours after ignition with PIM (d) 10 hours after ignition with PIM ..... | 171 |

|      |  |     |
|------|--|-----|
| 3.82 | Results for endurance test immediately after ignition, $T_{inlet} = 21^{\circ}\text{C}$ ,<br>$Q = 600$ SLPM, $\phi = 0.70$ (a) SPL per 1/3 octave band, (b) Spectral power,<br>(c) NOx emissions, (d) CO emissions ..... | 172 |
| 3.83 | Results for endurance test 2 hours after ignition, $T_{inlet} = 21^{\circ}\text{C}$ ,<br>$Q = 600$ SLPM, $\phi = 0.70$ (a) SPL per 1/3 octave band,<br>(b) Spectral power, (c) NOx emissions, (d) CO emissions .....     | 173 |
| 3.84 | Results for endurance test 4 hours after ignition, $T_{inlet} = 21^{\circ}\text{C}$ ,<br>$Q = 600$ SLPM, $\phi = 0.70$ (a) SPL per 1/3 octave band,<br>(b) Spectral power, (c) NOx emissions, (d) CO emissions .....     | 174 |
| 3.85 | Results for endurance test 6 hours after ignition, $T_{inlet} = 21^{\circ}\text{C}$ ,<br>$Q = 600$ SLPM, $\phi = 0.70$ (a) SPL per 1/3 octave band,<br>(b) Spectral power, (c) NOx emissions, (d) CO emissions .....     | 175 |
| 3.86 | Results for endurance test 8 hours after ignition, $T_{inlet} = 21^{\circ}\text{C}$ ,<br>$Q = 600$ SLPM, $\phi = 0.70$ (a) SPL per 1/3 octave band,<br>(b) Spectral power, (c) NOx emissions, (d) CO emissions .....     | 176 |
| 3.87 | Results for endurance test 10 hours after ignition, $T_{inlet} = 21^{\circ}\text{C}$ ,<br>$Q = 600$ SLPM, $\phi = 0.70$ (a) SPL per 1/3 octave band,<br>(b) Spectral power, (c) NOx emissions, (d) CO emissions .....    | 177 |
| A.1  | Details of plenum base .....   | 186 |
| A.2  | Details of support pipe and flange .....   | 187 |
| A.3  | Details of assembled plenum base .....   | 188 |
| A.4  | Details of enclosure .....   | 189 |
| A.5  | Detail of faces of enclosure .....   | 190 |
| A.6  | Details of cross section of enclosure .....  | 191 |
| A.7  | Details of access ports on enclosure .....   | 192 |
| A.8  | Details of windows ports .....   | 193 |
| A.9  | Details of window covers .....   | 194 |
| A.1  | Details of window .....  | 195 |
| B.1  | Schematic of flow swirler .....  | 196 |

# CHAPTER 1

## INTRODUCTION

### 1.1 Background

Combustion is a major source of noise production in gas turbine engines and industrial burners. As a result of heightened awareness in both industry and society, noise emissions have become increasingly important and have gained considerable attention among the scientific community. Unsteady heat release in a turbulent reacting mixture causes pressure fluctuations, which propagate outwards as sound waves (Sequera & Agrawal, 2011). Resulting sound waves not only create an audible disturbance for nearby personnel, but may also lead to excessive structural vibrations which can severely damage components and cause catastrophic failure. Component damage from combustion instability is especially relevant in highly critical applications such as gas turbine engines for aircraft propulsion. Most modern combustion systems involve complex, embedded combustion chambers coupled with highly turbulent flow fields. As a result, combustion noise generation in these systems is often a result of a combination of multiple mechanisms that work in combination to cause fluctuations within the combustor flame region. These individual mechanisms and the manner in which they couple with one another are not entirely understood. Thus, an opportunity is presented for engineers to develop a more complete knowledge of the noise generation process in combustion systems and to develop robust methods for mitigating combustion noise and acoustic instability.

## 1.2 Previous Research

Early research on combustion noise was investigated by Putnam (1971) and Strahle (1978), who present analytical models and provide empirical data for sound pressure level (SPL) as a function of common combustion parameters such as combustor geometry, fuel type, reactant flow rate, and air/fuel ratio. More recently, research emphasis has focused on lean premixed (LPM) combustion systems. The extensive use of LPM combustion systems for large-scale industrial and commercial applications is largely driven by compliance requirements of increasingly stringent emissions regulations. While LPM combustion systems operate at reduced flame temperatures and have proven to provide reduced levels of harmful emissions, especially nitrous oxides (NO<sub>x</sub>), these systems are inherently susceptible to combustion noise as well as acoustic instability resulting from fluctuating heat release coupled with fixed-frequency feedback oscillations (Sequera & Agrawal, 2009).

In a conventional swirl-stabilized LPM combustion system, a premixed stream of reactants is routed through an annular swirler and into the combustion chamber. The swirling flow undergoes rapid expansion at the dump plane where an inner recirculation zone (IRZ) and an outer recirculation zone (ORZ) are created on either side of the annular jet (Lieuwen & Yang, 2005; Schefer, Wicksall, & Agrawal, 2002). A diagram illustrating the respective locations of recirculation zones within the combustion chamber is given in Figure 1.1. The recirculation zones function to stabilize the flame as hot product gases are trapped and recirculated to ignite incoming reactants, thereby sustaining reactions in a compact region. The local flow field within these recirculation zones is highly turbulent, characterized by the existence of vortical structures having a broad range of length and time scales (Wicksall, Agrawal, Schefer, & Keller, 2005). In a swirl-stabilized system, vortical structures are generally formed in the shear layer along the

interface of high speed flow of incoming reactants and low speed flow of recirculating product gases (Schadow & Gutmark, 1992). Furthermore, characteristics of these structures are largely influenced by combustor geometry, dump ratio, and system operating conditions (Huang & Yang, 2009).

While combustion noise and acoustic instability are unique outcomes, both originate from the same source - unsteady heat release in a turbulent reacting flow. In accordance with Rayleigh's criterion (Rayleigh, 1945), combustion instability develops if heat release from the oxidation of fuel adds energy to the acoustic field faster than energy can be removed by viscous dissipation and heat transfer. As such, fluctuating vortical flow structures tend to excite pre-existent pressure oscillations, thereby increasing the likelihood of instability formation (Schadow, Gutmark, Wilson, & Smith, 1988)

Recently, a variety of experimental and computational studies have been conducted in an attempt to gain a more complete understanding of combustion noise generation (Choi, Tanahashi, & Miyauchi, 2005; Duchaine, Zimmer, & Schuller, 2009; Flemming et al., 2005; Hirsch, Wasle, Winkler, & Sattelmayer, 2007; Rajaram, Gray, & Lieuwen, 2006; Schwarz & Janicka, 2009; Tiribuzi, 2008). Additionally, a number of studies have been performed to investigate formation mechanisms and control of combustion instability (Huang & Yang, 2009; Lee & Santavicca, 2003; Noiray, Durox, Schuller, & Candel, 2009; Richards & Straub, 2003; Sreenivasan & Raghu, 2000; Steele, Cowell, Cannon, & Smith, 2000). Most notably, advances in computational fluid dynamics (CFD) capability have presented the opportunity to model reacting flows in greater detail. Detailed chemical kinetics can be incorporated with turbulent flow and acoustic fields to generate a moderately robust computational model. The aforementioned studies have identified a number of passive and active techniques to control

combustion noise and thermo-acoustic instabilities. Usefulness of an active control system is highly dependent on the synchronous operation of sensors, actuators, and control schemes (Sequera & Agrawal, 2011). Considerable advances have been made in these areas; however extensive reliability is still a major concern with the use of active control techniques. Complete reliability is of great importance since powerful instabilities can destroy the combustor within a fraction of a second. Current passive techniques make use of baffles intended to suppress standing acoustic waves, acoustic liners, and Helmholtz resonators, which provide dampening and dissipation of acoustic energy within the system (Richards & Straub, 2003; Sreenivasan and Raghu, 2000; Steele et al., 2000). Helmholtz resonators employ a quarter-wave tube aimed at introducing favorable interference between interactions of acoustic pressure waves and waves caused by unsteady heat release during combustion. These strategies seek to dissipate acoustic energy as flow enters and exits the damping element.

Recently, a passive technique to mitigate combustion noise in a swirl-stabilized, LPM combustor using an in-situ passive device was developed by Agrawal & Vijaykant (2010). The technique involves placing an open-cell structure of porous inert material (PIM) directly at the dump plane of the combustor. The PIM is a ceramic matrix alloyed with a hafnium carbide / silicon carbide (HfC/SiC) coating which resists high temperature oxidation while being exposed to combustion. Refractory surface oxides can withstand operating temperatures up to 1800 °C (Agrawal & Vijaykant, 2010). The porous foam is distinguished by its porosity (percentage of void volume) and pore density (number of pores per unit length). The pore density is generally indicated in units of pores per inch (ppi) or pores per cm (ppcm). Both porosity and pore density of the insert have been shown to affect flow structure and pressure drop across the PIM (Marbach & Agrawal, 2005).

As shown in Figure 1.2, the ring-shaped porous insert is placed at the dump plane of the combustor. In accordance with Richards and Straub (2003), the PIM functions as an acoustic dampener by dissipating energy through porous channels in the porous material. While the PIM does provide significant acoustic damping, it also drastically affects the combustor flow field. The insert modifies the flow field in such a way as to shift location and intensity of recirculation zones, and thus heat release rates within the combustor. The concept is fundamentally different from previous PIM techniques which utilize flame stabilization on either the surface or interior regions of the porous media (Fernandez-Pello, 2002; Howell, Hall, & Ellzey, 1996; Marbach, Sadasivuni, & Agrawal, 2007; Trimis & Durst, 1996; Waitz, Gauba, & Tzeng, 1998). The technique prescribed by Agrawal and Vijaykant (2010) involves positioning the porous insert around the flame produced in a swirl-stabilized combustor to improve performance. A CFD analysis was performed by Sequera and Agrawal (2011) to gain a preliminary understanding of the flow field without and with porous media.

The CFD analysis is not entirely detailed regarding full characterization of the wide variety of length and time scales of vortical and shear layer structures within the combustor. Rather, it is performed to acquire preliminary insight into the mean flow field without and with PIM. As such, the combustor is modeled as a two-dimensional (2D) axisymmetric geometry with swirling flow, in which it is assumed that no circumferential gradients exist in the flow field (Sequera & Agrawal, 2009). Continuity and momentum equations are solved in the axial, radial, and circumferential directions to predict resulting flow behavior within the combustor. A sink term in the momentum equation is used to represent flow resistance associated with the porous media. The sink term is determined by a power law correlation based on experimental data obtained by Marbach and Agrawal (2006). The turbulent flow regime is modeled with the RNG

k- $\epsilon$  turbulence model and thermal conductivity is computed as a weighted average of solid and fluid conductivities characterized by the porosity of the PIM (Sequera & Agrawal, 2009).

Combustion reactions are modeled with a turbulent premixed combustion model based on the work of Zimont et al. (1995, 1998, & 2000). The model entails solving a transport equation for the reaction progress variable, where solution closure is established using the definition of turbulent flame speed.

The combustor is represented by a computational domain extending 300 mm in the axial direction and 40 mm in the radial direction. Porous foam is modeled to be 80 mm outer diameter (OD), 40 mm inner diameter (ID), and 25 mm in height, placed directly at the combustor dump plane. Flow enters the combustor at a swirl angle of  $28^\circ$  through an annular channel between radial locations of 10 and 20 mm. Velocity components in the radial, axial, and swirl directions are specified at the inlet boundary based on simplified assumptions coupled with experimental data of Gupta, Lilley, and Syred (1984). Axial velocity is taken to be 5 m/s, which corresponds with bulk inlet velocity of the experimental combustor. Turbulent intensity is specified as 10% of the total kinetic energy and turbulent length scale is taken as 1.5 mm. At the combustor inlet, reaction progress is specified to be zero, representing the unburnt mixture of reactants. The computational model is presented in greater detail in a dissertation by Sequera (2011), which also contains grid size convergence analysis and validation with experimental data of Wicksall et al. (2005).

A velocity vector plot for combustion of premixed methane-air without and with PIM is shown in Figure 1.3 for equivalence ratio,  $\phi = 0.58$ . For combustion without porous media, depicted in Figure 1.3(a), large recirculation zones are present in the central and corner regions of the combustor, just downstream of the dump plane. Corner recirculation zones are formed as

a result of a sudden expansion in cross-sectional area as the reactants enter the combustor. The central recirculation zone is very wide, which forces combustion reactions to take place near the wall of the combustor. Figure 1.3(b) shows that the addition of porous material has a dramatic effect on the flow field within the combustor. PIM eliminates corner recirculation zones and produces a more evenly distributed flow profile. Because radial flow is restricted by the PIM, the central recirculation zone is much narrower and combustion takes place in a more central region above the swirler, rather than near the combustor wall.

In conjunction with CFD analysis, Sequera and Agrawal (2011) conducted a range of experimental tests to examine the effectiveness of using porous media to mitigate noise in a swirl-stabilized combustor. The study also seeks to identify effects of PIM characteristics such as porosity, pore density, and PIM geometry on the overall effectiveness of the technique. Figure 1.4 gives a schematic diagram and brief description for each case examined. Photographs of the combustion chamber without and with PIM are provided in Figure 1.5. The experiment is conducted for methane-air combustion with air flow rate of 300 SLPM at equivalence ratios  $\phi = 0.70$  and  $0.80$ . Total sound pressure level (SPL) is measured for each configuration of porous material and compared with a baseline case without PIM. Configurations B, C, and D are compared with the baseline case A to examine effects of pore density on total SPL reduction. As shown in Table 1.2, total SPL decreases with increasing pore density, and the greatest reduction is achieved with case D, where pore density is 18 ppcm. For case D, SPL reduction is 7.6 dB at  $\phi = 0.7$  and 4.1 dB at  $\phi = 0.8$ . To investigate effects of PIM geometry, configurations D, E, F, G, and H are compared with baseline case A. The shape of the annular void is varied to achieve straight, divergent, and convergent geometries by stacking two porous inserts as depicted in Figure 1.4. Total SPL is measured for each case as shown in Table 1.2. The divergent shapes,

cases D and E, are most effective in reducing combustion noise. While constant and convergent shaped configurations provide some reduction at  $\phi = 0.7$ , they are not as effective as the divergent shape, especially at  $\phi = 0.8$ . The lack of reduction in these cases can likely be attributed to flame stabilization within the porous media rather than on the downstream surface of the PIM (Sequera and Agrawal, 2011).

Flame stabilization modes for combustion with porous media are shown to have a drastic effect on noise production. In the study by Sequera and Agrawal (2011), two distinct modes of combustion are identified: interior combustion and surface combustion. Interior combustion mode occurs when combustion reactions are sustained within the porous media as displayed in Figure 1.6(a). The porous foam becomes orange in color as intense heat release takes place within the PIM. In surface combustion mode, a portion of reactants diffuse through the porous material and small flamelets stabilize along the upper surface of the PIM as shown in Figure 1.6(b). In both modes, the central flame is swirl-stabilized within the annular void of the porous insert. Figure 1.7 provides a schematic illustration of both interior and surface combustion modes. The study identifies surface combustion as the most effective mode for noise reduction in a swirl-stabilized LPM combustor. Interior combustion mode provides significantly less noise reduction while exposing the PIM to high temperatures, resulting in the possibility of structural damage to the porous material.

Table 1.1

*Effect of pore density on total SPL reduction,  $Q = 300$  SLPM (Sequera & Agrawal, 2011)*

| Configuration | $\Phi = 0.7$ | $\Phi = 0.8$ | Pore density (ppcm) |
|---------------|--------------|--------------|---------------------|
| A             | 103.0 dB     | 103.9 dB     | N/A                 |
| B             | 100.1 dB     | 107.1 dB     | 4                   |
| C             | 96.2 dB      | 104.9 dB     | 8                   |
| D             | 95.4 dB      | 99.8 dB      | 18                  |

Table 1.2

*Effect of PIM geometry on total SPL reduction,  $Q = 300$  SLPM (Sequera & Agrawal, 2011)*

| Configuration | $\Phi = 0.7$ | $\Phi = 0.8$ | Inside wall |
|---------------|--------------|--------------|-------------|
| A             | 103.0 dB     | 103.9 dB     | N/A         |
| D             | 95.4 dB      | 99.8 dB      | Divergent   |
| E             | 95.4 dB      | 99.9 dB      |             |
| F             | 95.7 dB      | 99.8 dB      | Constant    |
| G             | 96.1 dB      | 104.8 dB     |             |
| H             | 96.2 dB      | 106.8 dB     | Convergent  |
| I             | 96.2 dB      | 106.8 dB     |             |

Interior and surface combustion modes alter the combustion process in fundamentally different manners. As previously stated, the PIM functions as a damper to dissipate acoustic energy in the nearby flame. Since reactions occur adjacent to the porous foam during surface combustion, the PIM is able to suppress turbulent fluctuations in the swirl-stabilized central flame. In interior mode, however, reactions are contained within the PIM and inhibit the ability of the porous material to dampen pressure fluctuations. Additionally, surface flamelets help to distribute reaction zones, and thus, local heat release. Distributed heat release zones reduce pressure fluctuations, thereby decreasing the opportunity of coupling within the system. Conversely, interior combustion concentrates reactions into a region of dense heat release within the PIM, which adversely affects noise generation and combustion instability. In either mode, the PIM functions to eliminate turbulent structures created in the corner recirculation zone. This may explain the reduction in noise for some cases undergoing interior combustion (Sequera & Agrawal, 2011). Even so, the most favorable mode is surface combustion since it provides three mechanisms to reduce noise: attenuation of thermo-acoustic waves, distribution of heat release rate, and elimination of corner recirculation zones. Sequera and Agrawal (2011) point out that a non-porous block could be used to eliminate corner recirculation zones, but would not offer the benefit of pressure attenuation or distributed heat release rate.

For all experiments conducted by Sequera and Agrawal (2011), exhaust products are sampled to measure concentrations of NO<sub>x</sub> and CO. Transverse profiles of emissions are shown in Figure 1.8 for cases where  $Q = 300$  SLPM,  $\phi = 0.8$ ,  $T_{\text{inlet}} = 100$  °C and  $Q = 600$  SLPM,  $\phi = 0.8$ ,  $T_{\text{inlet}} = 120$  °C. In each case, profiles are relatively flat, indicating spacial uniformity of the flame. For the case of  $Q = 300$  SLPM, emission levels are not significantly affected by the presence of PIM in the combustor. In fact, the best case configuration for noise reduction

(divergent shape) yields NO<sub>x</sub> and CO emissions which are very similar to the baseline case, without PIM. For the Q = 600 SLPM case, emissions with the PIM are somewhat peculiar. CO emissions are reduced from approximately 70 ppm without PIM to below 30 ppm with all configurations of PIM. Alternatively, NO<sub>x</sub> emissions increase from around 20 ppm without PIM to levels between 30 and 60 ppm with PIM. As this study is a preliminary step towards optimization of the porous media combustion technique, it is reasonable to assume that an appropriate geometry of PIM could be chosen to provide adequate noise reduction without adversely affecting concentrations of harmful emissions.

As a follow-up to preliminary work at atmospheric pressure, Sequera (2011) conducted a range of tests using a combustor designed to operate at conditions more similar to those in a gas turbine combustor. The high pressure combustor offers extended capability in that air may be preheated to higher temperatures, reactants supplied at higher flow rates and inlet velocities, and the combustion chamber can be pressurized to levels well above atmospheric. The study conducted by Sequera (2011) demonstrates effectiveness of combustion noise reduction with PIM, in a new combustor with distinctly different geometry and operating conditions. Total SPL is shown for air flow rates of 1020 and 1400 SLPM in Tables 1.3 and 1.4, respectively. Results shown are for tests conducted at atmospheric conditions at air inlet temperatures of 20, 130, and 260 °C and equivalence ratios of 0.65, 0.70, and 0.75. As shown, PIM is successful in reducing total SPL over a variety of conditions and is especially effective at lower air inlet temperatures.

Table 1.3

Summary of sound pressure levels for  $Q=1020$  SLPM (Sequera, 2011)

| $T_{\text{inlet}}$ ( $^{\circ}\text{C}$ ) | $\Phi$ | $Q_c$ (slpm) | Total sound pressure level (dB) |             |             |
|---|--------|--------------|---------------------------------|-------------|-------------|
|   |        |              | No PIM                          | 18 ppcm PIM | 32 ppcm PIM |
| 20  | 0.65   | 990          | 117.0                           | 110.2       | 111.4       |
|   | 0.70   | 990          | 120.0                           | 111.7       | 111.0       |
|   | 0.75   | 990          | 120.6                           | 114.9       | 113.2       |
| 130                                       | 0.65   | 1160         | 120.5                           | 113.9       | 114.7       |
|   | 0.70   | 1160         | 125.8                           | 116.4       | 116.4       |
|   | 0.75   | 1160         | 124.3                           | 118.3       | 116.2       |
| 260                                       | 0.65   | 1350         | 122.1                           | 117.4       | 118.2       |
|   | 0.70   | 1350         | 119.0                           | 119.0       | 118.2       |
|   | 0.75   | 1350         | 118.8                           | 119.8       | 118.8       |

Table 1.4

*Summary of sound pressure levels for  $Q=1400$  SLPM (Sequera, 2011)*

| $T_{\text{inlet}}$ ( $^{\circ}\text{C}$ ) | $\Phi$ | $Q_c$ (slpm) | Total sound pressure level (dB) |               |
|---|--------|--------------|---------------------------------|---------------|
|   |        |              | No PIM                          | PIM (18 ppcm) |
| 20  | 0.65   | 1300         | 118.0                           | 113.6         |
|   | 0.70   | 1300         | 120.4                           | 115.6         |
|   | 0.75   | 1300         | 120.8                           | 116.6         |
| 130                                       | 0.65   | 1550         | 124.3                           | 117.8         |
|   | 0.70   | 1550         | 125.6                           | 119.0         |
|   | 0.75   | 1550         | 125.4                           | 120.5         |
| 260                                       | 0.65   | 1750         | 119.6                           | 119.7         |
|   | 0.70   | 1750         | 119.1                           | 121.3         |
|   | 0.75   | 1750         | 119.2                           | 122.8         |

### 1.3 Objectives of Present Study

The present study seeks to examine effects of several parameters on noise reduction and instability mitigation with porous media. Among other parameters, swirler vane angle and axial location of swirler are investigated to observe effect on total SPL without and with PIM. The study also examines thermo-acoustic instabilities and quantifies the ability of PIM as a passive mitigation strategy. Differing from the work by Sequera (2011), the current experiments are conducted with a much larger swirler vane angle, which imparts considerably more radial momentum to the incoming reactants. As a result, recirculation zones are altered in both

intensity and location. Likewise, the axial location of the swirler is varied to observe effects on the performance of porous media regarding noise reduction and instability. For the current study, a number of experiments are conducted where instability is the dominant component of total SPL without the presence of porous foam. Thus, effectiveness of PIM in mitigating combustion instability is characterized in detail. In addition, an endurance test is performed with the porous insert to identify any variation in performance over extended operation. All experiments are performed at atmospheric pressure and will serve as a baseline assessment for subsequent high pressure testing in the experimental test facility.

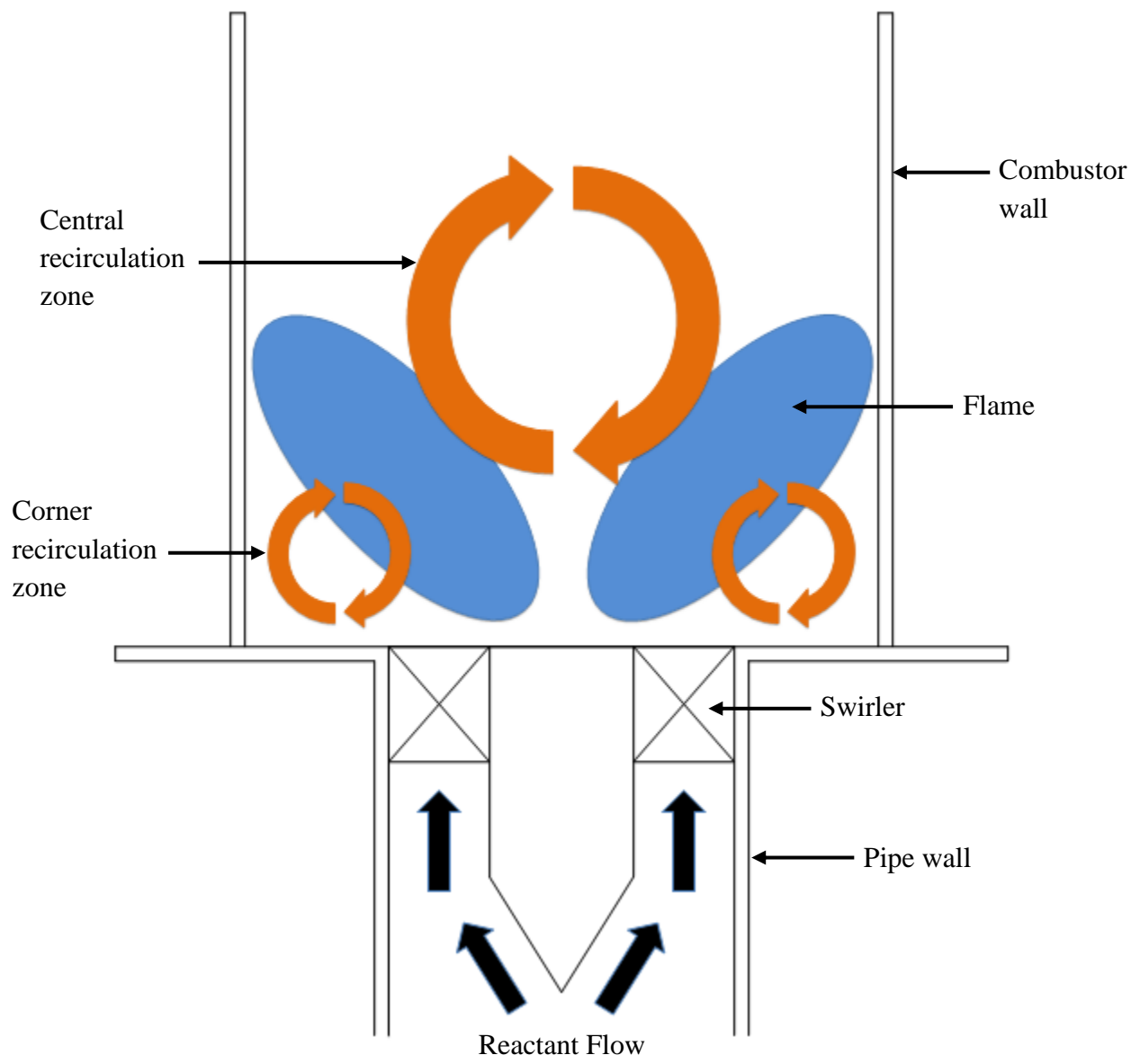
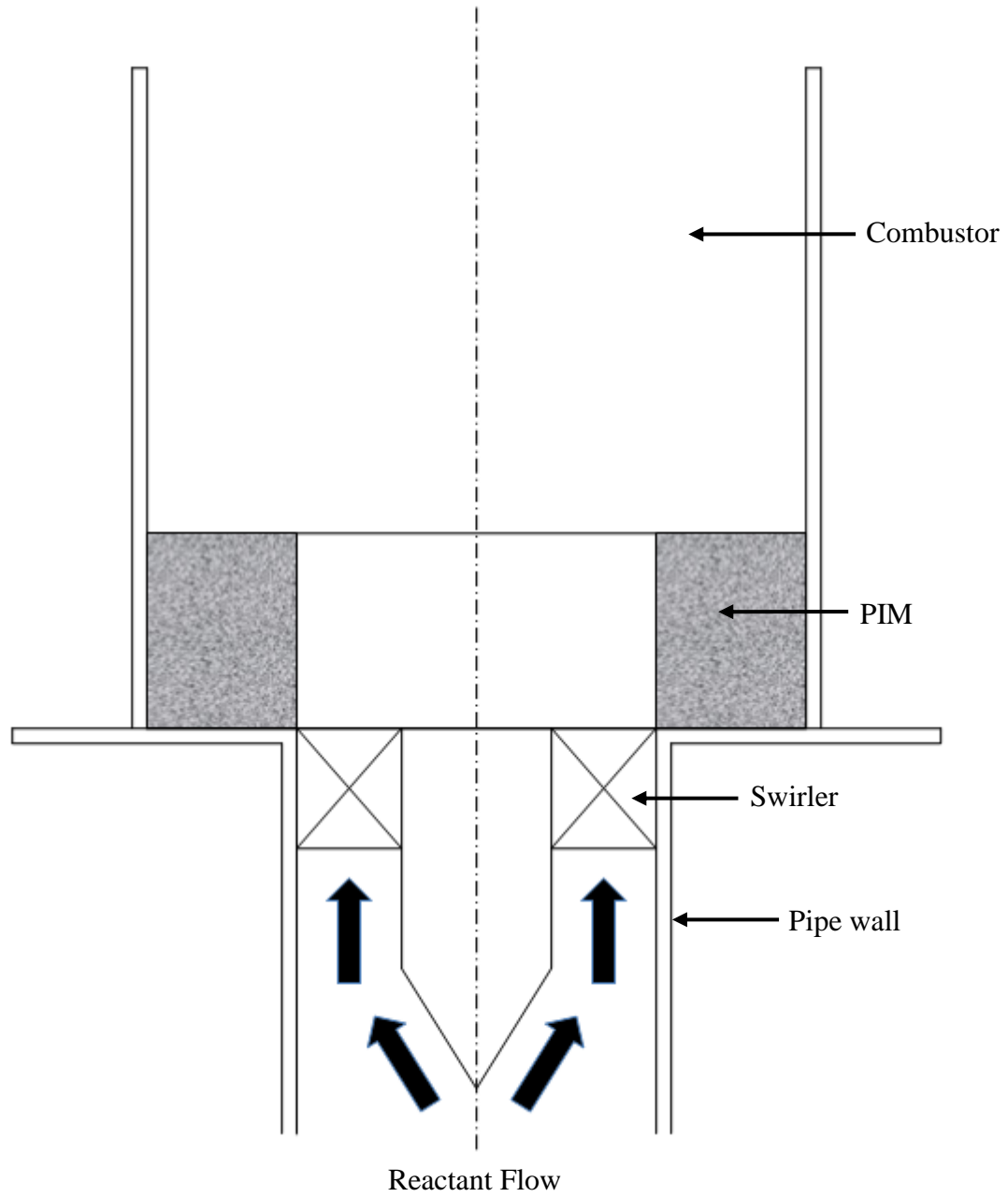


Figure 1.1. Schematic diagram of swirl-stabilization process



*Figure 1.2.* Porous insert located inside a swirl-stabilized combustor

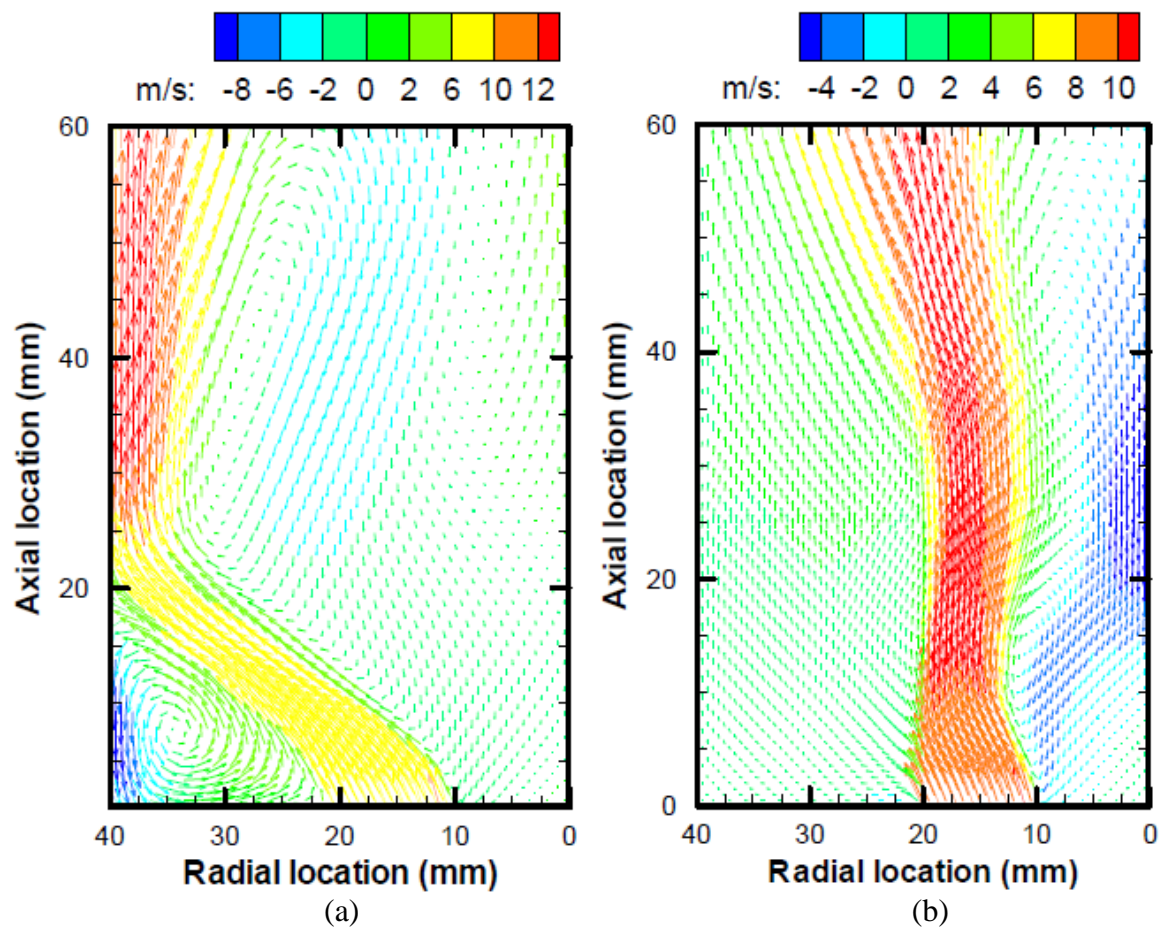


Figure 1.3. Velocity vectors for reacting flow where  $\phi = 0.58$  (a) Without PIM (b) With PIM (Sequera, 2011)

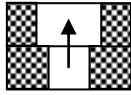
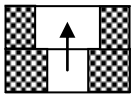
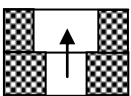
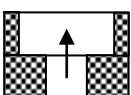
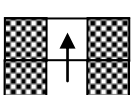
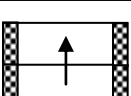
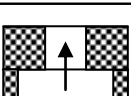
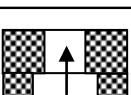
|  |  |
|--|--|
| Configuration A<br>Pore density: None    | None   |
| Configuration B<br>Pore density: 4 ppcm  |    |
| Configuration C<br>Pore density: 8 ppcm  |    |
| Configuration D<br>Pore density: 18 ppcm |    |
| Configuration E<br>Pore density: 18 ppcm |    |
| Configuration F<br>Pore density: 18 ppcm |    |
| Configuration G<br>Pore density: 18 ppcm |  |
| Configuration H<br>Pore density: 18 ppcm |  |
| Configuration I<br>Pore density: 18 ppcm |  |

Figure 1.4. Schematic diagram of PIM configurations (Sequera & Agrawal, 2011)



(a)



(b)



(c)

*Figure 1.5.* Photographic images (a) PIM insert (b) Combustor without PIM (c) Combustor with PIM (Sequera, 2011)

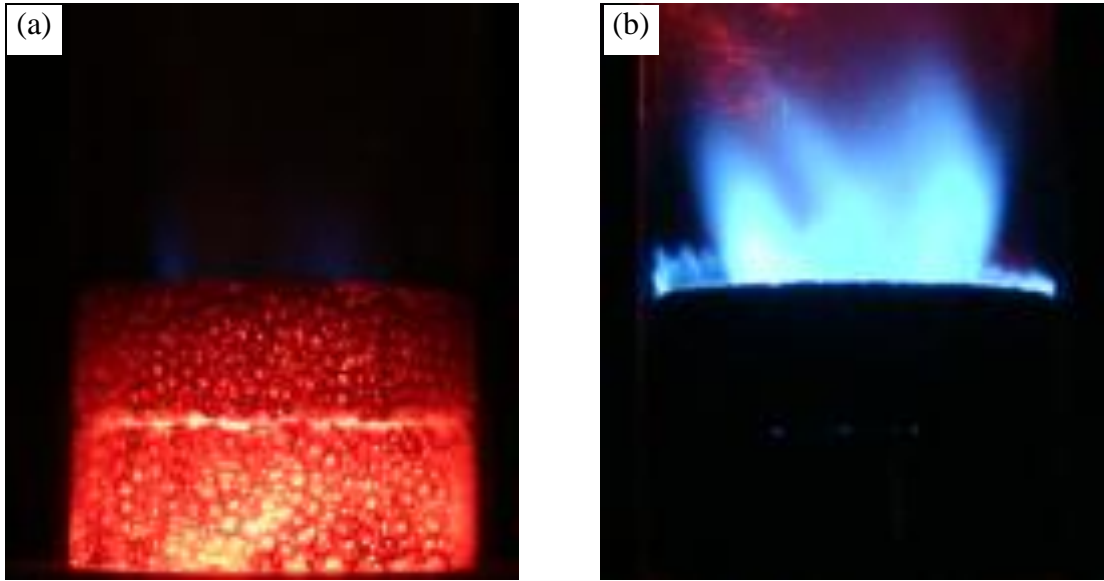


Figure 1.6. Flame images, (a) With PIM interior combustion (b) With PIM surface combustion (Sequera & Agrawal, 2011)

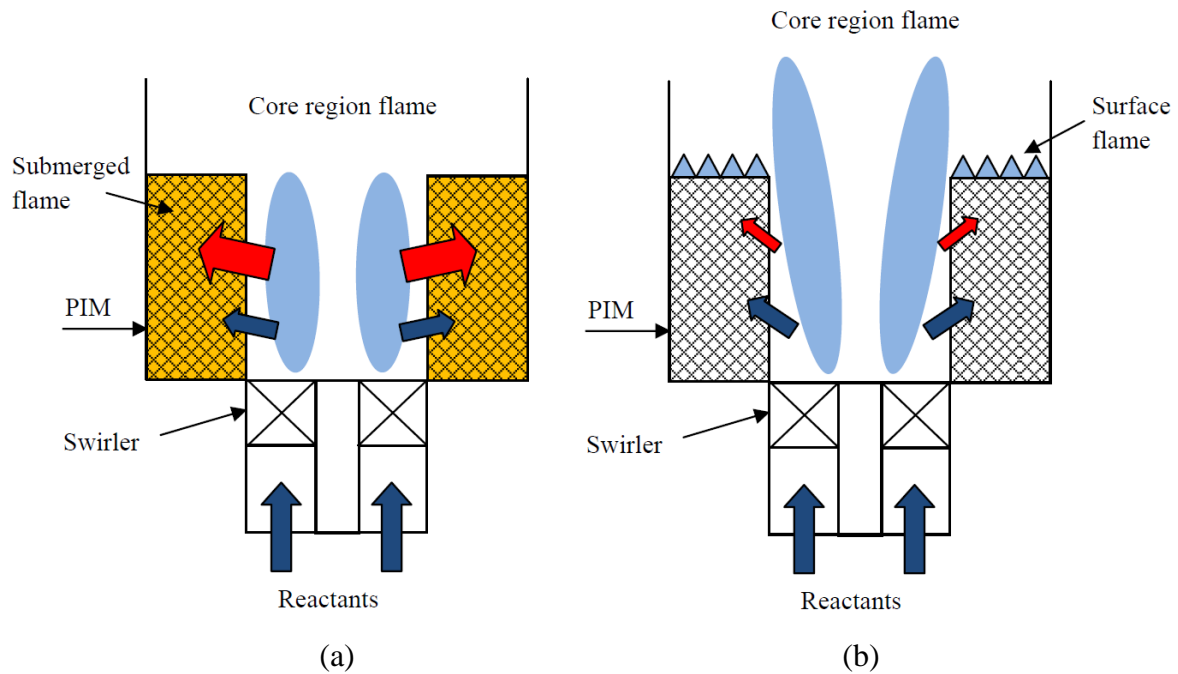


Figure 1.7. Schematic diagrams of PIM assisted combustion, (a) Interior combustion (b) Surface combustion (Sequera & Agrawal, 2011)

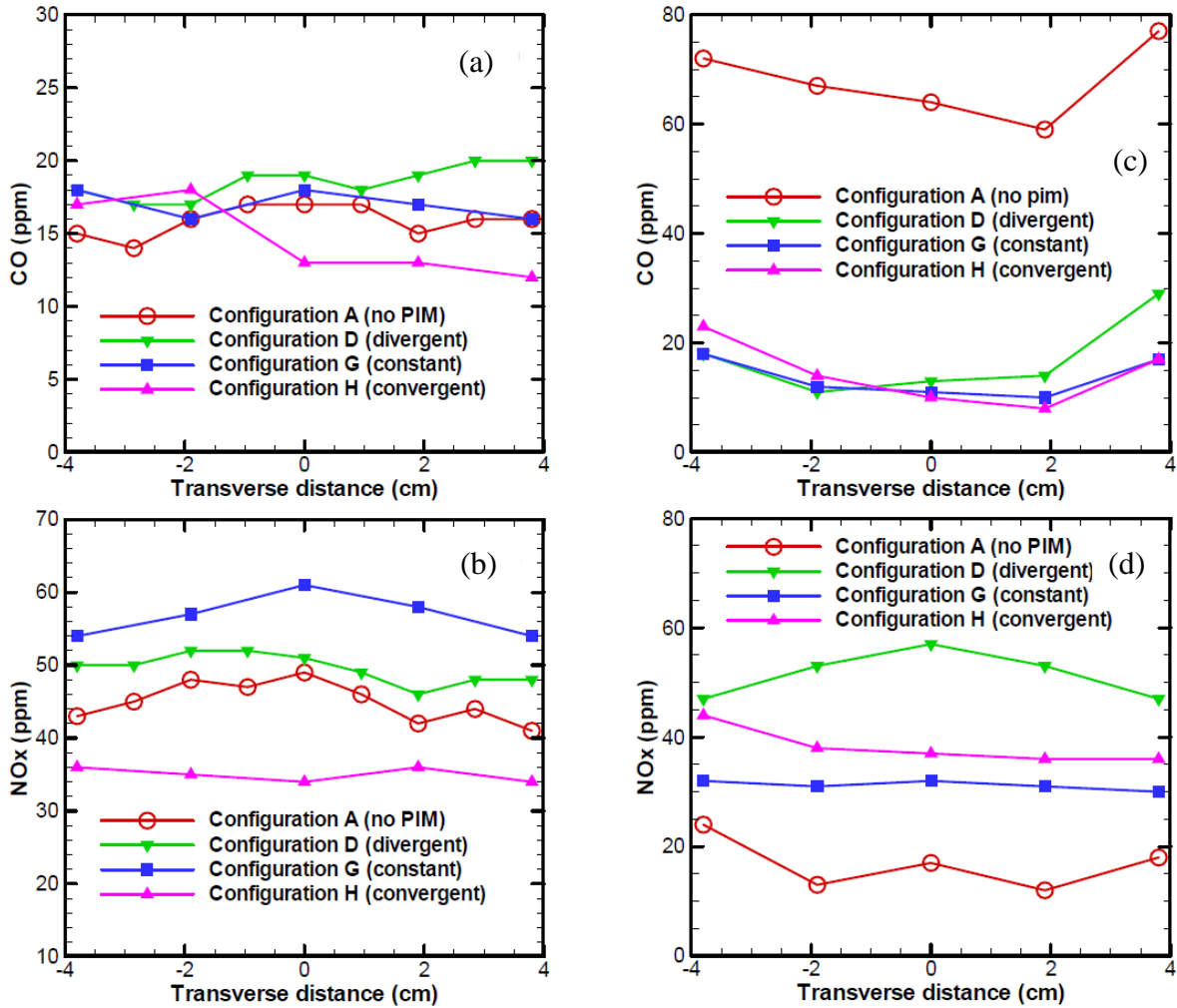


Figure 1.8. Transverse emissions profiles (a) CO at  $Q = 300$  SLPM,  $\phi = 0.8$ ,  $T_{inlet} = 100^\circ\text{C}$  (b) NOx at  $Q = 300$  SLPM,  $\phi = 0.8$ ,  $T_{inlet} = 100^\circ\text{C}$  (c) CO at  $Q = 600$  SLPM,  $\phi = 0.8$ ,  $T_{inlet} = 120^\circ\text{C}$  (d) NOx at  $Q = 600$  SLPM,  $\phi = 0.8$ ,  $T_{inlet} = 120^\circ\text{C}$

## CHAPTER 2

### EXPERIMENTAL APPROACH

#### 2.1 Overview

In recent years, combustion research has gained considerable attention among the scientific community. Stringent regulation of pollutant emissions, depletion of fossil fuels, and a rapidly expanding demand for energy has driven engineers to produce combustion systems capable of efficiently supplying large amounts of relatively clean energy. Due to simplicity of operation, current experimental work is generally conducted at atmospheric pressure. These studies have made valuable contributions to the combustion field by furthering the understanding of basic concepts associated with the combustion process. However, gas turbines for large-scale power generation and aircraft propulsion operate at pressures well above atmospheric. For this reason, a high pressure combustion test facility is necessary to gain further insight into gas turbine combustion.

The University of Alabama is a large player in the current field of experimental combustion work. However, existing combustion facilities are designed to perform at atmospheric conditions and are not capable of operating at elevated pressures. To extend the capability of the current combustion laboratories, a need arises for a facility to study combustion processes as they exist in gas turbine combustion chambers. Such a system requires precise coordination of large flow rates of fuel and preheated air, which replicates actual conditions in a

gas turbine engine. The experimental test chamber should be able to withstand long duration testing at high temperatures and pressures. The facility should also be operable over a wide variety of conditions as well as provide real-time diagnostic data to monitor system performance. Additionally, the laboratory should be equipped with a control scheme that can be operated remotely, at a safe distance from the combustion chamber. Air and fuel flow rates will need to be precisely measured and controlled to achieve a desired equivalence ratio and heat release rate. Performance indicators such as emission levels and combustion noise must also be integrated into the test facility. Combustion products should be safely routed to the exterior of the building to prevent potential inhalation of harmful product species. Lastly, the laboratory should be designed to provide general convenience and safety to the user. Access to flow control, electric heater, and measurement devices should be provided at safe locations within the laboratory. General layout of the laboratory is shown in Figure 2.1. The facility allows combustion experiments to be performed over a pressure range of 1 to 10 atmospheres (atm) using highly preheated air at temperatures up to 760 °C.

## 2.2 Air Supply System

The high pressure combustion laboratory is supplied with compressed air for both fuel oxidation and cooling purposes. Compressed air is generated with a dedicated compressor and is piped directly into the laboratory space. Entering air is directed through a pressure regulator followed by a Kammer Total Flow globe valve. The globe valve is operated remotely and is driven by a Kammer Series 5 (model 0350E3-P) electric actuator. The pressure regulator and flow control valve are used in combination to adjust and regulate total air flow as shown in Figure 2.2. Air leaving the flow control valve is directed upwards along a building column and

routed overhead to the combustor space using 5.1 cm [2 in] carbon steel pipe. The air flow is then split for supply to either the low pressure or high pressure combustor. General layout of the laboratory piping system is shown schematically in Figures 2.3 and 2.4. Airflow can be supplied to both combustors; however air flow rate cannot be accurately controlled for both systems in simultaneous operation. Downstream of the split, both air lines are outfitted with Nibco shutoff ball valves. The supply air for the high pressure system is split into two separate lines for combustion air and cooling air. Each branch is equipped with a Nibco Class 150 globe valve that is used to manually control the split between combustion and cooling air. Both of the air lines are equipped with a laminar flow element (LFE) to measure mass flow rate. Operational details of the LFE are further outlined in the flow measurement section. Combustion air is directed through an electric air heater before being delivered to the combustion chamber. One inch nominal schedule 80 stainless steel piping is used to transport air from the exit of the heater to the dump plane of the combustion chamber. Cooling air enters a 4-way manifold where it is distributed to the combustion chamber by four flexible hoses. Table 2.1 shows an itemized list of components used to construct the air supply system.

Table 2.1

*Air supply system components*

| Quantity | Description                 | Material / Model | Supplier          |
|----------|-----------------------------|------------------|-------------------|
| 50 ft    | 2" schedule 80              | Carbon steel     | Consolidated pipe |
| 16 ft    | 1" schedule 80              | Carbon steel     | Consolidated pipe |
| 4 ft     | 1" schedule 80              | Stainless steel  | Consolidated pipe |
| 9        | 2" 90° elbow schedule 80    | Carbon steel     | Consolidated pipe |
| 1        | 1" 90° elbow schedule 80    | Carbon steel     | Consolidated pipe |
| 2        | 1" 90° elbow schedule 80    | Carbon steel     | Consolidated pipe |
| 2        | 2" tee schedule 80          | Carbon steel     | Consolidated pipe |
| 2        | 2" x 1" reducer schedule 80 | Carbon steel     | Consolidated pipe |
| 1        | 2" x 1" reducer schedule 80 | Stainless steel  | Consolidated pipe |
| 2        | 6" x 2" reducer schedule 80 | Stainless steel  | Consolidated pipe |
| 1        | 2" tee 300# schedule 80     | Carbon steel     | Consolidated pipe |
| 1        | 1" tee 300# schedule 80     | Stainless steel  | Consolidated pipe |
| 10       | 2" ANSI 300# flange         | Carbon steel     | Consolidated pipe |
| 4        | 2" pipe unions              | Carbon steel     | McMaster-Carr     |
| 6        | 1" ANSI 300# flange         | Stainless steel  | Consolidated pipe |
| 2        | 6" ANSI 300# flange         | Stainless steel  | Consolidated pipe |
| 2        | 2" ¼ turn ball valve        | Carbon steel     | Nibco             |
| 1        | 2" globe valve              | Bronze           | Nibco             |
| 1        | Air pressure regulator      | R40-205          | Norgreen          |
| 1        | 2" flow control valve       | 0350E3-P         | Kammer            |

Combustion air flow is preheated with an electric heater to simulate operational conditions in a gas turbine combustion chamber. Shown in Figure 2.5, an Osram Sylvania 72 kilowatt 480 volt flanged in-line heater is used for heating the incoming combustion air. The heater is capable of heating air to temperatures up to 760 °C [1400 °F] and is operable over a pressure range of 0 to 1030 kPa [0 – 150 psi]. Temperature control is provided by an E5CN digital controller coupled with four Type K thermocouples installed inside the heater. Electrical power is supplied by a dedicated Avatar A3P power controller. The control station is mounted away from the combustor such that the heater can be operated remotely from a safe distance. The heater is equipped with a 15.2 cm [6 in] flange on both the entrance and exit port. Upstream piping is connected to the entrance of the heater using a 5.1 cm x 15.2 cm [2 in x 6 in] stainless steel diffuser. The exit of the heater is connected to the downstream piping with 15.2 cm x 2.5 cm [6 in x 1 in] stainless steel reducer. The heater is oriented vertically and mounted using a stand anchored to the floor of the laboratory. A gasket is installed between the stand and the heater to reduce any vibrations that may arise. All piping downstream of the heater is wrapped with 7.6 cm [3 in] thick high temperature insulation to reduce heat loss. Since heat loss cannot be completely eliminated, air temperature is measured again just upstream of the dump plane.

### 2.3 Fuel Supply System

An outdoor fuel station (shown in Figure 2.6) is used to store large amounts of compressed natural gas used for both the low and high pressure combustion experiments. Natural gas is obtained from the city supply lines, compressed to a pressure of 2,680 kPa [3,000 psi], and stored in a rack of ten 50 liter tanks enclosed in a safety fence. Compressed natural gas is piped from the tanks to the interior of the building where the fuel pressure is controlled with a

Meco Type P-1-D pressure regulator. After leaving the regulator, the fuel line is branched to supply both the low pressure and high pressure combustors. A manually operated Swagelok ball valve is installed in each line to provide quick fuel shutoff if needed. As an added safety measure, the high pressure fuel line is equipped with a solenoid valve operated by an electrical cutoff switch. As shown in Figure 2.7, the 1.3 cm [ $\frac{1}{2}$  in] high pressure line is routed overhead, alongside the air line, to the high pressure combustor. Fuel flow rate is measured and controlled using a Bronkhorst model F-203AV-M50 mass flow controller which is capable of delivering flow up to 465 normal liters per minute (LNPM). Using a RS-232 serial connection, the controller is wired to the NI CompactRIO data acquisition and control system for flow control and measurement display. Upon leaving the mass flow controller, the fuel flows in a flexible metal hose and is injected into the combustion air at a location 61 cm [2 ft] upstream of the dump plane. Fuel is injected downward into the upward flow to ensure adequate fuel/air mixing before the mixture reaches the combustion zone. Table 2.2 shows an itemized list of components used to construct the fuel delivery system.

## 2.4 Exhaust System

An exhaust duct is used to route hot combustion products to the exterior of the building. The exhaust system serves both the low pressure and high pressure combustion chambers and is constructed with 30.5 cm [12 in] stainless steel pipe. The duct is supported with steel rods attached to existing horizontal beams above the combustion laboratory. Flow in the exhaust duct is driven by a dedicated fan installed on the roof of the building. The layout of the exhaust system is shown in Figures 2.8 to 2.11.

Table 2.2

*Fuel supply system components*

| Quantity | Description               | Material / Model | Supplier   |
|----------|---------------------------|------------------|------------|
| 2        | 1/2" 1/4 turn ball valve  | Stainless steel  | Swagelok   |
| 33 ft    | 1/2" tube                 | Stainless steel  | Swagelok   |
| 30 ft    | 3/8" tube                 | Stainless steel  | Swagelok   |
| 1        | 1/2" by 3/8" reducer      | Stainless steel  | Swagelok   |
| 3        | 1/2" compression fittings | Stainless steel  | Swagelok   |
| 3        | 3/8" compression fittings | Stainless steel  | Swagelok   |
| 1        | Gas pressure regulator    | Stainless steel  | Swagelok   |
| 1        | Mass flow controller      | F-203AV-M50      | Bronkhorst |

## 2.5 Experimental Apparatus

Shown in Figure 2.12, the experimental apparatus is made up of a supply of preheated combustion air and fuel, a premixing region, a pressure vessel in which combustion takes place, and an exit throttle valve to control operating pressure. Figure 2.13 shows an exploded view of the high pressure combustion apparatus.

### 2.5.1 Inlet Pipe Section

The inlet pipe section of the combustor, shown in Figure 2.14, serves as a mixing chamber for reactants and delivers the mixture to the combustor. Supply air is routed from the heater exit to the inlet pipe section, where gaseous fuel is injected at a relatively high pressure.

Just downstream of the fuel injector, a section of porous material is placed inside the pipe to increase turbulent mixing of fuel and air. The reactant mixture flows through the length of the inlet pipe before reaching a flow swirler, which is fixed near the exit of the pipe. The exit of the inlet pipe is welded to a 7.6 cm [3 in] stainless steel flange which serves as the dump plane for the combustion chamber. The flange is sealed to the combustion chamber using a spiral wound gasket and a bolted connection. The inlet pipe flange also serves as a platform for mounting hardware such as the quartz flame enclosure and porous media. Absolute pressure and temperature measurements are taken along the inlet pipe section to closely monitor air/fuel mixture conditions upstream of the combustion zone. For safety, a burst disk rated at 1,035 kPa [150 psi] is placed in the inlet pipe section. Thus if system pressure reaches 1,035 kPa, the disk will burst and depressurize the system.

### *2.5.2 Combustion Chamber*

The combustion chamber is enclosed by a stainless steel pressure vessel which is sealed and bolted to a stainless steel plate, hereon referred to as the plenum base. The pressure vessel is a custom cast pipe with 22.9 cm [9 in] inner diameter (ID) and 38.1 cm [15 in] outer diameter (OD). The chamber is outfitted with twelve 1.3 cm [½ in] national pipe thread (NPT) access ports for measurement sensors, ignition, and sampling probe access. Photographic images of the pressure vessel are provided in Figures 2.15 and 2.16. For optical access, two window ports are machined into opposing sides of the pressure vessel. Quartz windows are held in place using a stainless steel rectangular window frame. If optical access is not necessary and quartz windows are not mounted, steel plates are inserted into the window ports to seal the combustion chamber.

A concentric reducer is mounted on the downstream side to connect the pressure vessel to the exit nozzle, where a throttle valve is located. As shown in Figure 2.16, the dump plane is located inside the chamber and is mounted horizontally at a location flush with bottom of the windows, which provides maximum optical access to the flame region. A quartz glass cylinder is placed on top of the dump plane to serve as the combustor. The quartz combustor is 30.5 cm [12 in] long by 7 cm [2.75 in] ID and is held in place by a stainless steel ring mounted on top of the quartz. The quartz fits into machined grooves at both the dump plane and the top ring, which are held in compression by threaded rods. Cooling air is routed from the four-way manifold into the bottom of the combustion chamber via four rubber hoses rated for high pressure air. Cooling air inlet location is chosen to provide maximum cooling to the stainless steel flange which serves as the dump plane of the combustor. As designed, the combustion chamber provides an environment capable of withstanding high pressures and temperatures while also facilitating adequate measurement and optical access for a variety of combustion experiments.

### *2.5.3 Inlet Swirler*

An inlet swirler is mounted upstream of the dump plane to induce a radial swirling motion to the incoming fuel and air mixture. This procedure is commonly used in industrial combustion applications to aid in flame stabilization. Swirler vane angle used for this study is  $28^\circ$  from horizontal at the dump plane. A photographic image of the flow swirler is provided in Figure 2.17. Figure 2.18 shows a detailed sketch of the swirler. Since swirler location needs to be varied for some combustion experiments, a mechanism is developed to move the swirler in the longitudinal direction within the inlet pipe. The mechanism is designed to allow the swirler to be mounted flush with the dump plane or recessed up to 3.8 cm [1.5 in] inside the inlet pipe.

As shown in Figure 2.19, the apparatus consists of six components: a supporting cylinder with threaded extension, three modular slip-on spacers, a threaded swirler, and an endcap. The supporting cylinder is mounted to the inlet pipe by using a set screw which is inserted through the pipe wall using a welded pipe fitting as shown in Figure 2.20. The upstream end of the supporting cylinder is milled into a sharp wedge to reduce flow disturbance in the pipe. A 0.64 cm [ $\frac{1}{4}$  in] threaded stud is extended from the top of the support cylinder to provide a method for stacking and securing the spacers and swirler. The spacers are stainless steel annular rings designed to slide on the threaded stud with minimal clearance and can be reconfigured and stacked to provide the desired swirler depth. Shorter spacers can be used when greater axial variability is required. The swirler is made of carbon steel and has a 0.64 cm [ $\frac{1}{4}$  in] tapped hole through the center that allows it to be tightened against the uppermost spacer. If the swirler is flush-mounted with the dump plane, the end cap is not necessary. However, if the swirler is recessed, appropriate spacers are stacked on top and the threaded end cap is used to secure the upper spacers. When the swirler is recessed, the top of the end cap remains flush with the dump plane to prevent recirculation zones (and accompanying flame anchoring) to form inside the pipe. The swirler location can be adjusted while the combustor is fully assembled, with access from only the top of the inlet pipe. A magnet is used in conjunction with a thin rod to manipulate spacers and swirlers into a desired configuration. Since disassembly of the combustor requires significant time and effort, the custom-built mechanism serves as a functional and convenient method for changing axial position of the swirler.

#### *2.5.4 Pressure Throttle Valve*

For combustion experiments at elevated pressures, a throttle valve is used to restrict flow through the exit nozzle of the combustor. By closing the valve and thus decreasing the exit area of the nozzle, flow becomes choked and pressure is built upstream in the combustion chamber and supply piping system. The throttle valve is designed to build pressure in the chamber over a wide range of flow rates and is relatively simple in design. As shown in Figures 2.21 and 2.22, a traversing slide is outfitted with a clamp that secures a U-shaped stainless steel arm which extends over to the exit nozzle. The end of the stainless steel arm is equipped with a machined needle which is modular and can be removed from the arm and replaced if necessary. As the slide is traversed in the upward direction, the needle plunges down into the nozzle, thereby reducing the effective area of the exit. Shown in Figure 2.21, the traversing system is supported using a steel plate which is bolted between the reducer and the exit flange of the combustion chamber. High temperature graphite foil gaskets are used to provide an air tight seal around all flanged connections on the combustor. The pressure throttle valve provides a convenient method to vary the exit area of the nozzle, thereby decoupling reactant flow from chamber pressure. This capability is critical since it allows independent control of combustor pressure for specified fuel/air flow rates.

#### *2.5.5 Ignition System*

Ignition energy must be provided with the pressure vessel mounted where access to the combustor is limited. Thus, a probe igniter is developed and installed through one of the 1.3 cm [ $\frac{1}{2}$  in] access ports on the side of the pressure vessel, located just above the top edge of the quartz combustor. The ignition probe is similar to a spark plug found in common internal combustion engines. A stainless steel tube is used for the outer casing and contains a small steel

rod which is mounted inside the tube. The rod is mounted along the centerline of the tube and provides a gap between the inner diameter of the tube and the outer diameter of the rod. The power source from a commercial stun gun is used to supply an instantaneous voltage difference to the system where one leg of the circuit is connected to the tube and the other leg to the interior rod. Charge is sent from the power source and an electrical arc is created in the gap at the end of the probe. The interior rod is insulated along its length except for the tip, which is left bare to ensure that the arc is created at the end of the probe and not recessed inside the tube. A photographic image of the probe is provided in Figures 2.23 and 2.24. A Swagelok compression fitting is used to connect the ignition probe to the threaded access port. The power supply is enclosed within a plastic casing and is mounted on the side of the combustion chamber support stand. A two-way toggle switch, located near the operator computer at a safe distance from the combustion chamber, is used to activate the igniter. Once the reactant mixture is ignited, the probe is manually removed and a pipe plug is inserted into the open access port to seal the system. The ignition probe provides a robust method for initiating reactions even at relatively large fuel and air flow rates.

## 2.6 Instrumentation and Data Acquisition

### 2.6.1 Flow Measurement

As mentioned previously, flow rates for both cooling and combustion air are measured using LFEs. The MERIAM, model 50MW20 LFE's are calibrated for air flow rate of 0 to 1400 liters per minute. Pressure drop across the LFE is measured with a differential pressure transducer connected to upstream and downstream ports of the LFE. Absolute pressure and temperature are also measured upstream of the LFE. Current output from pressure transducers

and voltage output from thermocouples are connected to the NI CompactRIO system for signal conditioning and data acquisition. LabVIEW software is used to scale the acquired data and calculate total air mass flow rate through the LFE. An example of this calculation is included in Appendix C.

The fuel flow rate is controlled and measured with a Bronkhorst EL-FLOW model F-203AV-M50 mass flow controller. Manufacturer provided software is used in conjunction with the NI CompactRIO system current output module to control the set point of the mass flow controller. Fuel flow rate is measured and displayed to ensure that the flow controller is operating properly. A schematic layout of the flow control system is shown in Figure 2.25. A complete list of instrumentation used for air and fuel flow measurement is given in Table 2.3.

Table 2.3

*Instrumentation used for flow measurement*

| Description                  | Model                     | Range                       | Output Type | Accuracy*                         |
|------------------------------|---------------------------|-----------------------------|-------------|-----------------------------------|
| Laminar flow element         | MERIAM<br>50MW20          | 1400 LPM                    | N/A         | 0.72% reading                     |
| K-type thermocouple          | Omega<br>KQSS-14G-10      | 1250 °C                     | Voltage     | 0.75% reading                     |
| Absolute pressure sensor     | Omega<br>MMA150           | 150 psi                     | Current     | 0.20% reading                     |
| Differential pressure sensor | Omega<br>MMDDU10WC        | 10 in H <sub>2</sub> O      | Current     | 0.03% reading                     |
| Mass flow controller         | Bronkhorst<br>F-203AV-M50 | 465 LNPM of CH <sub>4</sub> | Voltage     | 0.5% reading +<br>0.1% full scale |

\*Specified by manufacturer

### 2.6.2 Pressure and Temperature Measurement

Absolute pressure of the reactant mixture is measured in the combustor inlet pipe 10.1 cm [4 in] upstream of the dump plane. Combustion chamber pressure is also measured with an absolute pressure transducer connected through an access ports in the wall of the pressure vessel. Both transducer outputs are wired to the NI CompactRIO data acquisition system and displayed in LabVIEW software.

Temperature is measured at several locations within the system. As mentioned previously, Type K thermocouples are used to measure air temperature inside the heater as well as a location 30.5 cm [12 in] upstream of the dump plane of the combustor. In addition, combustion chamber temperature is monitored using a Type K thermocouple mounted through an access port in the chamber, downstream of the quartz combustor. Thermocouple outputs are routed to the NI CompactRIO and displayed using LabVIEW software.

### *2.6.3 Noise Measurement*

For combustion experiments, SPL is measured at two locations. Combustion noise is measured using a dynamic pressure transducer flush mounted along the interior of the combustion chamber, at a location even with the top of the quartz cylinder. Jet noise is measured outside the combustor with a condenser microphone located at a specified distance away from the top flange of the combustion chamber. Measurements are made at these locations to observe any correlation between noise generated by combustion and noise generated by the resulting high velocity jet of hot exhaust products.

Combustion noise is measured with a Kistler, model 601B1, water-cooled pressure transducer. Sensor output is sent to a Kistler 5051 charge amplifier, where the charge signal is amplified and converted to voltage. Finally, voltage is digitized by a NI PCI-6254 data acquisition card embedded in a laboratory computer equipped with LabVIEW software. LabVIEW software is used to scale voltage to pressure fluctuation using the sensitivity of the transducer (1.132 pC/psi) and the sensitivity of the charge amplifier (1 V/pC). Resulting overall sensitivity of the combustion noise measurement system is 0.164 mV/Pa. It is important to note that because the signal generated by combustion noise is on the order of the electrical noise of

the dynamic pressure sensor, absolute SPL measured by the transducer cannot be considered reliable. However, relative difference in SPL can still be quantified.

Jet noise is measured by a Bruel & Kjaer (model 8149) condenser microphone. Output from the microphone is digitized by a NI PCI-6254 data acquisition card where measured voltage is converted to pressure fluctuation using the sensitivity (45.8 mV/Pa) of the condenser microphone. The condenser microphone is calibrated by the manufacturer and is periodically verified with a piston-phone. The piston-phone generates a pure tone of 114 dB dB at 251.2 Hz.

Sound pressure measurements of both instruments are sampled at 4000 Hertz (Hz). Scaled voltage signals are processed using LabVIEW's embedded fast Fourier transform (FFT) function to obtain root mean squared (RMS) pressure fluctuations vs. frequency. A Matlab script is written to calculate SPL from RMS pressure fluctuations using Equation 3.1 (Bussman, 2001). All values for SPL are expressed in decibels (dB). See Appendix D for further details regarding Matlab code.

$$SPL = 10 * \log_{10} \left( \frac{P_{rms}^2}{P_{ref}^2} \right) \quad (2.1)$$

Where  $P_{ref} = 20 \mu\text{Pa}$ . Total SPL is calculated by:

$$SPL_{total} = 10 * \log_{10} \left( \sum_{i=1}^n 10^{0.1 * SPL_i} \right) \quad (2.2)$$

#### *2.6.4 Emissions Sampling*

Combustion emissions are measured using a sampling probe and a portable gas analyzer. The sampling probe shown in Figure 2.26 consists of a straight piece of stainless steel tubing used in conjunction with an L-shaped piece of quartz glass tubing. The stainless steel tubing is mounted through an access port in the wall of the pressure vessel and sealed with a Swagelok compression fitting. The steel tube is married to the quartz tube inside the combustor with a Swagelok compression fitting. The fitting used to seal the stainless steel tube at the combustor wall is manually loosened when traversing the probe. The L-shaped quartz tubing is outfitted with a tapered tip to aid in quenching reactions in the sample. Acquired product samples are routed through flexible plastic tubing into an ice bath used to condense any water vapor present in the sample. After leaving the ice bath, samples are fed into a Nova model 376WP gas analyzer capable of detecting concentrations of oxygen ( $O_2$ ), carbon dioxide ( $CO_2$ ), carbon monoxide (CO), and nitrous oxides ( $NO_x$ ).

#### *2.6.5 Data Acquisition System*

Sound pressure measurements are acquired with the aforementioned data acquisition card and processed in LabVIEW. An NI CompactRIO system is used to acquire data from all other measurement devices. Displayed in Figure 2.27, the NI CompactRIO system is a robust data acquisition and control system capable of sending and receiving current and voltage signals at a high data rate, under relatively harsh operating conditions. The CompactRIO includes a reconfigurable chassis which can accommodate up to eight I/O modules and also contains the field-programmable gate array (FPGA) chip. The NI CompactRIO is currently configured to house four I/O modules: one 32-channel 10 V voltage input, one 16-channel preconfigured

thermocouple input, one 8-channel 20 mA current input, and one 4-channel 20 mA current output. Figure 2.25 shows the layout of the flow measurement sensors along with their respective I/O connections to the individual modules of the NI CompactRIO system. To avoid task priority issues associated with a Windows based operating system, a large portion of the signal conditioning is performed by the FPGA chip. The real-time controller embedded in the NI CompactRIO acts as a standalone PC and makes use of a 533 MHz processor, 2 GB of storage, and 256 MB of RAM. The real-time controller outputs directly to the dedicated operator PC using an Ethernet cable.

The dedicated operator PC is equipped with LabVIEW software used to post-process data from the NI CompactRIO. A virtual control panel (shown in Figure 2.28) is created in LabVIEW and serves as the primary user interface for measurement display and output control. The control panel is coupled with the current output module of the NI CompactRIO to allow remote adjustment of the control valve for supply air. Additionally, the operator PC houses software supplied by Bronkhorst that couples with the NI CompactRIO current output module to provide user control of the fuel mass flow controller. As a safety measure, fuel flow rate is manually entered into LabVIEW which, in turn, calculates the equivalence ratio of the fuel and air mixture. By decoupling the fuel flow measurement from the equivalence ratio calculation, the user is able to predict the resulting equivalence ratio for a given fuel flow rate. Thus, a desired value for fuel flow rate is established before actually sending any fuel to the combustor.

LabVIEW programming is a graphically-based, three step process involving the FPGA chip, the real-time controller, and the operator PC. First, the embedded FPGA chip is programmed to read input signals at a desired sampling rate as well as provide initial signal conditioning. Each time new programming is introduced at the FPGA level, the chip

reconfigures itself to embed the new code as hardware. For this reason, the FPGA is a robust mechanism that provides increased reliability in the data acquisition process. Next, the real-time controller is programmed to receive and temporarily store data from the FPGA chip. In this way, the real-time controller provides a buffer zone from the FPGA to the operator PC and reduces any risk of hardware failure. Because of its functionality as a stand-alone PC, the real-time controller is also used to perform most of the scaling and mathematical calculations necessary to generate measurement output. Finally, the PC itself is programmed to read data from the real-time controller. Output from the controller is routed to the operator PC where it is conveniently displayed on the LabVIEW control panel. This allows the user to monitor system parameters as well as send remote instructions to the control valves for fuel and air supply lines.

## 2.7 Operating Procedure

### 2.7.1 Preliminary Tasks

The high pressure combustion facility is a complex system capable of producing large heat release rates from the rapid oxidation of fuel at high temperatures and pressures. As a result, a robust operating procedure is developed and must be strictly adhered to for all experimental operation of the system. First, the reducer is removed to allow access to the inside of the combustor. Next, the pressure vessel should be visually inspected for any signs of component malfunction or excessive wear and tear. Swirler location is adjusted as needed and quartz combustor, porous media, and holding mechanism are placed on the dump plane and secured by threaded rods. Next, the ignition probe and emission sampling probe are mounted through access ports on opposing sides of the pressure vessel. After all interior components are in place, the reducer is mounted along with the exit nozzle and pressure throttle valve. The pressure throttle valve should be fully open to prevent pressure buildup in the system. At this

point, all bolted connections are checked for proper tightness and fit. Then, the operator PC is turned on and appropriate LabVIEW software is initiated to read various instruments. Finally, the three-panel safety enclosure is placed in such a way that the operator is fully protected from potential system malfunction. After all preliminary tasks are completed; air flow can be initiated through the system.

### *2.7.2 Air Flow*

First, the manual air supply valve is opened and desired supply pressure is set by the regulator. Then, the LabVIEW interface is used to adjust the automated control valve to provide a desired air flow rate. At this point, the globe valves in the cooling and combustion air lines are manually adjusted to produce a specified split between cooling and combustion air flow rates. As a general rule, cooling and combustion air mass flow rates should be nearly equal to ensure proper cooling of critical components inside the combustor. If needed, the electrical heater is turned on to preheat the combustion air flow. If the heater is used, inlet temperature just upstream of the dump plane is monitored until temperature reaches the desired value. After desired air flow rate and inlet temperature are achieved, the LabVIEW control panel is reviewed to monitor system diagnostics and check for potential problems. If the system appears to be functioning properly, fuel flow can be safely initiated.

### *2.7.2 Fuel Flow and Ignition*

First, the electrical shutoff valve for the fuel is opened, followed by the manual gate valve (both valves are located on the building column). Fuel pressure is then adjusted with the fuel pressure regulator, located downstream of the manual gate valve. To determine required

fuel flow rate for a desired equivalence ratio, a percentage value (0 – 100%) is entered into the LabVIEW interface. This percentage value represents valve opening size of the fuel flow controller where zero corresponds to fully closed and one hundred corresponds to fully open. Resulting equivalence ratio is calculated for the current air flow and is displayed by LabVIEW. A trial and error procedure is used to determine the exact percentage value needed to obtain a desired equivalence ratio. Once the required fuel flow is determined, Bronkurst software is used to open the valve to the desired percentage, thereby injecting fuel into the supply of preheated combustion air. The fuel control process is slightly convoluted, but provides added safety for the user by allowing equivalence ratio to be calculated before supplying any fuel. After desired fuel and air flow are established, the mixture is ignited by turning on the two-way toggle switch to activate the ignition probe. Once the mixture is successfully ignited, the probe is removed from the access port and a pipe plug is inserted in its place.

### *2.7.3 System Operation*

Once the reactant mixture is ignited and a stable flame is present within the combustor, fuel and air flow rates are adjusted to vary equivalence ratio as needed. For each condition tested, emissions are sampled with the portable gas analyzer. In some cases, the sampling probe is traversed across the quartz combustor to obtain a radial profile of emission levels. Also, sound pressure level is recorded for each test case. The noise measurement program is automated to take data for five seconds and write results to a location specified by the user. For atmospheric combustion, the throttle valve is left in the fully open position for the duration of testing. For operation at elevated pressures, the throttle valve can be adjusted after ignition to produce the desired operating pressure in the combustion chamber. The throttle valve is adjusted in small

increments until the specified pressure is reached and displayed on the LabVIEW control panel. Since chamber pressure affects reactant flow rate, the fuel and air flow rates are adjusted in response to pressure changes induced by the throttle valve. In this way, chamber pressure can be built in a safe and gradual manner.

#### *2.7.4 System Shutdown*

Shutdown procedure must be followed correctly to prevent flashback and/or component failure. In all cases, fuel flow must be turned off before air flow. For low pressure operation, fuel flow is disabled by manually turning off the gate valve in the fuel line. By turning off the most upstream valve first, no residual fuel is left in the fuel line. All downstream valves in the fuel supply system are then closed. The electric heater is then turned off and air is allowed to flow through the system until all components are sufficiently cooled. This procedure is developed to facilitate gradual cooling of the system, thereby decreasing any chance of component failure. For high pressure operation, the fuel and air shutoff procedure is the same as low pressure operation. However, chamber pressure must be reduced to atmospheric before reactant flows are shutoff. Chamber pressure can be reduced by gradually opening the throttle valve until the system is depressurized. Again, fuel and air flow rates can be adjusted in response to changes induced by decreasing operating pressure. By gradually reducing pressure, the quartz combustor is protected from large pressure gradients incurred if the reactant flow is suddenly shutoff in a pressurized system. Once the system is sufficiently cooled, air flow is turned off by closing the manual gate valve in the air supply system. All downstream valves are closed and the system is inspected for any component failure that may have occurred during operation.

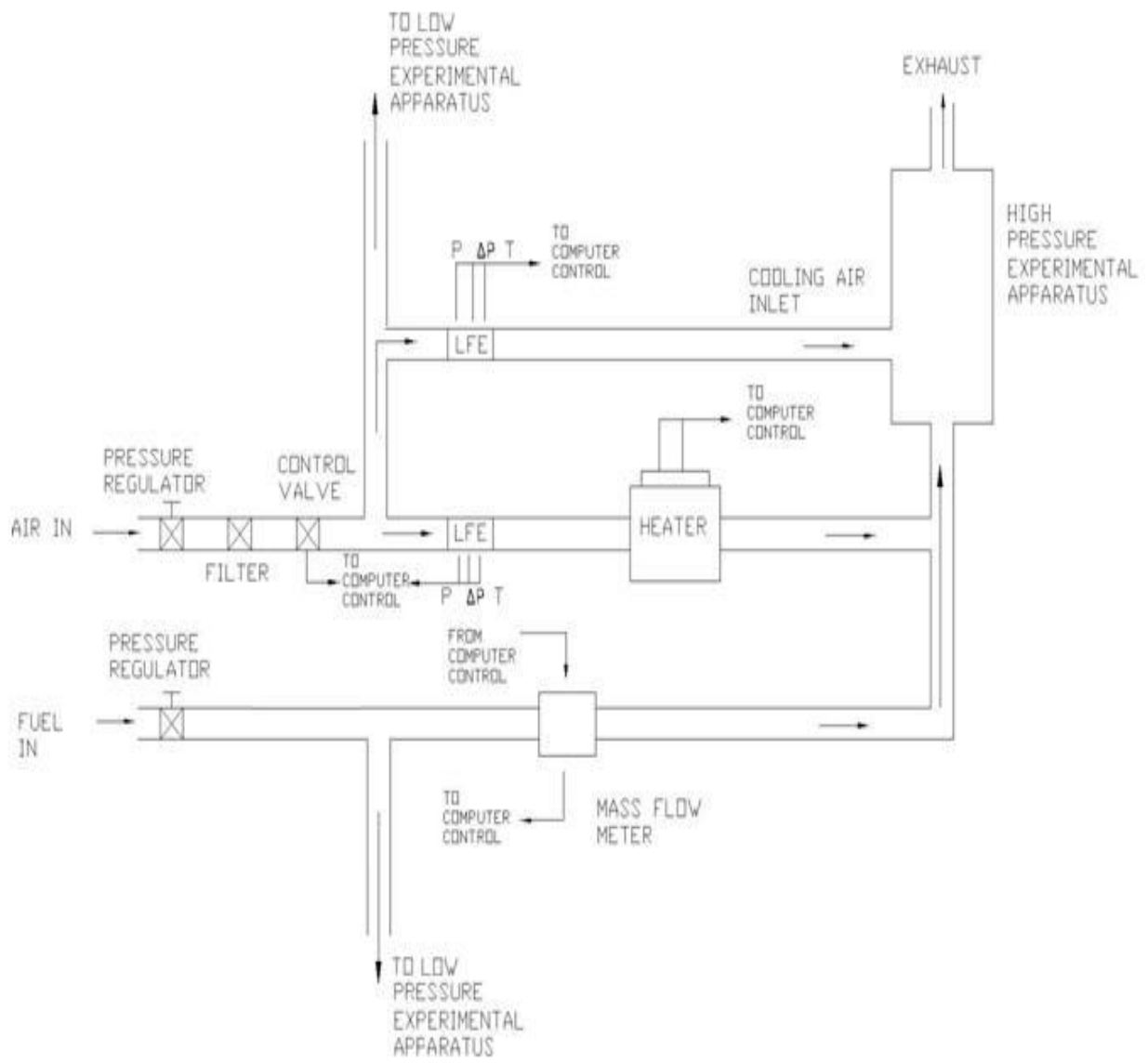


Figure 2.1. General schematic of high pressure combustion laboratory

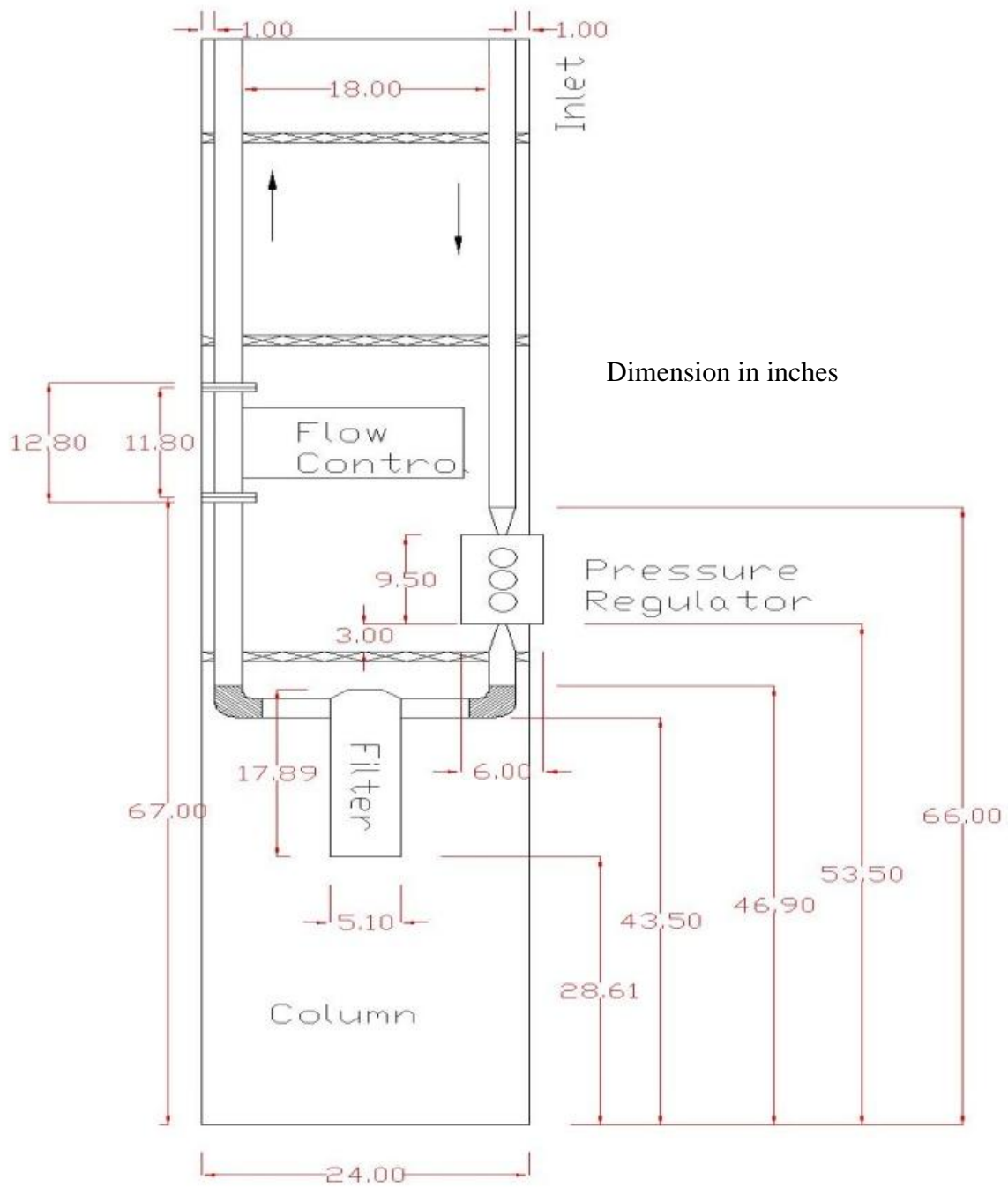


Figure 2.2. Layout of air flow control system

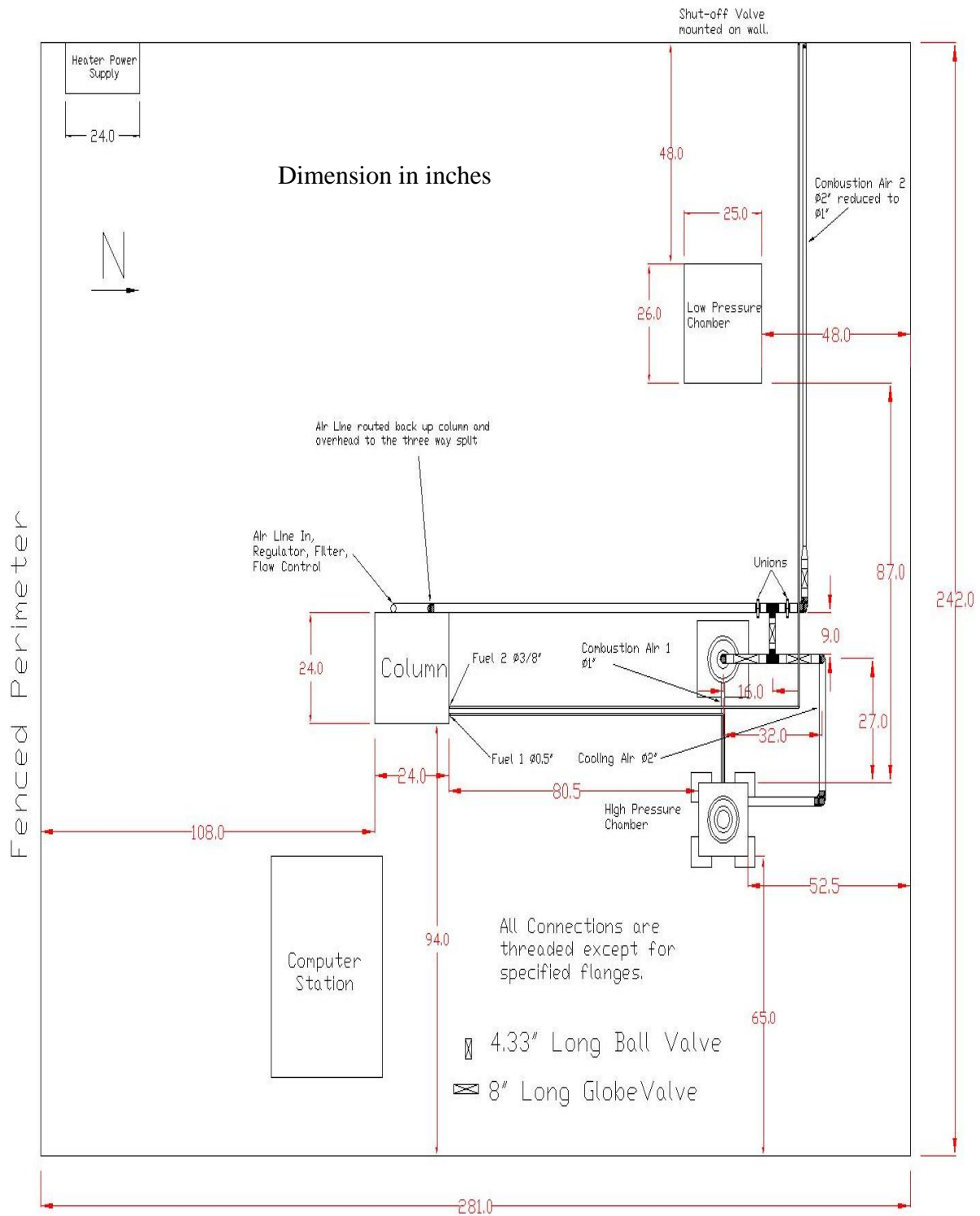


Figure 2.3. Top view layout of high pressure combustion laboratory

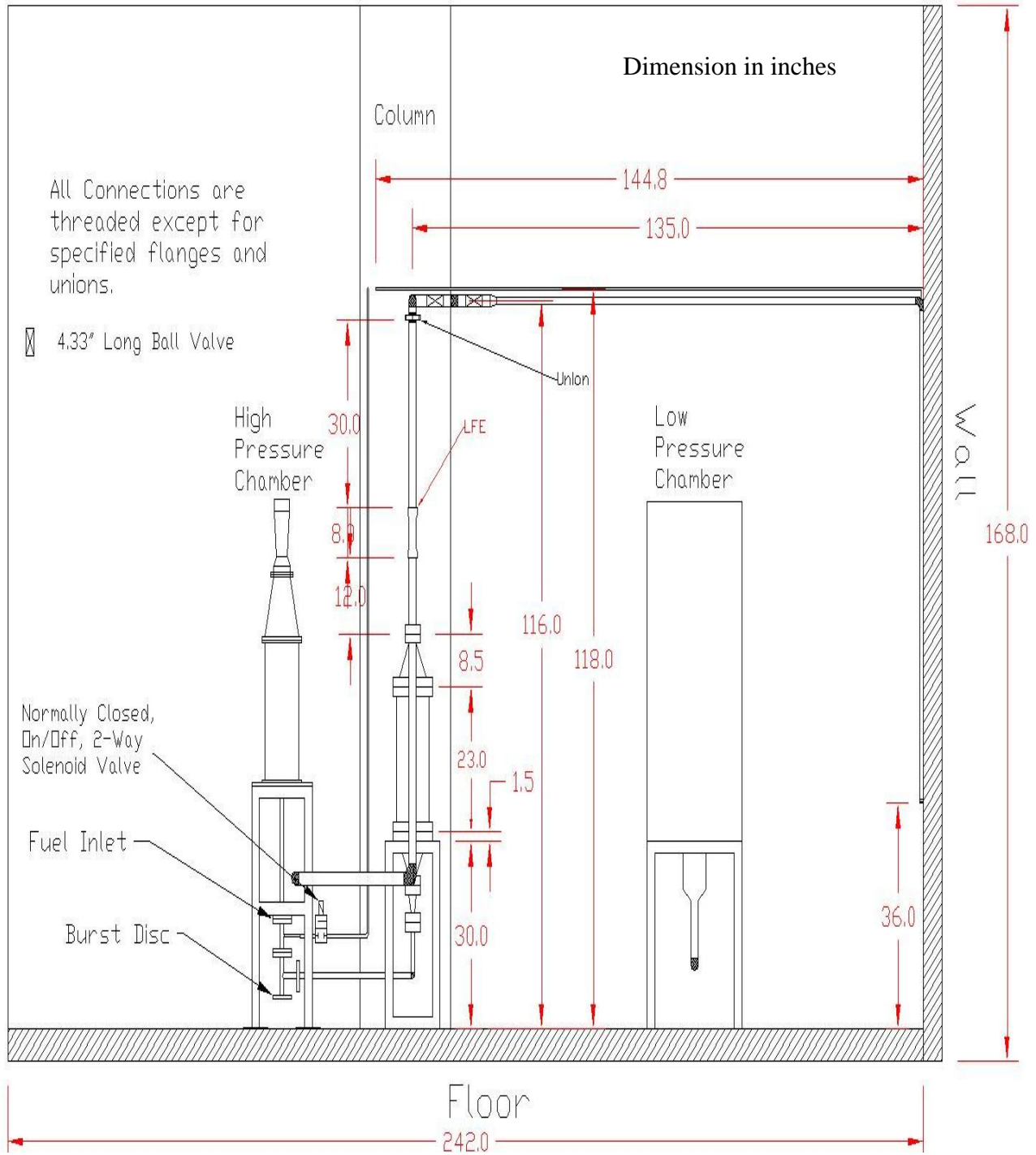


Figure 2.4. Side view layout of high pressure combustion laboratory

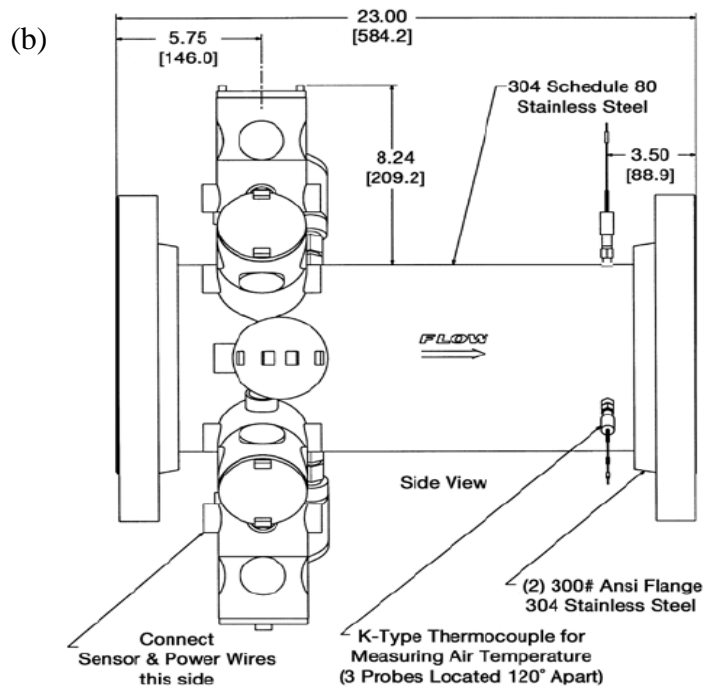
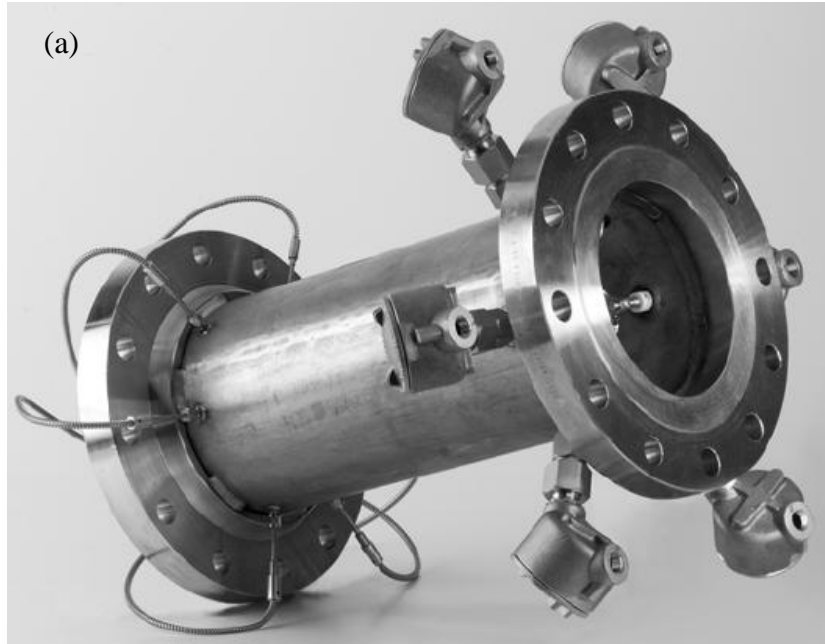


Figure 2.5. Electric air heater (a) Photographic image (b) Schematic diagram

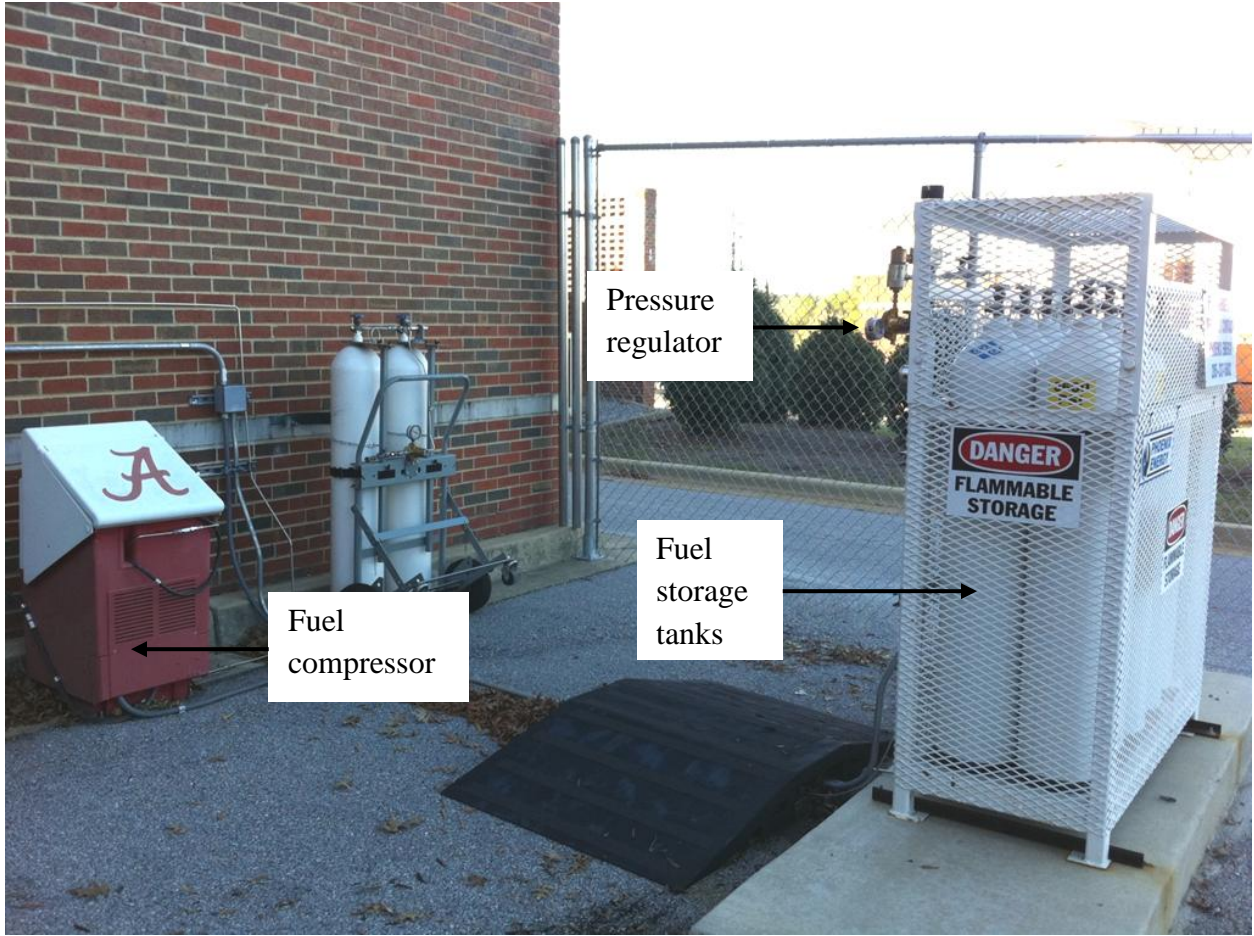


Figure 2.6. Outdoor fuel station

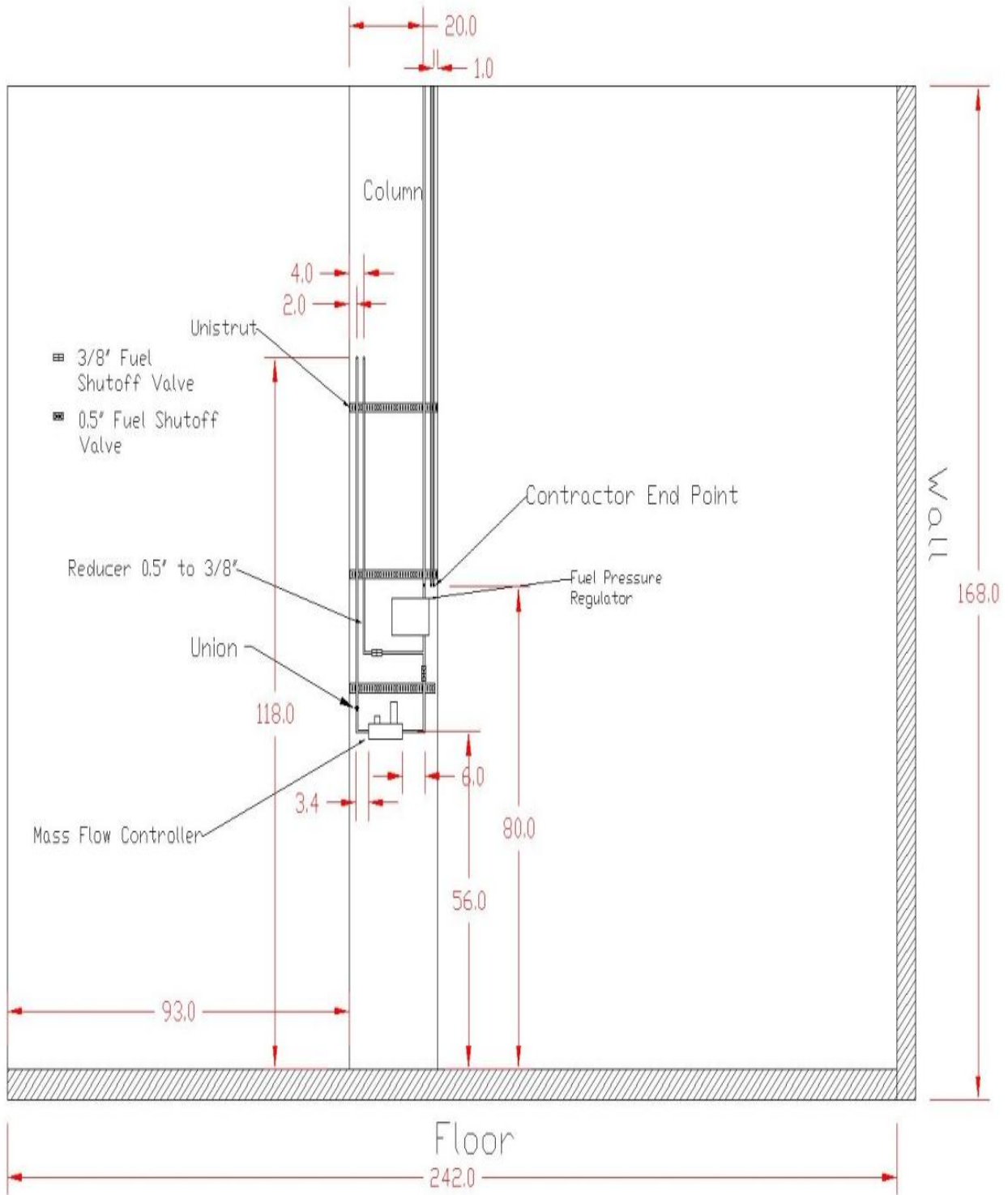


Figure 2.7. Layout of fuel flow control system

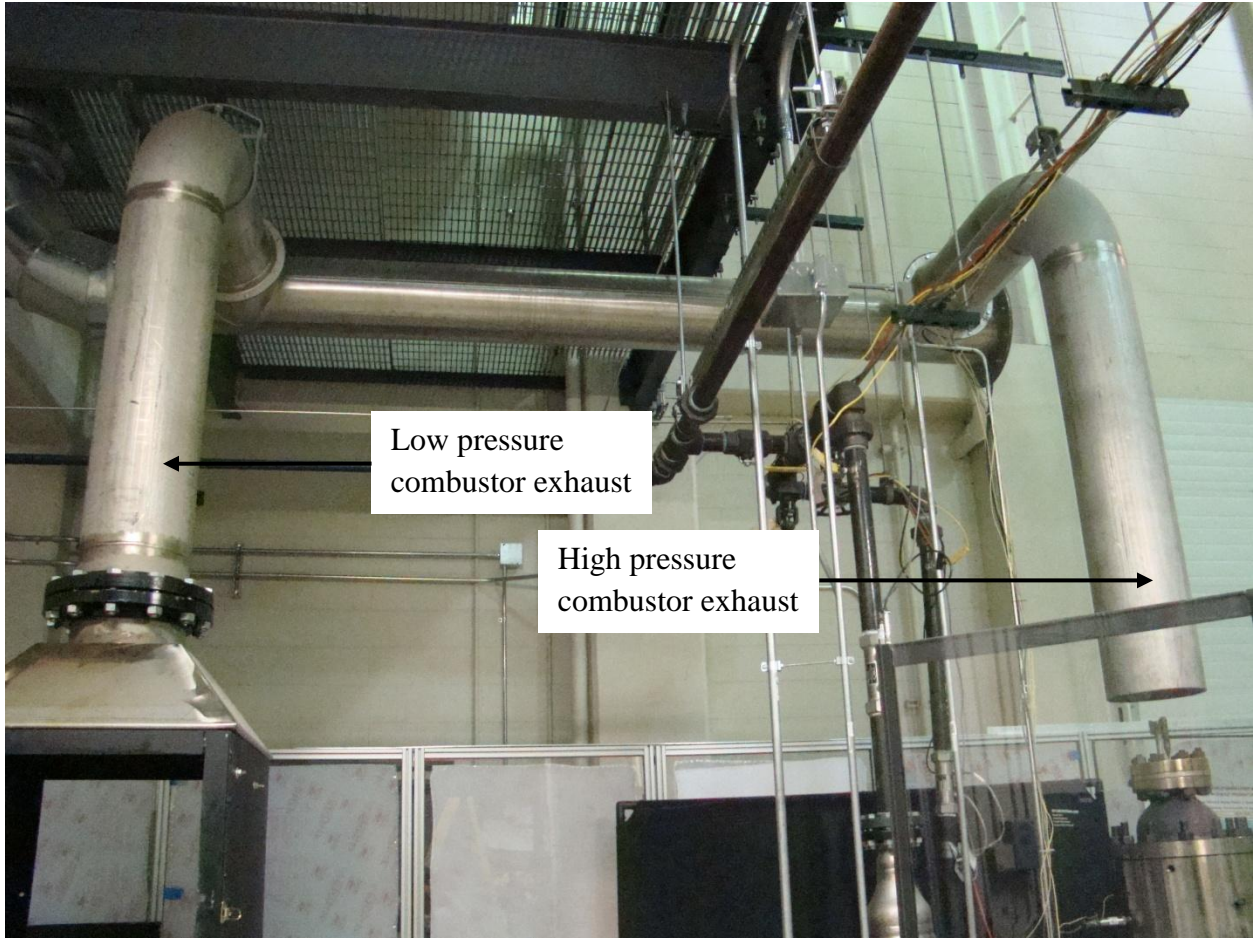


Figure 2.8. Photographic image (front view) of exhaust system

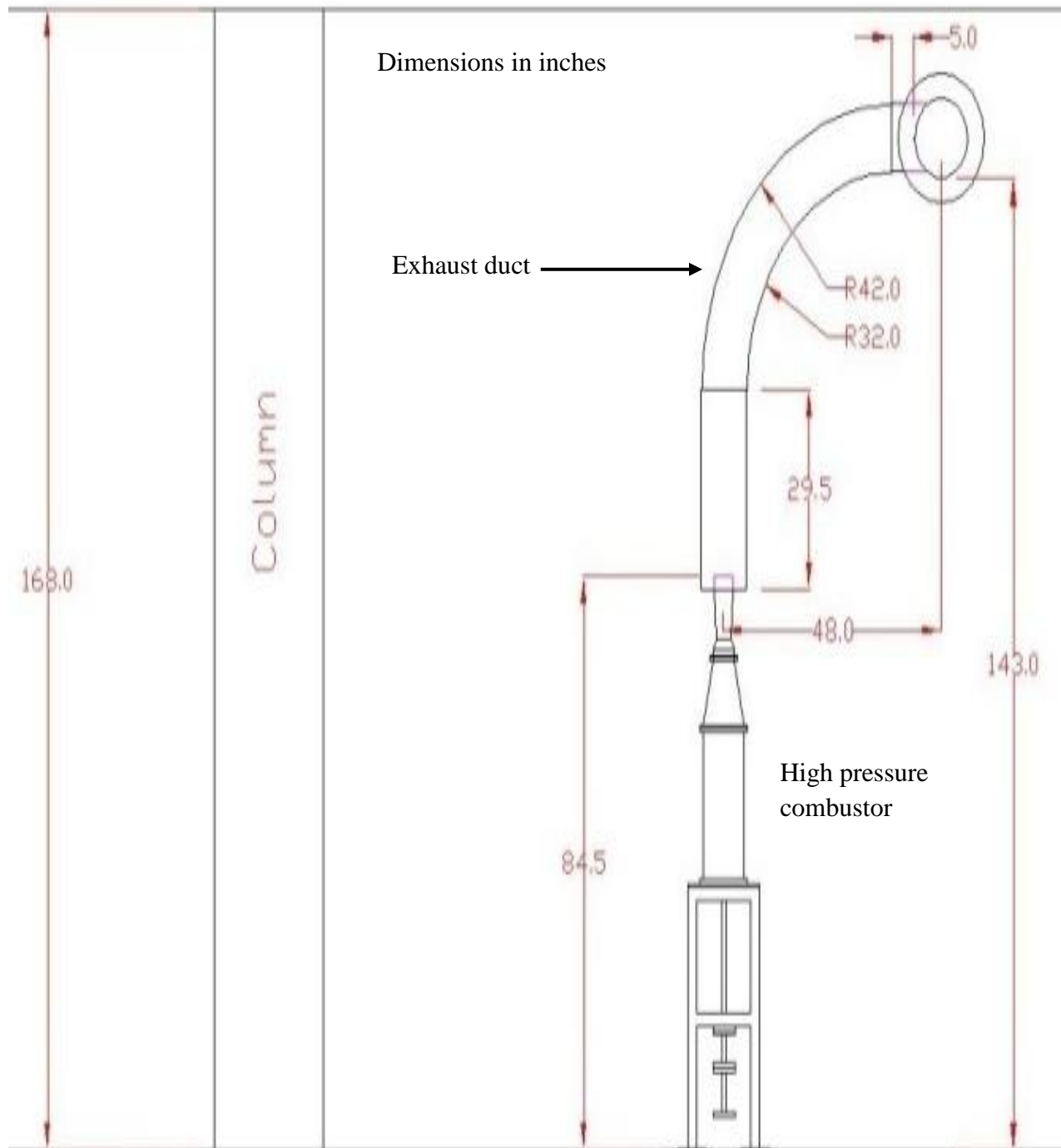


Figure 2.9. Side view of layout for exhaust system

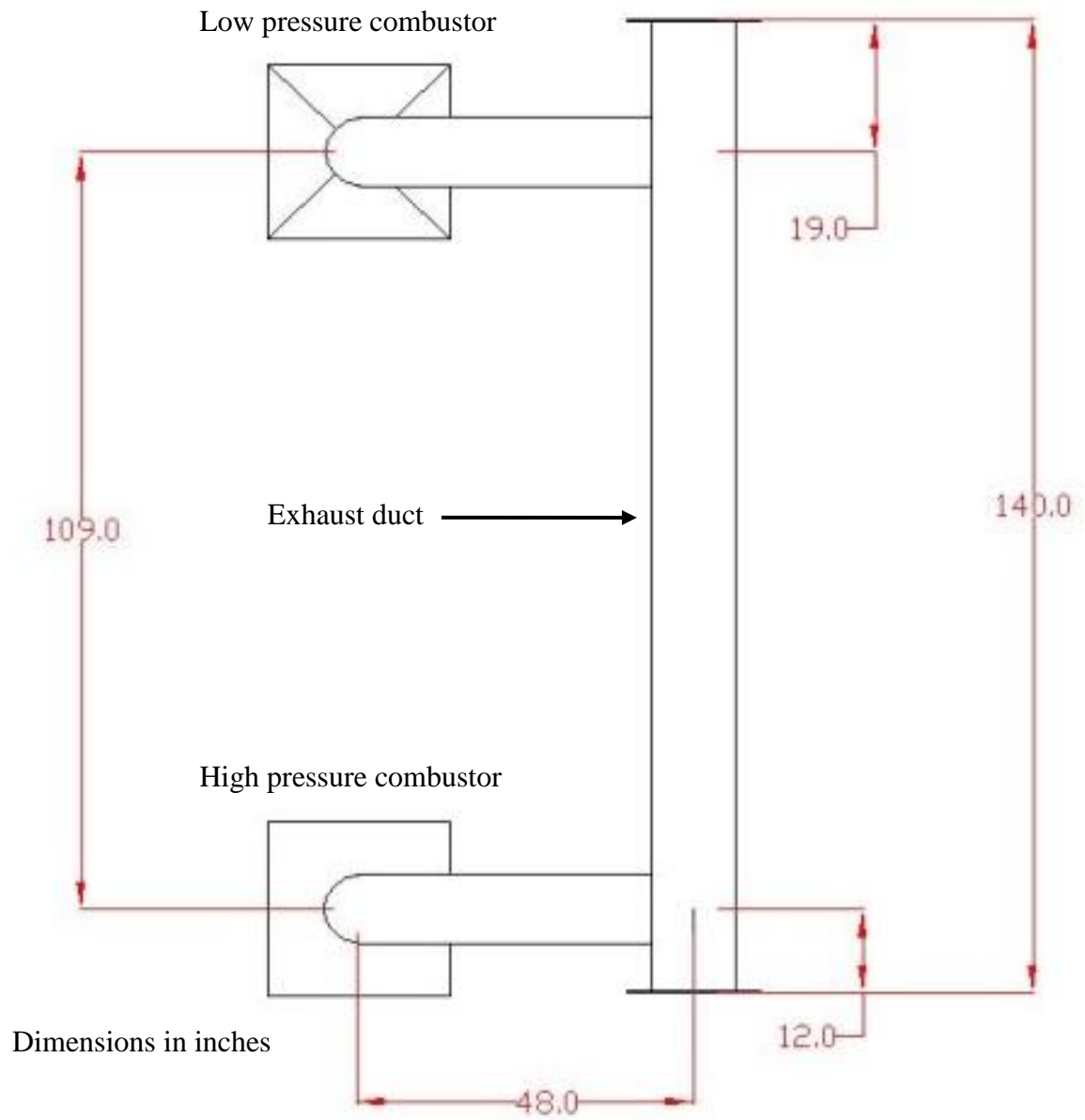


Figure 2.10. Overhead view of layout for exhaust system

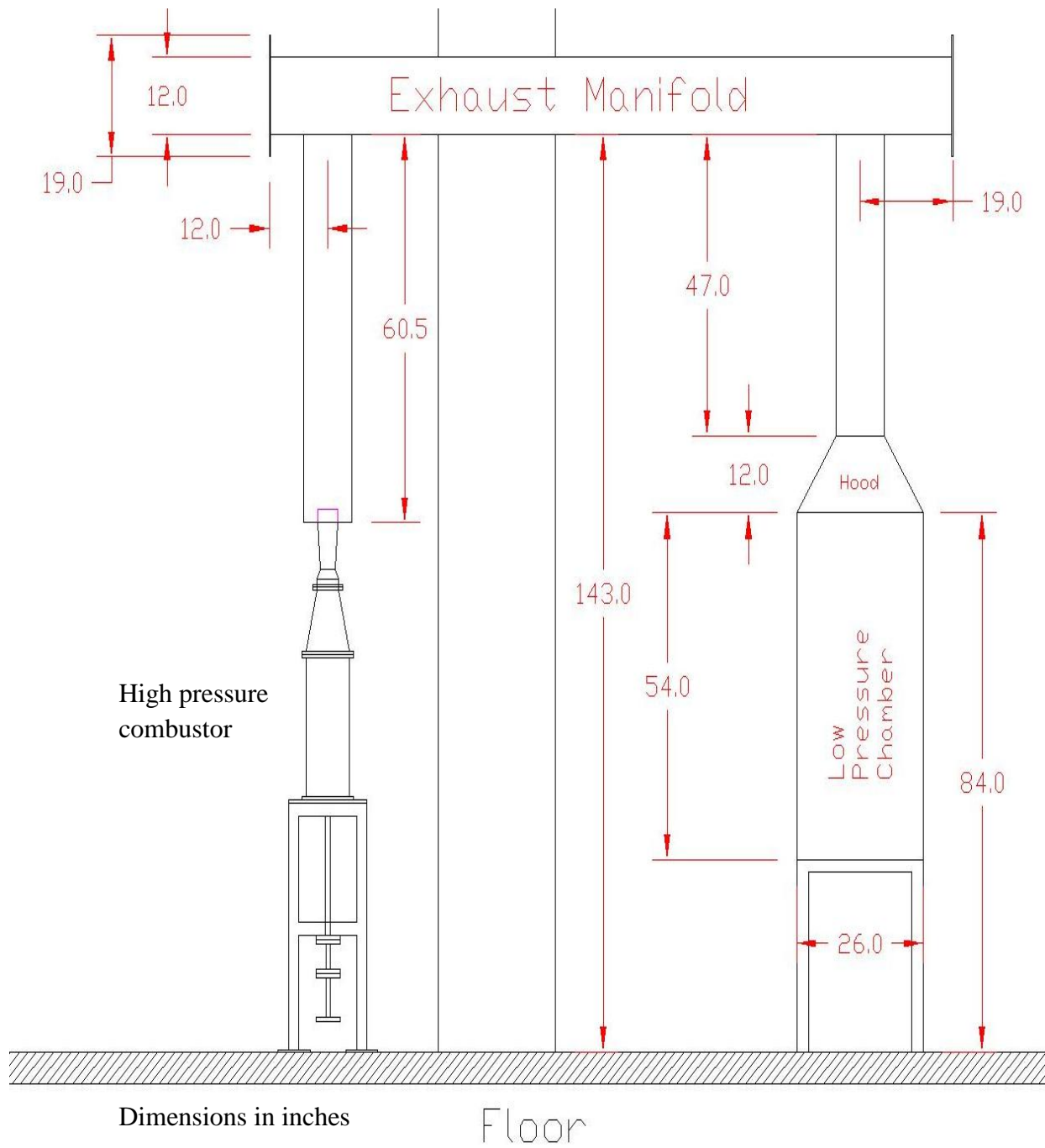


Figure 2.11. Back view of layout for exhaust system

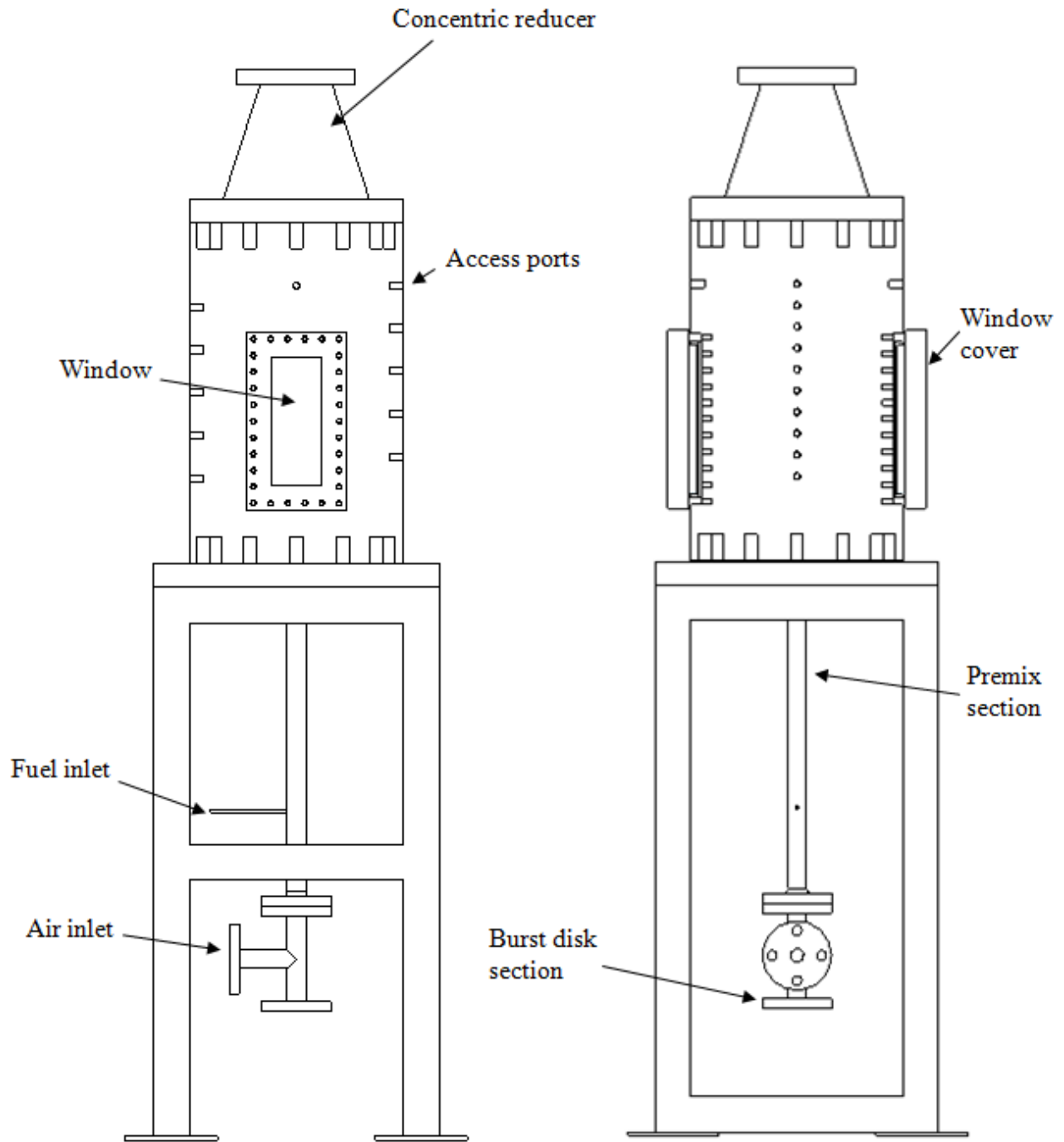


Figure 2.12. Schematic of assembled experimental apparatus

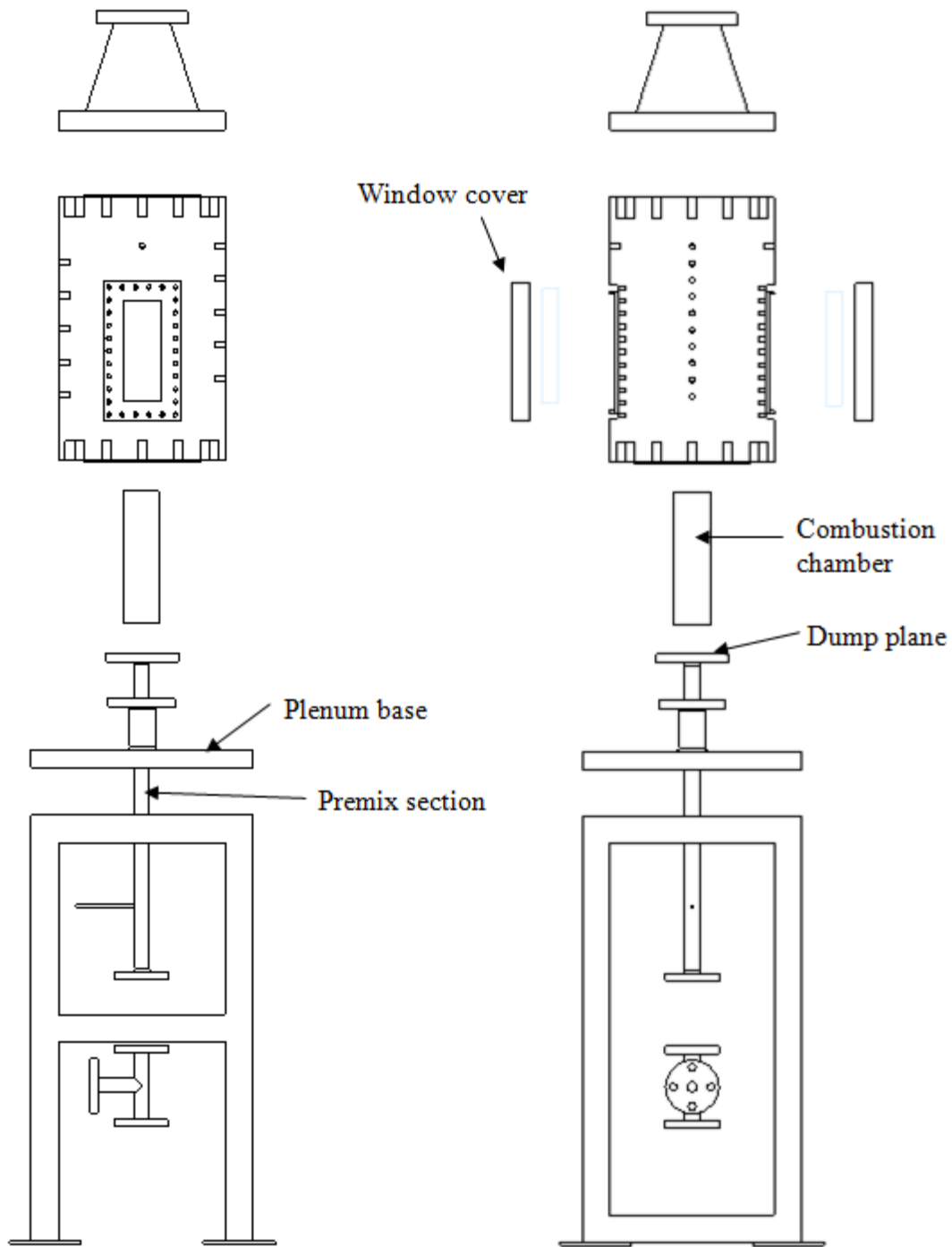


Figure 2.13. Exploded view of experimental apparatus

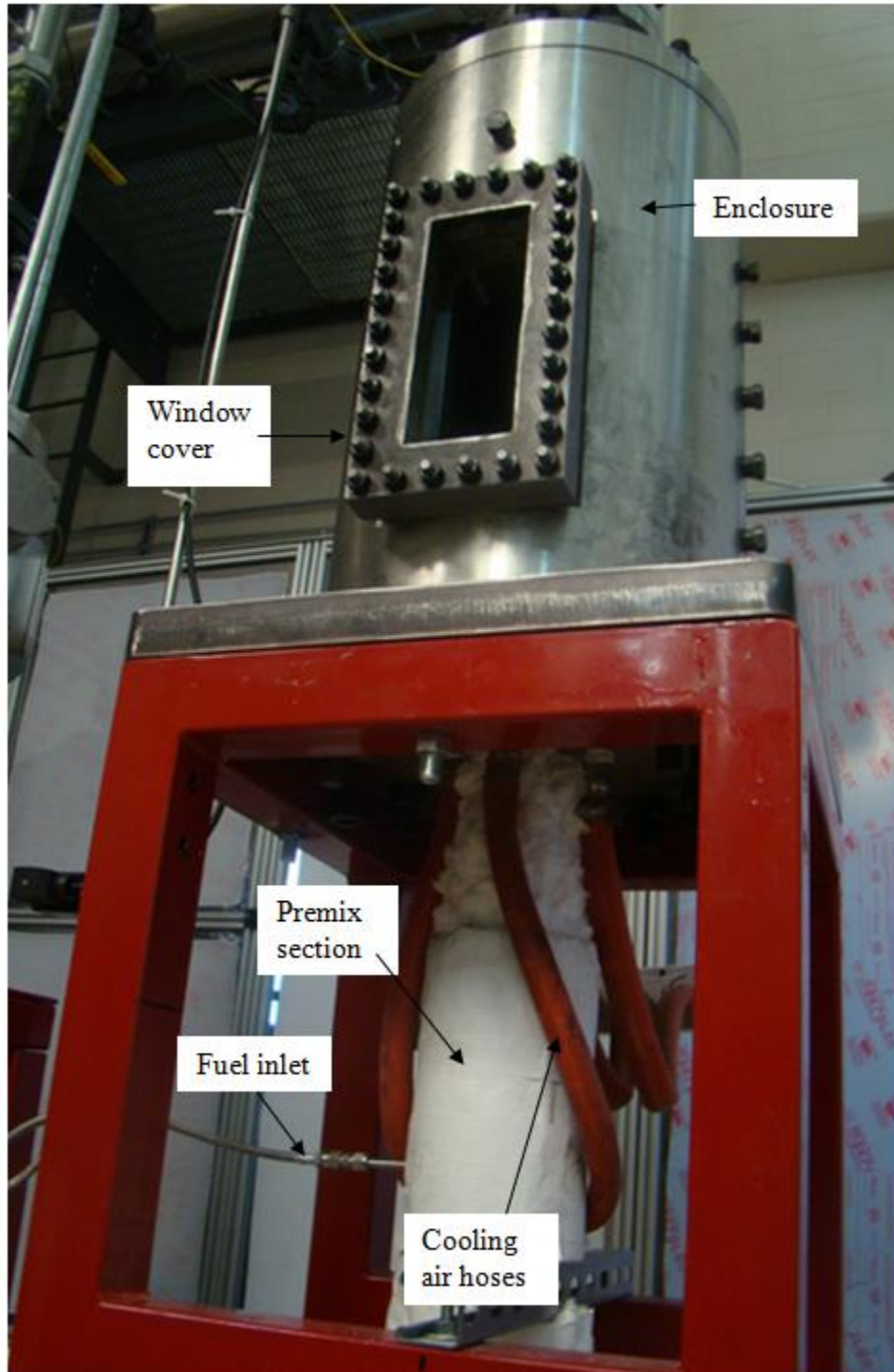


Figure 2.14. Photographic image of experimental apparatus

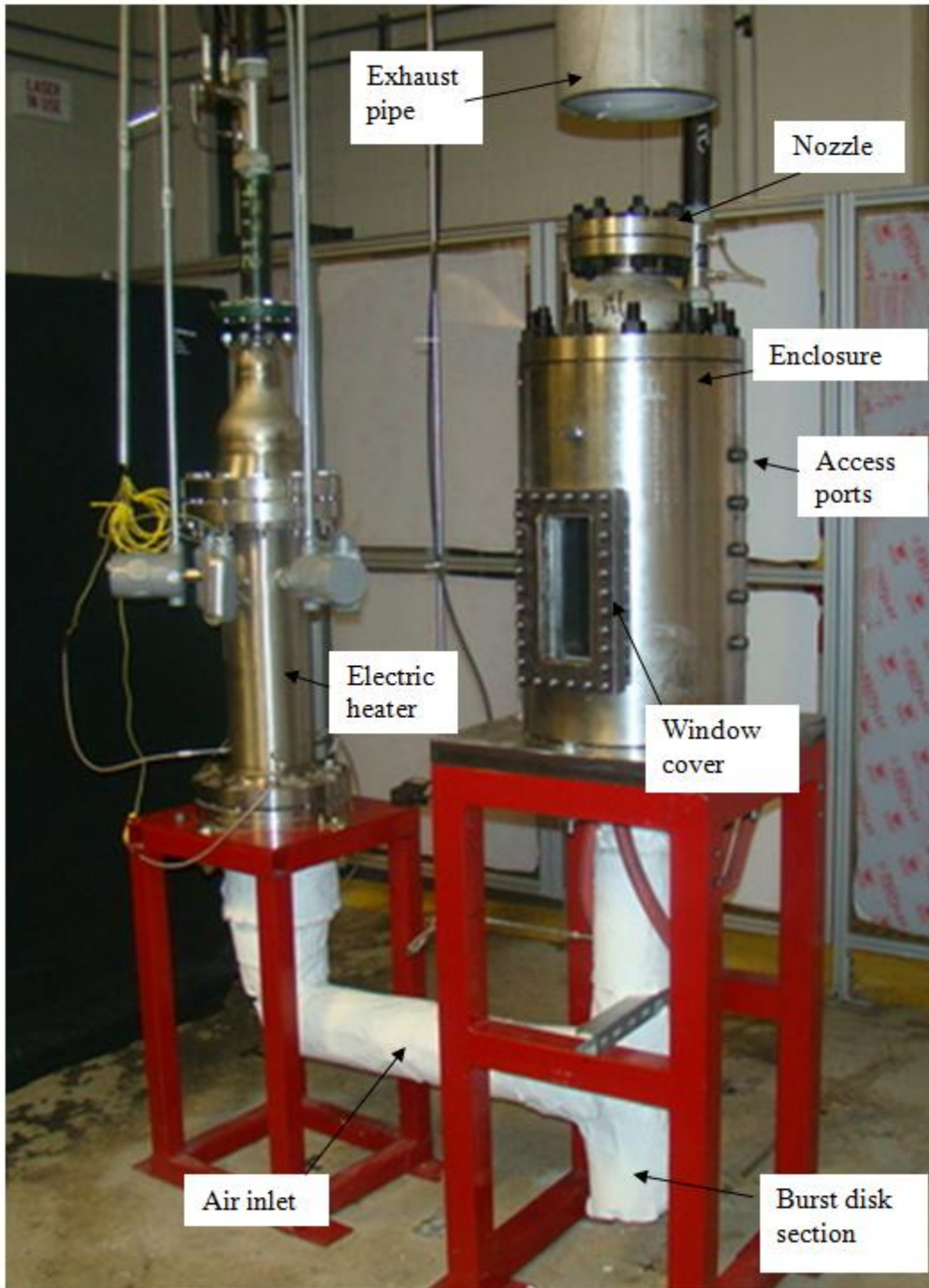


Figure 2.15. Photographic image of experimental apparatus

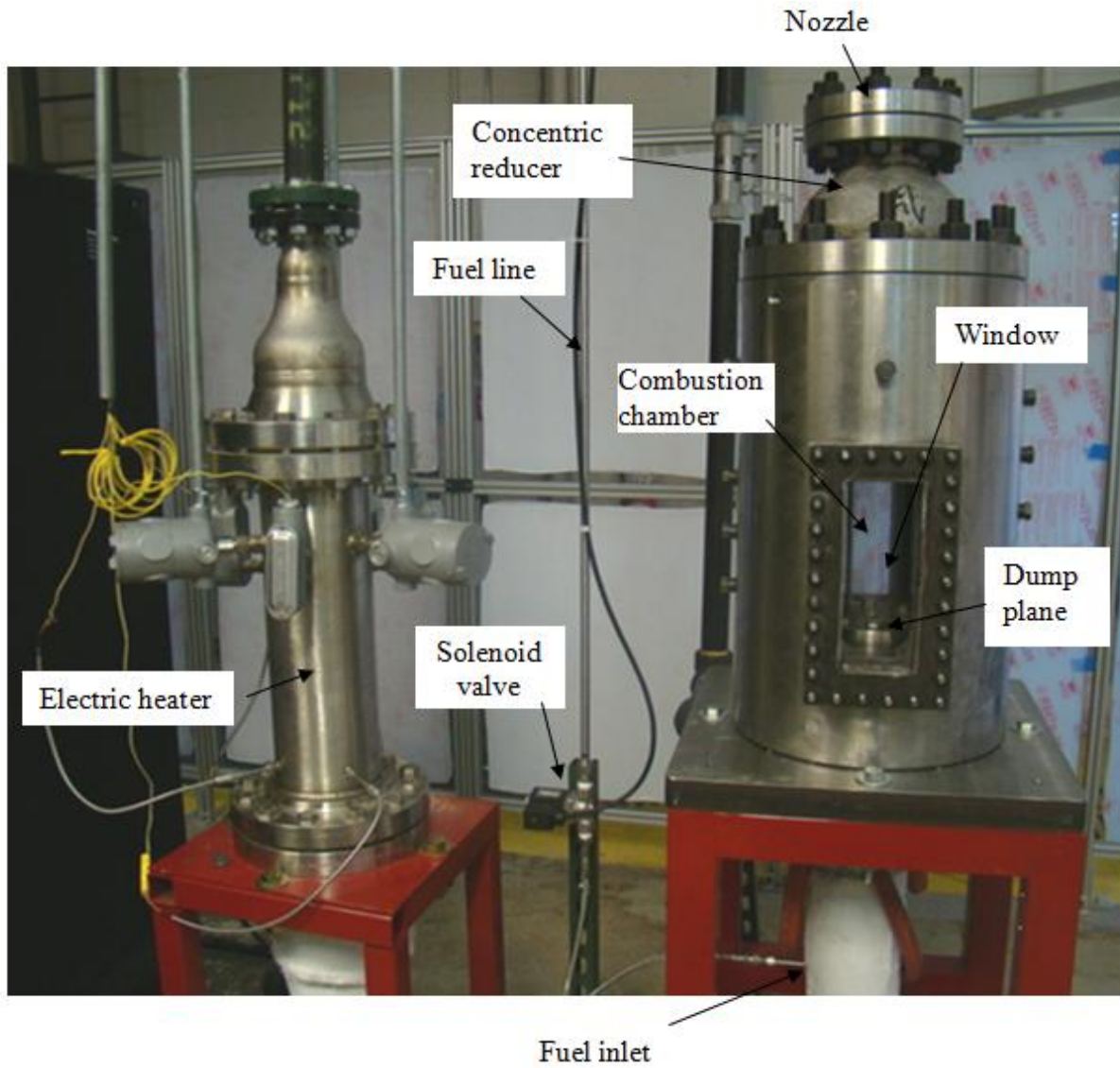


Figure 2.16. Photographic image of experimental apparatus



*Figure 2.17.* Photographic image of swirler

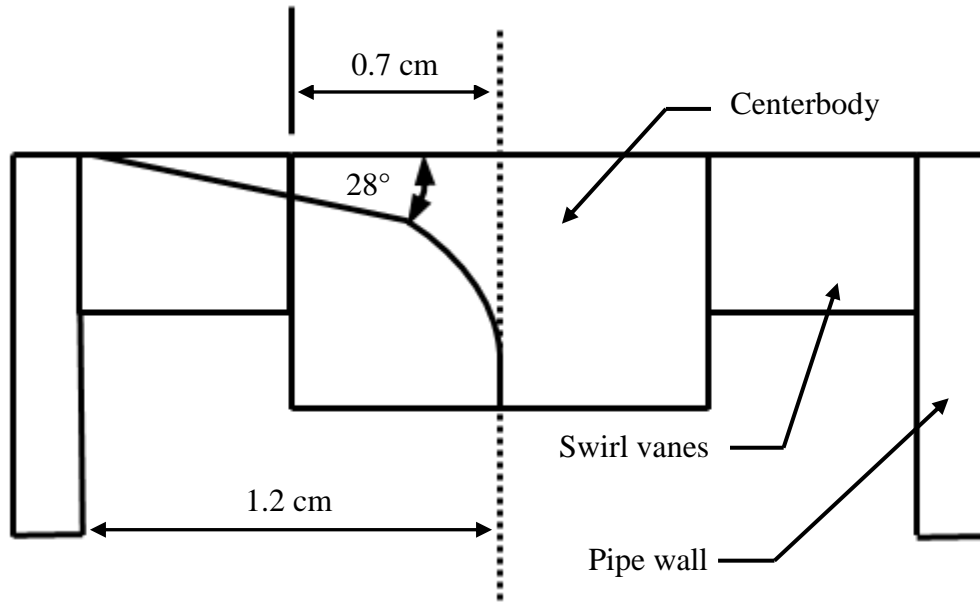


Figure 2.18. Detailed drawing of swirler

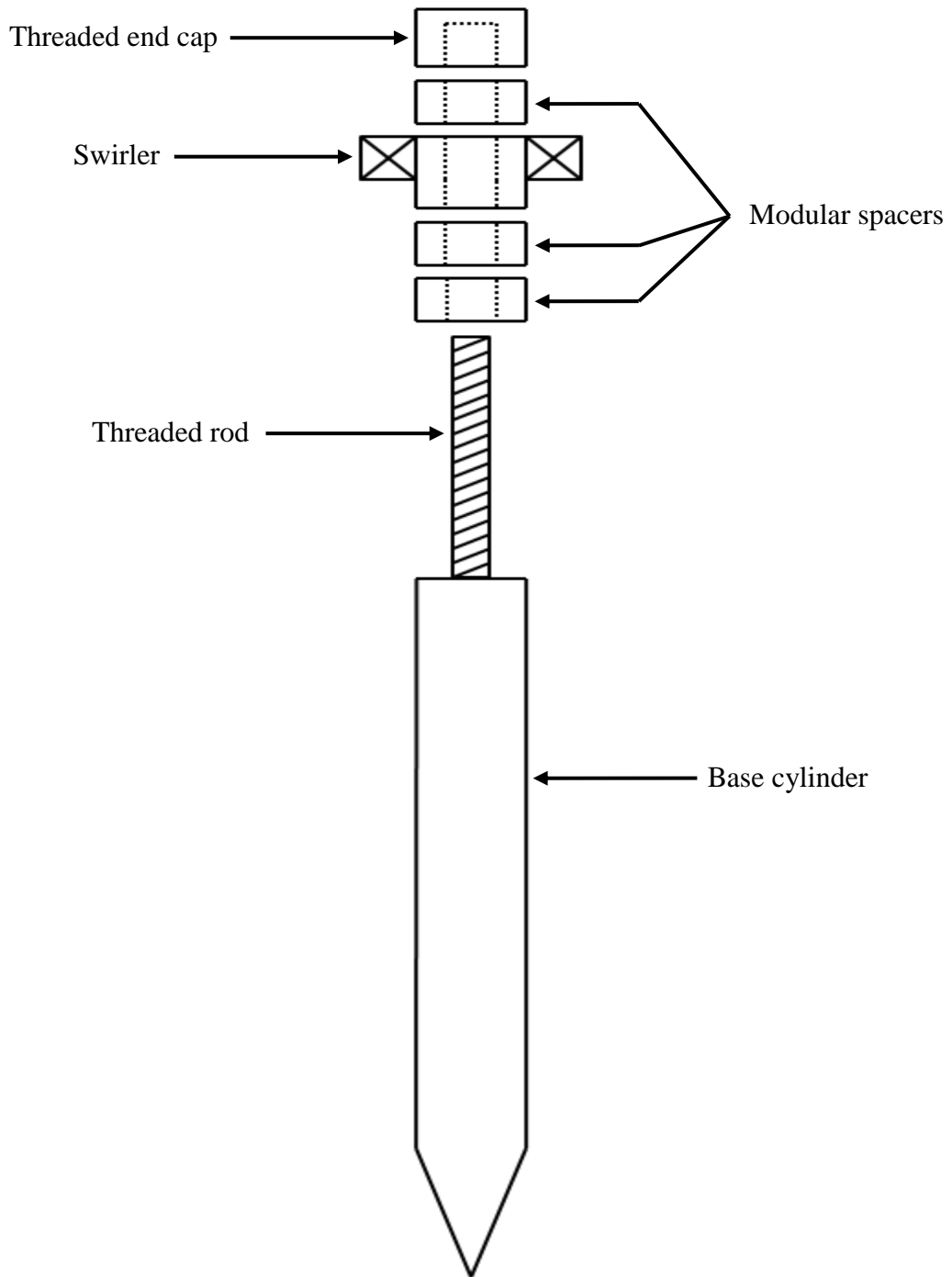


Figure 2.19. Exploded schematic of variable swirler mechanism

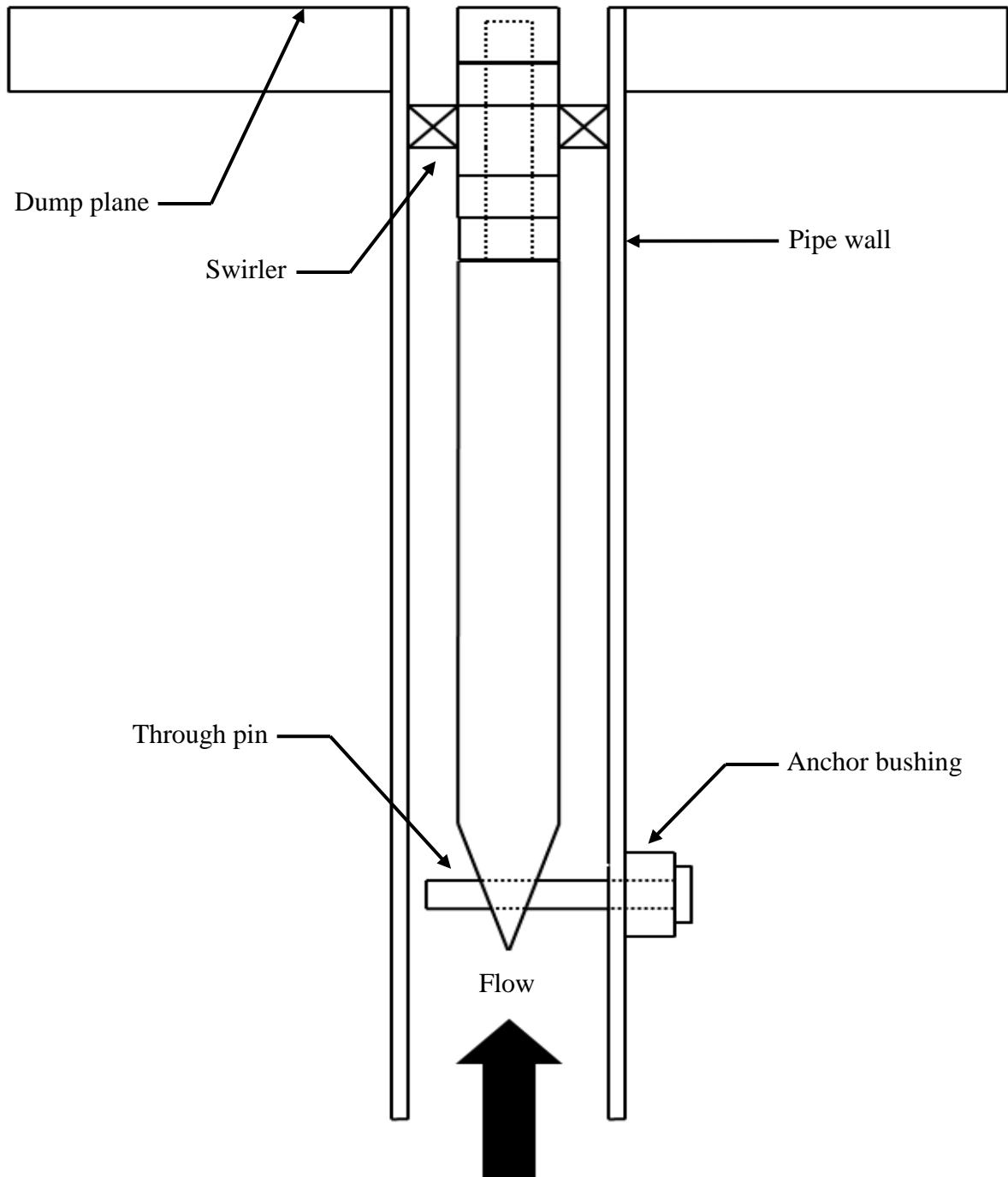
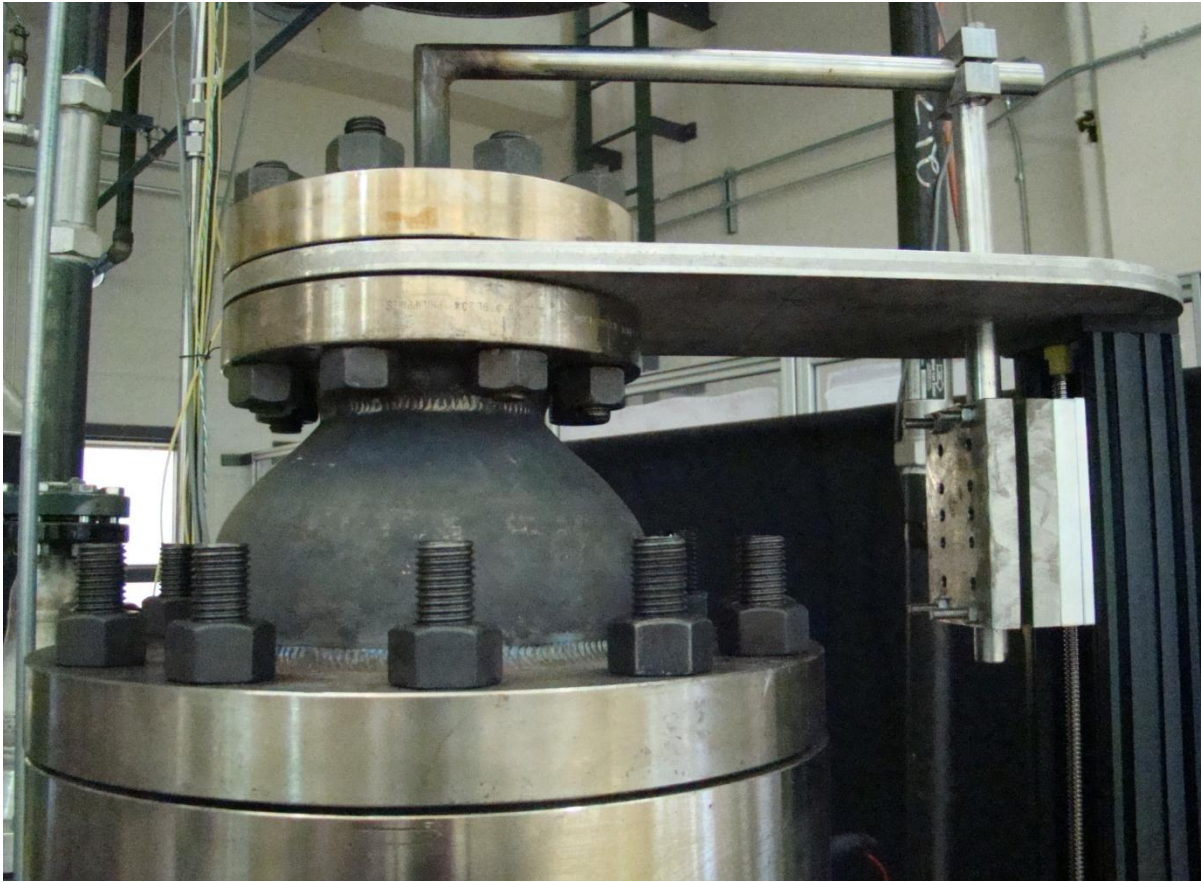


Figure 2.20. Schematic diagram of swirler mechanism mounted inside inlet pipe



*Figure 2.21.* Photographic image of pressure throttle valve

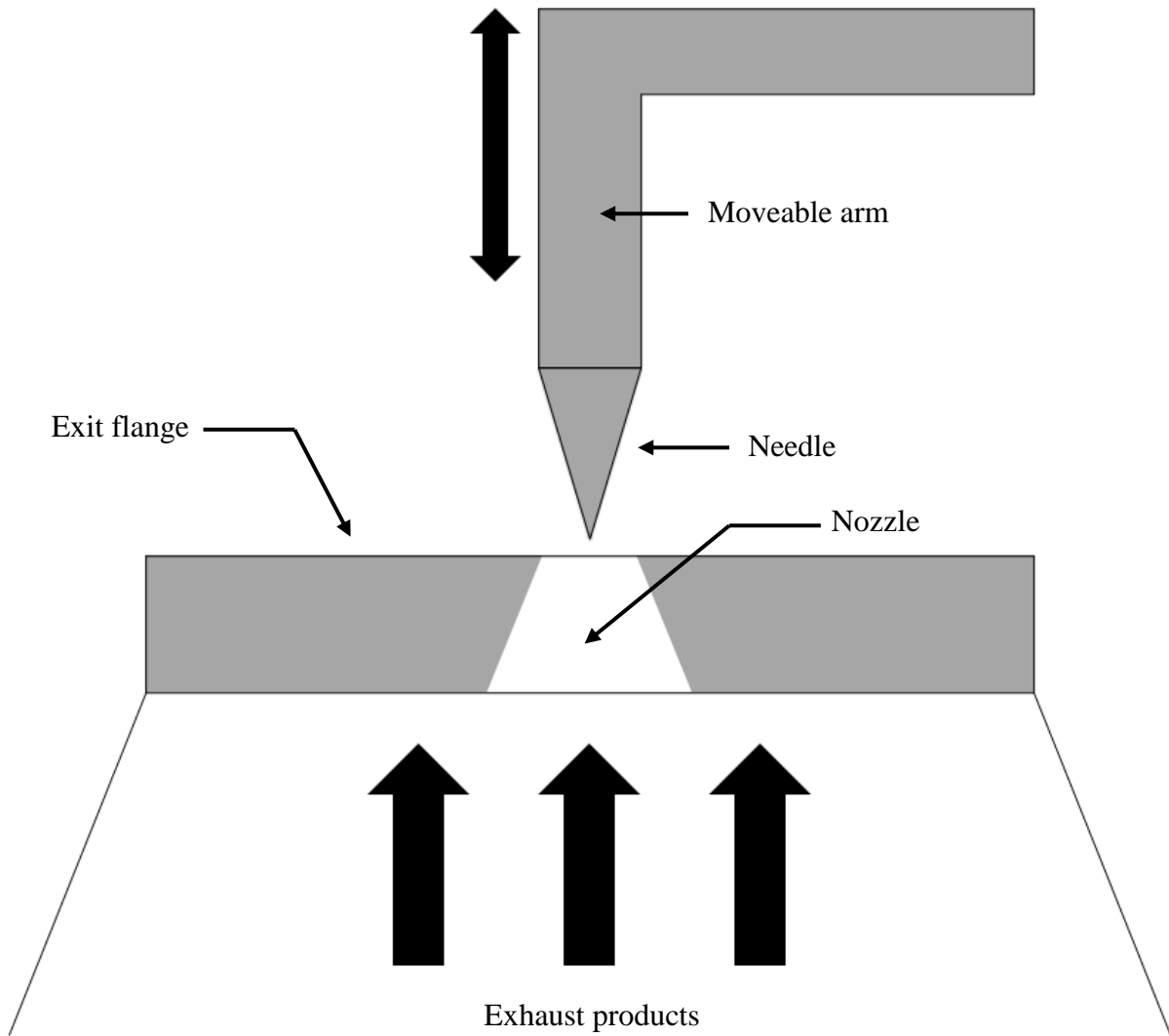


Figure 2.22. Schematic of pressure throttle valve

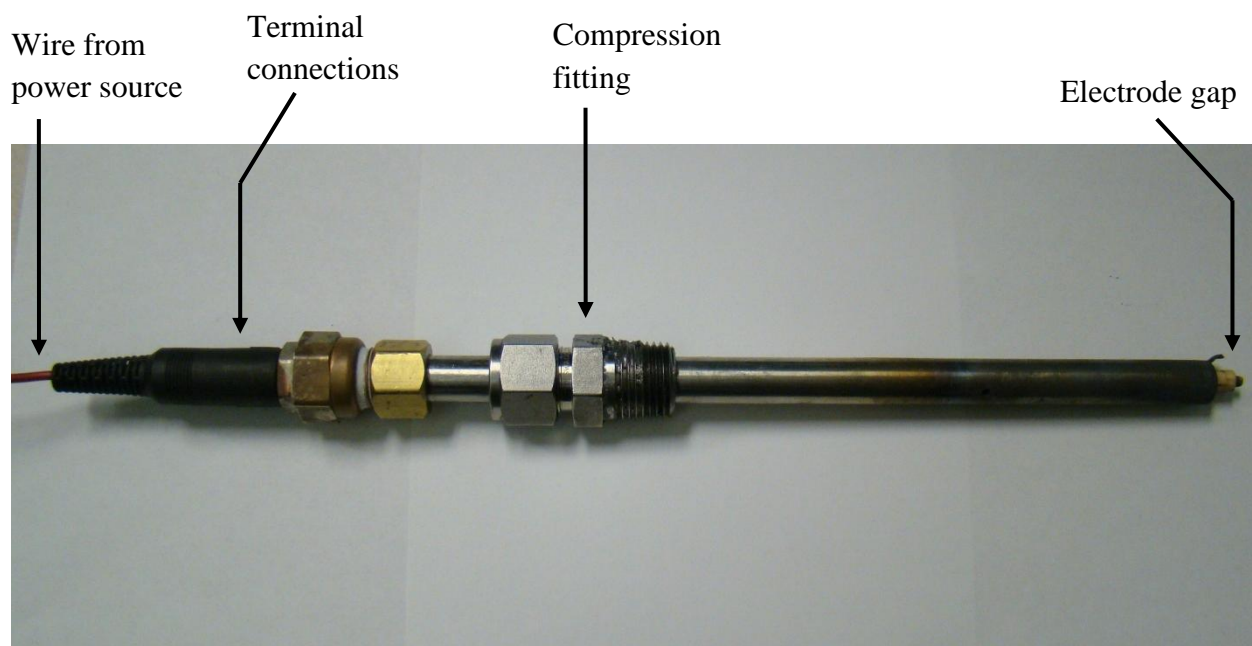


Figure 2.23. Photographic image of ignition probe

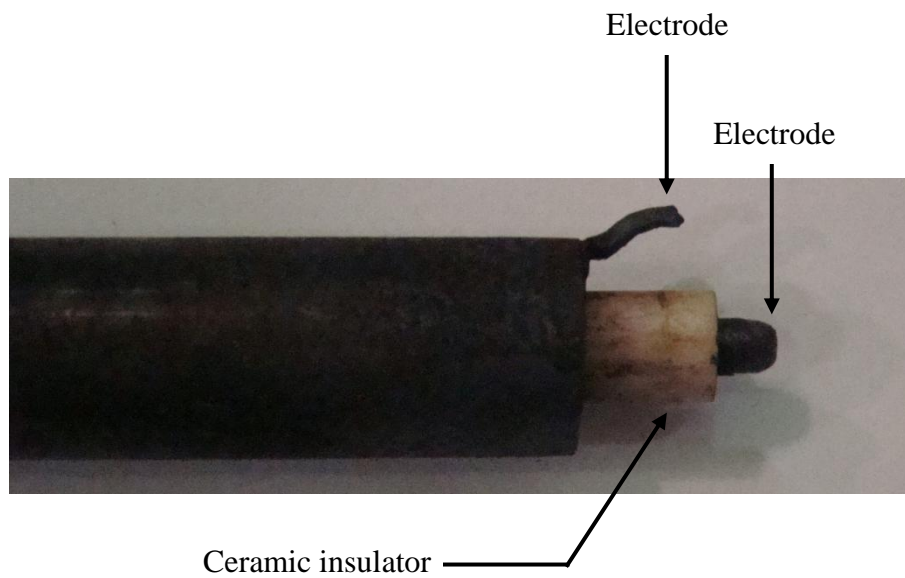


Figure 2.24. Photographic image of electrode gap

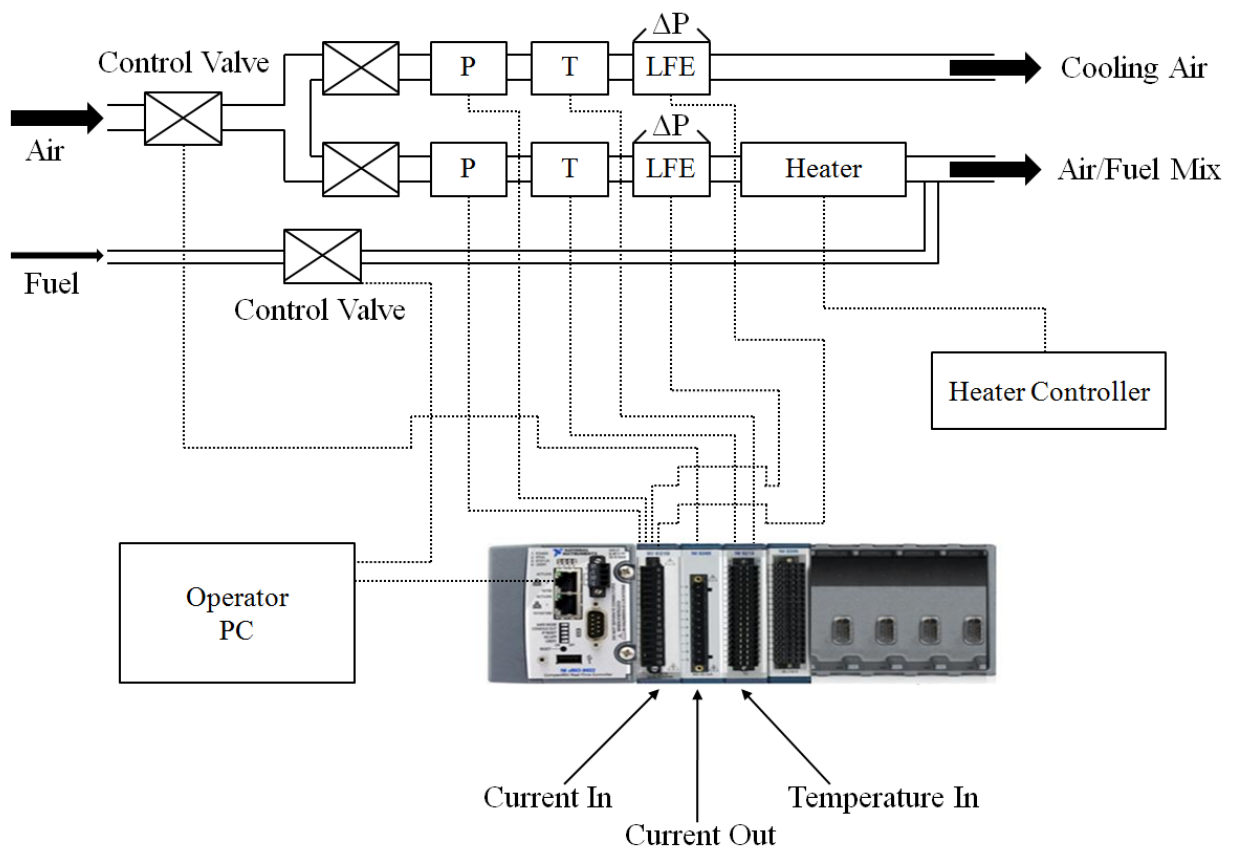


Figure 2.25. Schematic layout of flow control system

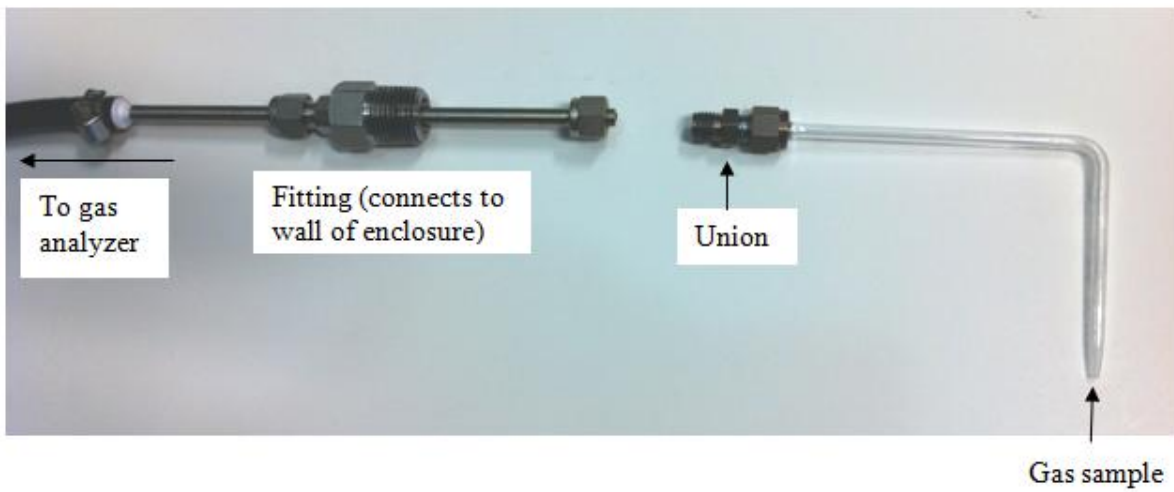
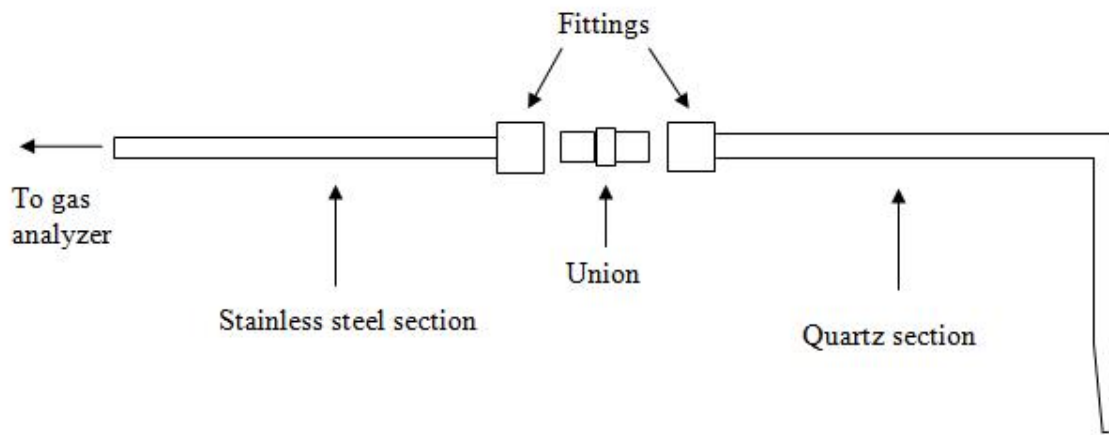


Figure 2.26. Emissions sampling probe

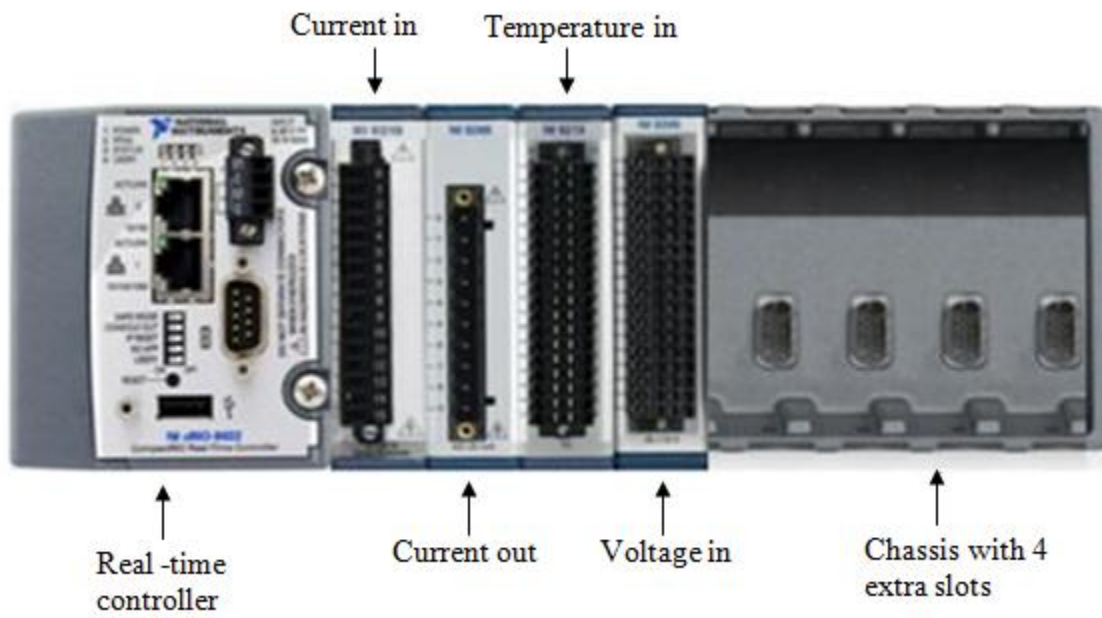


Figure 2.27. Layout of NI CompactRIO data acquisition system



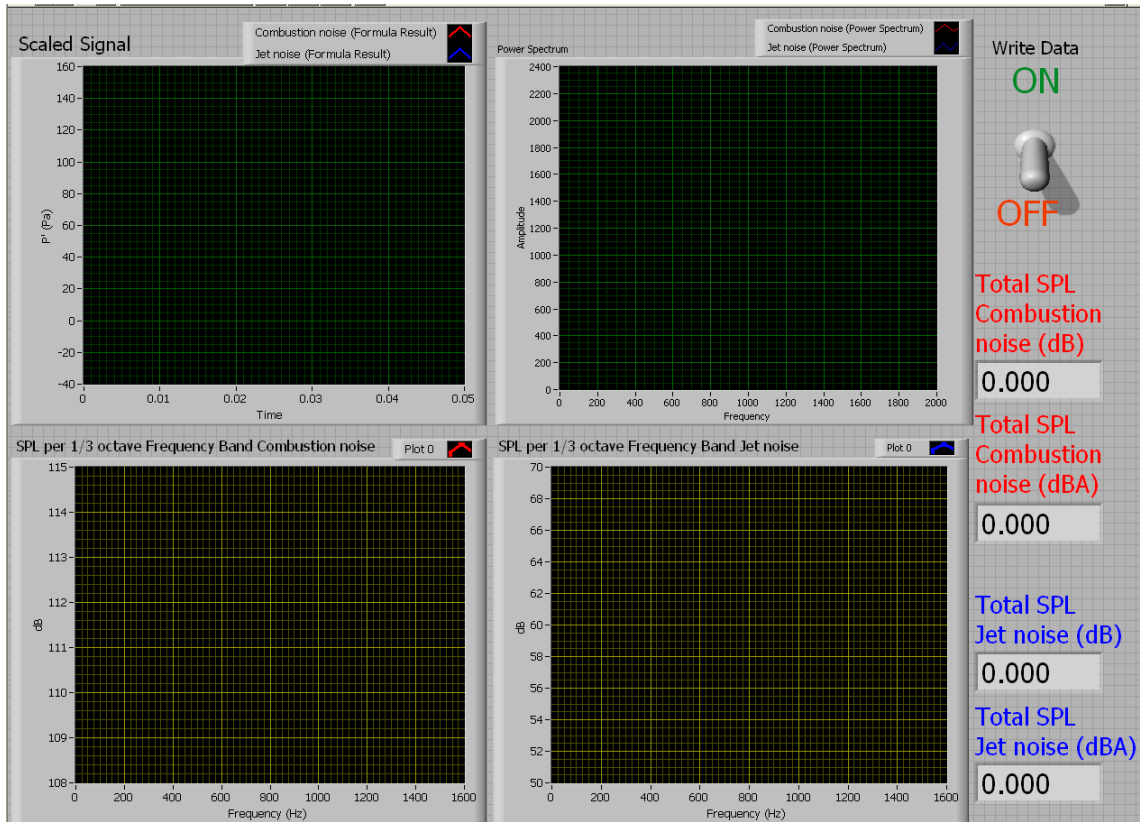


Figure 2.29. LabVIEW noise measurement front panel as displayed on operator PC

## CHAPTER 3

### REDUCTION OF COMBUSTION NOISE AND ACOUSTIC INSTABILITIES WITH POROUS INERT MEDIA

#### 3.1 Overview

In a swirl-stabilized combustion system, flame stabilization is achieved by inducing a swirling motion to premixed reactants upstream of the combustor dump plane. As reactants pass through the swirler and enter the combustion chamber, a sudden increase in cross-sectional area takes place. This rapid expansion of swirling flow produces central and corner recirculation zones within the combustion chamber. The recirculation of hot product gases provides a mechanism for delivering ignition energy to the incoming reactants, thereby sustaining combustion in a region downstream of the dump plane of the combustor. While these recirculation zones are necessary to achieve a stable flame, they are also thought to be the primary source of noise in swirl-stabilized combustion systems (Sequera & Agrawal, 2009). Highly turbulent structures are generally present within these zones and may cause significant fluctuations in flow, heat release rate, and pressure. Pressure fluctuations within the flame zone propagate outwards as sound waves which may cause excessive structural vibrations and potential system failure.

Thermo-acoustic instability occurs when pressure waves generated by fluctuations in heat release rate interact with those generated by oscillating pressure within the reaction zone. When these wave interactions are coupled in accordance with Rayleigh's criterion, acoustic instability

occurs within the combustor. Conventional active methods of eliminating these instabilities involve flow control schemes that can be complex and require the use of costly equipment. This study presents a passive approach to suppress fluctuations within the system that lead to combustion noise. Additionally, combustion noise and combustion instabilities are both driven by the same fundamental mechanisms. Therefore, any effort to reduce total combustion noise is also an attempt to alleviate acoustic instabilities within the system.

The present approach is a passive technique in which a porous insert is placed within the flame zone of a swirl-stabilized combustion system to directly alter the flow field within the combustor. Thus, the present methodology is capable of mitigating combustion noise and instability at the source of turbulent fluctuations in the reaction zone. In addition to altering the incoming flow field, the ring shaped porous foam also modifies turbulent structures inside the combustion chamber in an advantageous manner (Sequera & Agrawal, 2009). In a typical swirl-stabilized combustor, corner recirculation zones of hot product gases are widely presumed to be the dominant source of noise production (Sequera & Agrawal, 2011). In the current study, porous inserts are placed downstream of the combustor dump plane to eliminate formation of corner recirculation zones, thereby eliminating the dominant source of noise producing fluctuations. Furthermore, the present technique provides significant damping of acoustic waves inside the combustor. Sound waves created by flame dynamics are attenuated by pores within the PIM.

### 3.2 Experimental Procedure

The experimental test facility described in detail in Chapter 2 is shown schematically in Figure 3.1. The present study is primarily concerned with characterizing noise production with

and without porous media at atmospheric pressure and may be viewed as a preliminary step towards evaluating effectiveness of the technique at elevated pressures. As such, all experiments in this study are performed at atmospheric conditions, without the use of the stainless steel pressure vessel used for high pressure combustion.

Combustion air is supplied with a dedicated compressor and is controlled with a pressure regulator and automated flow control valve. Since tests are conducted at atmospheric pressure, no cooling air is used in this study and all supply air is directed for combustion purposes only. The 72 kW electric heater is used to preheat combustion air to temperatures up to 260 °C. Compressed natural gas is supplied by a fuel station and controlled with a pressure regulator and mass flow controller. Fuel pressure is set to 690 kPa [100 psi] for all tests. Fuel is injected into the preheated combustion air, where mixing occurs within the premixer pipe. In the premixer pipe section, a swirler is used to impart a radial swirling motion to the mixture of preheated fuel and air prior to entering the combustion chamber. As detailed in Chapter 2, the swirler can be mounted flush with the dump plane or recessed as much as 3.8 cm [1.5 in] upstream of the dump plane. The present study compares cases where the swirler is flush mounted to cases where the swirler is fully recessed. Pressure drop across the swirler and/or PIM is measured using a differential pressure transducer. Differential measurements are used to determine pressure loss penalty incurred by using porous media.

After passing through the premixer section, reactants enter the combustion chamber, a 30.5 cm [12 in] long quartz tube with inside diameter of 7.4 cm [2.9 in], where combustion takes place. As shown in Figure 3.2, the quartz tube is secured to the dump plane flange using a stainless steel ring and 0.32 cm [1/8 in] diameter threaded rods. The porous inserts are provided by Ultramet Corporation and are secured inside the combustion chamber using a press fit

technique. Any gap between the OD of the PIM and the ID of the quartz tube is filled by a graphite foil layer to ensure tightness of fit. Sheets of 1.6 mm [1/16 in] thick graphite foil are cut into strips of and layered around the PIM as needed. The graphite foil layer also blocks reactants from flowing around the outside of the PIM, thereby directing flow through the porous material. Based upon conclusions from previous work (Sequera & Agrawal, 2011), porous rings are fabricated with a diffuser shaped opening in the center to provide the best performance regarding noise reduction. For endurance tests, a piece of foam with pore density of 18 ppcm [45 ppi] was used. Referred to as PIM #1, the insert is 2.5 cm tall with 7 cm OD. For all other tests, two pieces of porous foam are used, referred to as PIM #2 and PIM #3. Both of these inserts are 5 cm in height with 7 cm OD. PIM #2 has pore density of 18 ppcm [45 ppi], while PIM #3 has pore density of 40 ppcm [100 ppi]. The diffuser angle for PIM #1 is 14.0°, while the angle for PIM #2 and PIM #3 is 7.1°. PIM #3 is only used in cases where interior combustion takes place with PIM #2. In such cases, the denser porous foam acts as a flame arrestor, preventing flashback into the porous insert. Dimensions for all porous pieces used in this study are shown in Table 3.1 and Figure 3.3.

Table 3.1

*Characteristics of PIM*

| PIM    | Diffuser ID (cm) | Diffuser OD (cm) | Major OD (cm) | Height (cm) | Pore Density (ppcm) | Diffuser Angle |
|--------|------------------|------------------|---------------|-------------|---------------------|----------------|
| PIM #1 | 2.50             | 3.75             | 7.0           | 2.5         | 18                  | 14°            |
| PIM #2 | 2.50             | 3.75             | 7.0           | 5.0         | 18                  | 7.1°           |
| PIM #3 | 2.50             | 3.75             | 7.0           | 5.0         | 40                  | 7.1°           |

Noise measurements are made at the combustor exit plane with a condenser microphone positioned at a radial distance of 30.5 cm [12 in] from the central axis of the quartz combustion chamber. For one particular case ( $T_{\text{inlet}} = 21^{\circ}\text{C}$ ,  $Q = 600$  SLPM,  $\phi = 0.65$ ), combustion noise is measured for seven different radial locations to understand the combustor sound propagation process. Noise measurements are taken at 4000 Hz and are routed into a dedicated DAQ board. LabVIEW software is used to process all sound measurements for this study.

For all combustion tests, emissions are continuously sampled by a 5 mm OD quartz probe. The probe is tapered to 1 mm ID at the upstream end to ensure reaction quenching within the probe. The probe is mounted to a one-dimensional traversing system such that a 5-point emissions profile can be taken across the ID of the quartz tube for each test case. Product samples are routed through an ice bath followed by a water trap to condense and collect water vapor before being fed into the gas analyzer. Dry samples are then routed through electrochemical analyzers to measure concentrations of carbon monoxide (CO) and nitrous oxides (NO<sub>x</sub>) in units of ppm. Diatomic oxygen and carbon dioxide gas concentrations are also measured to provide a method to cross-check equivalence ratio as calculated from measured flow rates of fuel and air.

### 3.3 Results and Discussion

The primary objective of this study is to characterize combustion noise and thermo-acoustic instability without and with the existence of porous material within the combustion chamber. Therefore, a parametric study is performed for a variety of test conditions. Parameters varied include preheat air temperature, air flow rate, and equivalence ratio. Combustion air is supplied at temperatures of 21 °C, 130 °C, and 260 °C. For each air inlet temperature, the air

flow rate is taken as 300, 600, and 900 SLPM. Finally, for each combination of air inlet temperature and flow rate, equivalence ratios of 0.60, 0.65, 0.70, and 0.75 are used. For each case, a flame photograph without and with PIM is shown. Measured pressure drop is plotted for each case to examine pressure loss without and with PIM. Noise measurements are presented by showing two types of plots: SPL per one-third octave band and spectral power over a frequency range of 0 to 2,000 Hz. SPL per one-third octave band provides an overall representation of noise levels across the measured frequency range. SPL is summed up and plotted for each one-third octave band and is shown in dB. On the other hand, spectral power plots show the full frequency sound signature and provide a more complete depiction of broadband noise and/or instability. Spectral power plots are shown on a dB scale to highlight dominant frequencies and magnitudes of noise, especially in cases where instabilities exist. Finally, NO<sub>x</sub> and CO emissions without and with PIM are shown for each case.

### *3.3.1 Effect of Microphone Location*

All sound measurements in this study are made at a distance of 30.5 cm [12 in] from the top of the quartz combustion chamber. A brief study is conducted to investigate any unforeseen effects of moving the microphone nearer to or further from the combustion chamber. In this study, sound measurements are taken with the microphone at seven different radial locations. The microphone distance from the combustor exit plane is varied between 15.2 and 45.7 cm [6 - 18 in] as shown in Table 3.2. Figure 3.4 presents a summary of these measurements, expressed as SPL per one-third octave band. For this test, total SPL decreases in a linear fashion as the microphone is moved away from the combustor. This result is expected due to increased surface area of sound waves as distance from source is increased. As surface area is increased, energy

density per unit area is decreased. Since the face of the microphone has fixed area, total measured SPL is reduced with increasing distance.

Table 3.2

*Microphone position and corresponding SPL*

| Microphone Distance (cm) | Microphone Distance (in) | Location (#) | Total SPL (dB) |
|--------------------------|--------------------------|--------------|----------------|
| 15.2                     | 6                        | Location 1   | 117.0          |
| 20.5                     | 8                        | Location 2   | 115.5          |
| 25.4                     | 10                       | Location 3   | 113.8          |
| 30.5                     | 12                       | Location 4   | 112.9          |
| 35.6                     | 14                       | Location 5   | 112.0          |
| 40.6                     | 16                       | Location 6   | 110.8          |
| 45.7                     | 18                       | Location 7   | 109.5          |

*3.3.2 Reduction in Combustion Noise*

Porous media is effective in reducing total combustion noise for the cases examined in this study. Particularly at low and intermediate preheat temperatures, combustion noise is significantly reduced with the addition of PIM. As shown in Table 3.3, combustion with porous media is most successful in mitigating noise when SPL without PIM is above approximately 120 dB. During the experiment, it was observed that intense combustion instabilities usually caused the total SPL to rise above 120 dB. Thus, combustion with porous media is most effective in cases where acoustic instability is the dominant component of total SPL. However, even for cases where instability is not dominant, the porous insert provides good reduction of noise over the full frequency range. In such cases, the existence of PIM reduces total SPL by as much as 20 dB. The reduction of broadband combustion noise is likely attributed to damping by the porous foam. While the PIM favorably affects turbulent fluctuations and distribution of heat release

rate, acoustic damping is probably responsible for most of the reduction in broadband noise when instabilities are not dominant.

Note that the overall flame shape for cases with PIM in this study is quite different than what was observed by Sequera (2011). In the current study, flamelets appear on the surface of the PIM; however the central flame is lifted above the PIM rather than constrained within the annular void. This behavior is likely caused by the difference in PIM and inlet swirler geometry as compared with Sequera (2011). Presumably, the central flame should be swirl-stabilized within the PIM to achieve the greatest amount of noise reduction. Acoustic damping is thought to be most effective when the PIM is located around the source of pressure oscillations, rather than upstream of the flame. Thus, PIM used in the current study could be further optimized to eliminate flame lifting by increasing the diffuser angle and/or decreasing the swirl angle of the inlet swirler.

Table 3.3

*Comparison of SPL without and with porous media*

| $T_{\text{inlet}}$ (°C) | $\dot{m}_{\text{air}}$ (SLPM) | $\phi$ | SPL without PIM (dB) | SPL with PIM (dB) | PIM    |        |
|-------------------------|-------------------------------|--------|----------------------|-------------------|--------|--------|
| 21                      | 300                           | 0.60   | 102.1                | 83.6              | PIM #2 |        |
|                         | 300                           | 0.65   | 101.4                | 85.9              | PIM #2 |        |
|                         | 300                           | 0.70   | 102.1                | 89.6              | PIM #2 |        |
|                         | 300                           | 0.75   | 104.5                | 92.0              | PIM #2 |        |
|                         | 600                           | 0.60   | 110.3                | 90.3              | PIM #2 |        |
|                         | 600                           | 0.65   | 112.4                | 92.7              | PIM #2 |        |
|                         | 600                           | 0.70   | 123.2                | 95.7              | PIM #2 |        |
|                         | 600                           | 0.75   | 133.1                | 98.8              | PIM #2 |        |
|                         | 900                           | 0.60   | 115.7                | 93.5              | PIM #2 |        |
|                         | 900                           | 0.65   | 118.2                | 96.7              | PIM #2 |        |
|                         | 900                           | 0.70   | 127.4                | 100.1             | PIM #2 |        |
|                         | 900                           | 0.75   | 132.6                | 102.9             | PIM #2 |        |
|                         | 130                           | 300    | 0.60                 | 101.7             | 95.1   | PIM #2 |
|                         |                               | 300    | 0.65                 | 104.9             | 98.4   | PIM #2 |
|                         |                               | 300    | 0.70                 | 109.7             | 99.9   | PIM #2 |
|                         |                               | 300    | 0.75                 | 109.6             | 98.6   | PIM #2 |
| 600                     |                               | 0.60   | 133.1                | 99.5              | PIM #2 |        |
| 600                     |                               | 0.65   | 135.8                | 103.4             | PIM #2 |        |
| 600                     |                               | 0.70   | 133.1                | 109.3             | PIM #2 |        |
| 600                     |                               | 0.75   | 131.3                | 112.5             | PIM #2 |        |
| 900                     |                               | 0.60   | 133.1                | 103.2             | PIM #2 |        |
| 900                     |                               | 0.65   | 130.6                | 106.7             | PIM #2 |        |
| 900                     |                               | 0.70   | 120.7                | 110.3             | PIM #2 |        |
| 900                     |                               | 0.75   | 119.2                | 113.5             | PIM #2 |        |
| 260                     | 300                           | 0.60   | 107.6                | 101.8             | PIM #2 |        |
|                         | 300                           | 0.65   | 107.1                | 99.2              | PIM #2 |        |
|                         | 300                           | 0.70   | 104.6                | 98.3              | PIM #2 |        |
|                         | 300                           | 0.75   | 103.0                | 98.3              | PIM #2 |        |
|                         | 600                           | 0.60   | 113.4                | 106.8             | PIM #3 |        |
|                         | 600                           | 0.65   | 112.9                | 108.7             | PIM #3 |        |
|                         | 600                           | 0.70   | 110.9                | 112.1             | PIM #3 |        |
|                         | 600                           | 0.75   | 110.2                | 113.0             | PIM #3 |        |

### 3.3.3 Elimination of Thermo-acoustic Instability

As previously discussed, combustion instabilities arise within the LPM combustor for a variety of cases without porous media. Instabilities are clearly observed and are characterized by large peaks in SPL at a specific frequency. When experiencing intense instability, sound power is dominated by a distinct tone, often referred to as a “singing flame.” This mode of combustion is repeatable in the experimental combustor, but not predictable. For instance, the instability grows with increasing equivalence ratio in some cases, while in others; the instability actually decreases as the equivalence ratio is increased. This is a major concern for many industrial and commercial combustion applications since component failure can occur very rapidly while undergoing extreme instability. In the current study, the use of PIM is shown to have a drastic impact on combustion instability. When instabilities appear in the combustion system, the presence of PIM essentially eliminates large peaks in sound power. In Figure 3.5, measured pressure fluctuations are plotted over a five second time period for a selected case, without and with PIM. The selected case ( $T_{\text{inlet}} = 21^{\circ}\text{C}$ ,  $Q = 600$  SLPM,  $\phi = 0.70$ ) is one in which instability is dominant at approximately 500 Hz without the use of PIM. Without PIM, peak pressure oscillations are on the order of 170 Pascal (Pa). With PIM, these peak oscillations are reduced to approximately 20 Pa. As shown in Figure 3.6, this reduction in peak pressure oscillations corresponds to reduction in total SPL of approximately 30 dB. Reductions of this magnitude are typical for cases where instability exists without the use of porous media.

### 3.3.4 CO and NO<sub>x</sub> Emissions

For many cases in this study, CO emission levels are increased with the addition of porous media. Although CO is generally formed as a result of incomplete combustion, increased

CO emissions in this study are likely attributed to an increase in flame length with porous media. For most cases examined, the addition of porous media significantly increased the flame length as shown in Figure 3.7. The increase in flame length is most likely a result of a considerable increase in intensity of the central recirculation zone. Consequently, the central flame is lifted above the porous foam and anchors along the top surface of the porous ring rather than residing within the annular opening. This issue could be resolved with geometric optimization by either decreasing the swirl vane angle or increasing the diffuser angle of the porous media. The current quartz combustor length is not sufficient to contain the longer flame and thus the sampling probe is positioned at a location where reactions are still taking place. Therefore, product samples contain an increased amount of CO which has not yet been oxidized into CO<sub>2</sub>.

For air inlet temperatures of 21°C, NO<sub>x</sub> emissions levels are similar for cases without and with porous media. Figures 3.9 to 3.32 show that measured NO<sub>x</sub> concentrations are below 20 ppm for all test cases when combustion air is not preheated. Furthermore, no significant increase in NO<sub>x</sub> is observed for combustion with porous media. This result is anticipated since low flame temperatures achieved in the lean premixed combustor inhibit the formation of thermal NO<sub>x</sub>. For tests where  $T_{\text{inlet}} = 130\text{ }^{\circ}\text{C}$ , a slight increase in NO<sub>x</sub> is observed for cases without and with PIM. In some cases, NO<sub>x</sub> emissions are comparable without and with PIM (i.e. Figure 3.56). In other cases, the existence of PIM significantly increases concentrations of NO<sub>x</sub> (i.e. Figure 3.60). The same effect is observed with air inlet temperature of 260 °C, presented in Figures 3.57 to 3.72.

The increase in NO<sub>x</sub> with PIM is likely caused by increased local flame temperatures of surface combustion. A portion of exhaust products leave the central flame and flow through the porous material. These exhaust gases mix with fresh reactants also flowing through the PIM

before combustion occurs at the downstream surface. Thus, the reactants are preheated beyond the air inlet temperature and burn at a higher flame temperature to produce higher thermal NO<sub>x</sub>. The aforementioned process is dependent on flame structure and location. Flame structure and location are dependent on operating conditions of the combustor. Therefore, an increase in NO<sub>x</sub> is not observed for every case. It is reasonable to assume that appropriate PIM geometry and porosity could be chosen to limit the amount of surface combustion for a given set of operating conditions. In this way, PIM could be used as a passive noise suppression technique without increasing NO<sub>x</sub> emissions.

### *3.3.5 Pressure Drop*

For all cases investigated in this study, pressure drop is measured across the PIM and/or swirler in order to identify pressure loss penalties incurred by combustion with porous media. In each case, measured pressure drop is similar for combustion without and with porous media. Small differences in measured quantities are within the uncertainty of the differential pressure transducer. Thus, combustion with porous media does not cause additional pressure loss in a swirl-stabilized combustion system. For some cases, pressure drop exceeded the range of the transducer. As such, no plots are presented for those cases.

Pressure drop across the swirler and PIM is dependent on the flow rate of incoming reactants. Increased flow rates cause higher pressure drop across the swirler and PIM. For instance, pressure drop increases from approximately 2.0 kPa at  $Q = 300$  SLPM to approximately 6.5 kPa at  $Q = 600$  SLPM and 13.5 kPa at  $Q = 900$  SLPM, as shown in Figures 3.9, 3.17, and 3.25. This result is anticipated since pressure drop across a flow disturbance is a strong function of flow rate. Again, for the range of reactant flow rates tested, the existence of PIM produces no

noticeable increase in pressure loss. It is important to point out that the highest flow rate (900 SLPM) is not tested for the highest inlet temperature (260 °C). At this condition, the porous insert could not be held in place by press fitting with graphite foil. A few seconds after ignition, the PIM became dislodged from the combustor and was carried downstream within the quartz tube. A possible explanation is that the large amount of heat release from combustion caused some dissimilar expansion among components, which resulted in degradation of the tightness of fit by graphite foil, necessary to constrain the porous insert at the dump plane.

### *3.3.6 Effect of Air Flow Rate*

As previously mentioned, combustion air flow rates of 300, 600, and 900 SLPM are examined in this study. As air flow rate is increased, average reactant inlet velocity is increased as well. Bulk inlet velocity ranges from 16 m/s for the lowest air flow rate and preheat temperature to 75 m/s for the highest air flow rate and preheat temperature. Reynolds number (as calculated in Appendix C) ranges from 7,600 to 35,200. As shown in Table 3.3, total SPL increases significantly as inlet velocity is increased. The increase in noise is highlighted in detail in Figures 3.9 to 3.32. Total SPL increases slightly without and with PIM as reactant flow rate is increased from 300 SLPM to 600 SLPM to 900 SLPM. Noise reduction with PIM is fairly uniform in cases where noise is broadband, as shown in Figures 3.9 to 3.28. In Figures 3.28 to 3.32, thermo-acoustic instability is dominant and reduction in total SPL is considerably higher. This result is expected since turbulent fluctuations are intensified at higher reactant inlet velocity and resulting acoustic waves are larger in amplitude. Instabilities, however, do not necessarily increase as reactant velocity is increased. As in the case of varying preheat temperature, instability formation is not predictable as a function of reactant inlet velocity. For example, in

test cases where  $T_{\text{inlet}} = 130 \text{ }^{\circ}\text{C}$ , instability is not present for any cases where  $Q = 300 \text{ SLPM}$ . When flow rate is increased to 600 SLPM, instability becomes dominant and results in total SPL above 130 dB. As flow rate is further increased to 900 SLPM, instability is dominant, but less intense than cases with  $Q = 600 \text{ SLPM}$ . Particularly, for equivalence ratios of 0.70 and 0.75, instability is less severe at 900 SLPM and produces total SPL of approximately 120 dB. With porous media, the same trend is observed. For cases where combustion noise is broadband, total SPL increases with increasing reactant inlet velocity. For cases dominated by instability, PIM is effective in reducing large peaks in SPL. The porous insert is successful in reducing instability for all cases; however, total reduction is highly dependent on the existence of instability without PIM.

### *3.3.7 Effect of Preheat Temperature*

Preheat temperature of the incoming reactants has a fairly significant effect on total sound pressure level. For cases without and with PIM, broadband combustion noise increases with increasing air inlet temperature, as highlighted in Table 3.3. Effect of air inlet temperature is shown in detail by comparing cases where  $T_{\text{inlet}} = 21 \text{ }^{\circ}\text{C}$  (Figures 3.9 to 3.32) to those where  $T_{\text{inlet}} = 130 \text{ }^{\circ}\text{C}$  (Figures 3.33 to 3.56) and to those where  $T_{\text{inlet}} = 260 \text{ }^{\circ}\text{C}$  (Figures 3.57 to 3.72). The effect is evident in cases where instabilities are not dominant in the combustor and is likely the result of higher flame temperatures and increased heat release rate. Turbulent fluctuations are amplified with increased air temperature to produce more noise over the entire frequency range. Air inlet temperature also affects the likelihood of instability formation without the use of porous material. For instance, at  $Q = 600 \text{ SLPM}$  and  $\phi = 0.65$ , instability is not dominant for the case with  $T_{\text{inlet}} = 21 \text{ }^{\circ}\text{C}$ , and total SPL is measured to be 112.4 dB. However, for the same air

flow rate and equivalence ratio, intense instability is observed when  $T_{inlet}$  is increased to 130 °C. For this case, total SPL is measured to be 135.8 dB. When the combustion air is preheated to 260 °C, instability disappears and noise becomes broadband in nature with a total SPL of 107.1 dB. This result is not unusual, as instabilities in a swirl-stabilized LPM combustor are inherently unpredictable. It is important to notice that regardless of when the instability appears without porous media, PIM is highly effective in eliminating large peaks in total SPL.

For cases where reactants enter the combustor at 21 °C, total SPL is reduced drastically with PIM. At 21 °C, total SPL ranges from 102.1 to 132.6 dB without PIM. With PIM, total SPL is reduced to a range between 83.6 dB and 102.9 dB. When reactants are heated to 130 °C, the PIM is still effective, especially for cases dominated by instability. For instance, at  $Q = 600$  SLPM and  $\phi = 0.65$ , SPL is reduced from 135.8 dB without PIM to 103.4 dB with PIM.

Broadband noise reduction for cases without instability is slightly less effective at the elevated inlet temperature of 130 °C. For  $T_{inlet} = 260$  °C, some interior combustion is observed along the inner wall of the porous insert, as shown in Figures 3.57 to 3.62. At this temperature, interior combustion propagates further as the equivalence ratio is increased. At  $Q = 300$  SLPM and  $\phi = 0.75$ , interior combustion becomes extremely intense which can cause severe damage to the porous insert (shown in Figure 3.63). From this point forward, PIM #3 is used to complete the remainder of the tests at  $T_{inlet} = 260$  °C. As previously stated, PIM #3 (100 ppi) is much denser than PIM #2 (45 ppi) and functions as an arrestor to prevent flame propagation into the porous material. Interior combustion is successfully avoided with PIM #3 for all cases except for  $Q = 600$  SLPM and  $\phi = 0.75$ , in which case a very small amount of interior combustion is observed.

For experiments without PIM at  $T_{inlet} = 260$  °C, instabilities are not dominant for any of the cases. Even so, broadband noise reduction is achieved for most of the test cases. For  $Q =$

600 SLPM and  $\phi = 0.70$ ,  $\phi = 0.75$ , total SPL actually increases by a few decibels with PIM. Reduced effectiveness of combustion with PIM at elevated preheat temperatures is consistent with previous experiments conducted by Sequera & Agrawal (2011). This intriguing result should be investigated in future studies. As expected, air inlet temperature does have a slight effect on pressure drop across the PIM. Increased temperatures produce higher reactant velocities and therefore higher pressure drop across the swirler and porous insert. However, for all air temperatures tested, addition of the PIM did not affect pressure drop. Thus, no pressure loss penalty is incurred with PIM, even at elevated preheat temperatures.

### 3.3.8 *Effect of Equivalence Ratio*

Equivalence ratios of 0.60, 0.65, 0.70, and 0.75 are investigated in the current study. As the equivalence ratio increases, resulting heat release rate also increases, for a given air flow rate. Consequently, fluctuations in heat release rate are intensified to increase total SPL. For cases where SPL is broadband, total sound pressure level increases with increasing equivalence ratio as shown in Table 3.3. Effect of equivalence ratio on broadband noise production is clearly observed by examining Figures 3.9 to 3.32. As is the case for air flow rate and inlet temperature, effect of equivalence ratio on cases dominated by instability is highly unpredictable. For instance, with  $T_{\text{inlet}} = 130 \text{ }^\circ\text{C}$  and  $Q = 600 \text{ SLPM}$ , no visible trend is observed for increasing equivalence ratio. Figures 3.41 to 3.44 show that total SPL increases as equivalence ratio is changed from 0.60 to 0.65. Subsequently, as presented in Figures 3.43 to 3.46, total SPL decreases as the equivalence ratio increases from 0.65 to 0.70. Total SPL decreases even further for equivalence ratio of 0.75, as shown in Figures 3.47 and 3.48. Total SPL reduction with PIM is reasonably uniform with increasing equivalence ratio, and is again highly dependent on the

nature of instability without the use of porous material. With porous media, flame structure is also affected by equivalence ratio. For leaner mixtures, a few large flamelets are anchored to the top surface of the PIM as shown in Figure 3.9. Flamelets are elongated and anchor at only a few locations on top of the porous foam. At higher equivalence ratios, a multitude of small flamelets appear, covering the entire downstream surface of the PIM. Flamelets are considerably smaller than those under leaner conditions, and are densely packed on top of the porous ring as shown in Figure 3.15.

### *3.3.9 Effect of Swirler Location*

Swirler location within the pre-mixer is varied to examine its effect on combustion noise for two cases. In one case, the swirler exit is flushed with the dump plane of the combustor. For the second case, the swirler is recessed inside the pre-mixer to a location 3.8 cm [1.5 in] upstream of the dump plane. Both swirler positions are tested for  $T_{\text{inlet}} = 21 \text{ }^\circ\text{C}$ ,  $Q = 600 \text{ SLPM}$ , and equivalence ratios of 0.60, 0.65, 0.70, and 0.75. PIM #1 is used for both cases. Flame photographs and SPL plots for the flush mounted swirler are shown in Figures 3.73 to 3.76. Flame photographs and SPL plots for the recessed swirler are shown in Figures 3.77 to 3.80. When the swirler is flush mounted, the central flame is contained within the annular void of the PIM and surface combustion is achieved on the downstream surface of the porous insert. SPL reduction for these cases is significant, especially if instability is dominant, as shown in Figures 3.75 and 3.76. Flame structure with the recessed swirler is similar, yet surface combustion is less prominent and the central flame is anchored closer to the dump plane. The lack of surface combustion and shifting of the flame is likely caused by slight modification of flow field and heat recirculation zones. The central recirculation zone is probably weakened, thereby altering

flame anchoring location. This effect is clearly shown in Figure 3.79, where the solid body of the swirler is glowing red. With the recessed swirler, broadband reduction of SPL with PIM (approximately 7 dB) is similar to that of the flush mounted case for  $\phi = 0.60$ , as shown in Figures 3.73 and 3.77. However, when equivalence ratio is increased to 0.65 and 0.70, SPL reduction is considerably less with the recessed swirler. For these cases, total SPL reduction is almost negligible, as shown in Figures 3.78 and 3.79. While broadband noise reduction is not good for some cases with the recessed swirler, instabilities are still successfully eliminated. As observed in Figure 3.80, combustion instability is mitigated with PIM to provide an overall reduction in SPL of approximately 20 dB. It is difficult to compare the recessed case with the flushed case on a one-to-one basis since instability formation without PIM is quite different for each case. However, it can be concluded that broadband reduction in SPL with PIM can be achieved with the recessed swirler for selected operating conditions, but not all. Thermoacoustic instability, on the other hand, is eliminated in its entirety.

### *3.3.10 Endurance Testing*

An endurance test was performed to evaluate performance characteristics of the PIM over a prolonged operating time. The porous insert was subjected to continuous combustion for 10 hours at conditions of  $T_{\text{inlet}} = 21 \text{ }^\circ\text{C}$ ,  $Q = 600 \text{ SLPM}$ , and  $\phi = 0.70$ . Noise and emissions measurements were taken at thirty minute intervals for the duration of the test. Flame photographs were also taken before, during, and after the test to observe any visible changes within the combustor. Flame photographs at several times during the test are shown in Figure 3.81. Noise and emission measurements from the endurance test are plotted in Figures 3.82 to 3.87. Porous media provided an initial noise reduction of approximately 20 dB. The

performance of the porous insert remained unchanged throughout the length of the test. Total SPL reduction remained at approximately 20 dB and the flame exhibited no visible change in structure. Emissions for this case were fairly similar without and with porous media and remained relatively constant throughout the duration of the test. After the test was completed, the porous foam was carefully inspected for any signs of damage from prolonged exposure to combustion. No visible damage was found. The PIM maintained functionality over the 10 hour test and was not compromised in the process. It is reasonable to assume that the porous media could be used for even longer periods of time while sustaining functionality and without experiencing material failure.

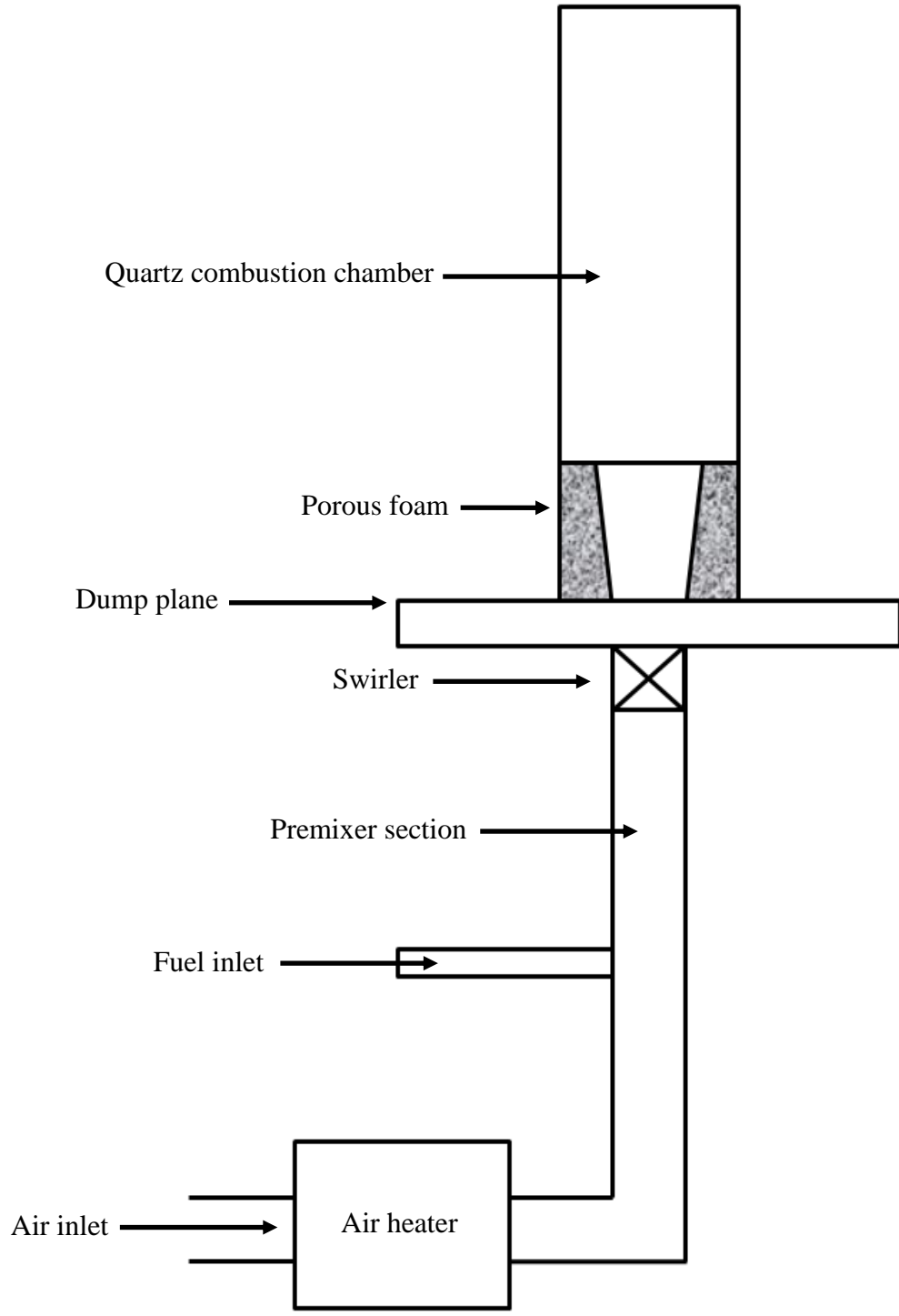


Figure 3.1. Schematic of experimental setup

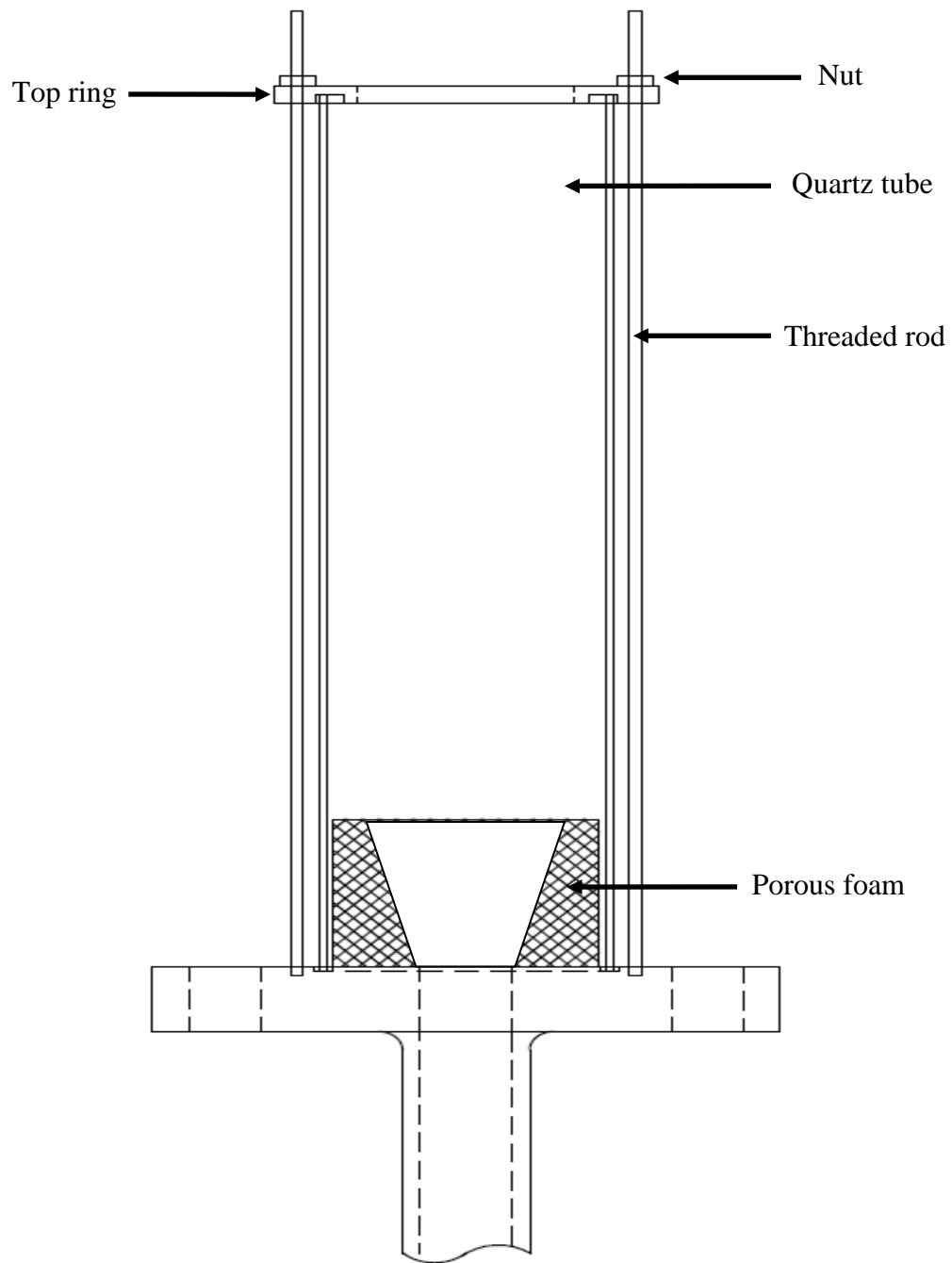


Figure 3.2. Schematic of holding mechanism for quartz tube

All dimensions in cm

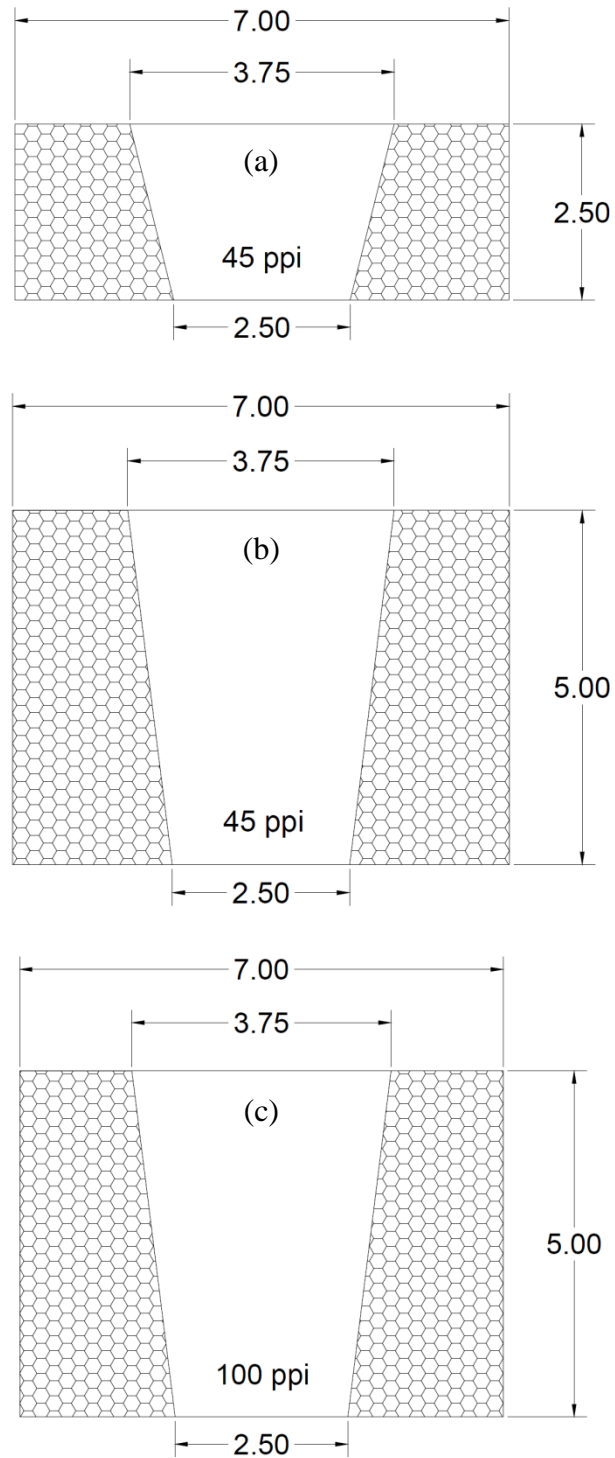


Figure 3.3. Drawing of porous inserts (a) PIM #1, (b) PIM #2, (c) PIM #3

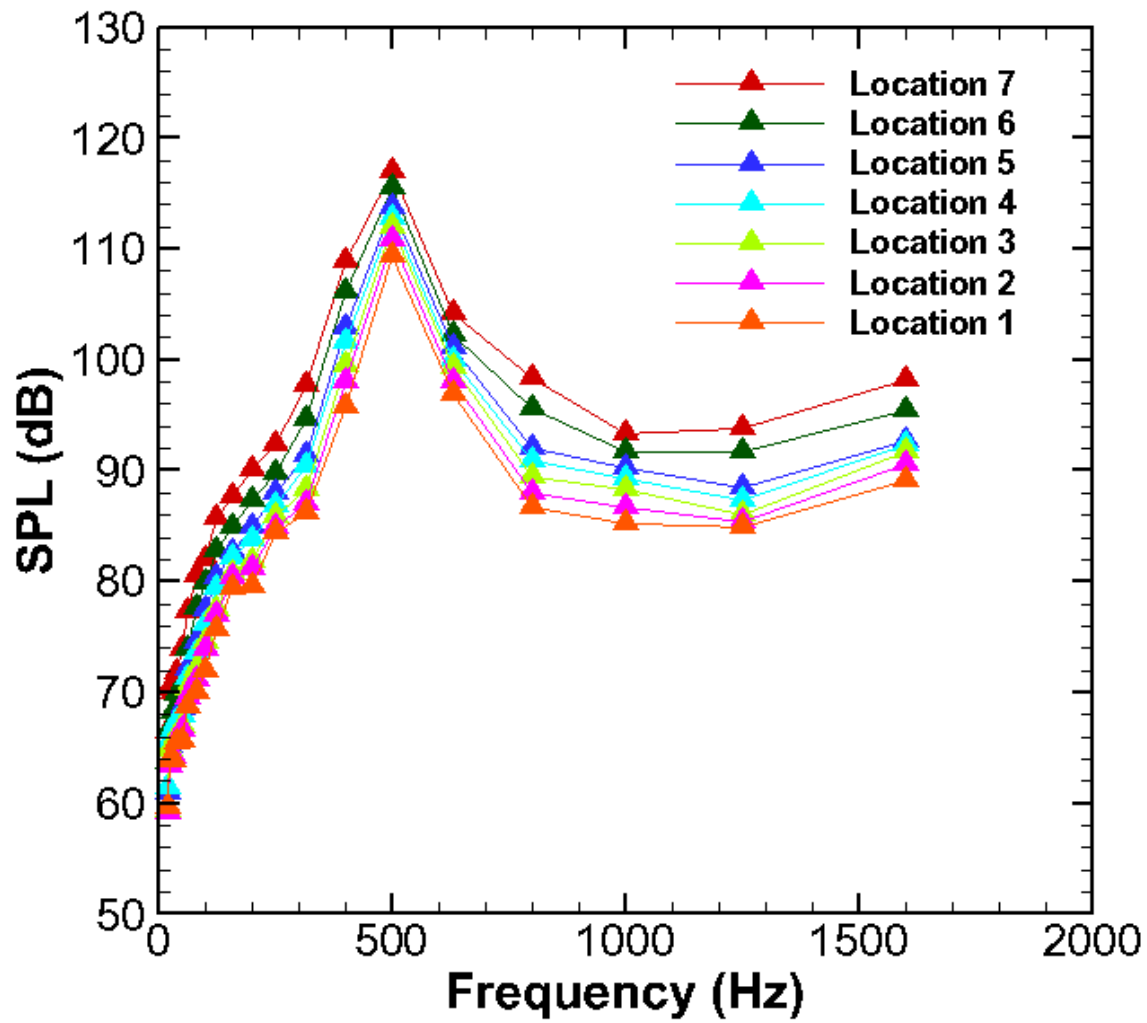


Figure 3.4. SPL per 1/3 octave band for microphone location test

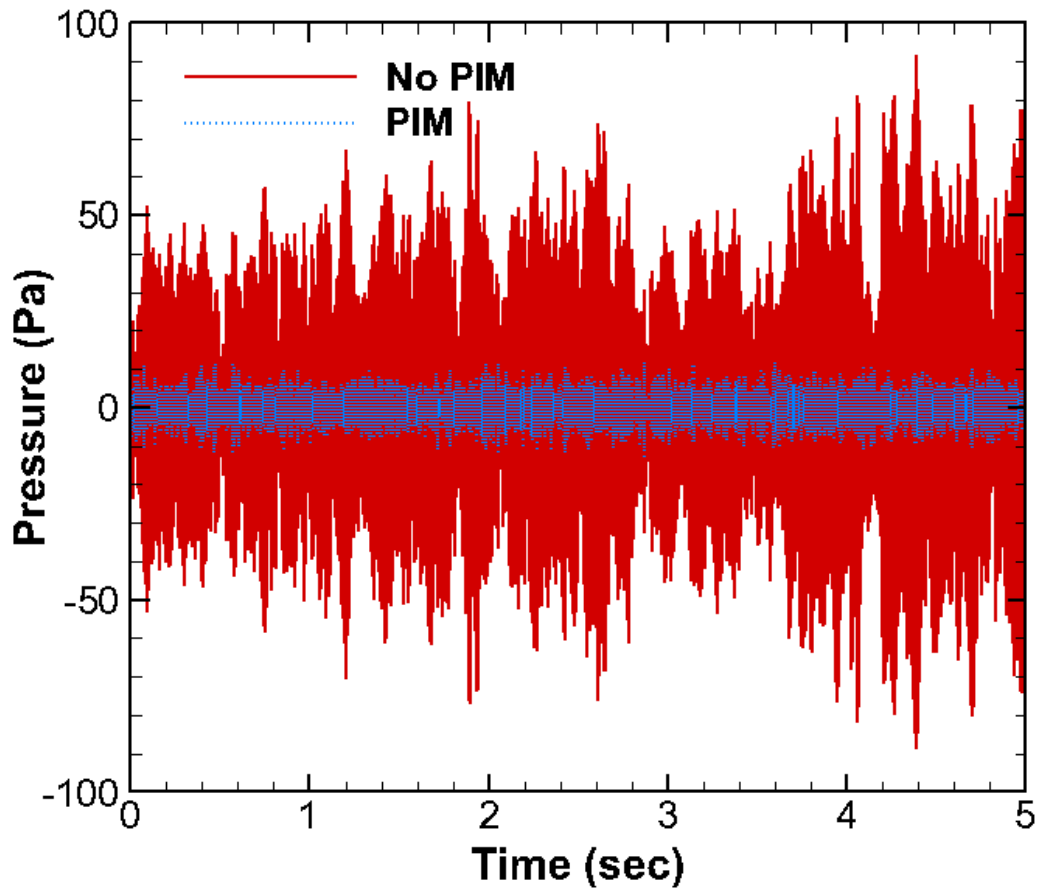


Figure 3.5. Pressure oscillations over a 5 second range for selected case in which instability is dominant,  $T_{\text{inlet}} = 21^{\circ}\text{C}$ ,  $Q = 600$  SLPM,  $\phi = 0.70$

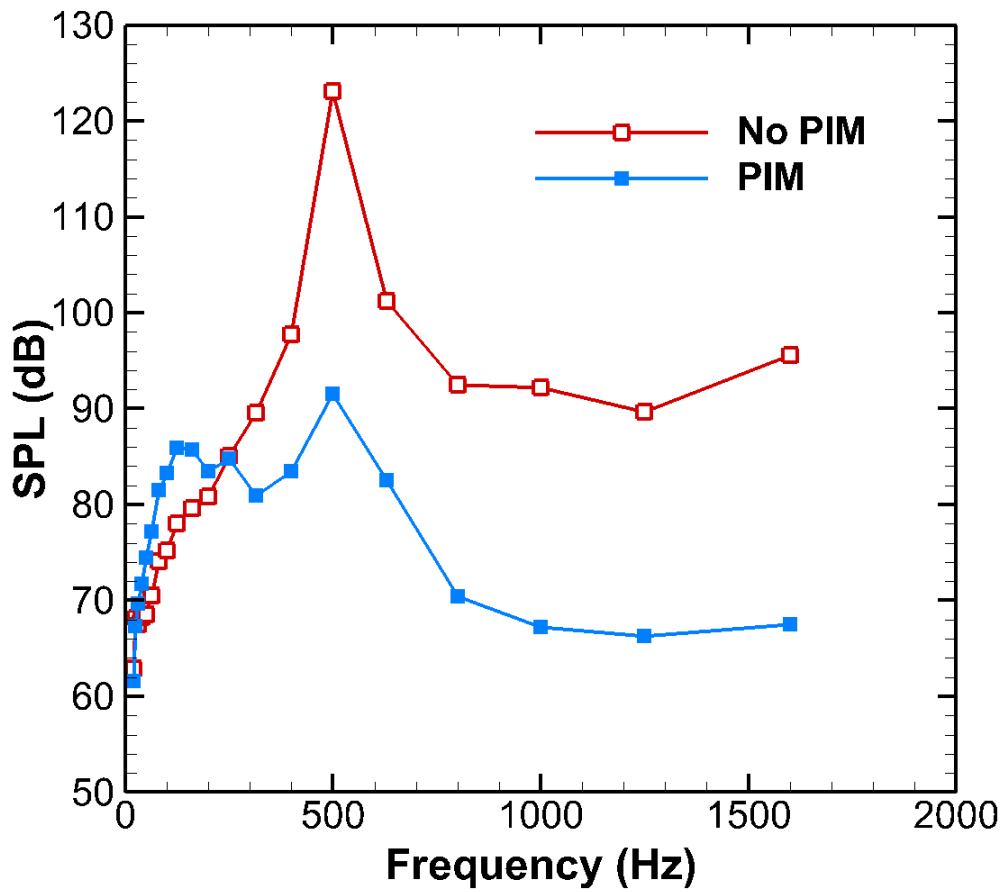
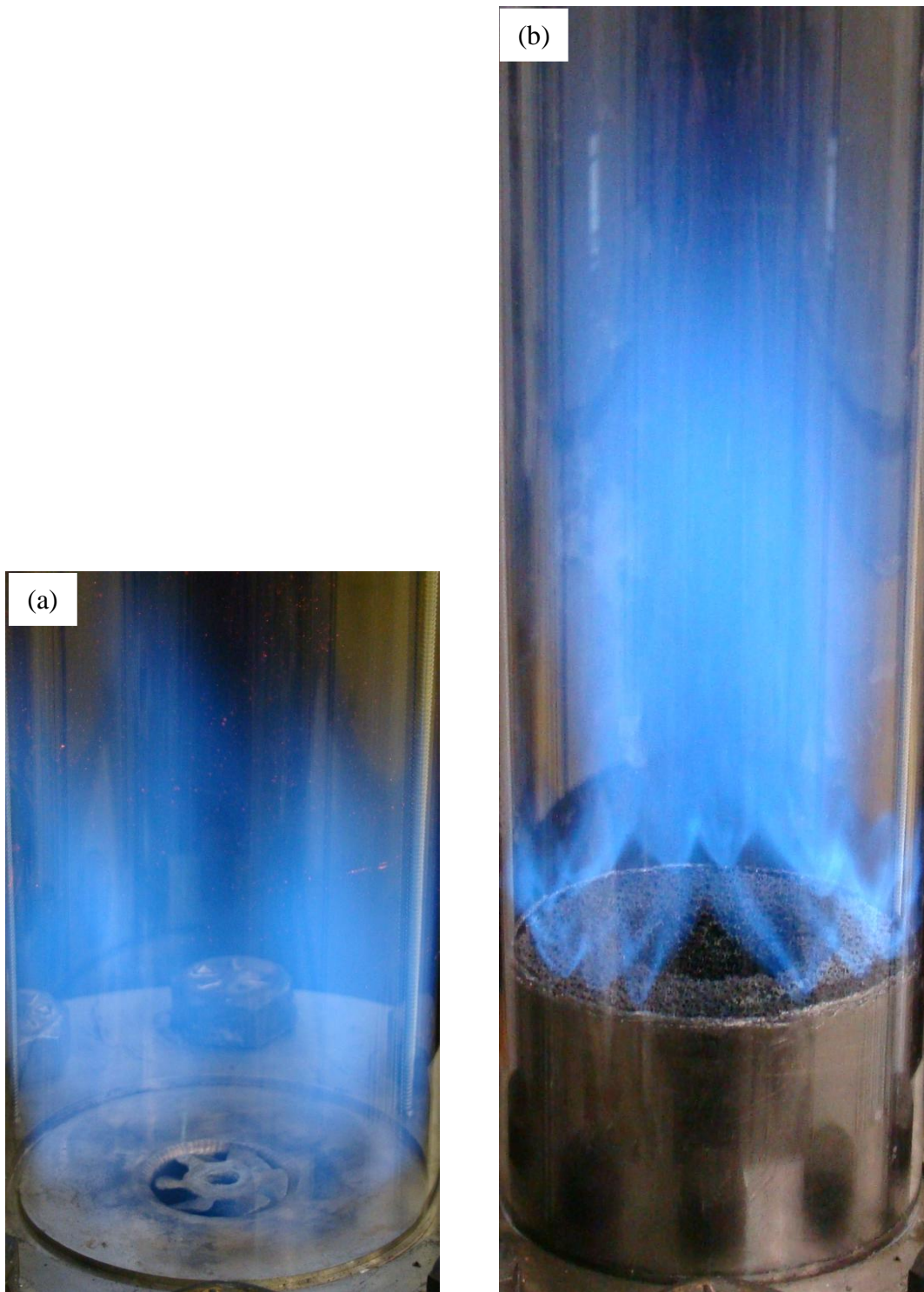


Figure 3.6. SPL per 1/3 octave band for selected case in which instability is dominant,  $T_{inlet} = 21^{\circ}\text{C}$ ,  $Q = 600$  SLPM,  $\phi = 0.70$



*Figure 3.7.* Photographic images showing an increase in flame length with porous media (a) Flame photograph without PIM, (b) Flame photograph with PIM

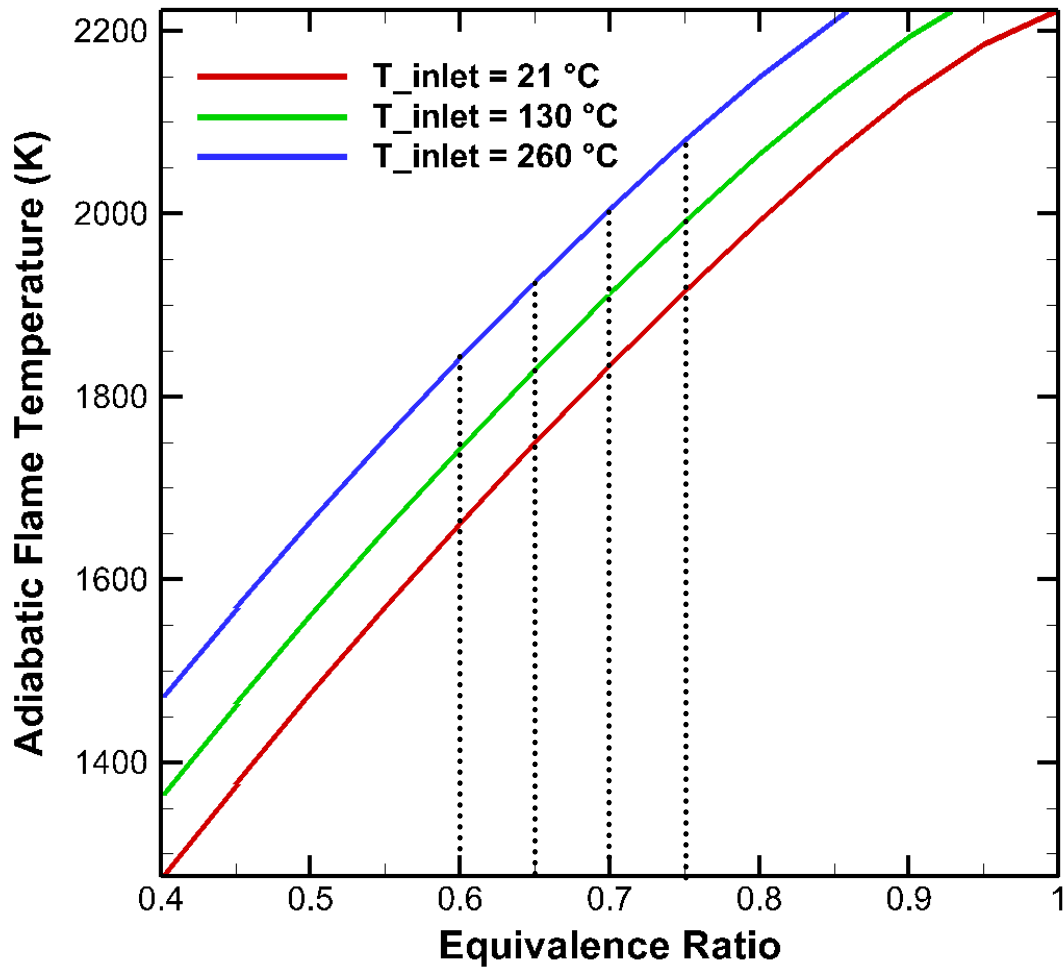


Figure 3.8. Adiabatic flame temperature for methane-air combustion with reactant inlet temperatures of  $T_{\text{inlet}} = 21^\circ\text{C}$ ,  $T_{\text{inlet}} = 130^\circ\text{C}$ , and  $T_{\text{inlet}} = 260^\circ\text{C}$ .

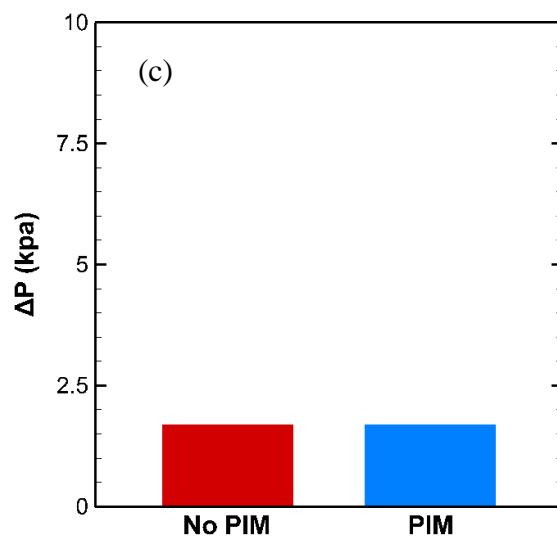
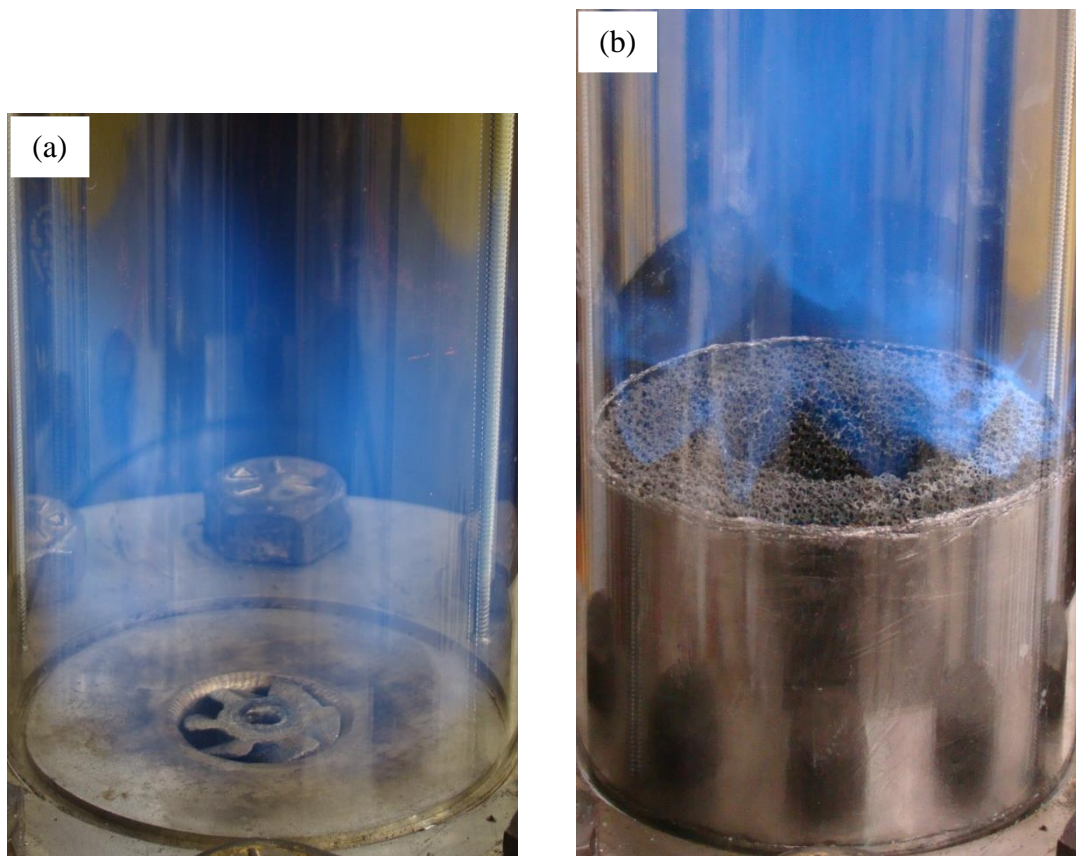


Figure 3.9. Results for  $T_{inlet} = 21^{\circ}\text{C}$ ,  $Q = 300$  SLPM,  $\phi = 0.60$  (a) Flame photograph without PIM, (b) Flame photograph with PIM, (c) Pressure drop measurements with and without PIM

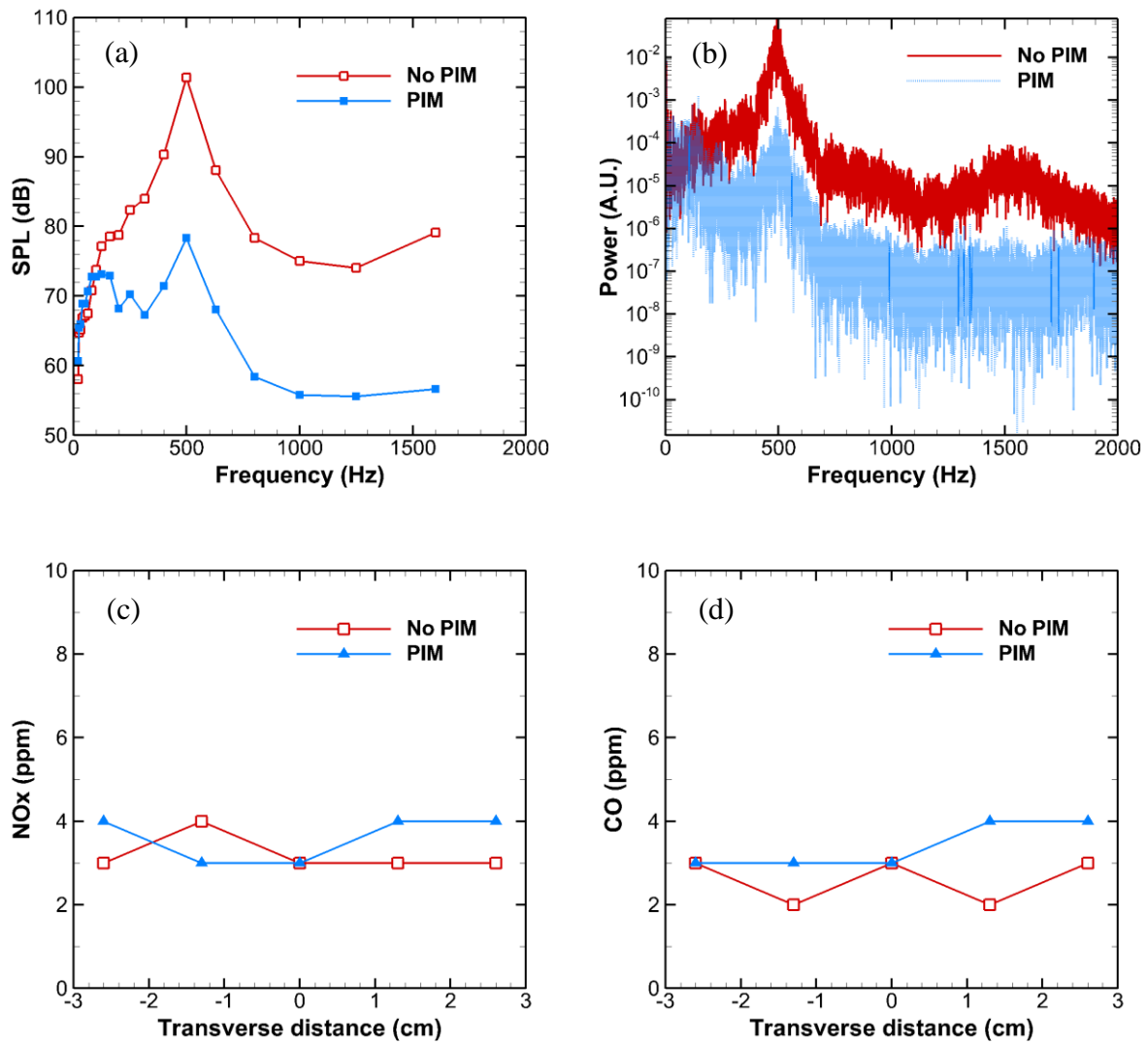


Figure 3.10. Results for  $T_{\text{inlet}} = 21^\circ\text{C}$ ,  $Q = 300$  SLPM,  $\phi = 0.60$  (a) SPL per 1/3 octave band, (b) Spectral power, (c) NOx emissions, (d) CO emissions

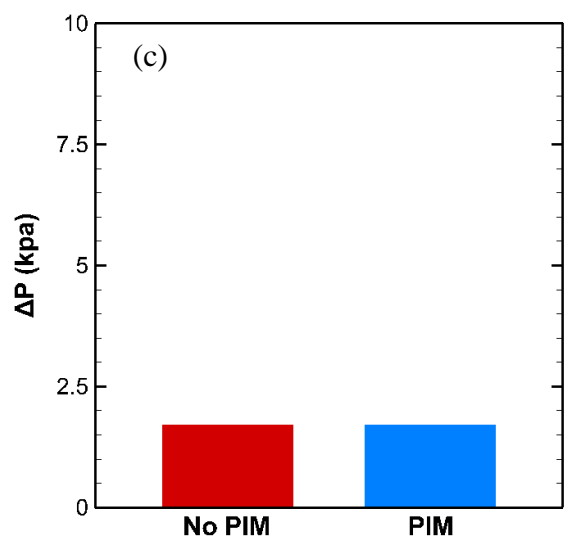
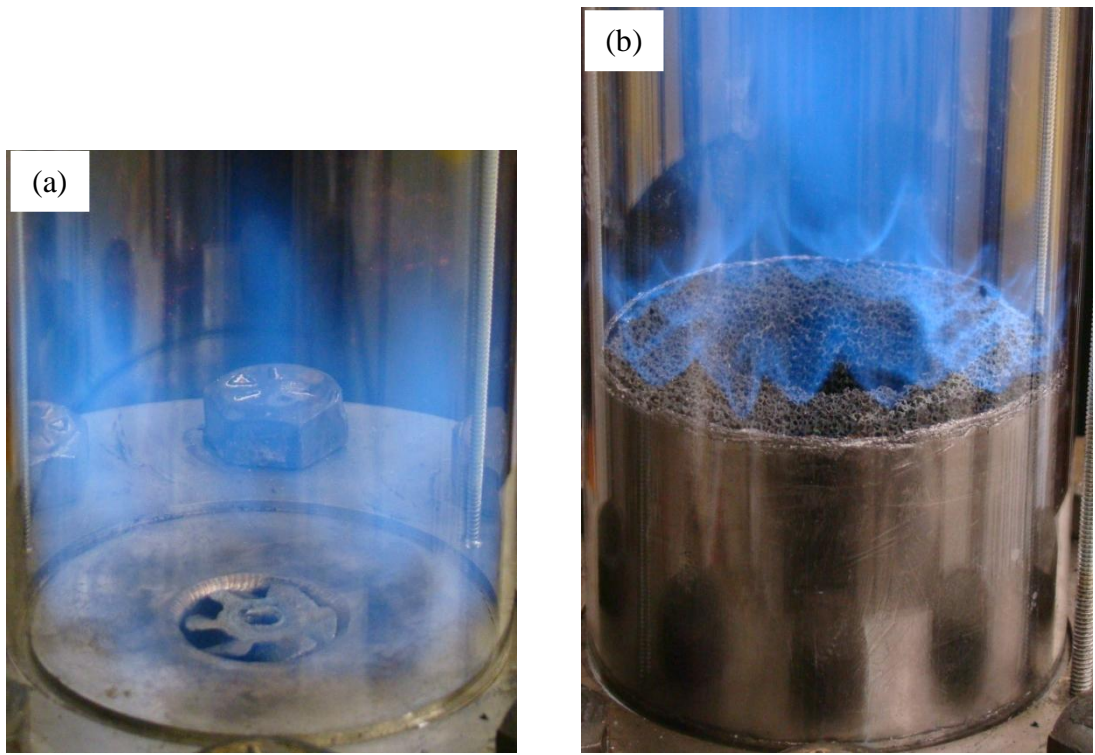


Figure 3.11. Results for  $T_{inlet} = 21^{\circ}C$ ,  $Q = 300$  SLPM,  $\phi = 0.65$  (a) Flame photograph without PIM, (b) Flame photograph with PIM, (c) Pressure drop measurements with and without PIM

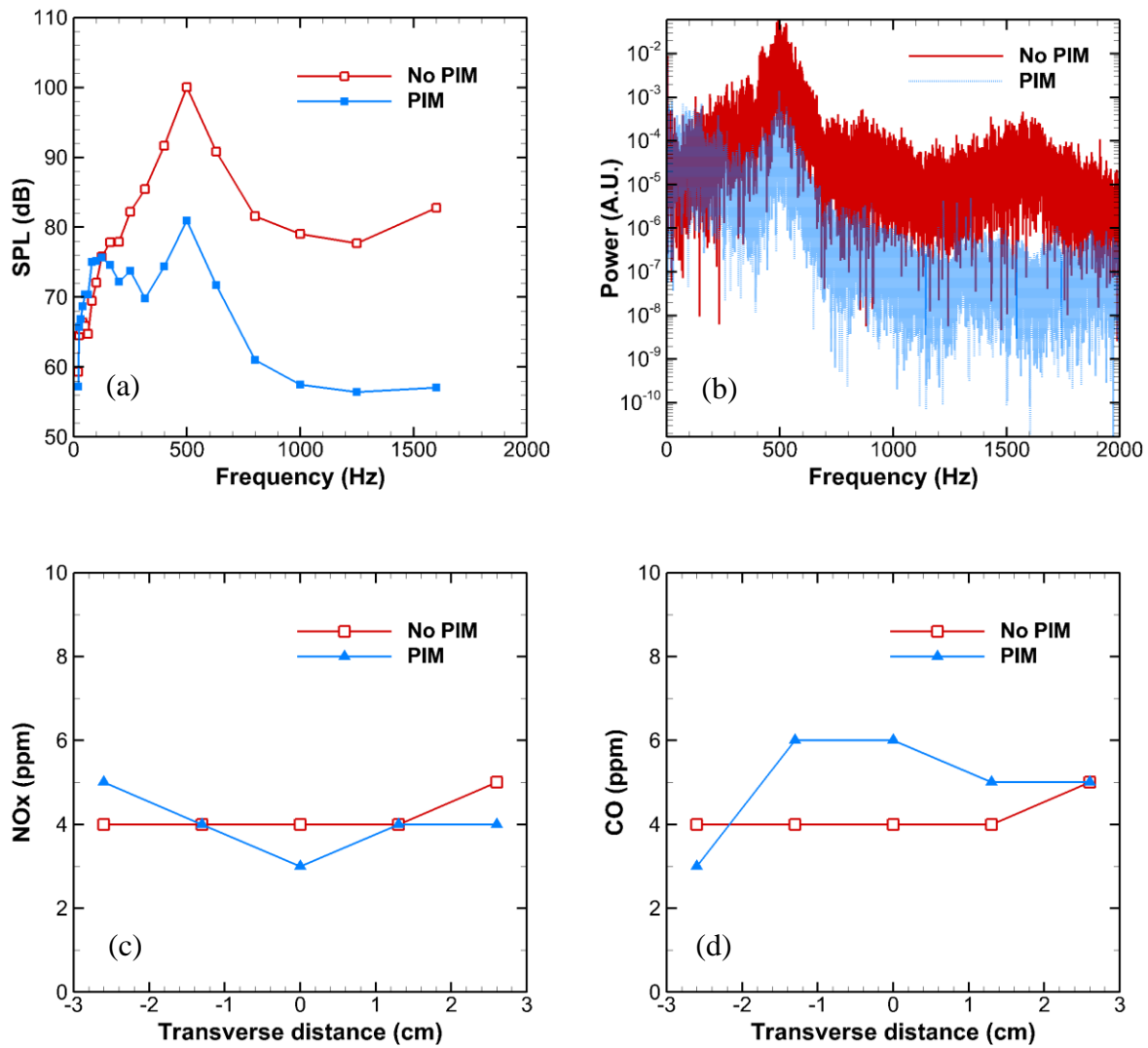


Figure 3.12. Results for  $T_{\text{inlet}} = 21^{\circ}\text{C}$ ,  $Q = 300$  SLPM,  $\phi = 0.65$  (a) SPL per 1/3 octave band, (b) Spectral power, (c) NOx emissions, (d) CO emissions

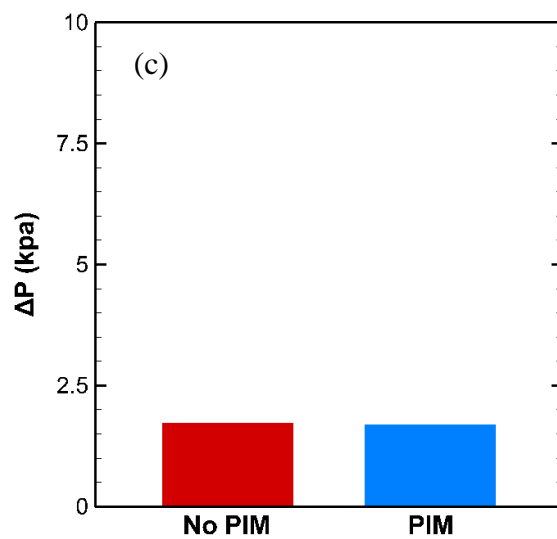
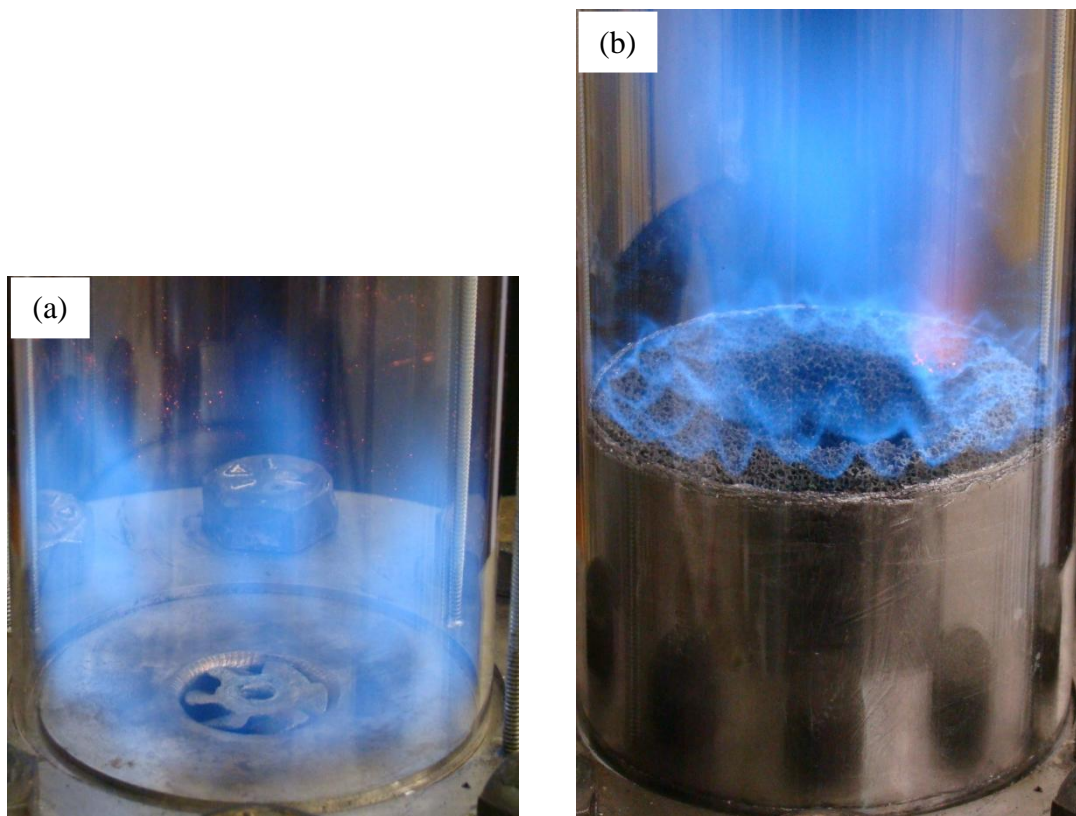


Figure 3.13. Results for  $T_{\text{inlet}} = 21^{\circ}\text{C}$ ,  $Q = 300$  SLPM,  $\phi = 0.70$  (a) Flame photograph without PIM, (b) Flame photograph with PIM, (c) Pressure drop measurements with and without PIM

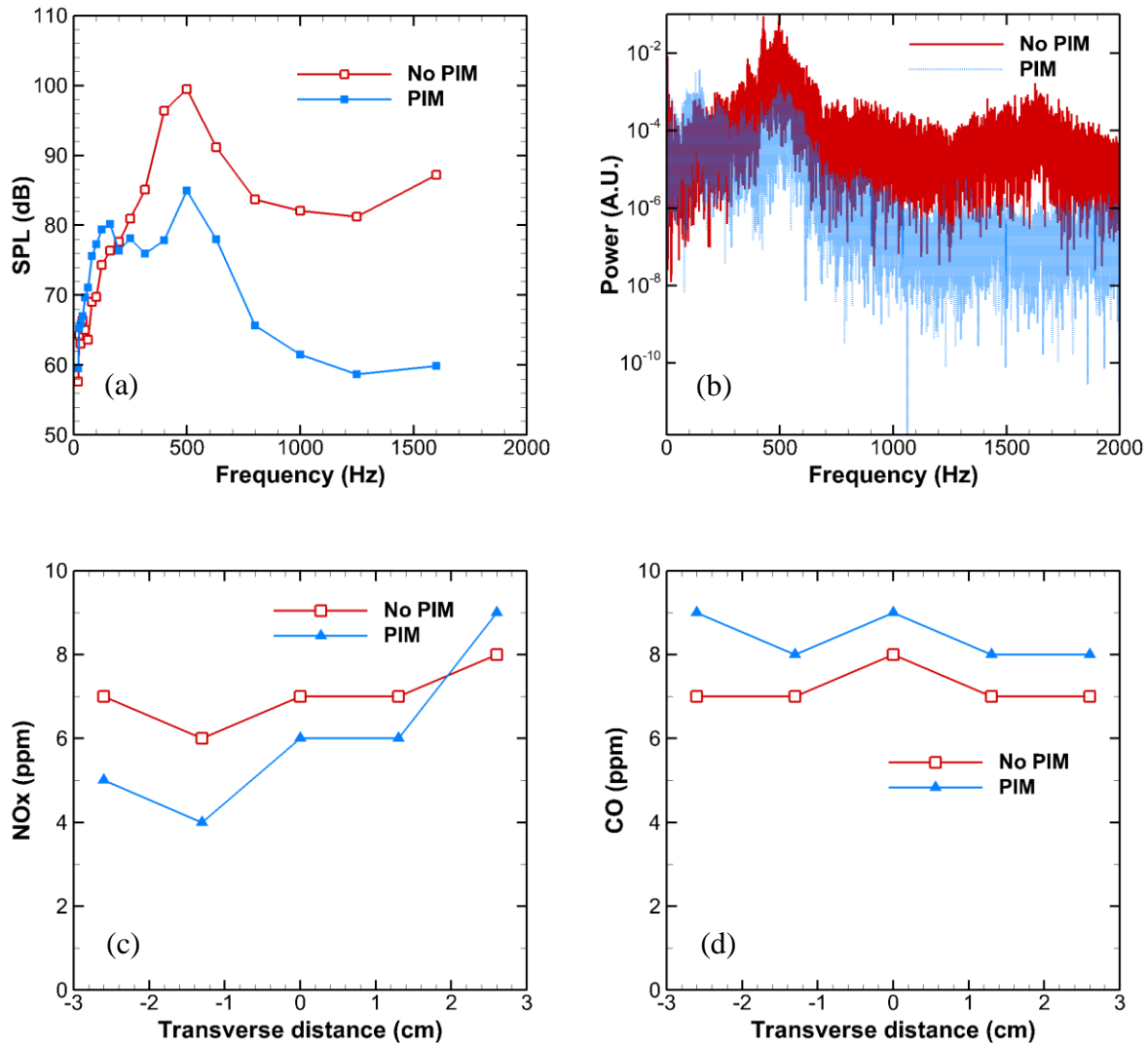


Figure 3.14. Results for  $T_{\text{inlet}} = 21^\circ\text{C}$ ,  $Q = 300$  SLPM,  $\phi = 0.70$  (a) SPL per 1/3 octave band, (b) Spectral power, (c) NOx emissions, (d) CO emissions

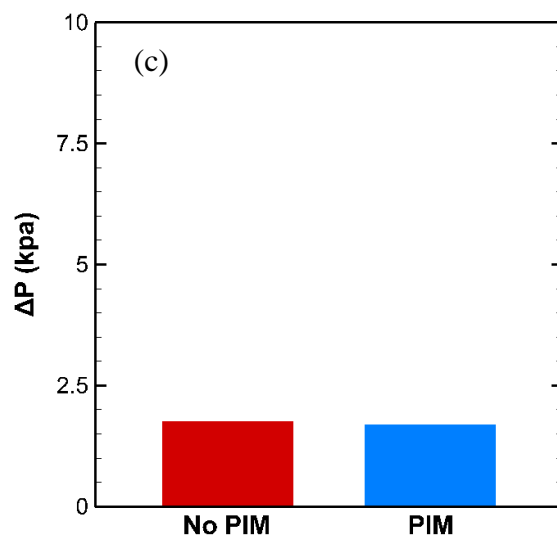
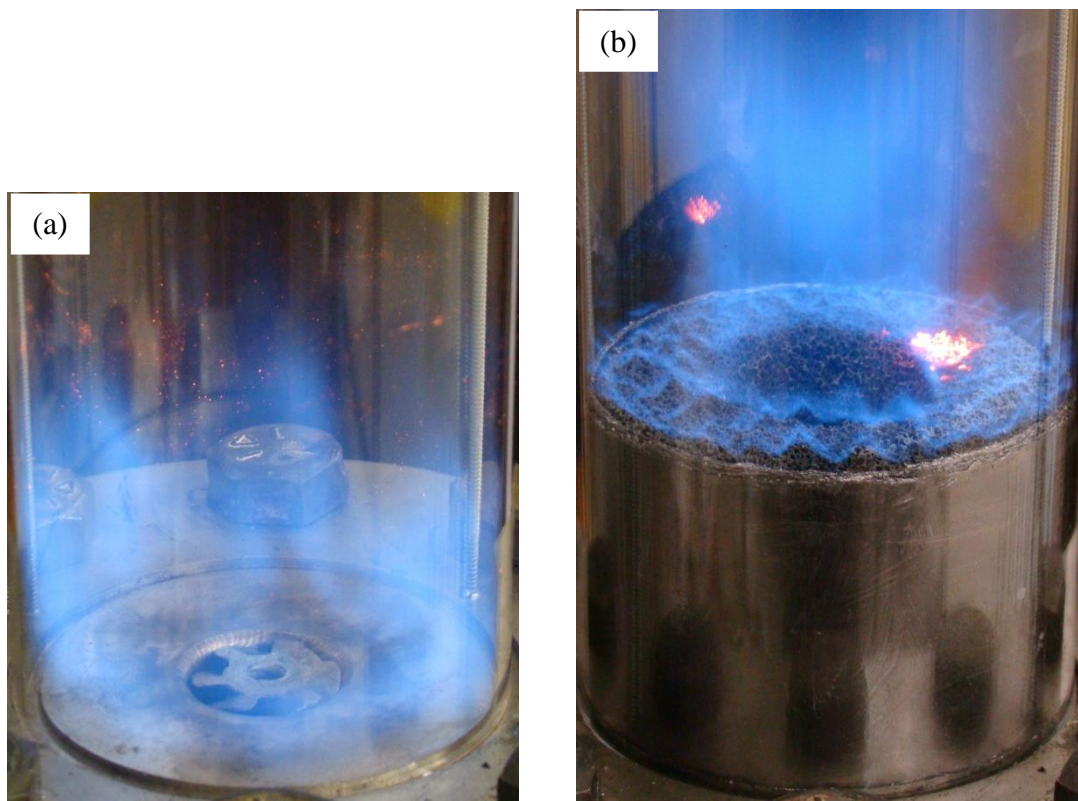


Figure 3.15. Results for  $T_{\text{inlet}} = 21^\circ\text{C}$ ,  $Q = 300$  SLPM,  $\phi = 0.75$  (a) Flame photograph without PIM, (b) Flame photograph with PIM, (c) Pressure drop measurements with and without PIM

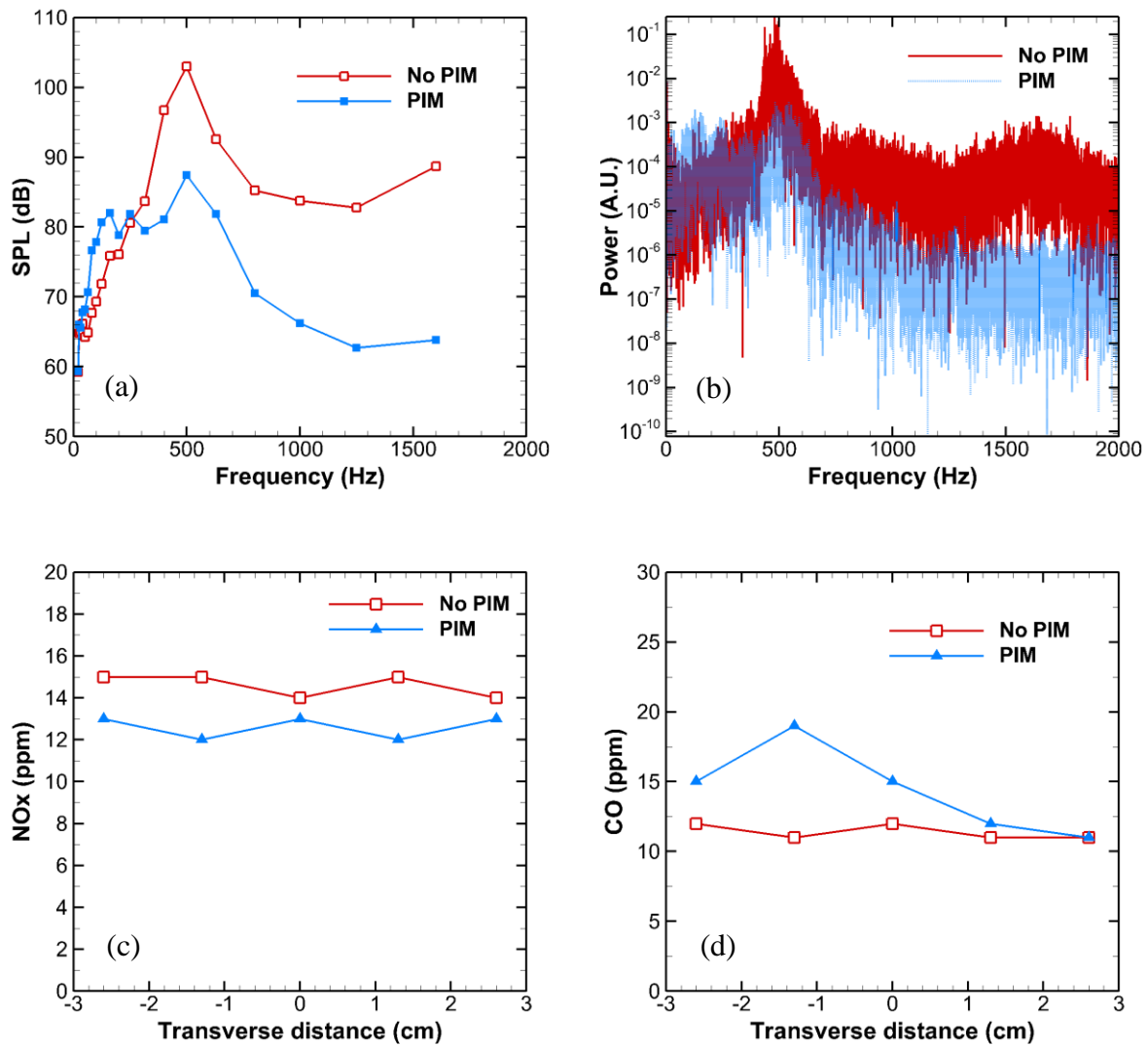


Figure 3.16. Results for  $T_{inlet} = 21^\circ\text{C}$ ,  $Q = 300$  SLPM,  $\phi = 0.75$  (a) SPL per 1/3 octave band, (b) Spectral power, (c) NOx emissions, (d) CO emissions

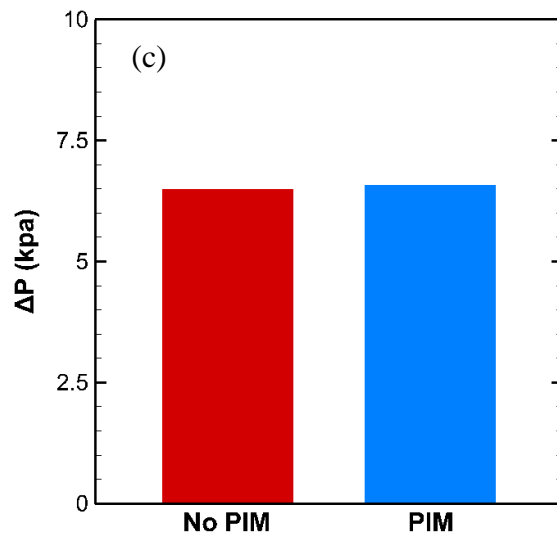
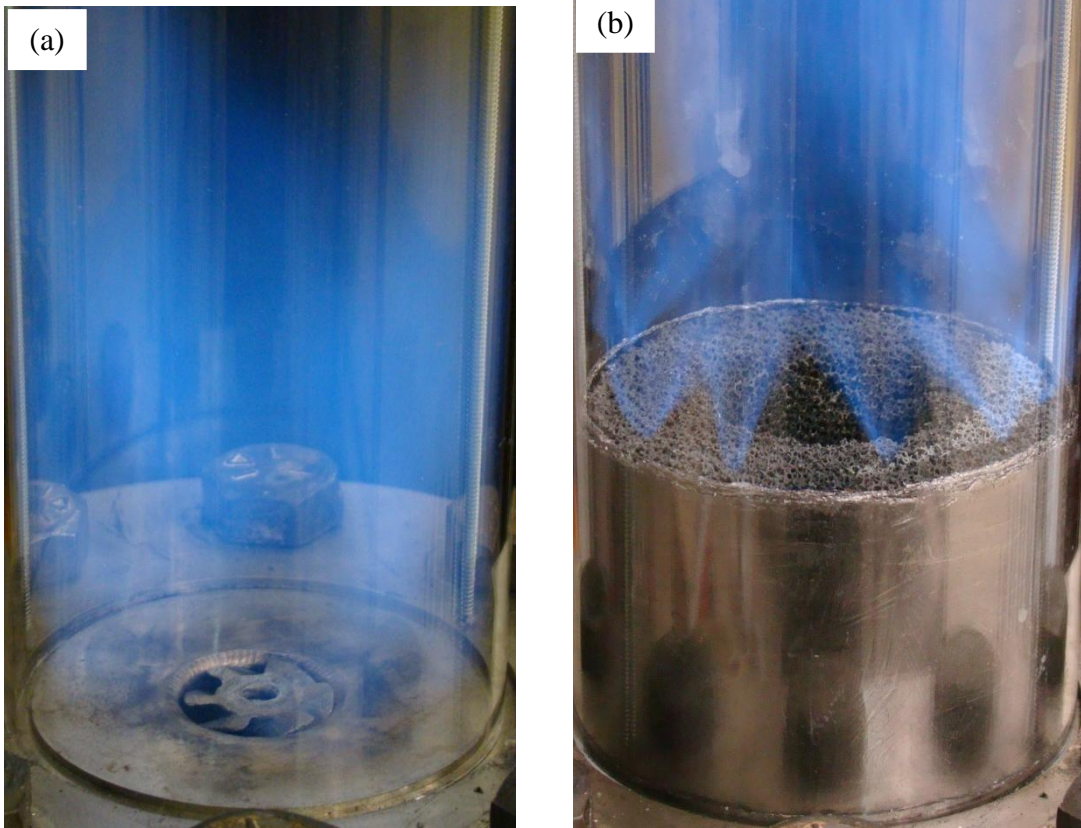


Figure 3.17. Results for  $T_{\text{inlet}} = 21^{\circ}\text{C}$ ,  $Q = 600$  SLPM,  $\phi = 0.60$  (a) Flame photograph without PIM, (b) Flame photograph with PIM, (c) Pressure drop measurements with and without PIM

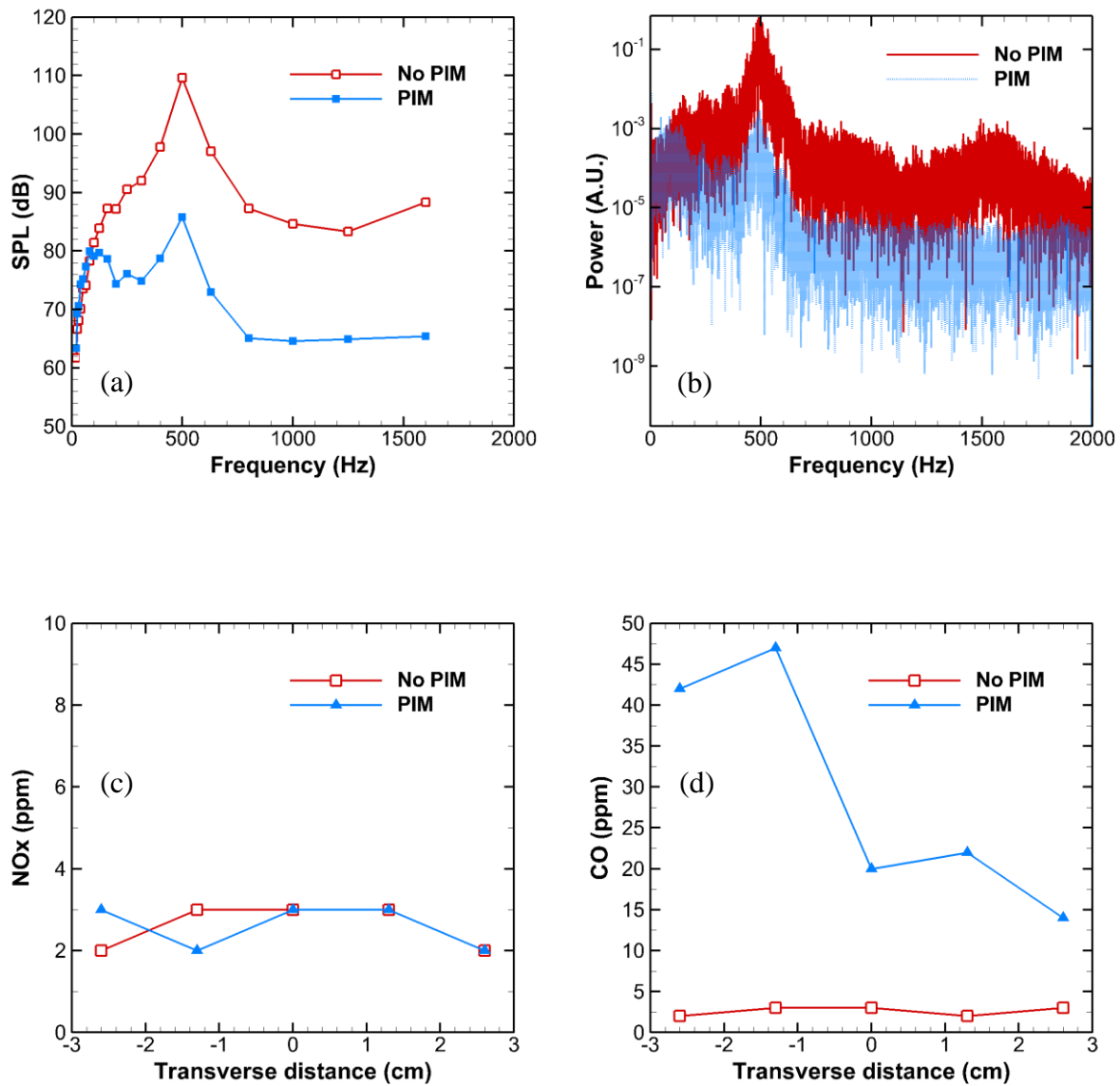


Figure 3.18. Results for  $T_{\text{inlet}} = 21^{\circ}\text{C}$ ,  $Q = 600$  SLPM,  $\phi = 0.60$  (a) SPL per 1/3 octave band, (b) Spectral power, (c) NOx emissions, (d) CO emissions

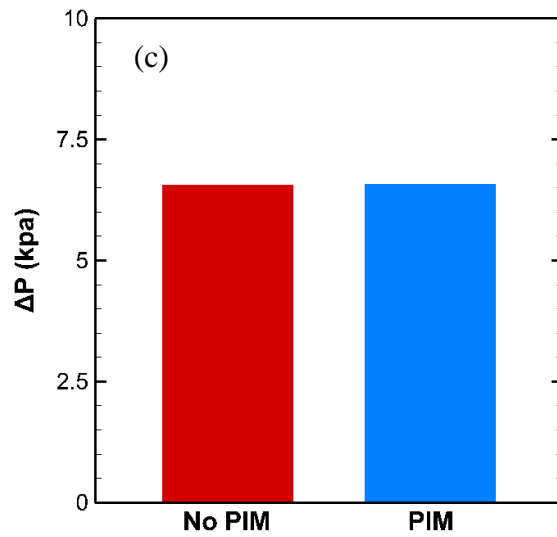
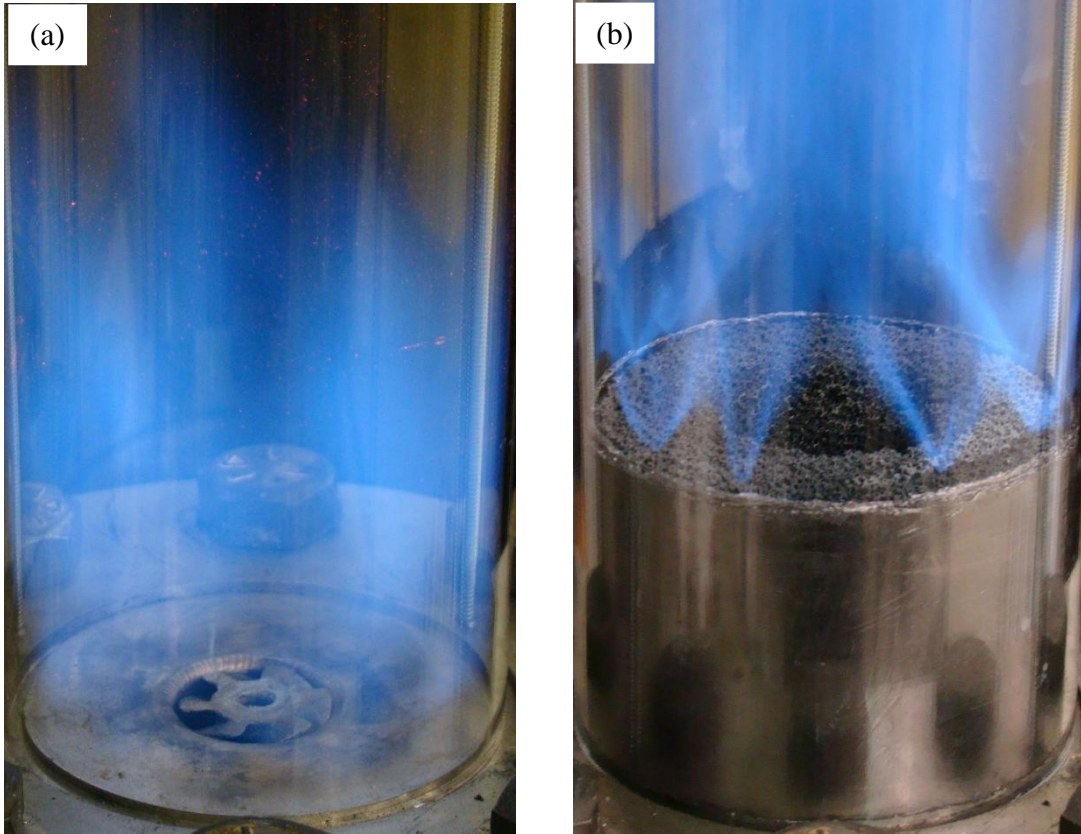


Figure 3.19. Results for  $T_{\text{inlet}} = 21^\circ\text{C}$ ,  $Q = 600$  SLPM,  $\phi = 0.65$  (a) Flame photograph without PIM, (b) Flame photograph with PIM, (c) Pressure drop measurements with and without PIM

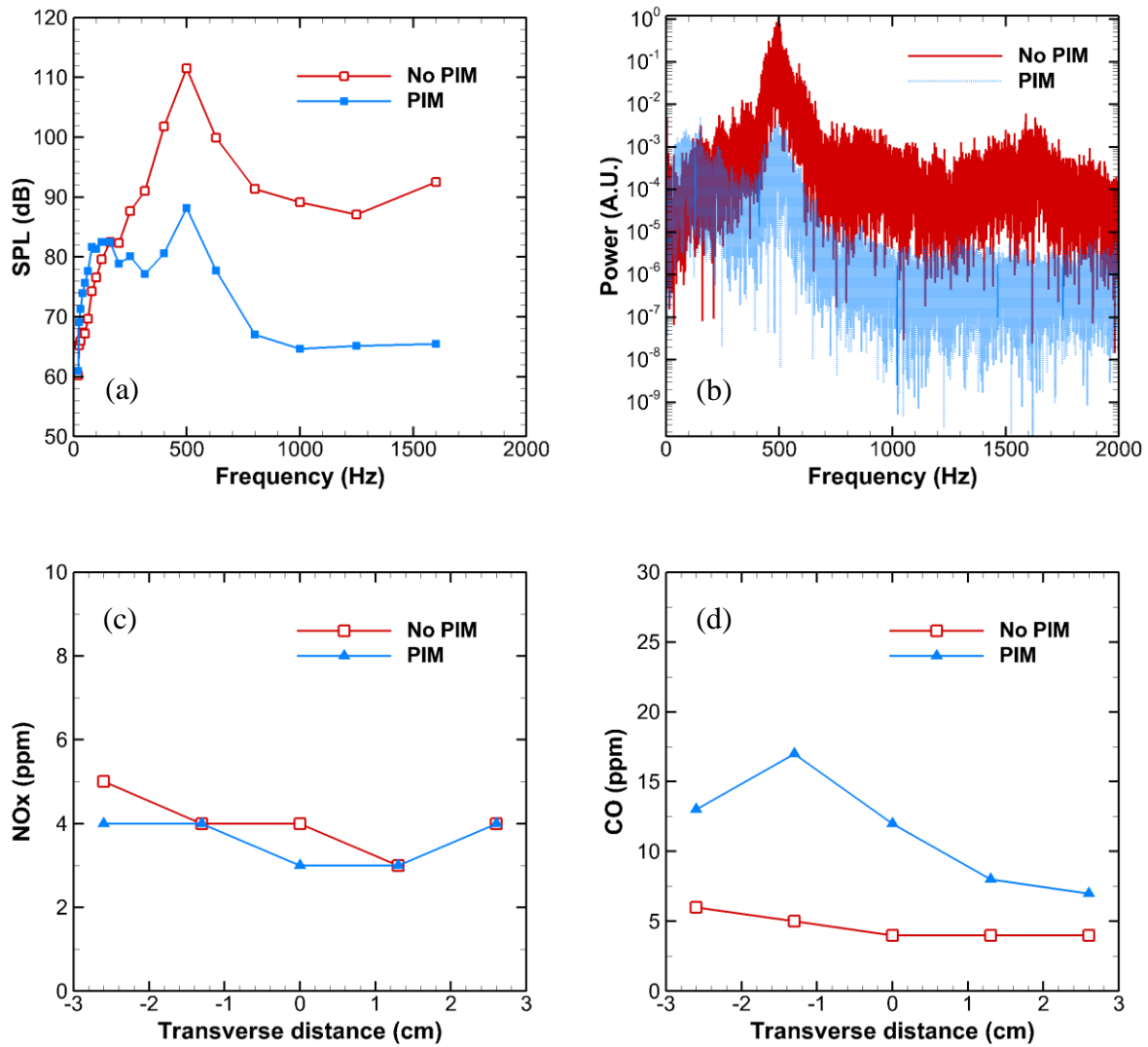


Figure 3.20. Results for  $T_{\text{inlet}} = 21^\circ\text{C}$ ,  $Q = 600$  SLPM,  $\phi = 0.65$  (a) SPL per 1/3 octave band, (b) Spectral power, (c) NOx emissions, (d) CO emissions

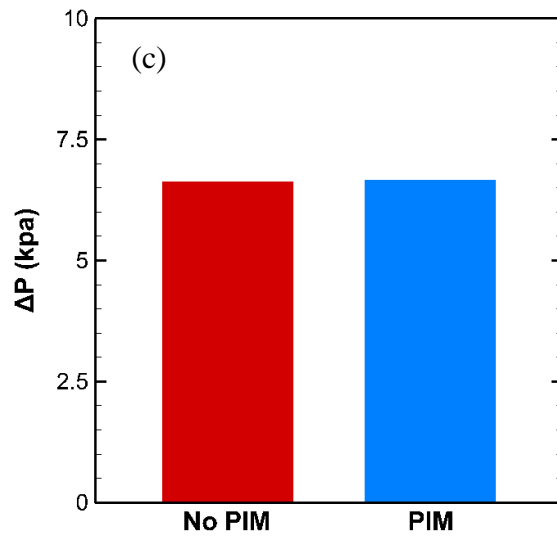
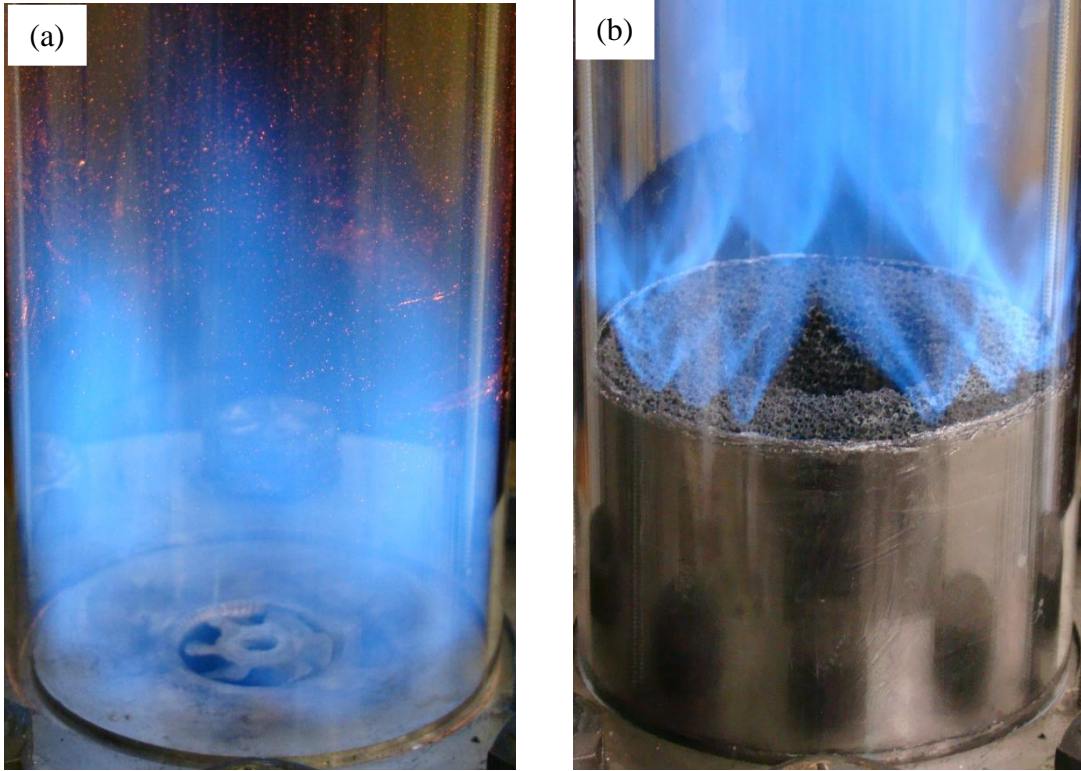


Figure 3.21. Results for  $T_{\text{inlet}} = 21^{\circ}\text{C}$ ,  $Q = 600$  SLPM,  $\phi = 0.70$  (a) Flame photograph without PIM, (b) Flame photograph with PIM, (c) Pressure drop measurements with and without PIM

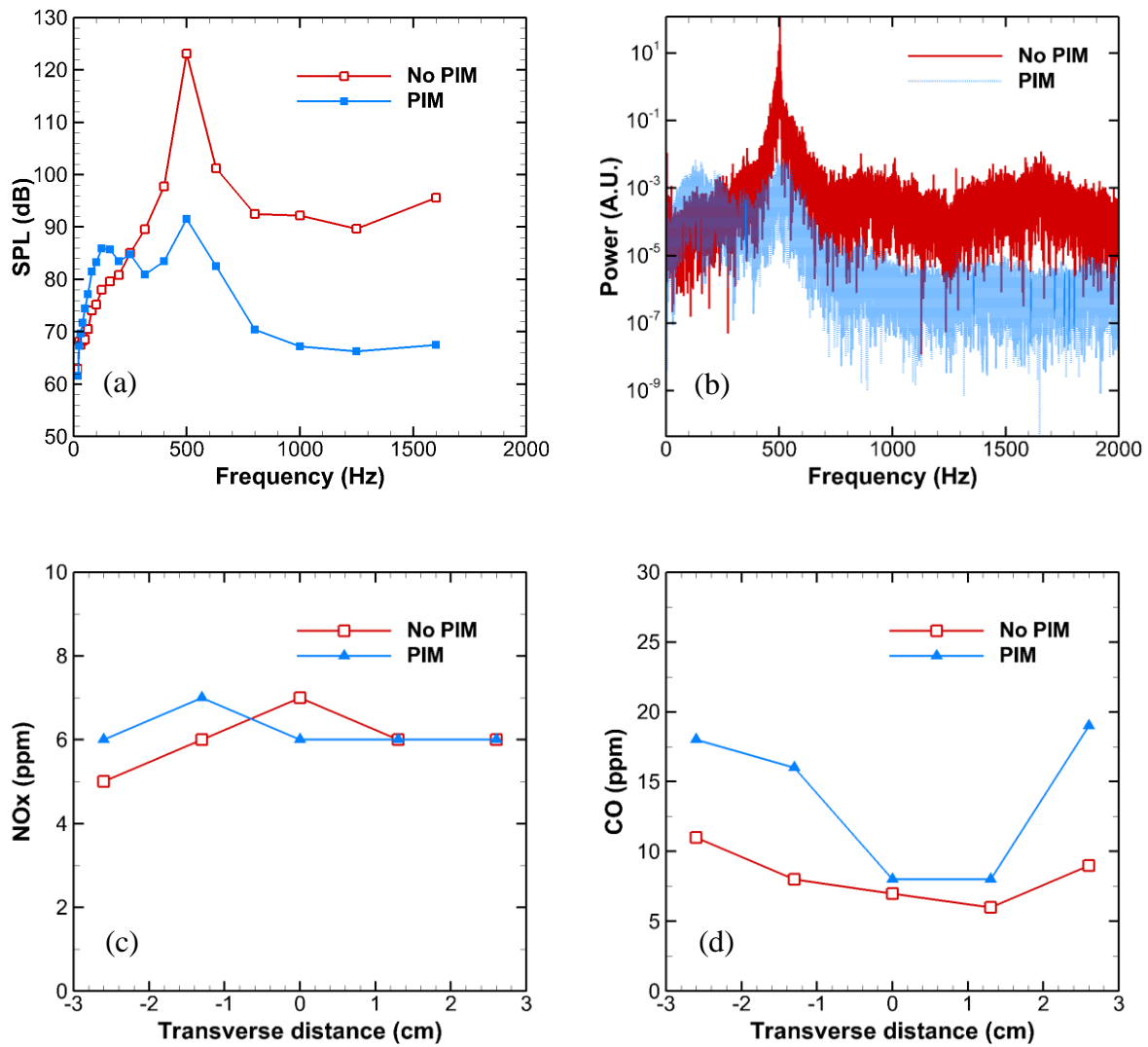


Figure 3.22. Results for  $T_{inlet} = 21^{\circ}\text{C}$ ,  $Q = 600$  SLPM,  $\phi = 0.70$  (a) SPL per 1/3 octave band, (b) Spectral power, (c) NOx emissions, (d) CO emissions

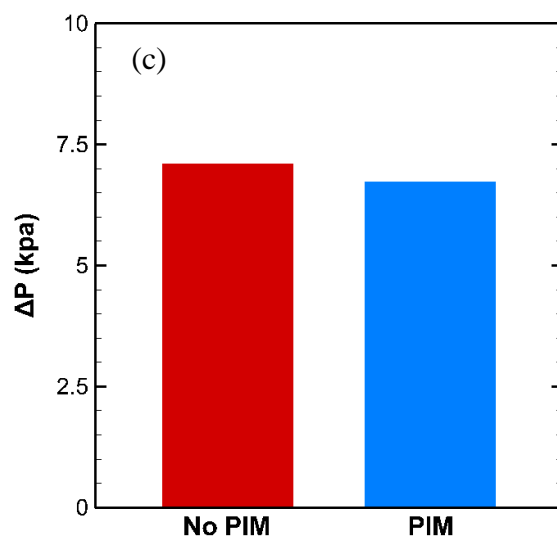
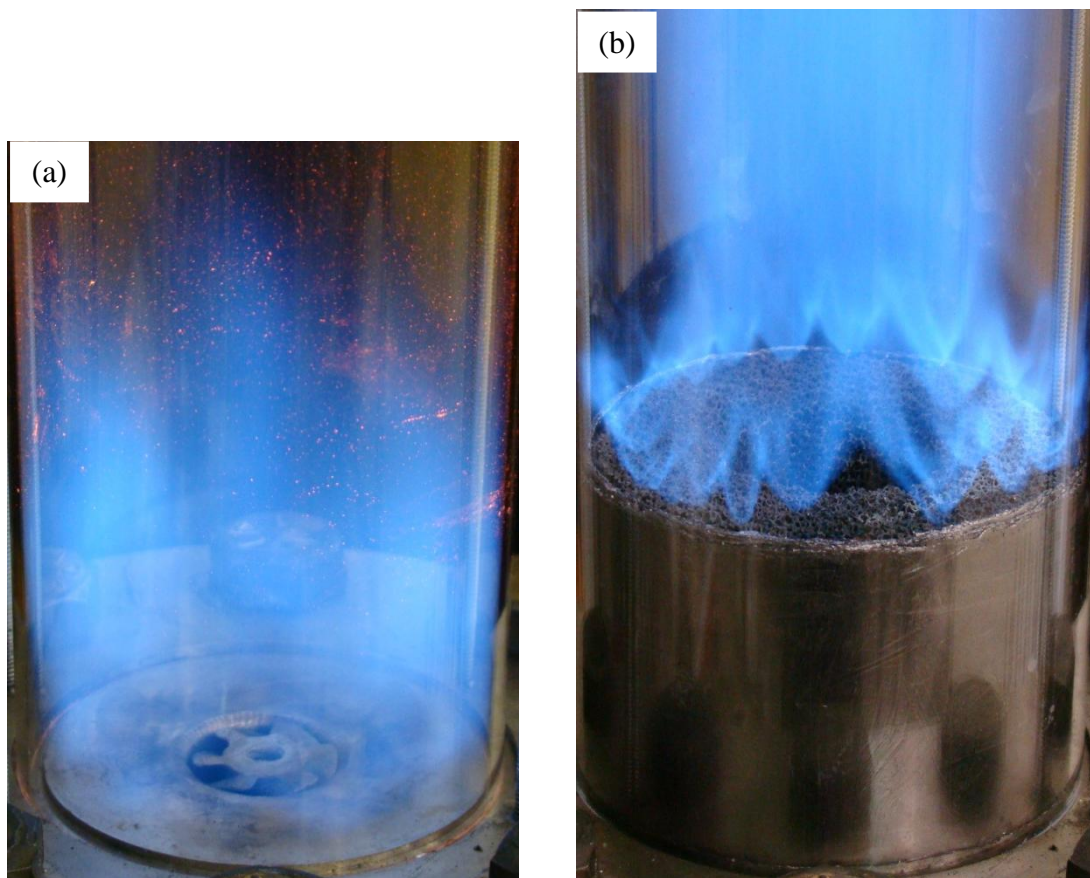


Figure 3.23. Results for  $T_{\text{inlet}} = 21^{\circ}\text{C}$ ,  $Q = 600$  SLPM,  $\phi = 0.75$  (a) Flame photograph without PIM, (b) Flame photograph with PIM, (c) Pressure drop measurements with and without PIM

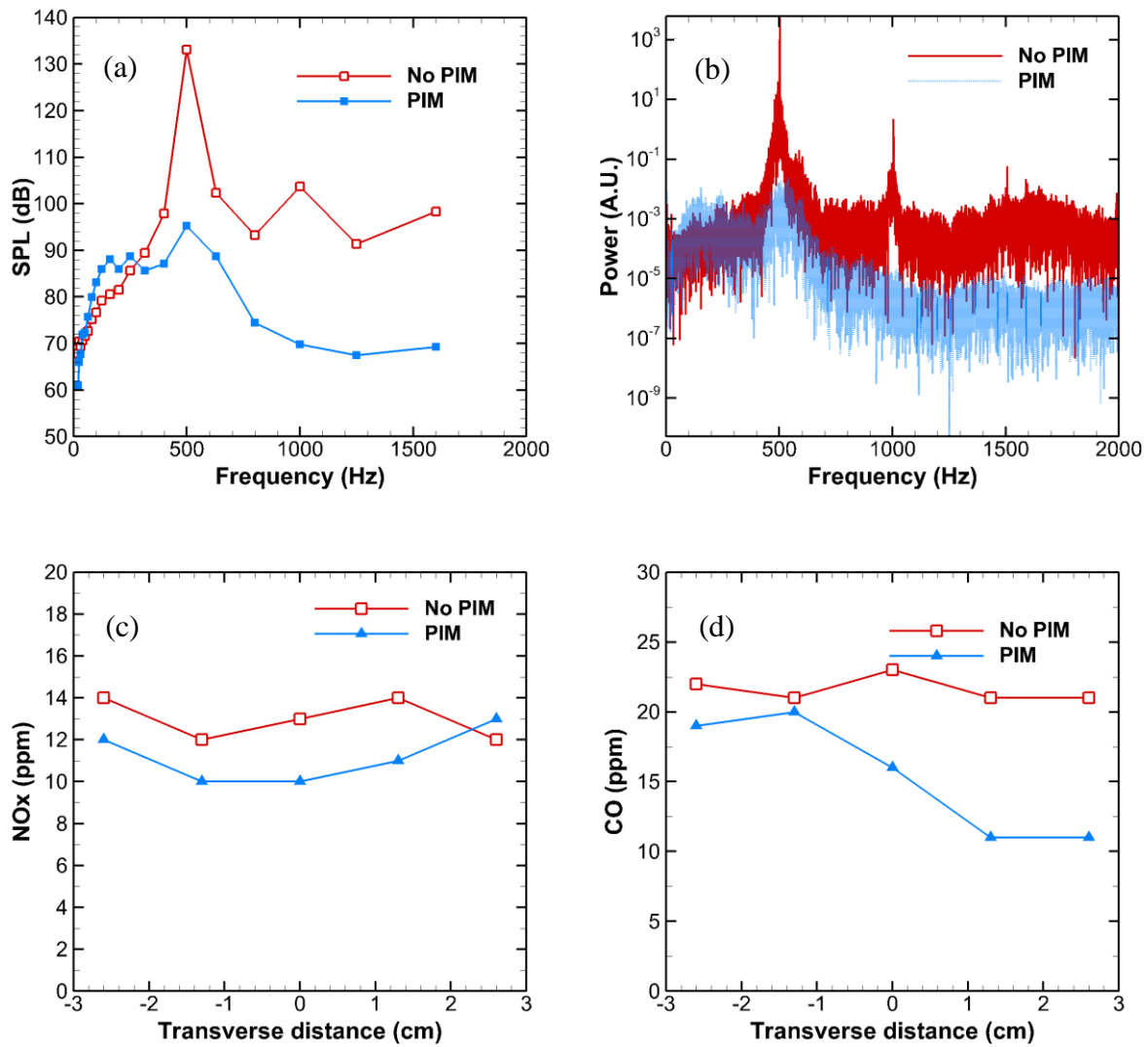


Figure 3.24. Results for  $T_{inlet} = 21^\circ\text{C}$ ,  $Q = 600$  SLPM,  $\phi = 0.75$  (a) SPL per 1/3 octave band, (b) Spectral power, (c) NOx emissions, (d) CO emissions

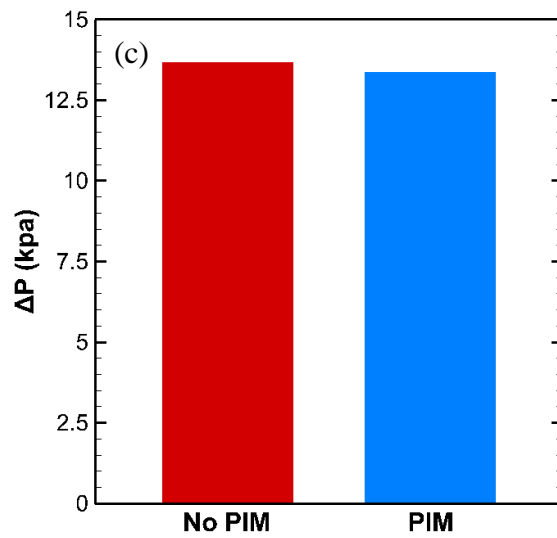
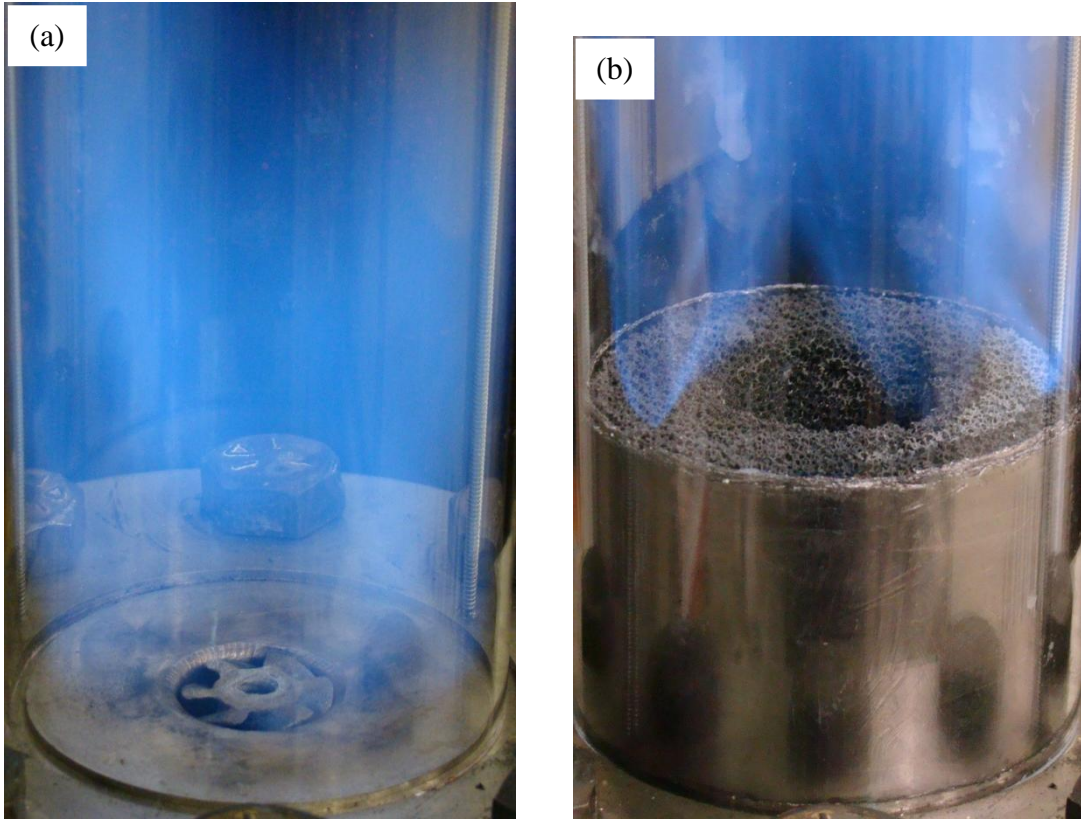


Figure 3.25. Results for  $T_{\text{inlet}} = 21^{\circ}\text{C}$ ,  $Q = 900$  SLPM,  $\phi = 0.60$  (a) Flame photograph without PIM, (b) Flame photograph with PIM, (c) Pressure drop measurements with and without PIM

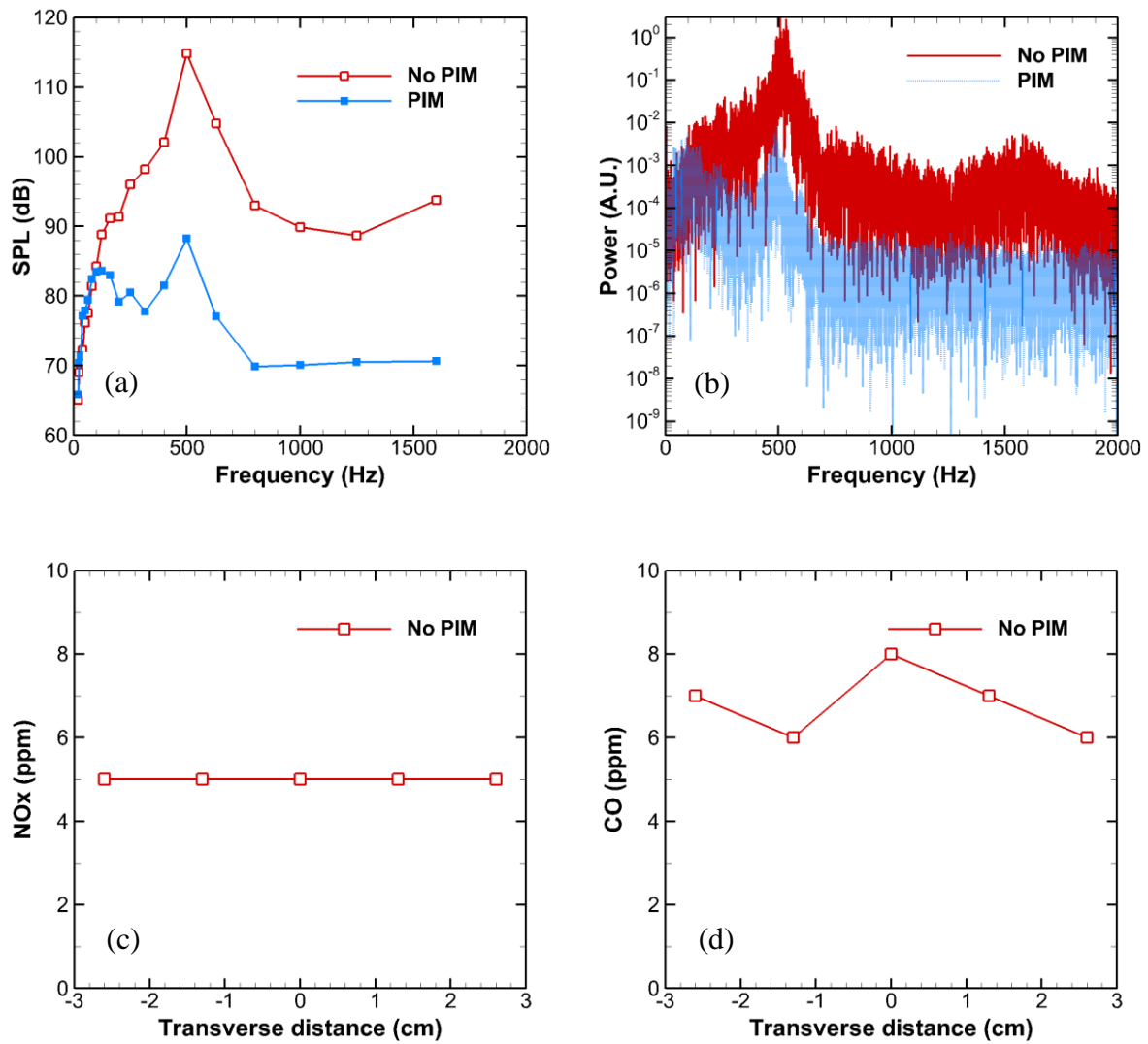


Figure 3.26. Results for  $T_{inlet} = 21^\circ\text{C}$ ,  $Q = 900$  SLPM,  $\phi = 0.60$  (a) SPL per 1/3 octave band, (b) Spectral power, (c) NOx emissions, (d) CO emissions

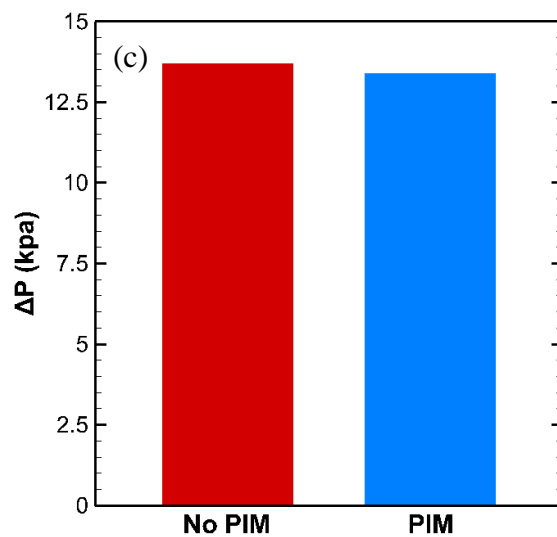
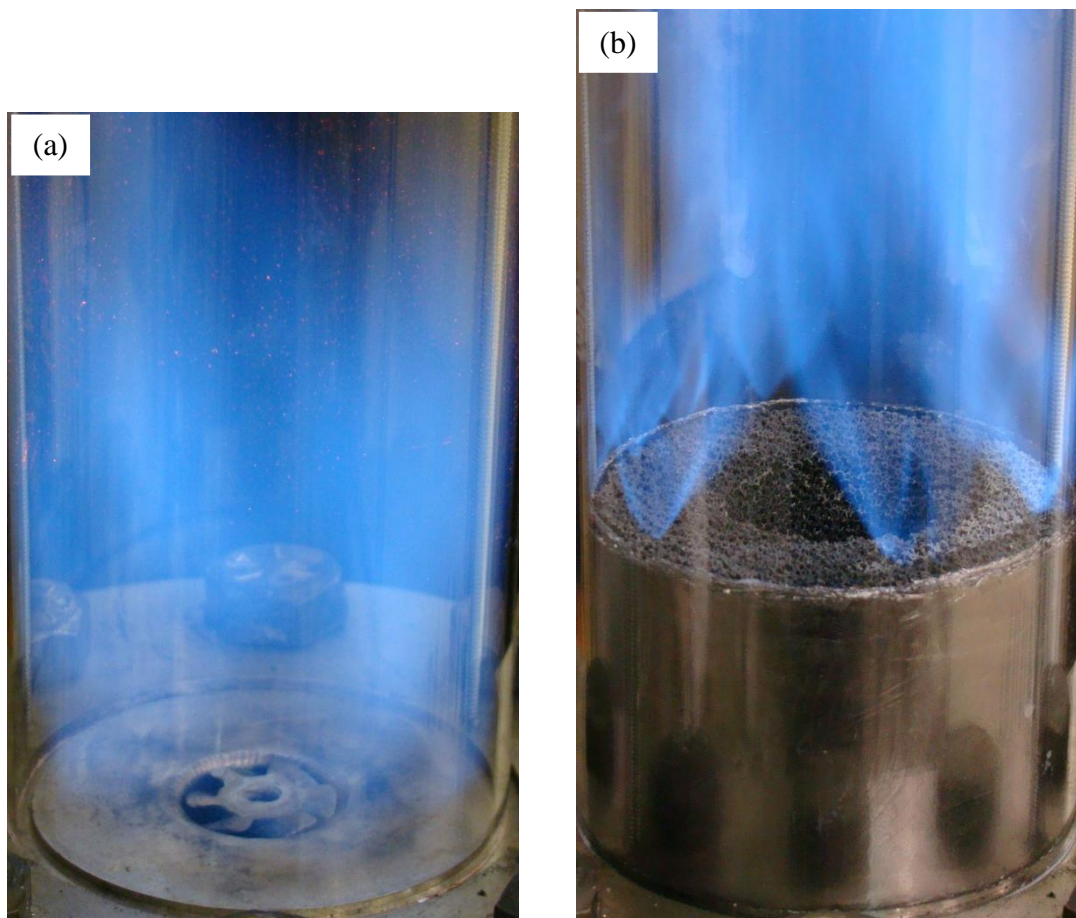


Figure 3.27. Results for  $T_{\text{inlet}} = 21^{\circ}\text{C}$ ,  $Q = 900$  SLPM,  $\phi = 0.65$  (a) Flame photograph without PIM, (b) Flame photograph with PIM, (c) Pressure drop measurements with and without PIM

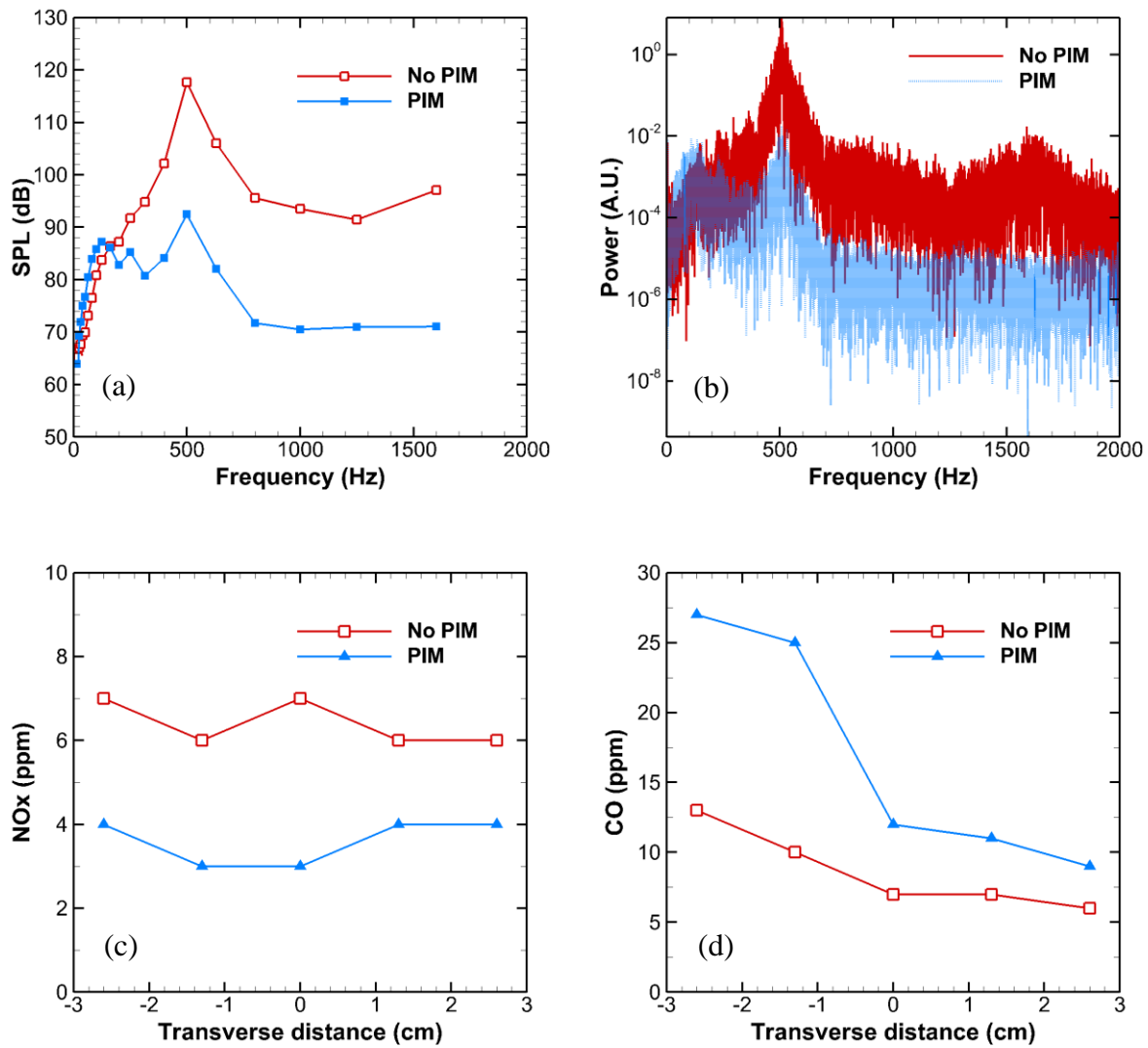
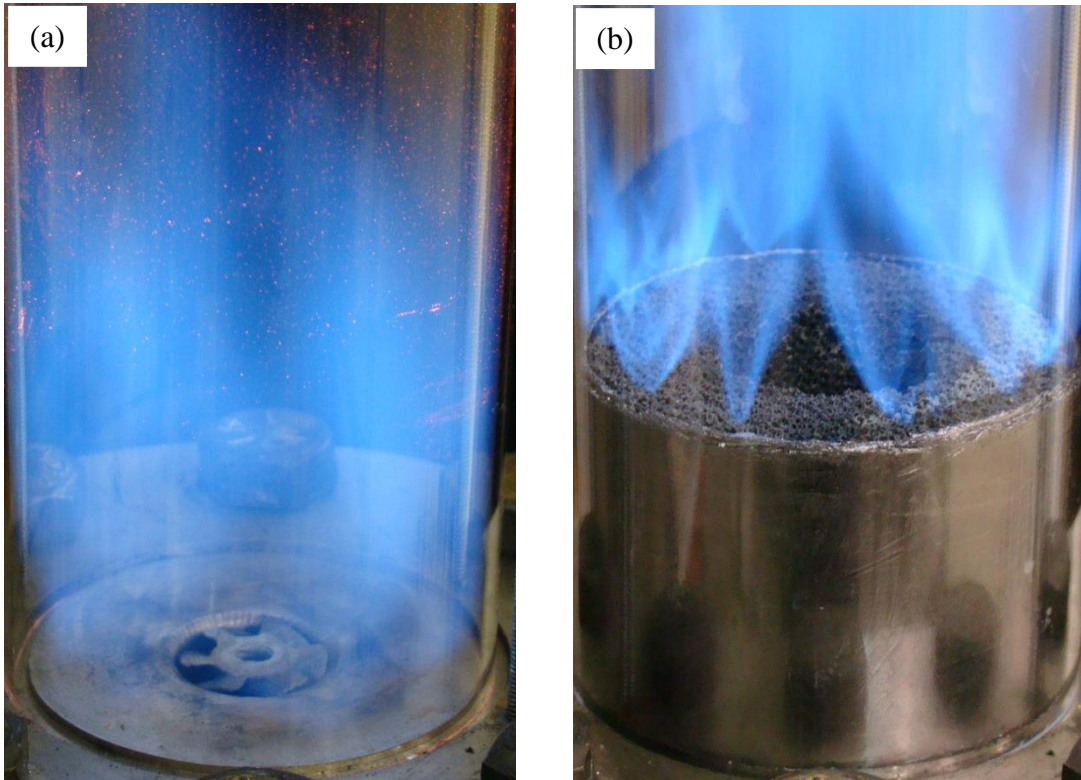


Figure 3.28. Results for  $T_{inlet} = 21^\circ\text{C}$ ,  $Q = 900$  SLPM,  $\phi = 0.65$  (a) SPL per 1/3 octave band, (b) Spectral power, (c) NOx emissions, (d) CO emissions



*Figure 3.29.* Results for  $T_{\text{inlet}} = 21^{\circ}\text{C}$ ,  $Q = 900$  SLPM,  $\phi = 0.70$  (a) Flame photograph without PIM, (b) Flame photograph with PIM

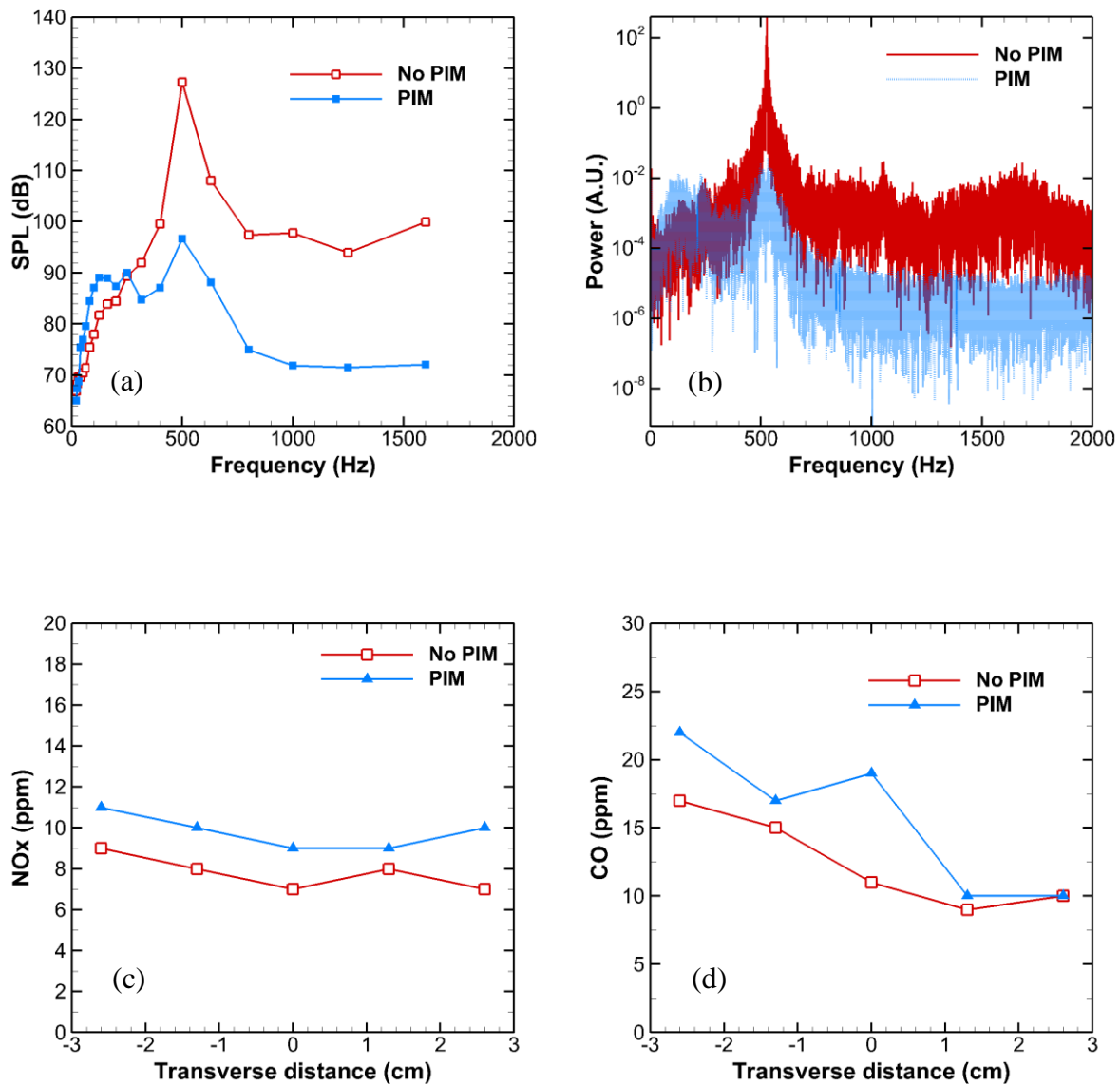


Figure 3.30. Results for  $T_{inlet} = 21^\circ\text{C}$ ,  $Q = 900$  SLPM,  $\phi = 0.70$  (a) SPL per 1/3 octave band, (b) Spectral power, (c) NOx emissions, (d) CO emissions



*Figure 3.31.* Results for  $T_{\text{inlet}} = 21^{\circ}\text{C}$ ,  $Q = 900$  SLPM,  $\phi = 0.75$  (a) Flame photograph without PIM, (b) Flame photograph with PIM

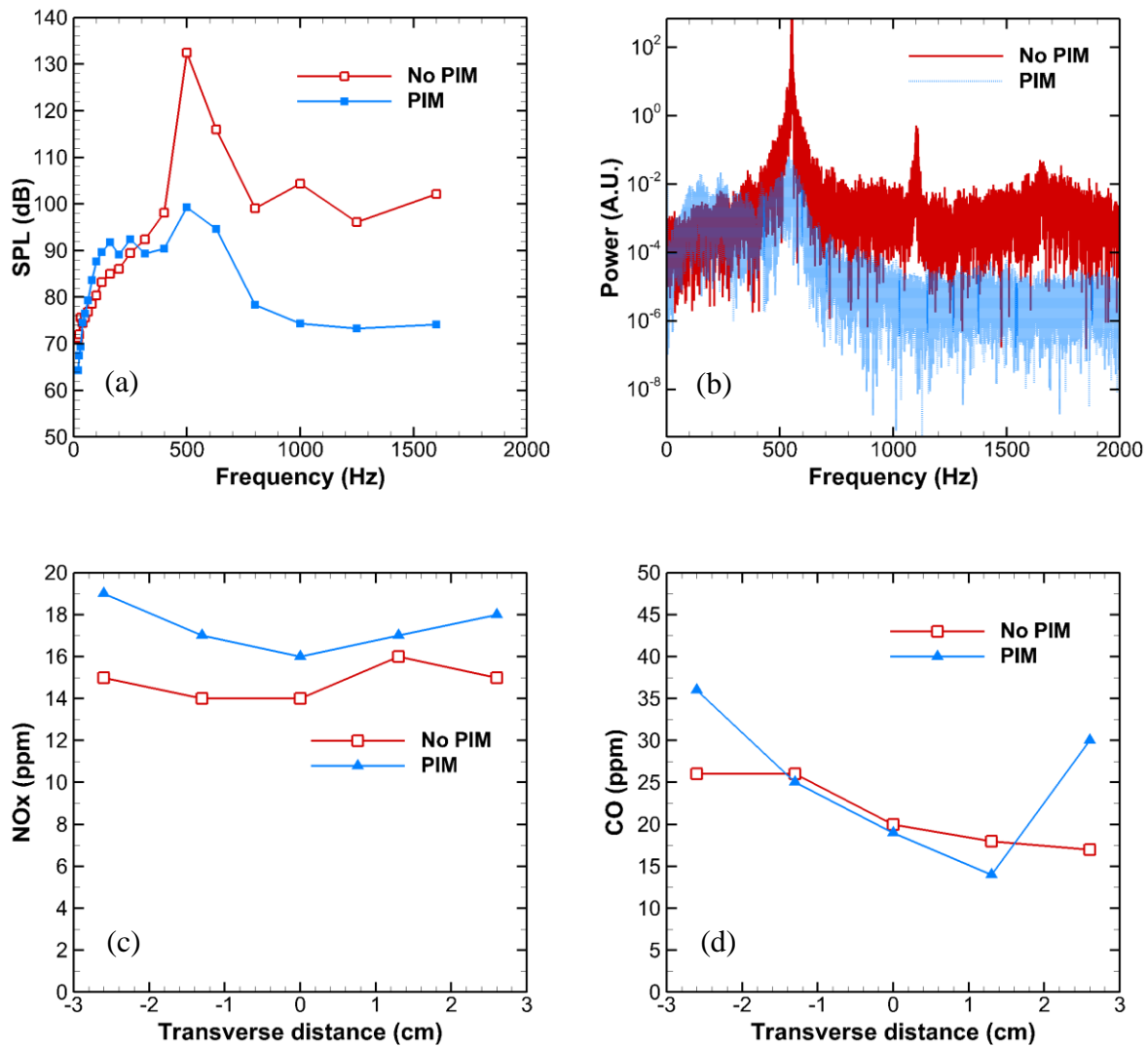


Figure 3.32. Results for  $T_{\text{inlet}} = 21^\circ\text{C}$ ,  $Q = 900$  SLPM,  $\phi = 0.75$  (a) SPL per 1/3 octave band, (b) Spectral power, (c) NOx emissions, (d) CO emissions

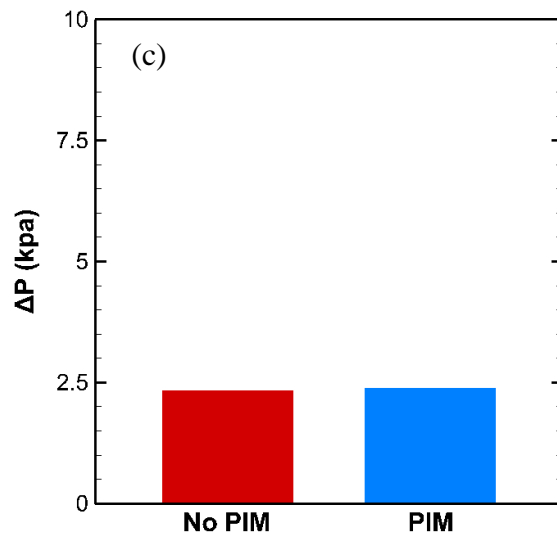
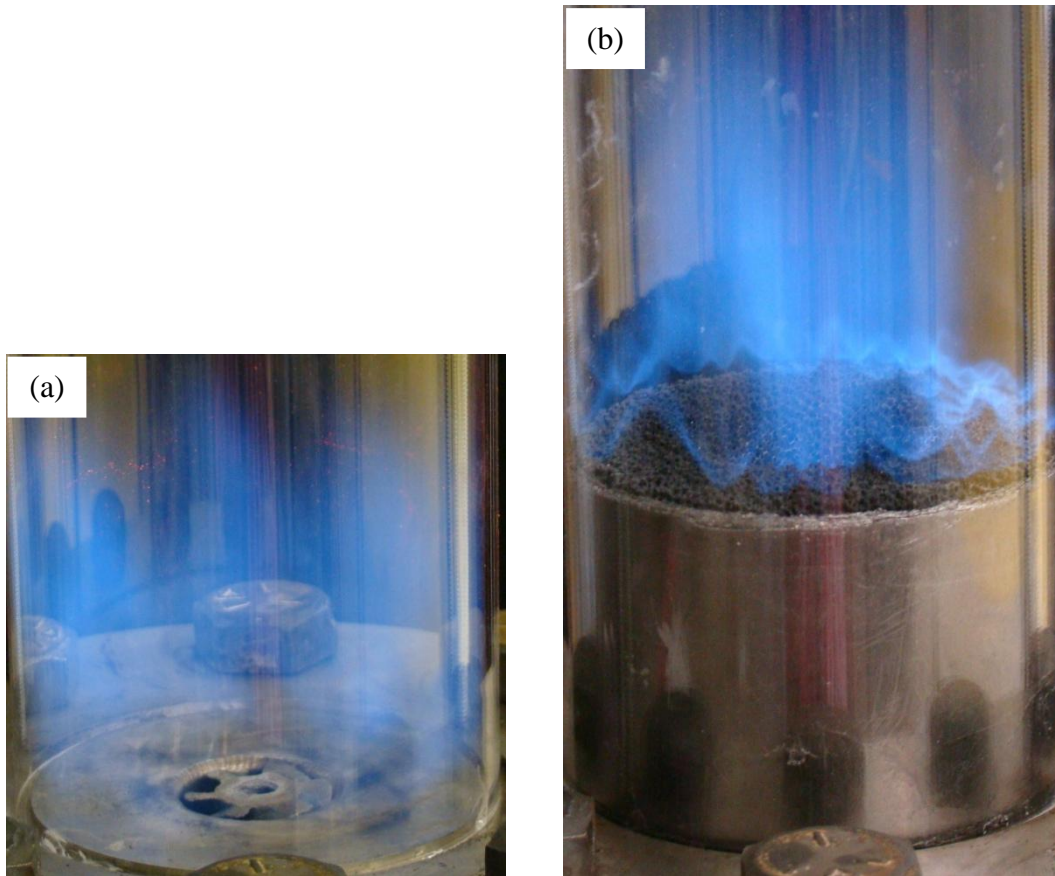


Figure 3.33. Results for  $T_{inlet} = 130^{\circ}C$ ,  $Q = 300$  SLPM,  $\phi = 0.60$  (a) Flame photograph without PIM, (b) Flame photograph with PIM, (c) Pressure drop measurements with and without PIM

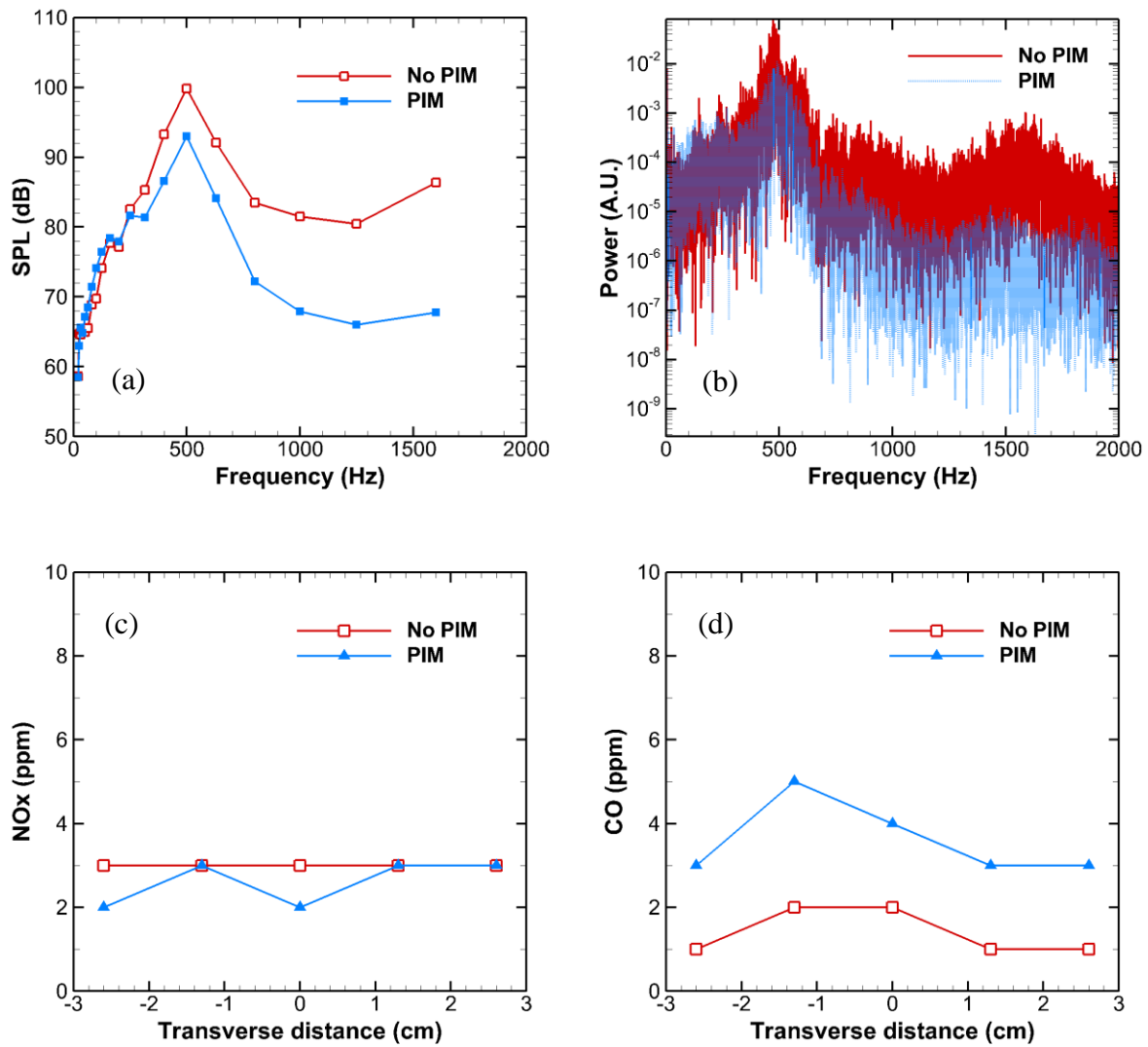


Figure 3.34. Results for  $T_{\text{inlet}} = 130^{\circ}\text{C}$ ,  $Q = 300$  SLPM,  $\phi = 0.60$  (a) SPL per 1/3 octave band, (b) Spectral power, (c) NOx emissions, (d) CO emissions

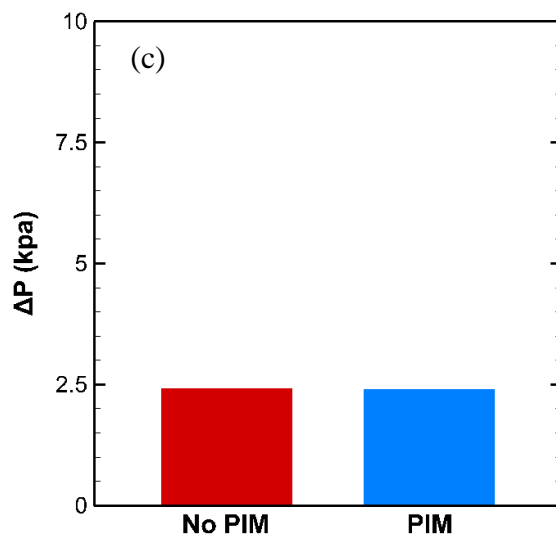
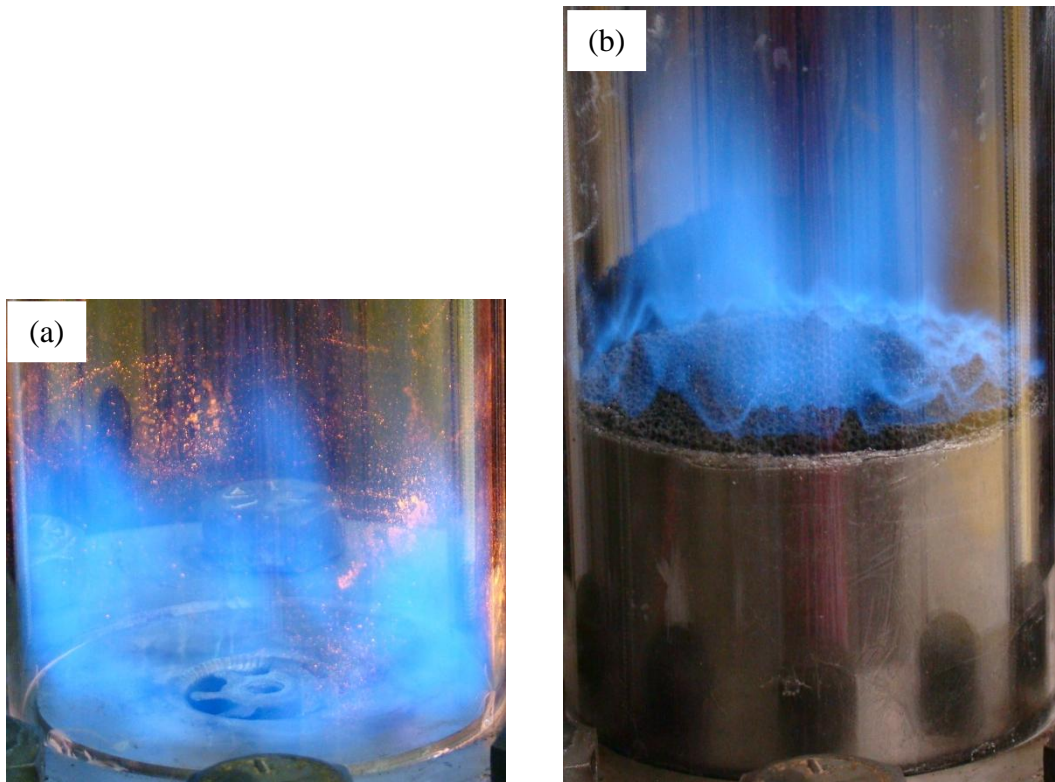


Figure 3.35. Results for  $T_{\text{inlet}} = 130^{\circ}\text{C}$ ,  $Q = 300$  SLPM,  $\phi = 0.65$  (a) Flame photograph without PIM, (b) Flame photograph with PIM, (c) Pressure drop measurements with and without PIM

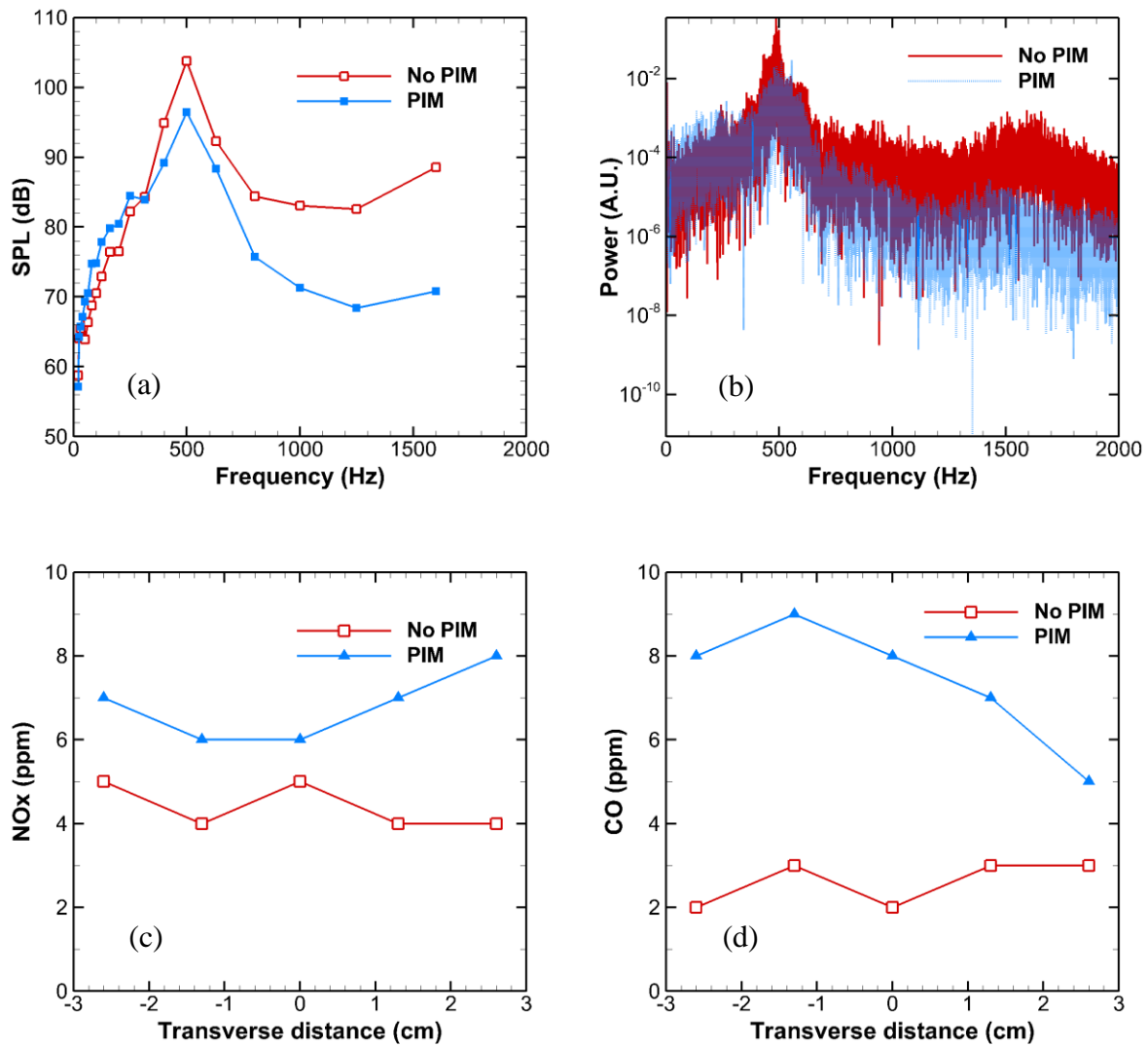


Figure 3.36. Results for  $T_{inlet} = 130^{\circ}\text{C}$ ,  $Q = 300$  SLPM,  $\phi = 0.65$  (a) SPL per 1/3 octave band, (b) Spectral power, (c) NOx emissions, (d) CO emissions

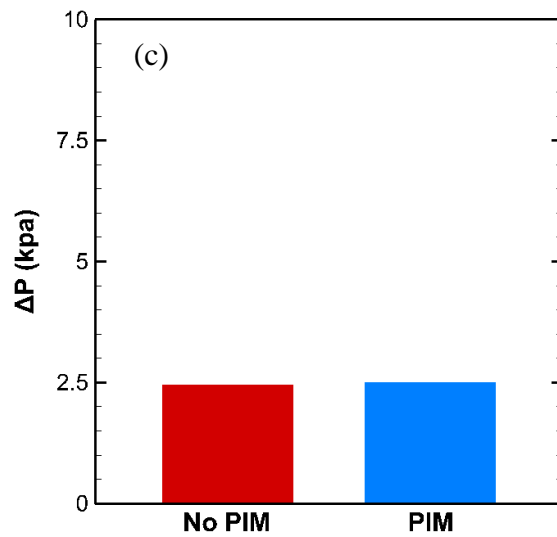
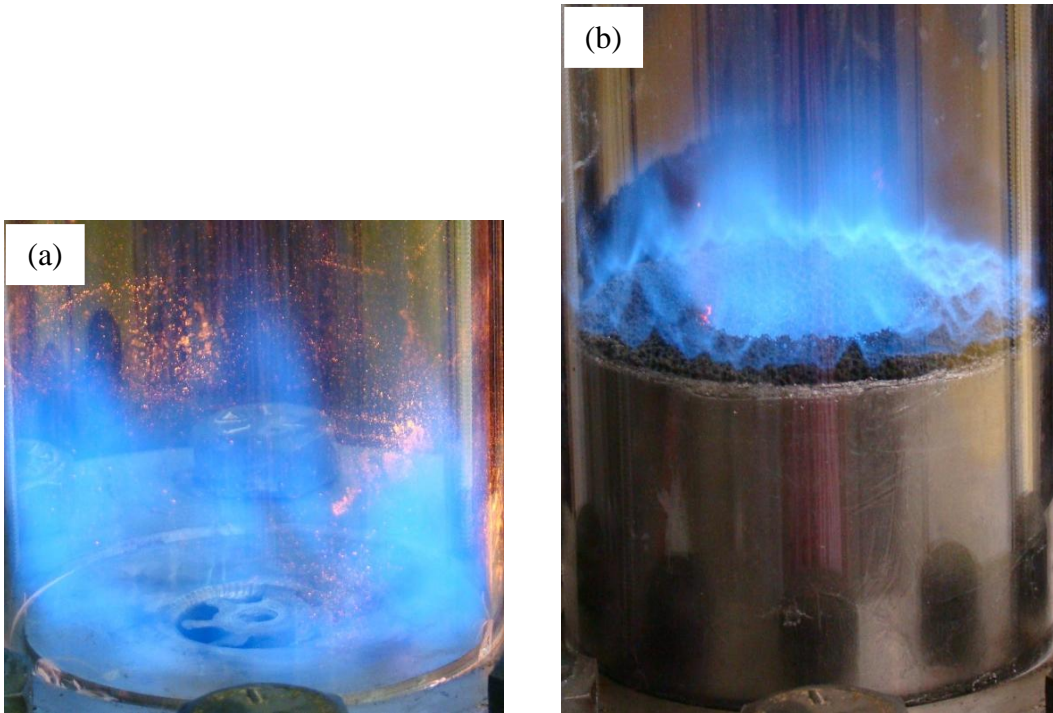


Figure 3.37. Results for  $T_{\text{inlet}} = 130^{\circ}\text{C}$ ,  $Q = 300$  SLPM,  $\phi = 0.70$  (a) Flame photograph without PIM, (b) Flame photograph with PIM, (c) Pressure drop measurements with and without PIM

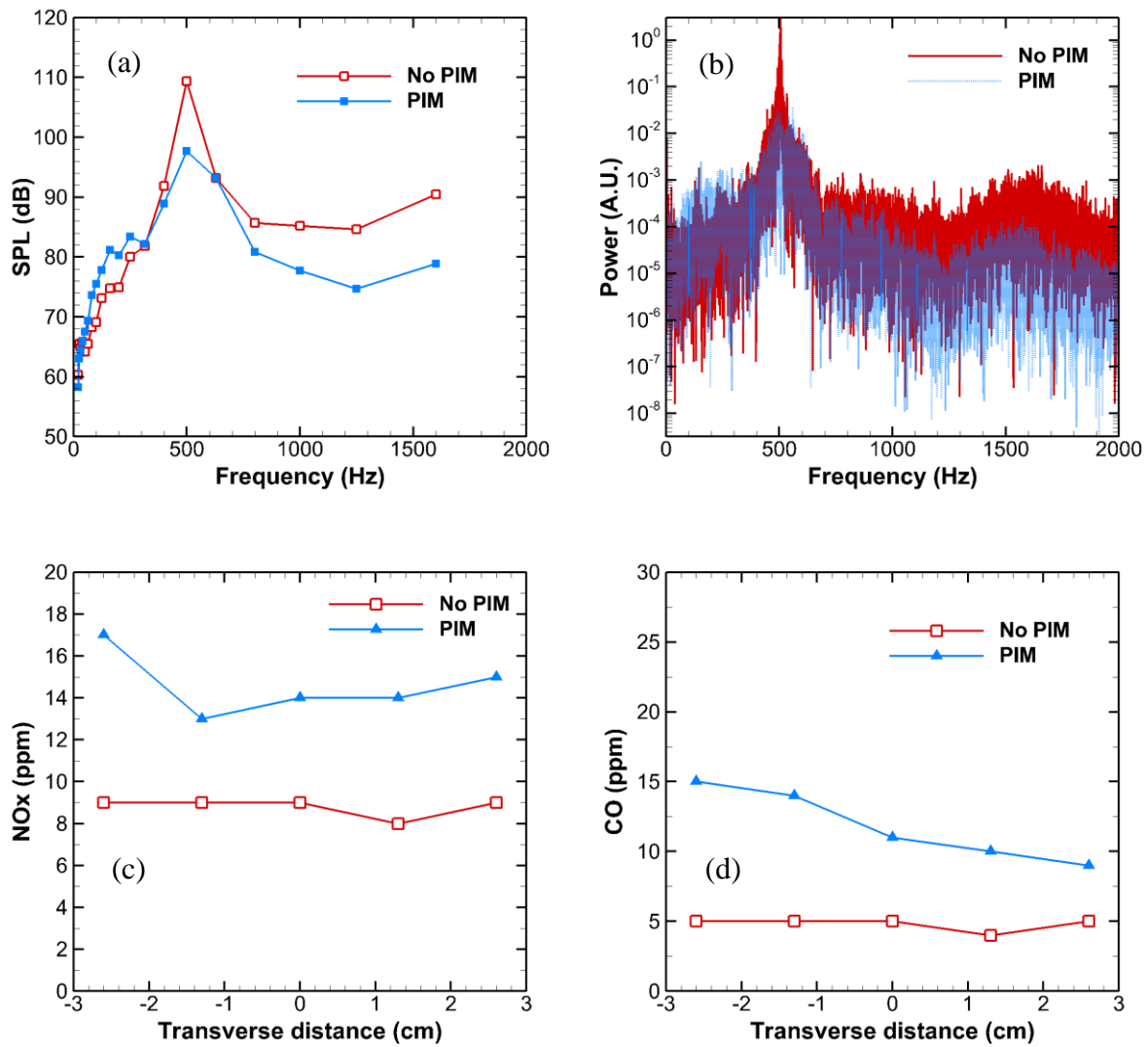


Figure 3.38. Results for  $T_{\text{inlet}} = 130^\circ\text{C}$ ,  $Q = 300$  SLPM,  $\phi = 0.70$  (a) SPL per 1/3 octave band, (b) Spectral power, (c) NOx emissions, (d) CO emissions

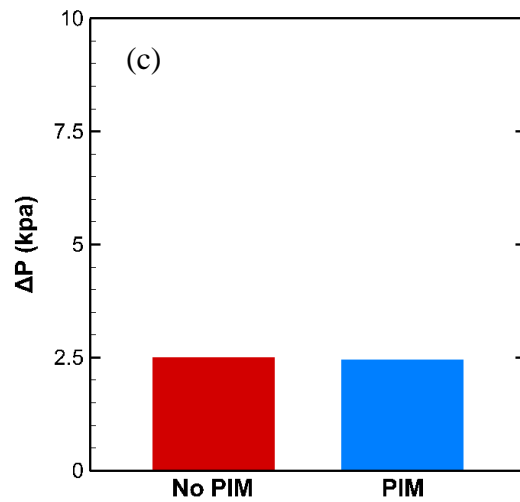
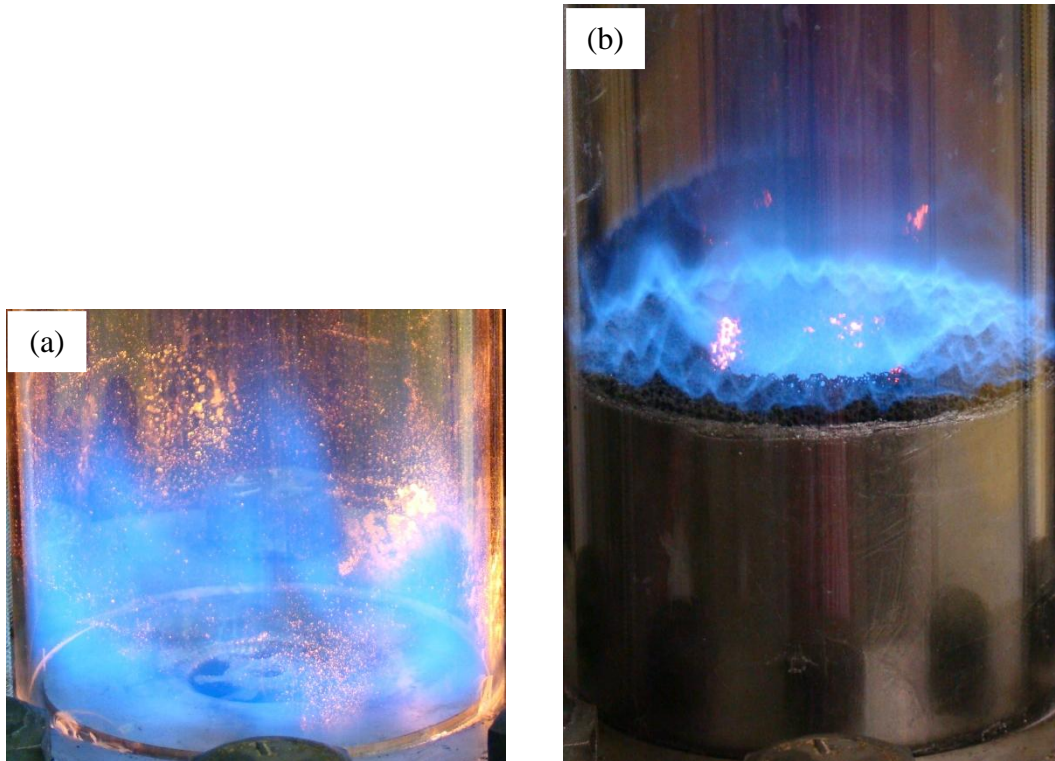


Figure 3.39. Results for  $T_{\text{inlet}} = 130^{\circ}\text{C}$ ,  $Q = 300$  SLPM,  $\phi = 0.75$  (a) Flame photograph without PIM, (b) Flame photograph with PIM, (c) Pressure drop measurements with and without PIM

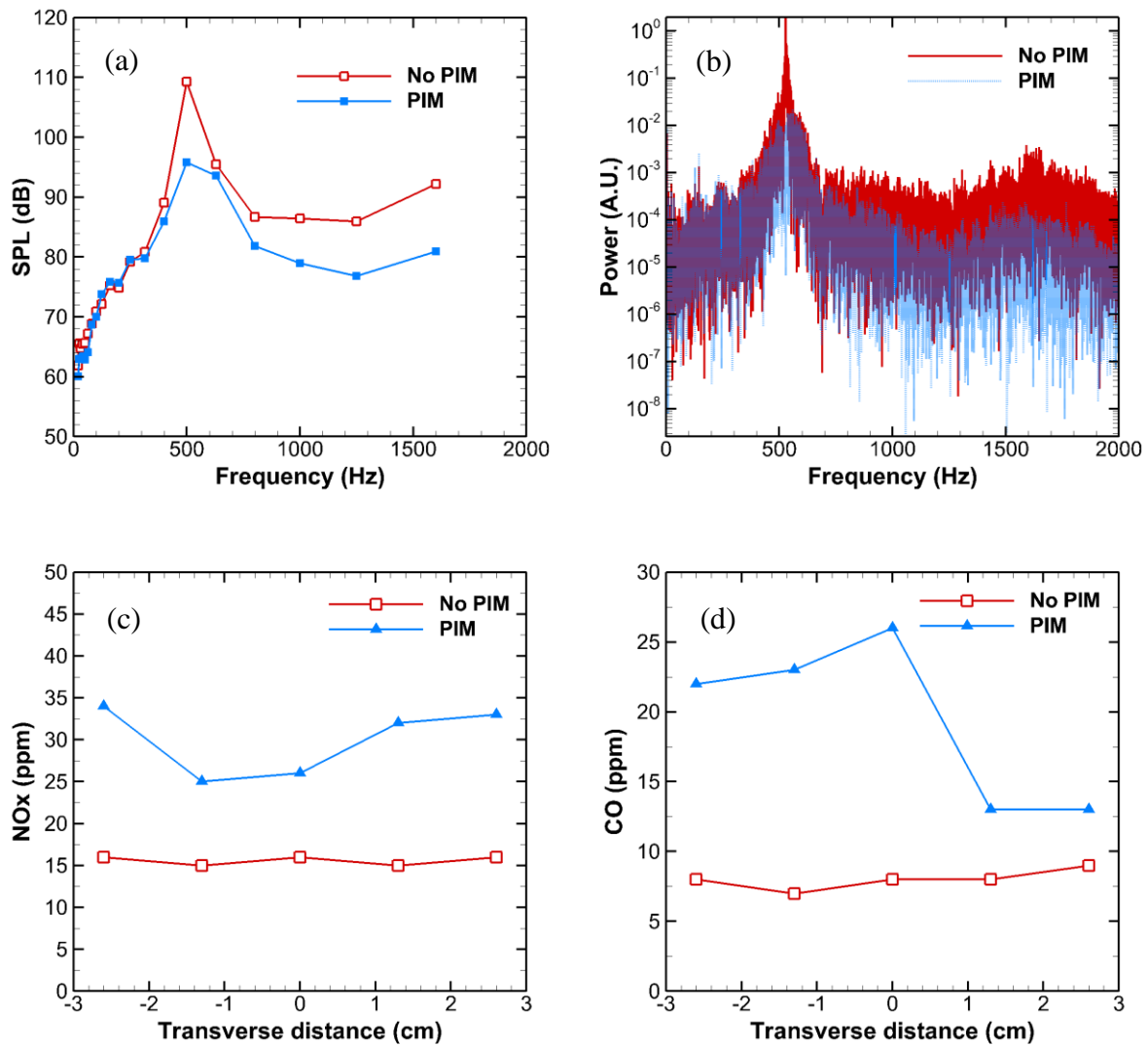


Figure 3.40. Results for  $T_{\text{inlet}} = 130^\circ\text{C}$ ,  $Q = 300$  SLPM,  $\phi = 0.75$  (a) SPL per 1/3 octave band, (b) Spectral power, (c) NOx emissions, (d) CO emissions

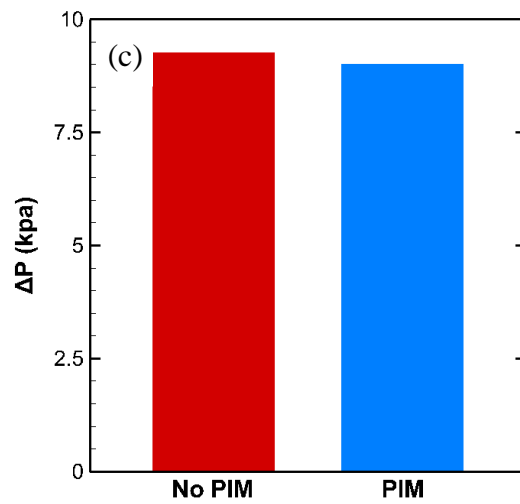
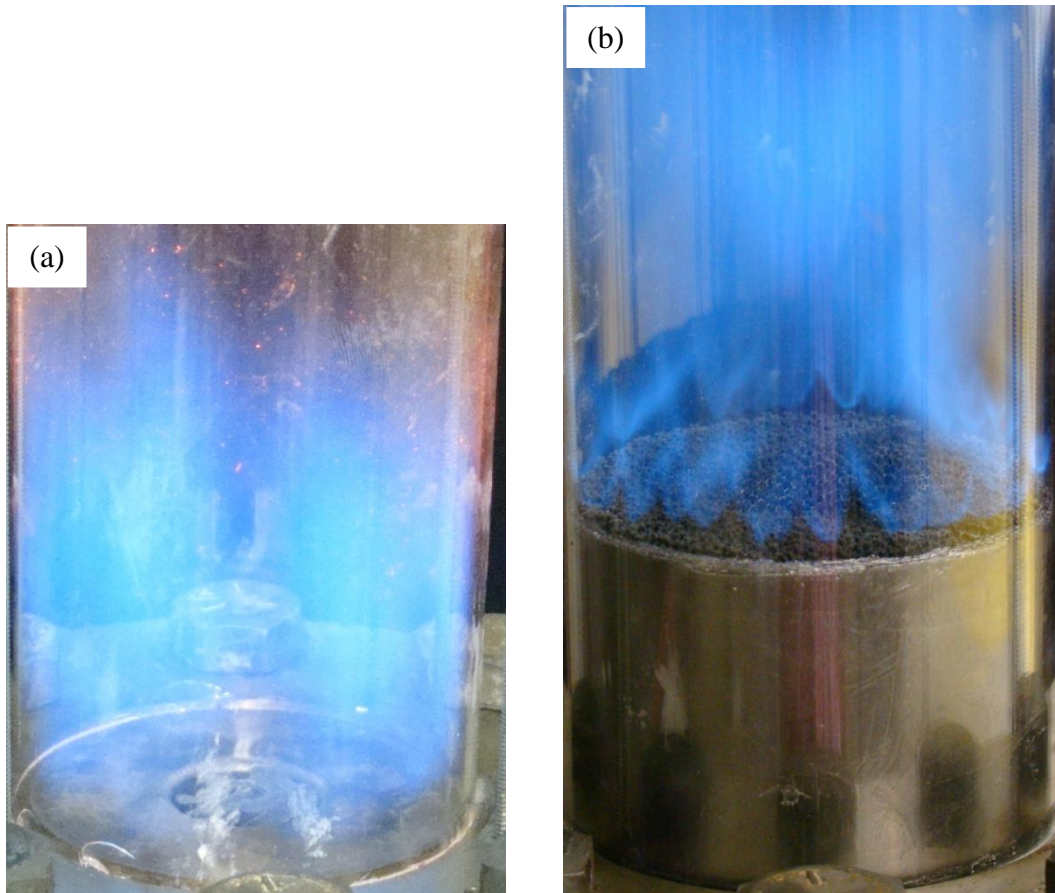


Figure 3.41. Results for  $T_{\text{inlet}} = 130^{\circ}\text{C}$ ,  $Q = 600$  SLPM,  $\phi = 0.60$  (a) Flame photograph without PIM, (b) Flame photograph with PIM, (c) Pressure drop measurements with and without PIM

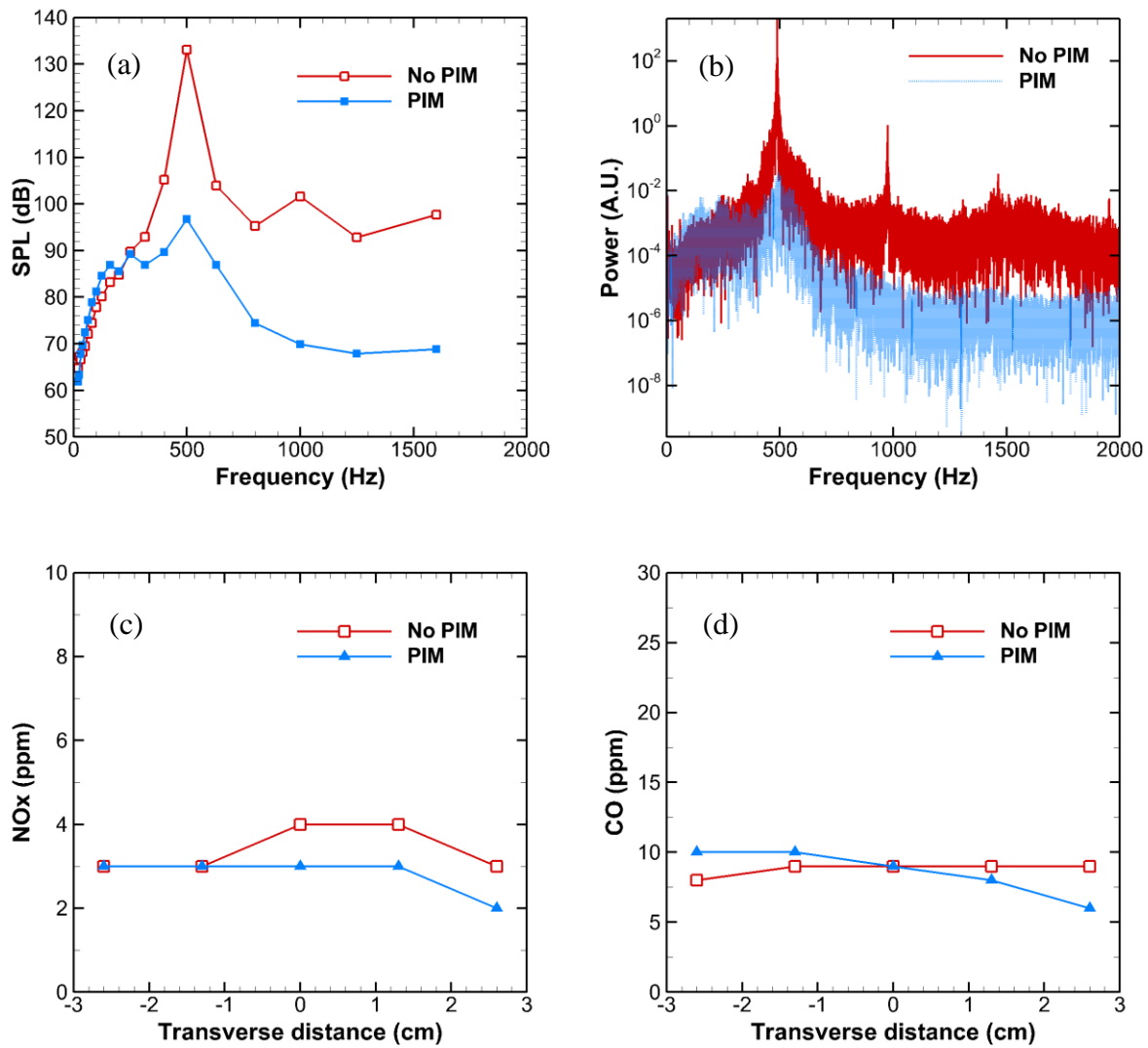


Figure 3.42. Results for  $T_{\text{inlet}} = 130^{\circ}\text{C}$ ,  $Q = 600$  SLPM,  $\phi = 0.60$  (a) SPL per 1/3 octave band, (b) Spectral power, (c) NOx emissions, (d) CO emissions

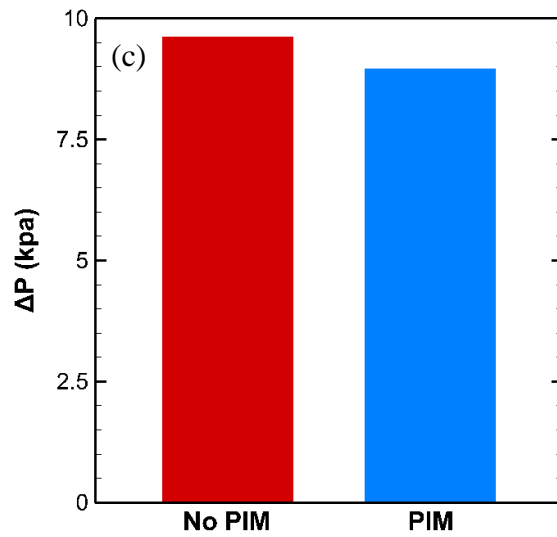
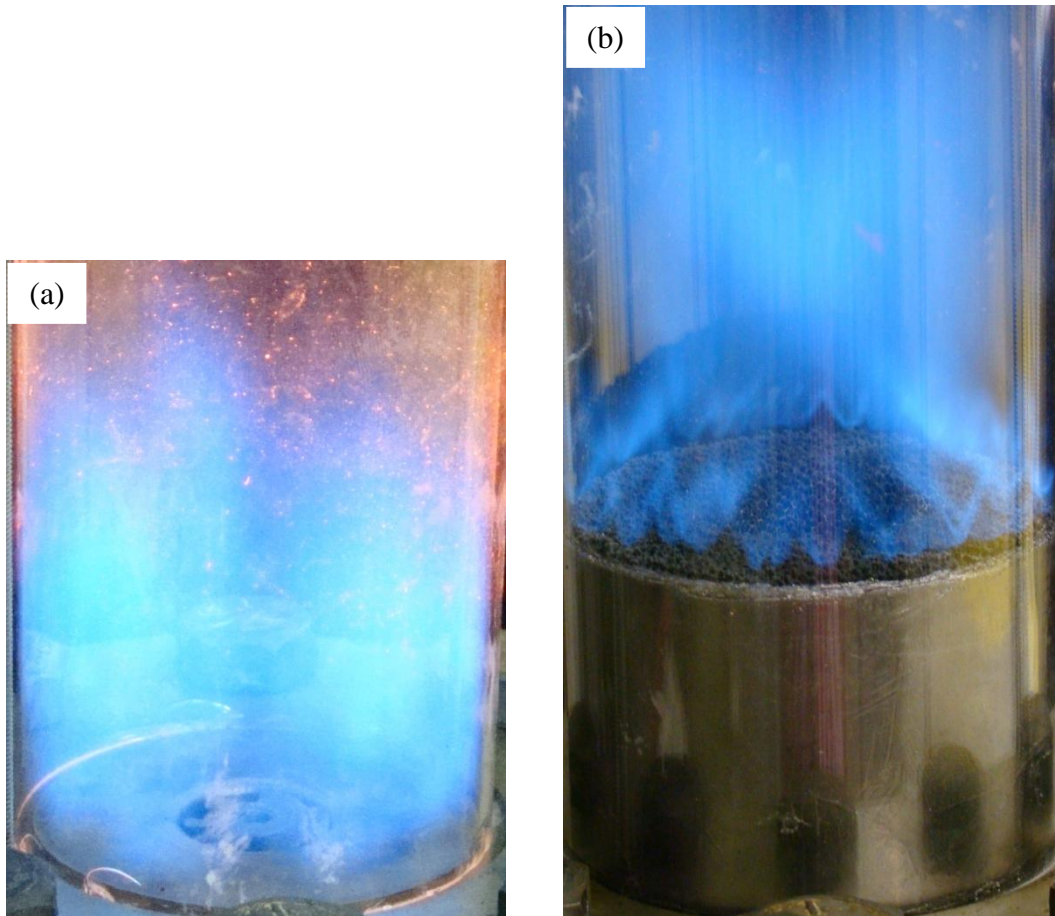


Figure 3.43. Results for  $T_{\text{inlet}} = 130^{\circ}\text{C}$ ,  $Q = 600$  SLPM,  $\phi = 0.65$  (a) Flame photograph without PIM, (b) Flame photograph with PIM, (c) Pressure drop measurements with and without PIM

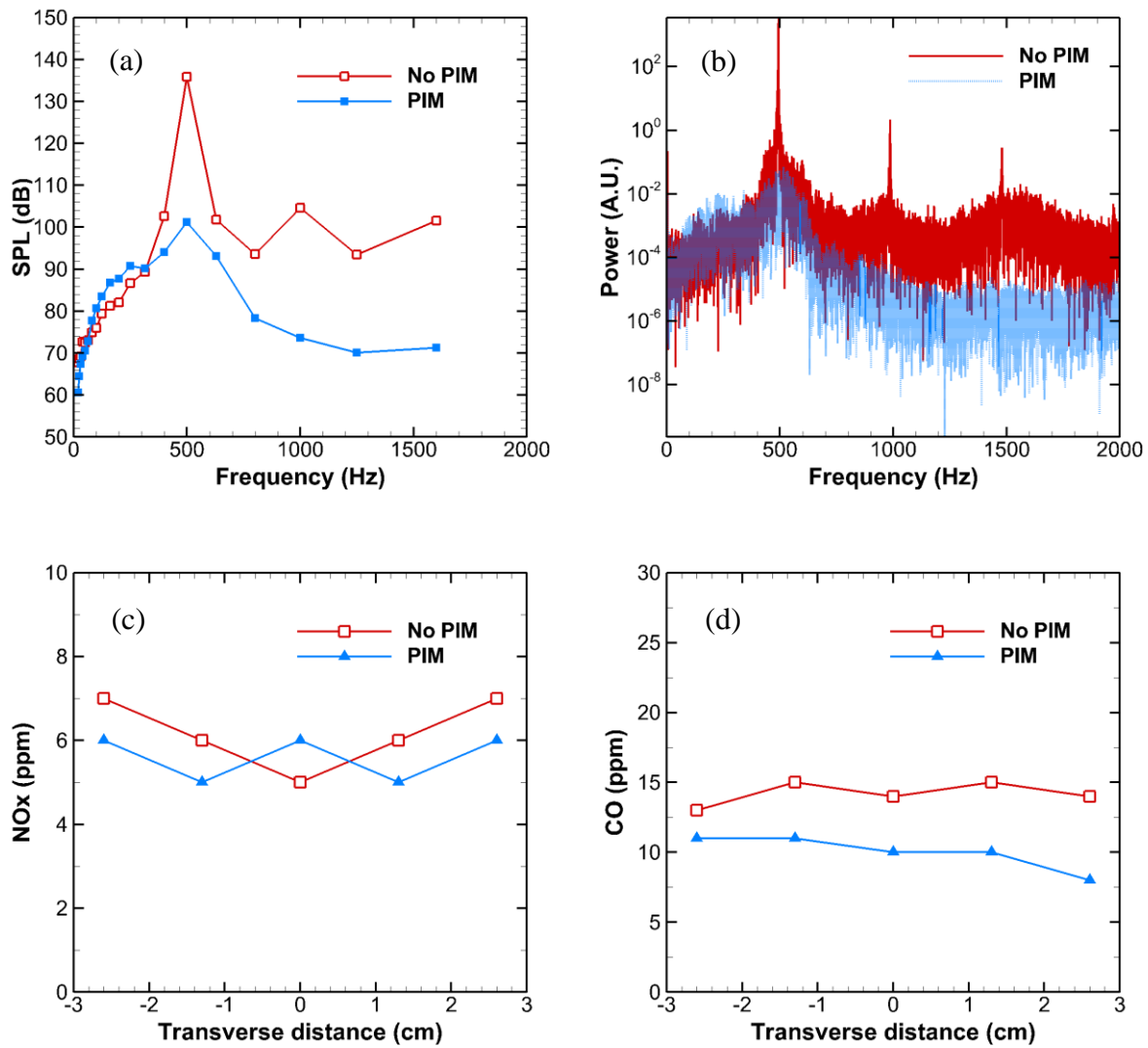


Figure 3.44. Results for  $T_{\text{inlet}} = 130^\circ\text{C}$ ,  $Q = 600$  SLPM,  $\phi = 0.65$  (a) SPL per 1/3 octave band, (b) Spectral power, (c) NOx emissions, (d) CO emissions

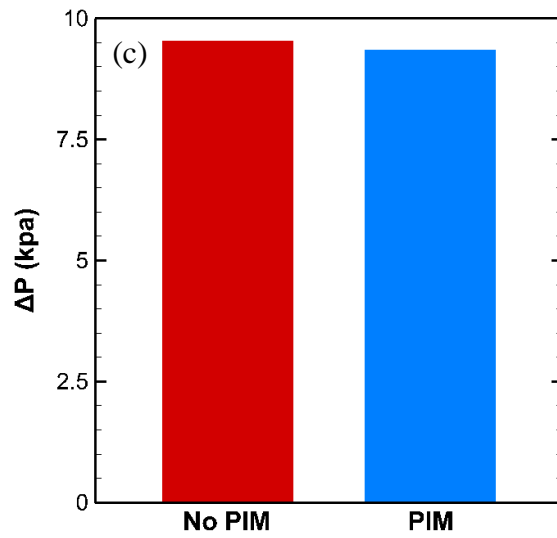
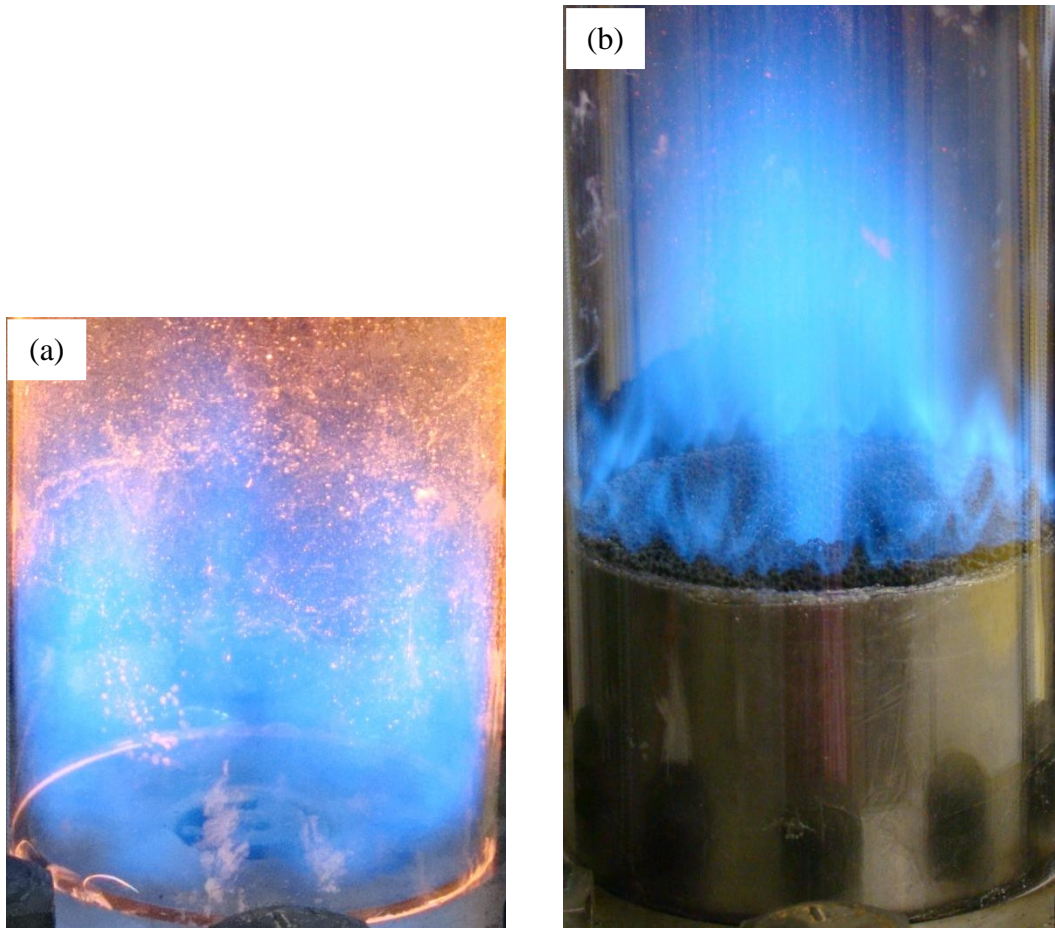


Figure 3.45. Results for  $T_{\text{inlet}} = 130^{\circ}\text{C}$ ,  $Q = 600$  SLPM,  $\phi = 0.70$  (a) Flame photograph without PIM, (b) Flame photograph with PIM, (c) Pressure drop measurements with and without PIM

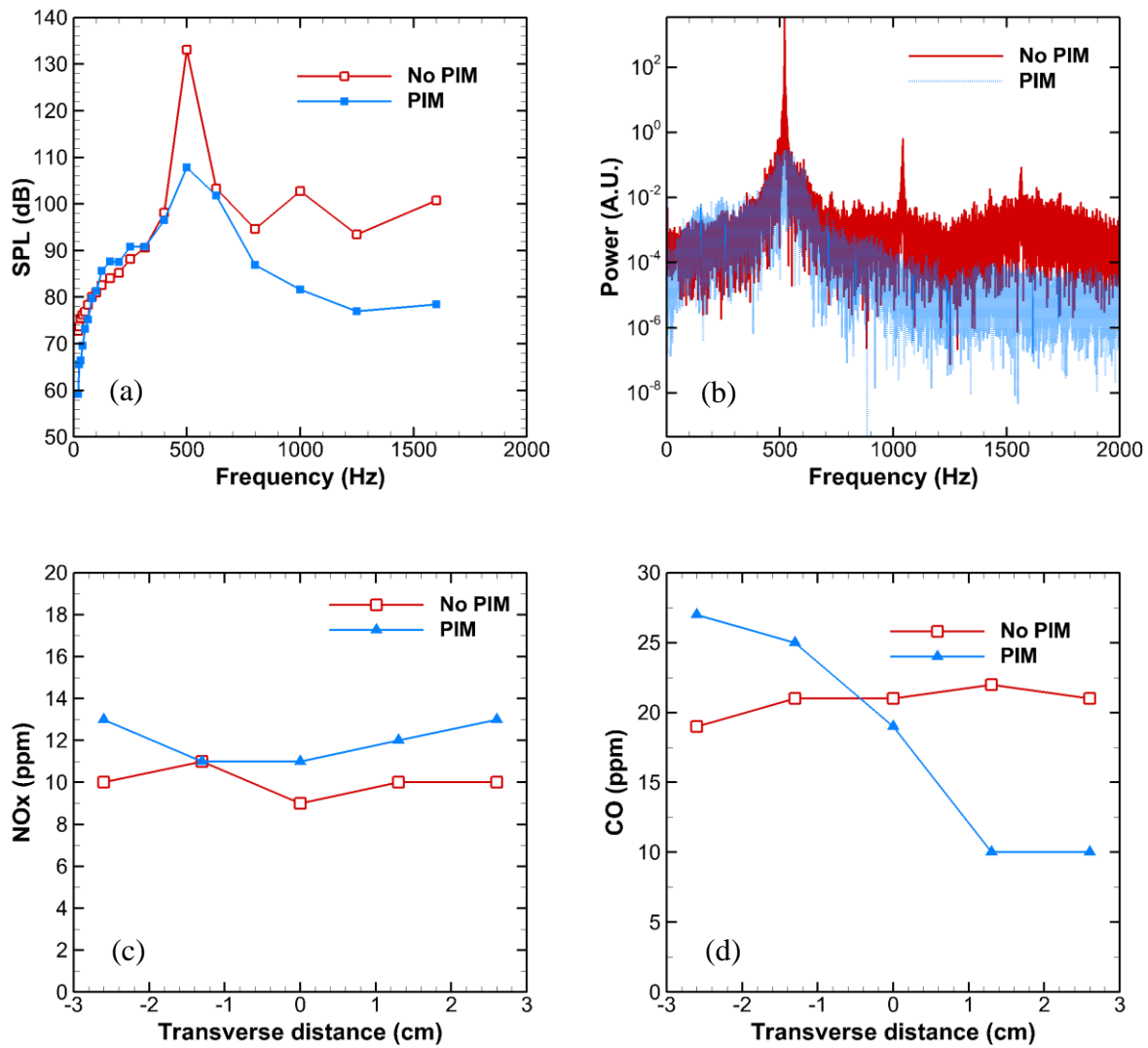


Figure 3.46. Results for  $T_{inlet} = 130^\circ\text{C}$ ,  $Q = 600$  SLPM,  $\phi = 0.70$  (a) SPL per 1/3 octave band, (b) Spectral power, (c) NOx emissions, (d) CO emissions

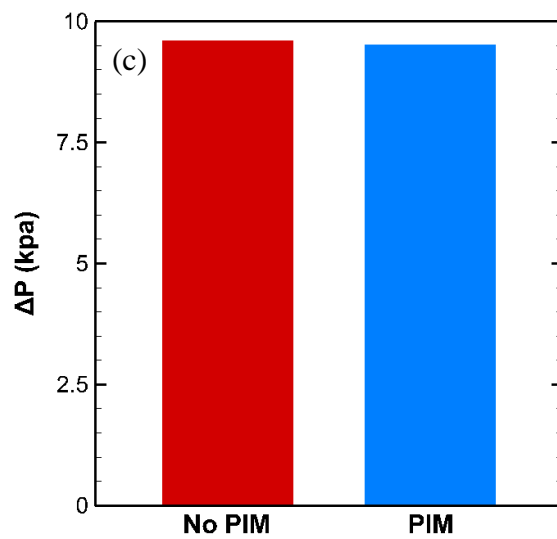
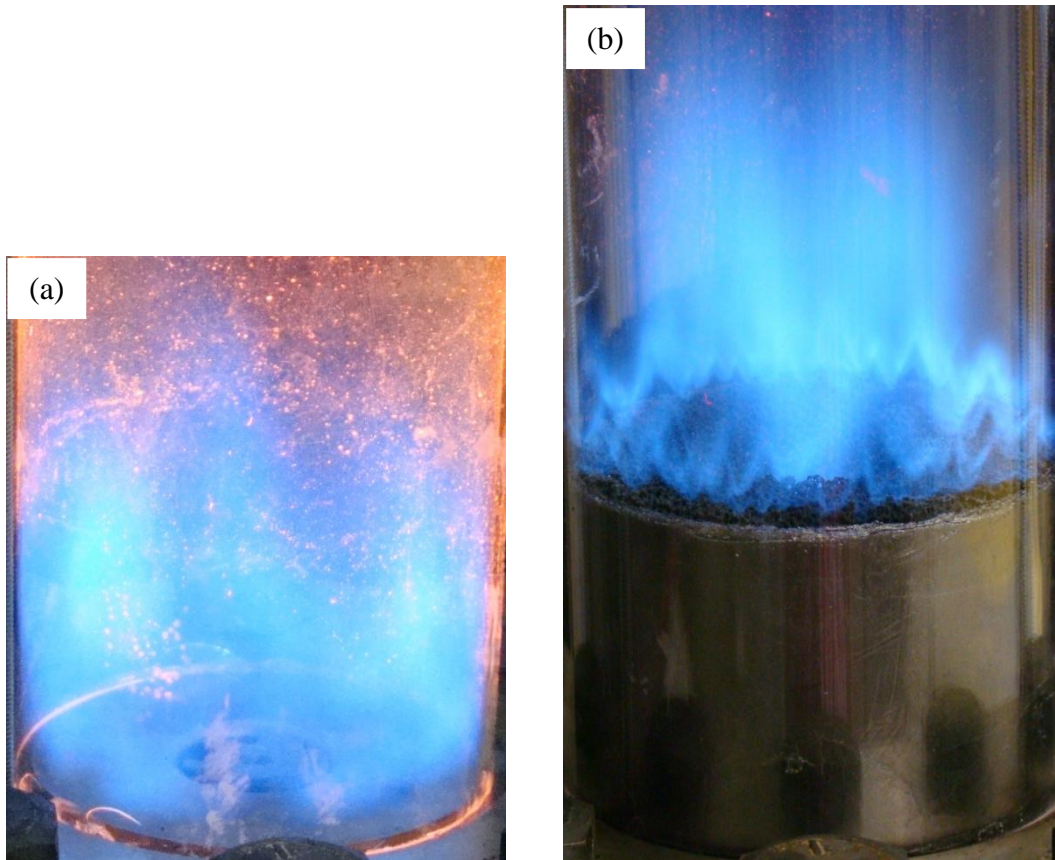


Figure 3.47. Results for  $T_{inlet} = 130^{\circ}C$ ,  $Q = 600$  SLPM,  $\phi = 0.75$  (a) Flame photograph without PIM, (b) Flame photograph with PIM, (c) Pressure drop measurements with and without PIM

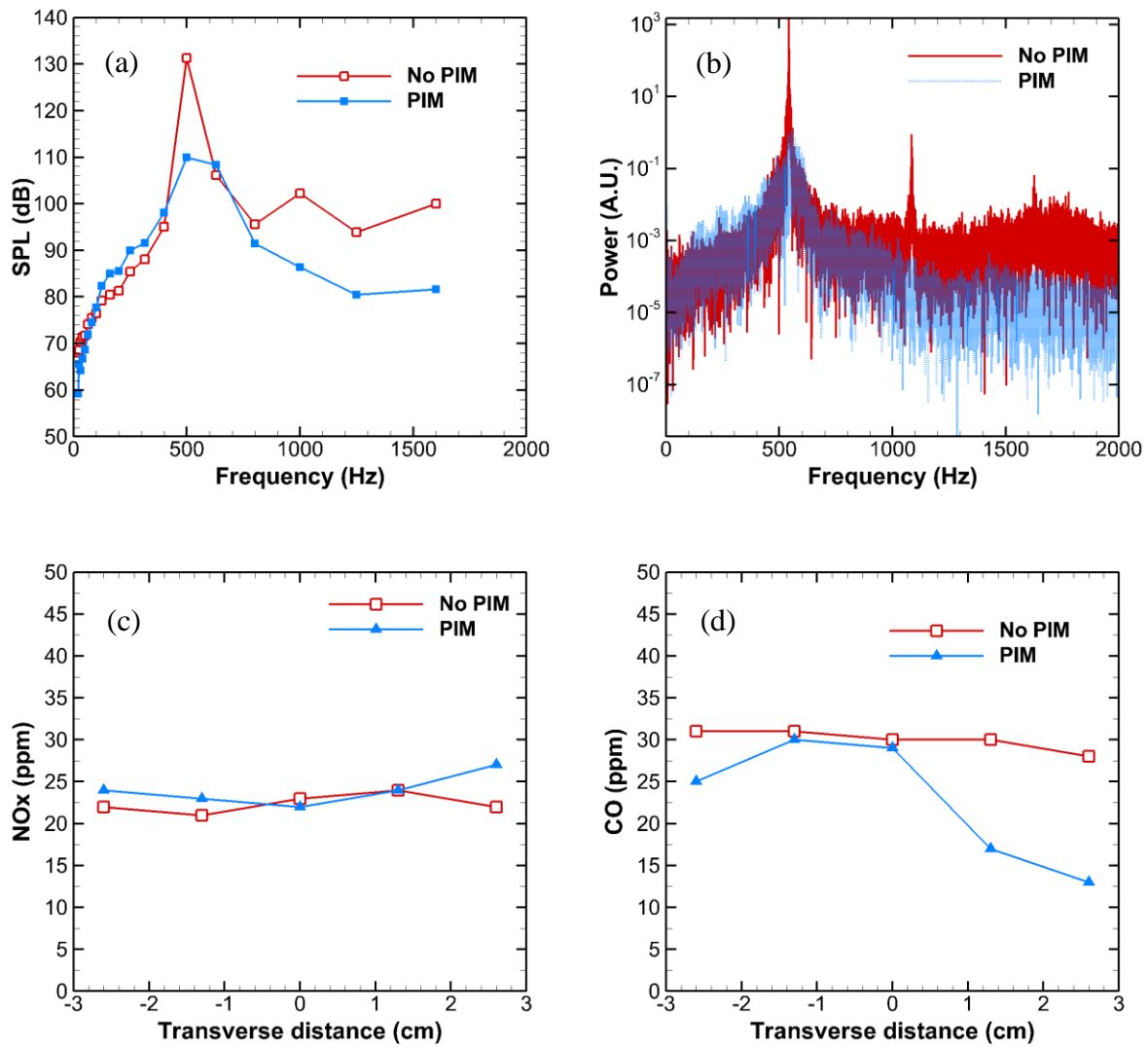


Figure 3.48. Results for  $T_{inlet} = 130^\circ\text{C}$ ,  $Q = 600$  SLPM,  $\phi = 0.75$  (a) SPL per 1/3 octave band, (b) Spectral power, (c) NOx emissions, (d) CO emissions



*Figure 3.49.* Results for  $T_{\text{inlet}} = 130^{\circ}\text{C}$ ,  $Q = 900$  SLPM,  $\phi = 0.60$  (a) Flame photograph without PIM, (b) Flame photograph with PIM

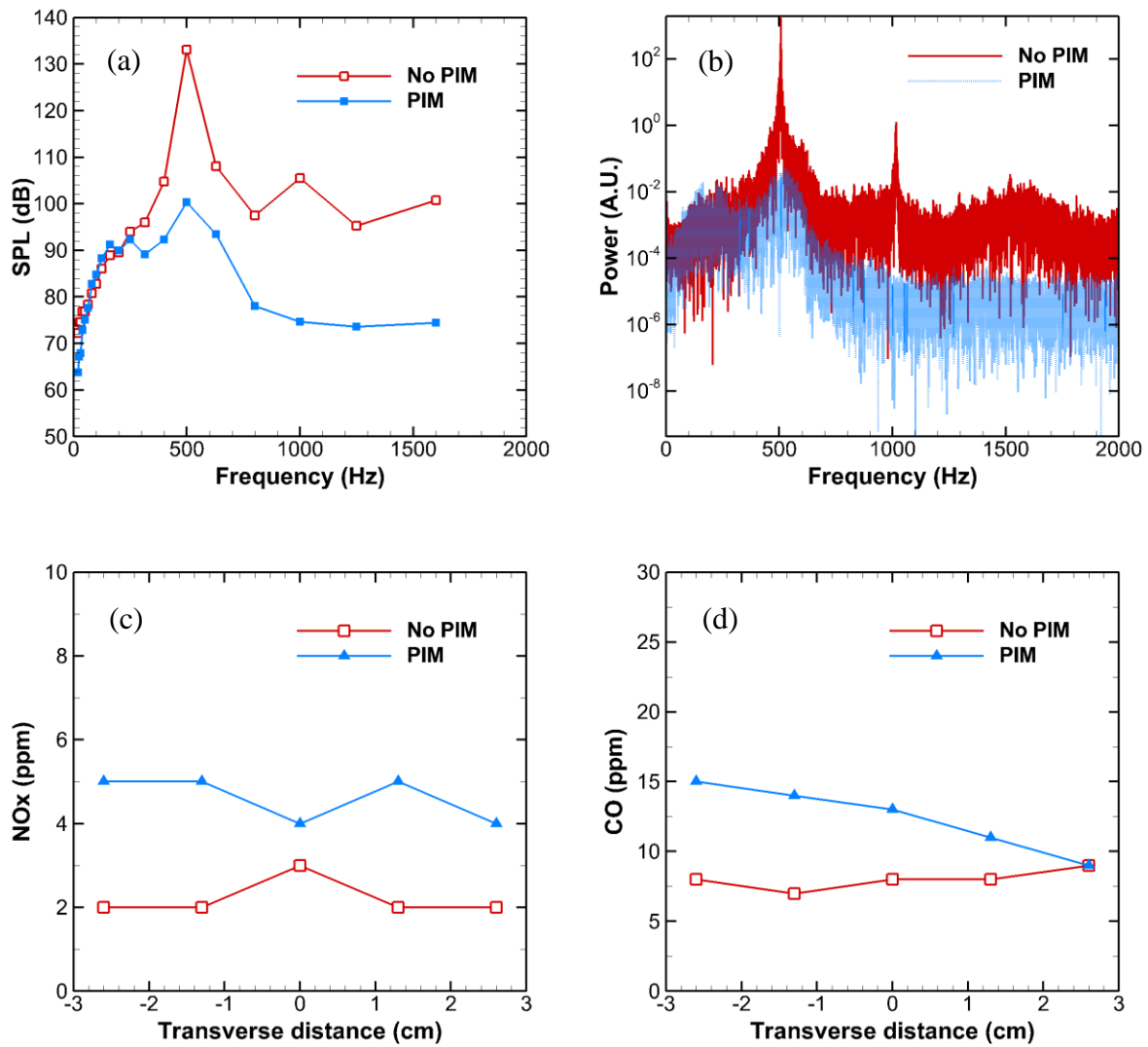
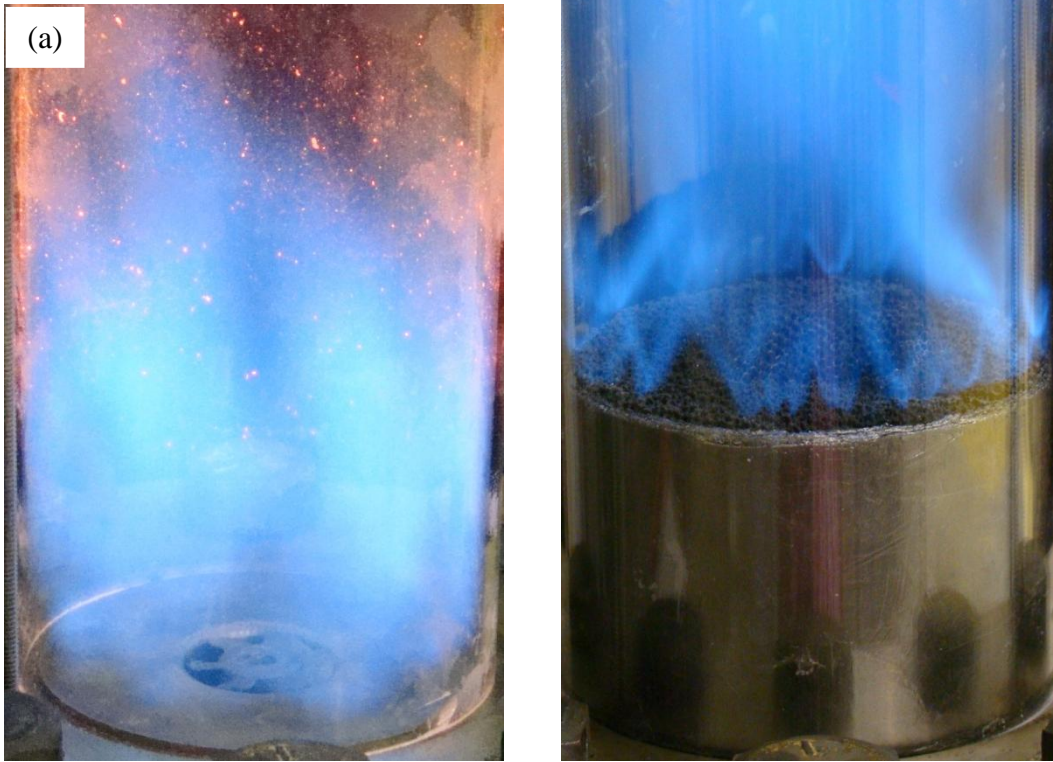


Figure 3.50. Results for  $T_{inlet} = 130^{\circ}\text{C}$ ,  $Q = 900$  SLPM,  $\phi = 0.60$  (a) SPL per 1/3 octave band, (b) Spectral power, (c) NOx emissions, (d) CO emissions



*Figure 3.51.* Results for  $T_{\text{inlet}} = 130^{\circ}\text{C}$ ,  $Q = 900$  SLPM,  $\phi = 0.65$  (a) Flame photograph without PIM, (b) Flame photograph with PIM

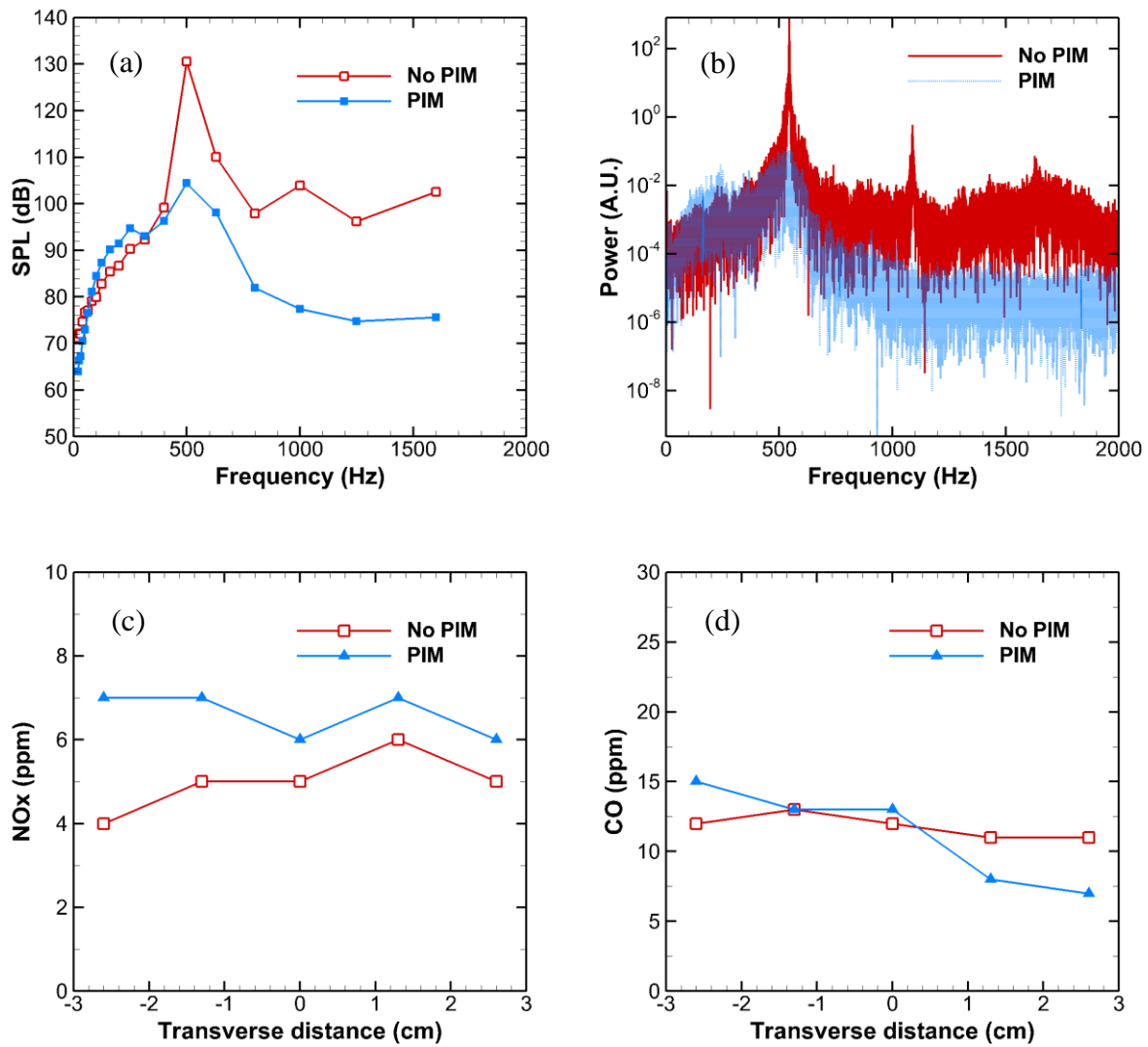
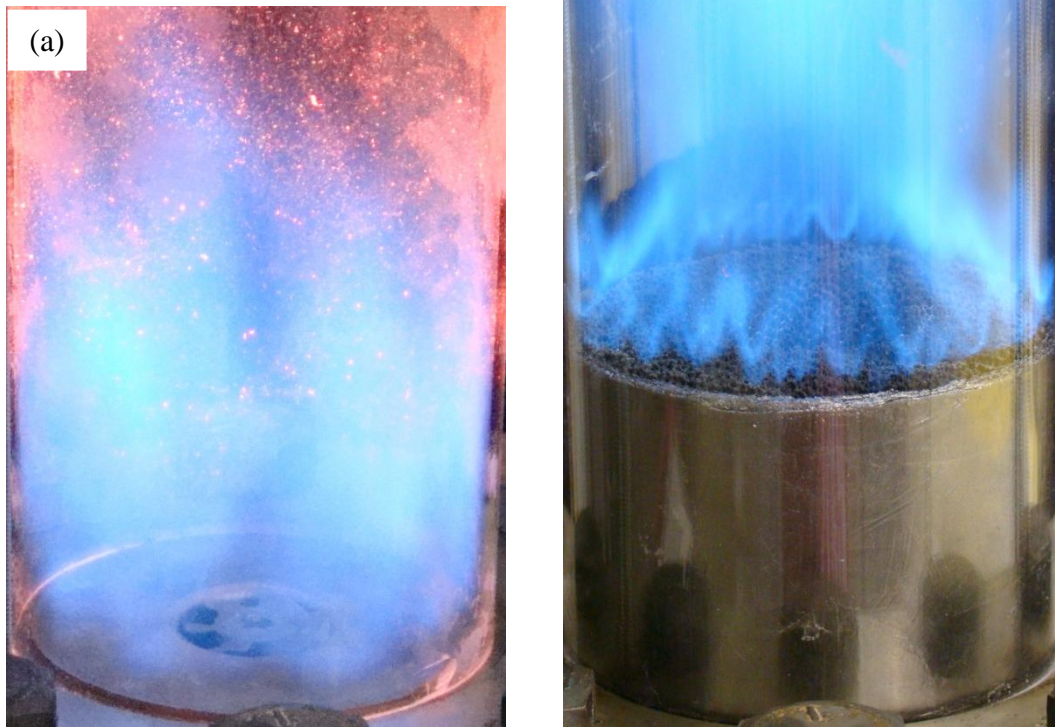


Figure 3.52. Results for  $T_{\text{inlet}} = 130^\circ\text{C}$ ,  $Q = 900$  SLPM,  $\phi = 0.65$  (a) SPL per 1/3 octave band, (b) Spectral power, (c) NOx emissions, (d) CO emissions



*Figure 3.53.* Results for  $T_{\text{inlet}} = 130^{\circ}\text{C}$ ,  $Q = 900$  SLPM,  $\phi = 0.70$  (a) Flame photograph without PIM, (b) Flame photograph with PIM

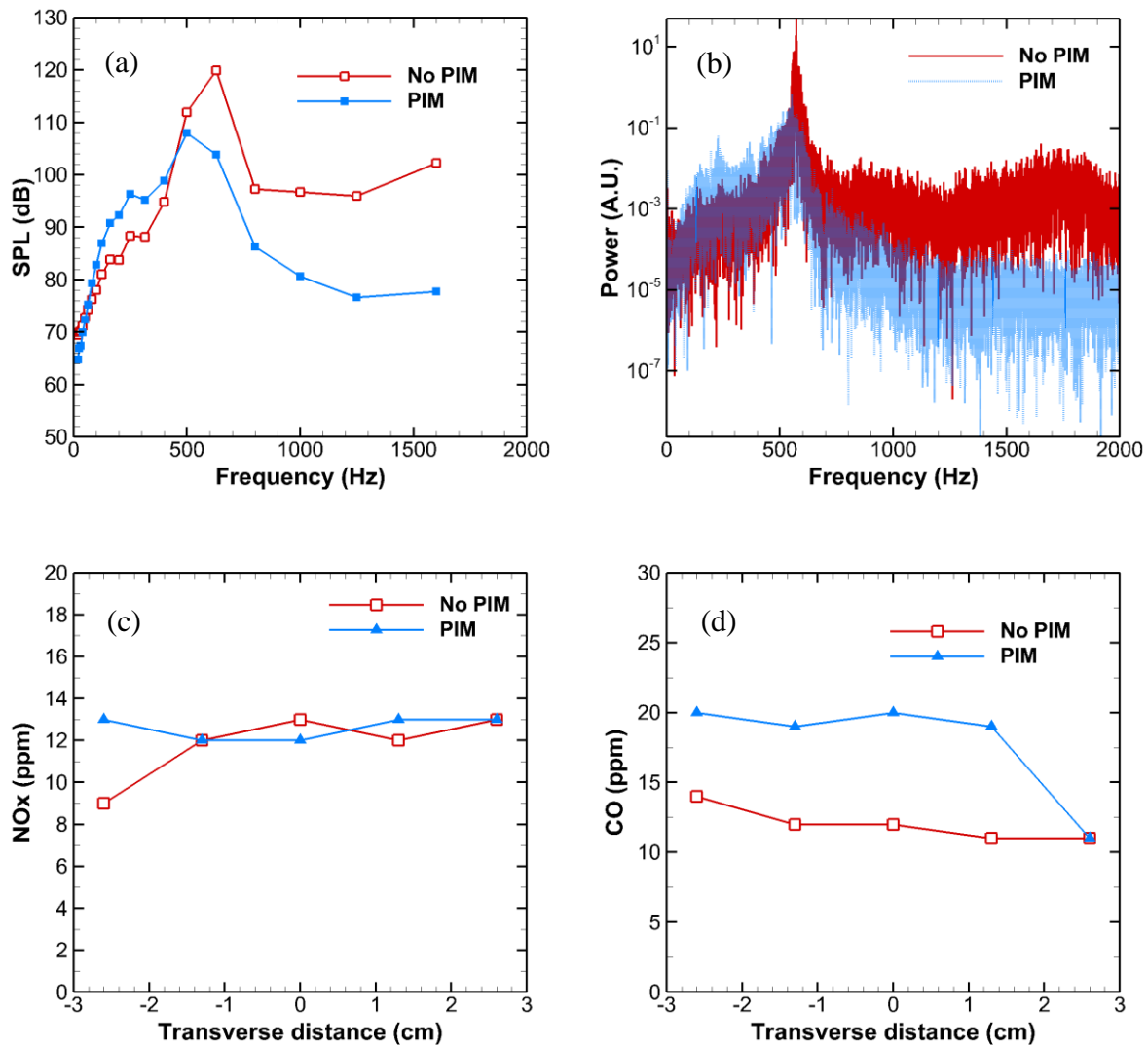
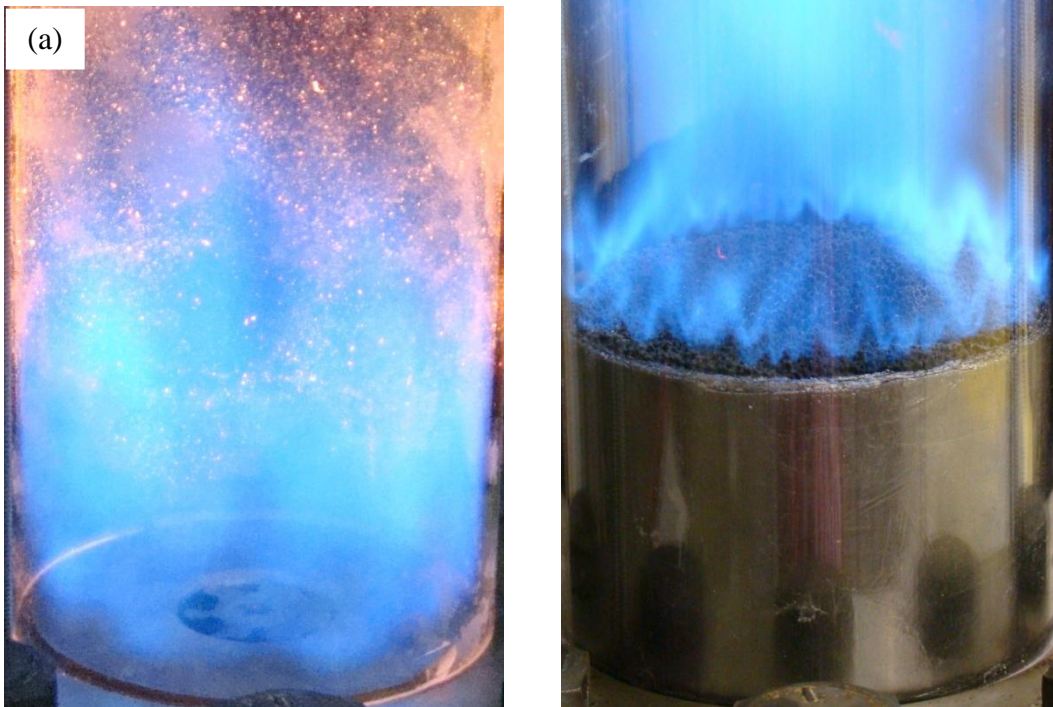


Figure 3.54. Results for  $T_{inlet} = 130^\circ\text{C}$ ,  $Q = 900$  SLPM,  $\phi = 0.70$  (a) SPL per 1/3 octave band, (b) Spectral power, (c) NOx emissions, (d) CO emissions



*Figure 3.55.* Results for  $T_{\text{inlet}} = 130^{\circ}\text{C}$ ,  $Q = 900$  SLPM,  $\phi = 0.75$  (a) Flame photograph without PIM, (b) Flame photograph with PIM

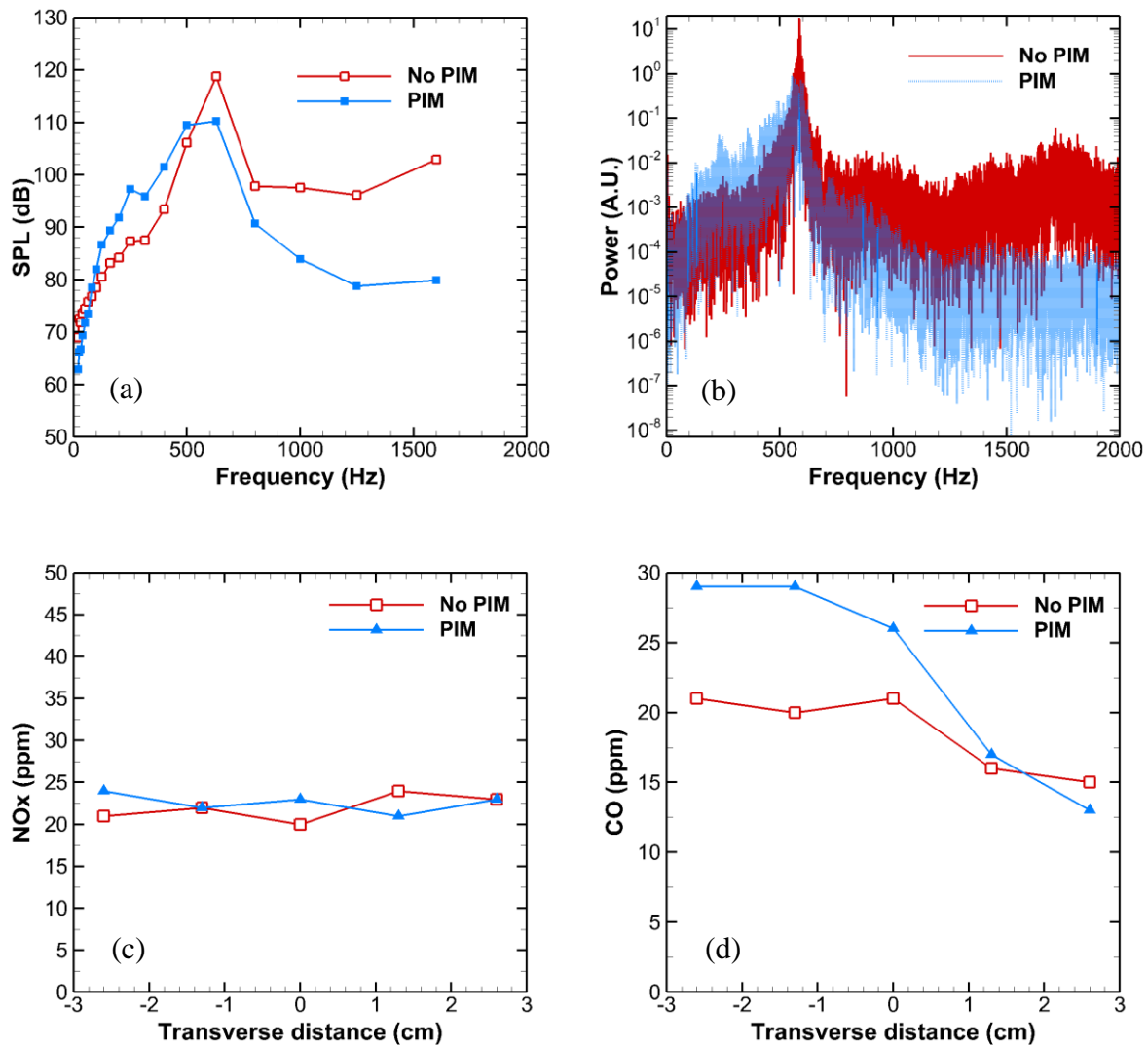


Figure 3.56. Results for  $T_{inlet} = 130^{\circ}\text{C}$ ,  $Q = 900$  SLPM,  $\phi = 0.75$  (a) SPL per 1/3 octave band, (b) Spectral power, (c) NOx emissions, (d) CO emissions

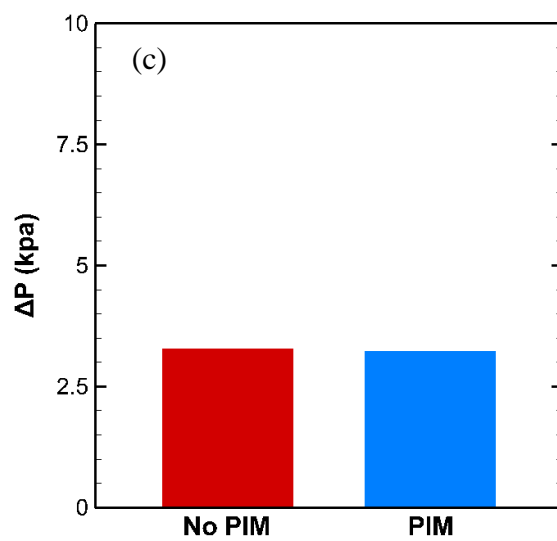
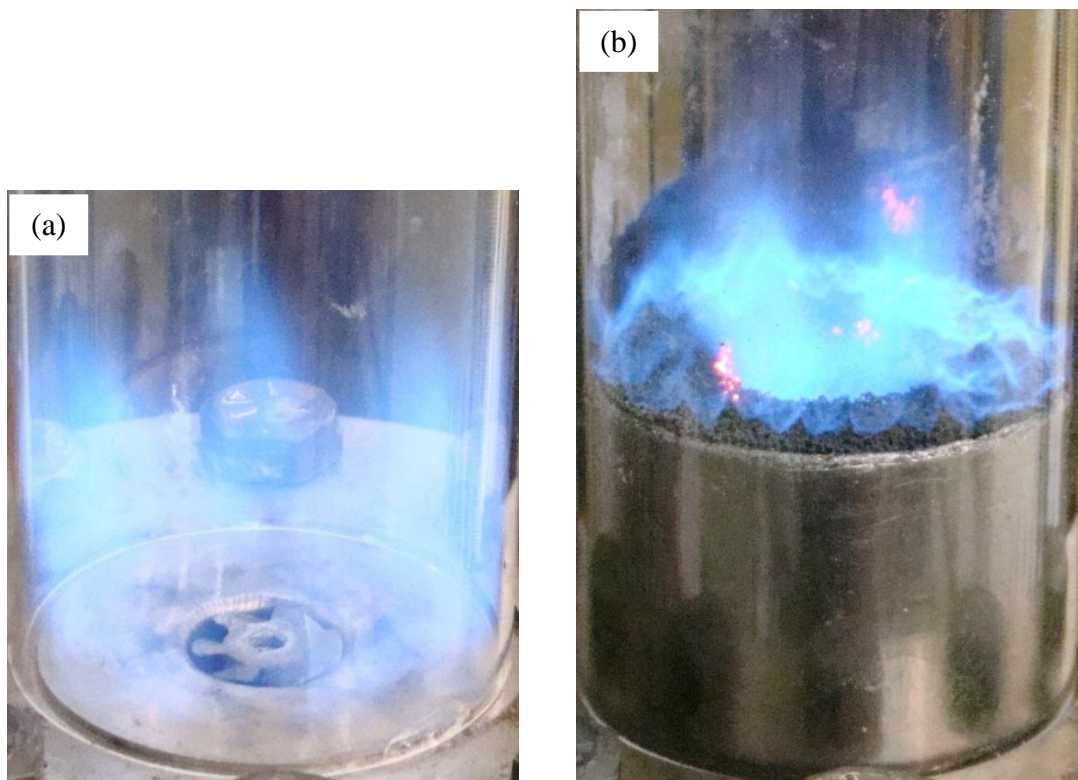


Figure 3.57. Results for  $T_{\text{inlet}} = 260^\circ\text{C}$ ,  $Q = 300$  SLPM,  $\phi = 0.60$  (a) Flame photograph without PIM, (b) Flame photograph with PIM, (c) Pressure drop measurements with and without PIM

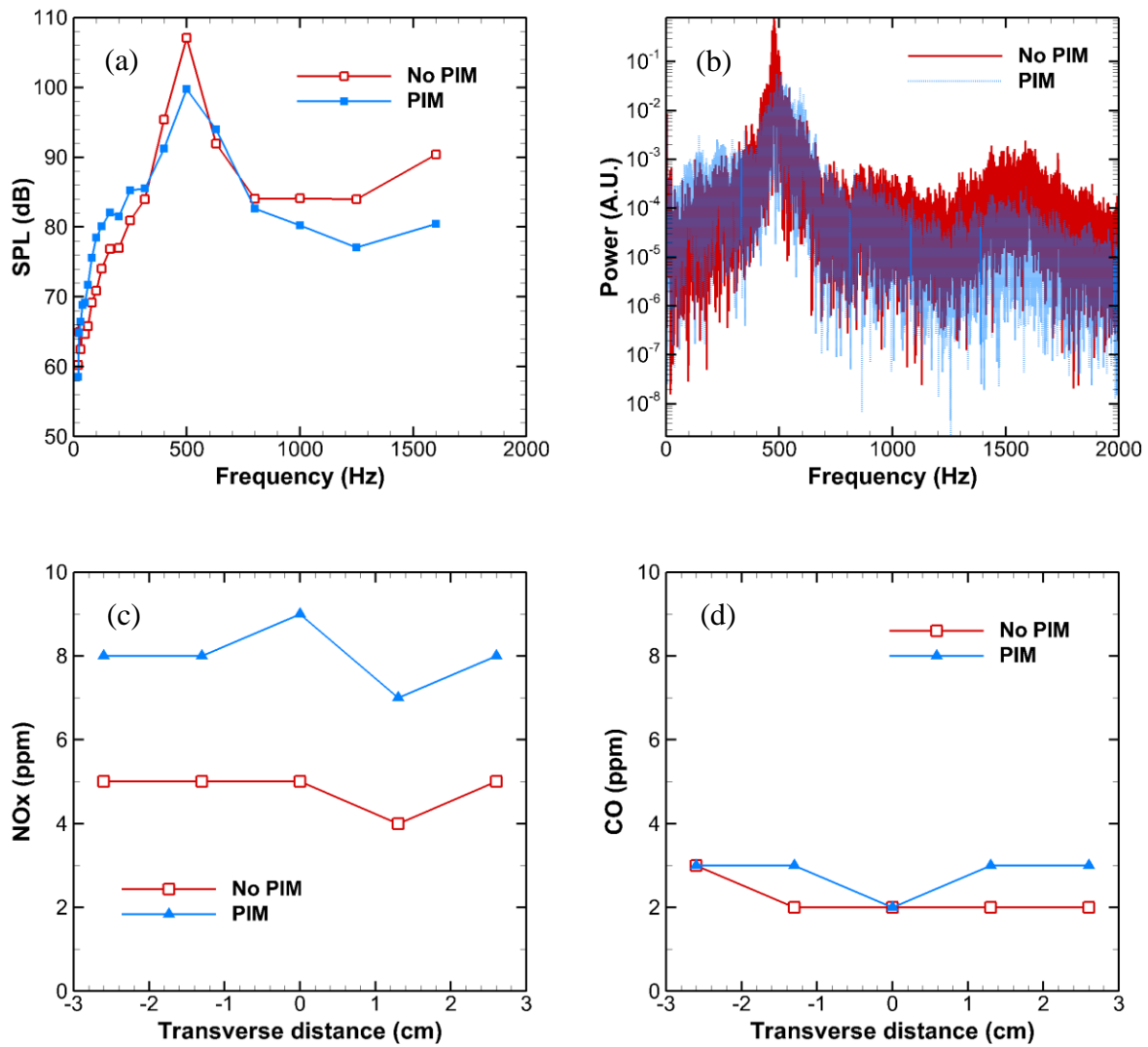


Figure 3.58. Results for  $T_{\text{inlet}} = 260^{\circ}\text{C}$ ,  $Q = 300$  SLPM,  $\phi = 0.60$  (a) SPL per 1/3 octave band, (b) Spectral power, (c) NOx emissions, (d) CO emissions

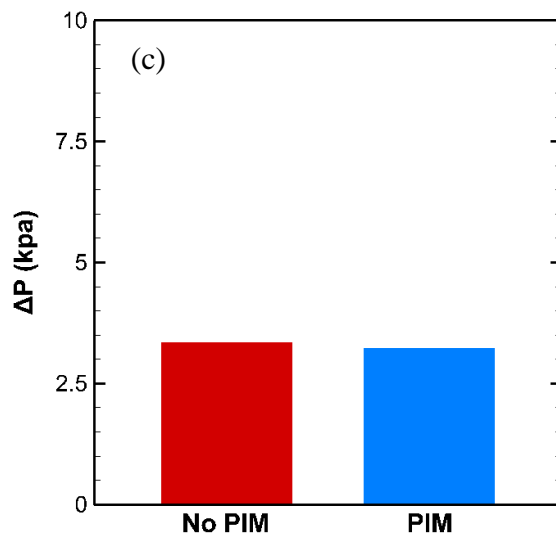
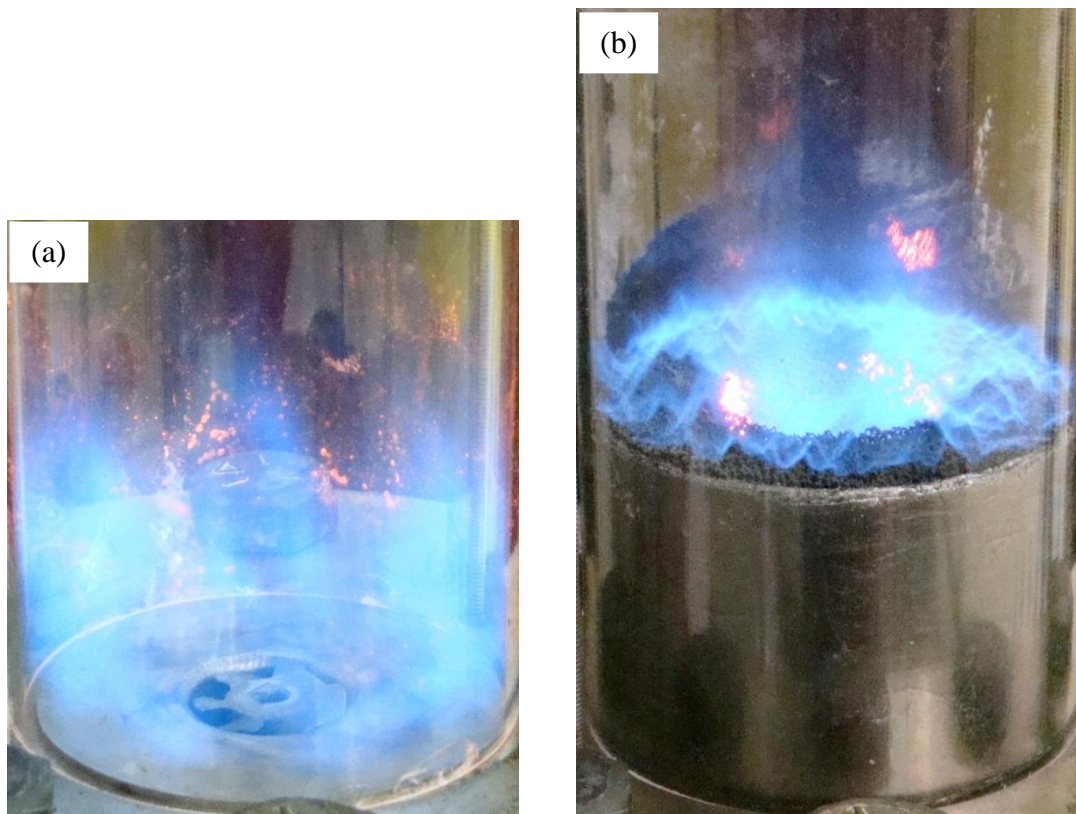


Figure 3.59. Results for  $T_{\text{inlet}} = 260^{\circ}\text{C}$ ,  $Q = 300$  SLPM,  $\phi = 0.65$  (a) Flame photograph without PIM, (b) Flame photograph with PIM, (c) Pressure drop measurements with and without PIM

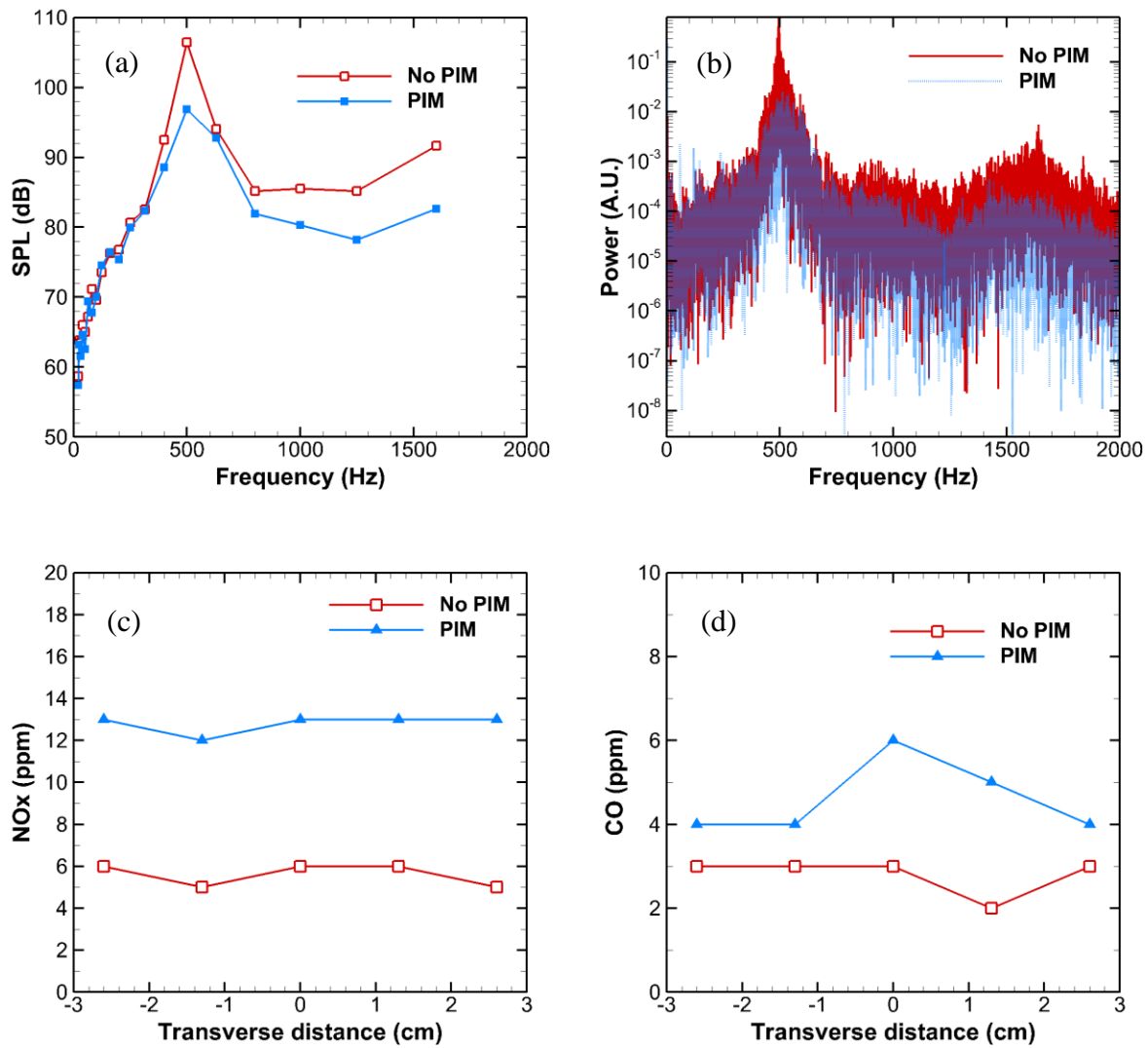


Figure 3.60. Results for  $T_{\text{inlet}} = 260^{\circ}\text{C}$ ,  $Q = 300$  SLPM,  $\phi = 0.65$  (a) SPL per 1/3 octave band, (b) Spectral power, (c) NOx emissions, (d) CO emissions

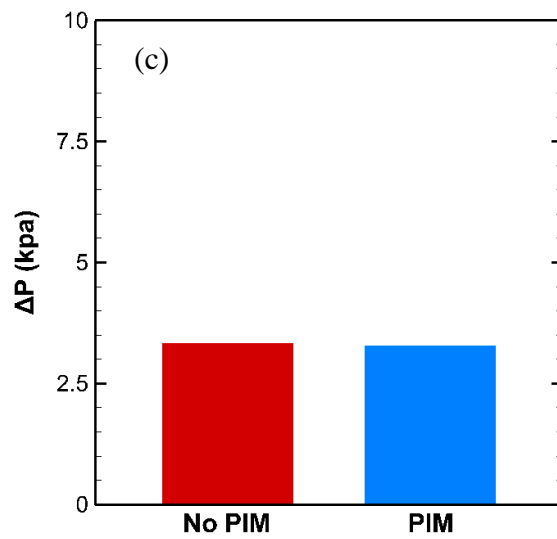
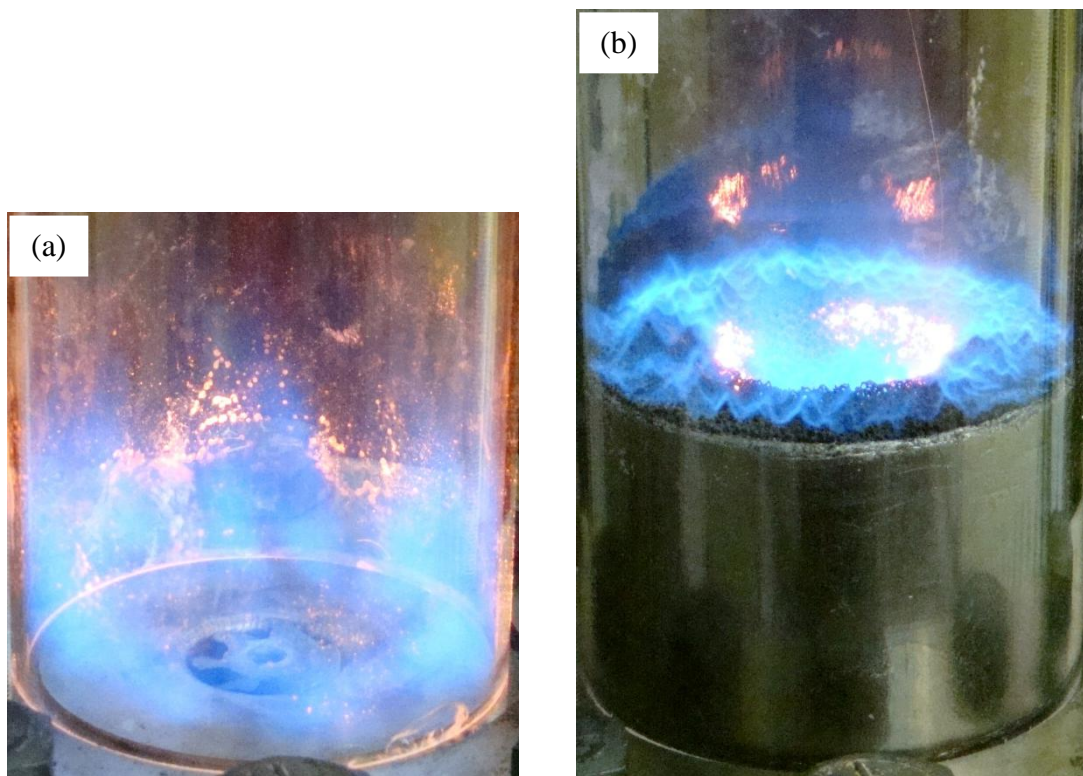


Figure 3.61. Results for  $T_{inlet} = 260^{\circ}\text{C}$ ,  $Q = 300$  SLPM,  $\phi = 0.70$  (a) Flame photograph without PIM, (b) Flame photograph with PIM, (c) Pressure drop measurements with and without PIM

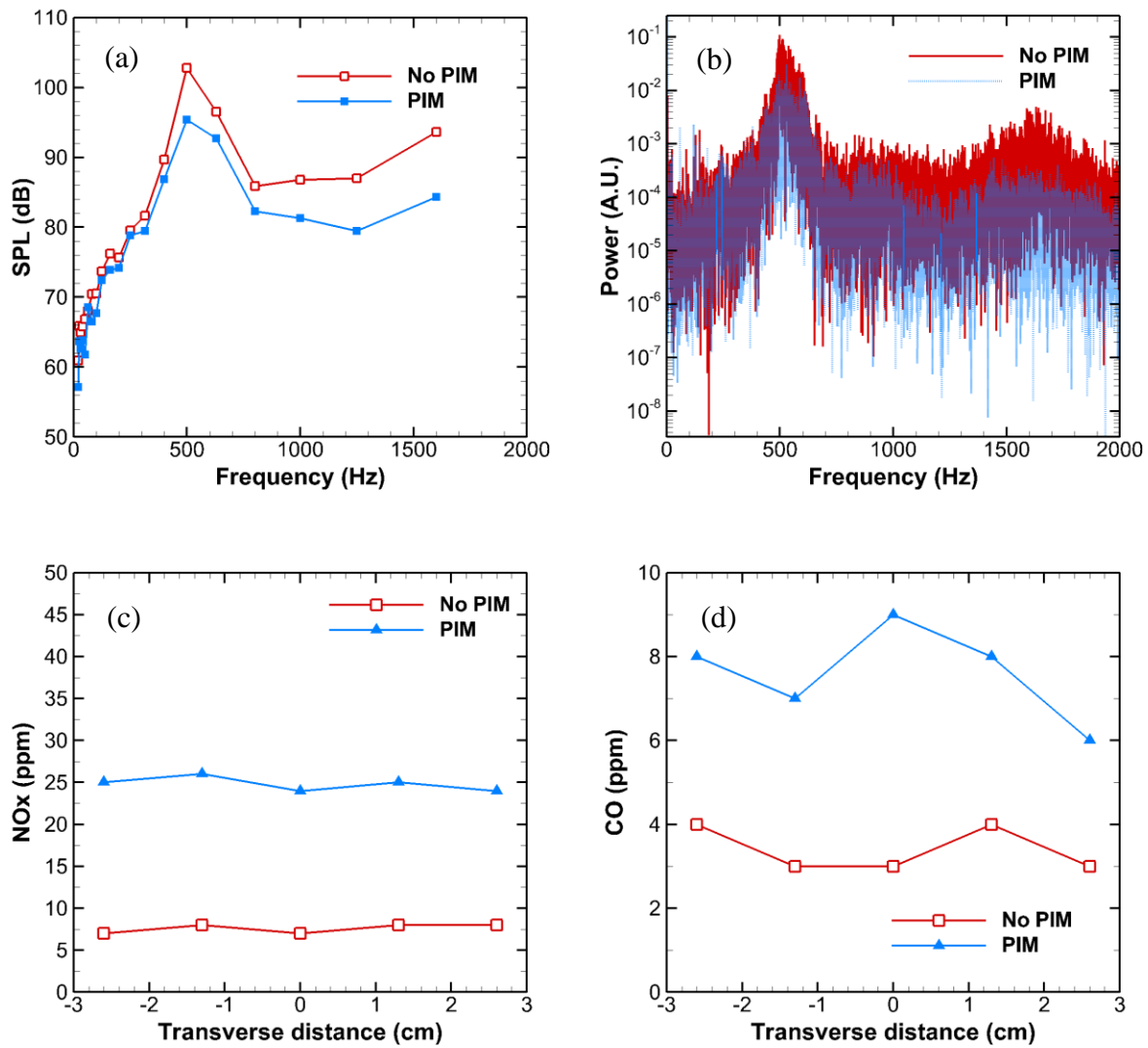


Figure 3.62. Results for  $T_{inlet} = 260^\circ\text{C}$ ,  $Q = 300$  SLPM,  $\phi = 0.70$  (a) SPL per 1/3 octave band, (b) Spectral power, (c) NOx emissions, (d) CO emissions

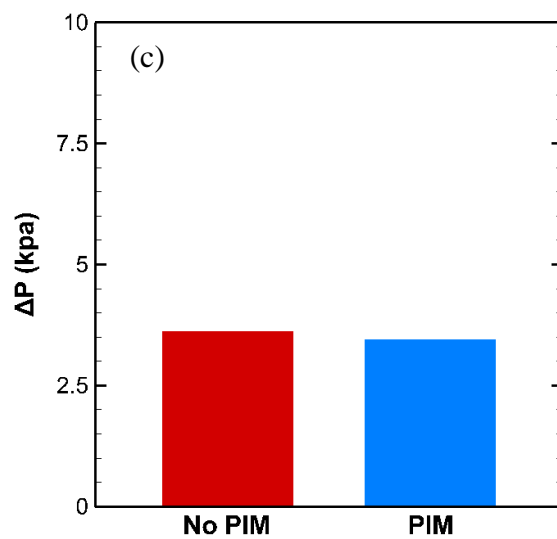
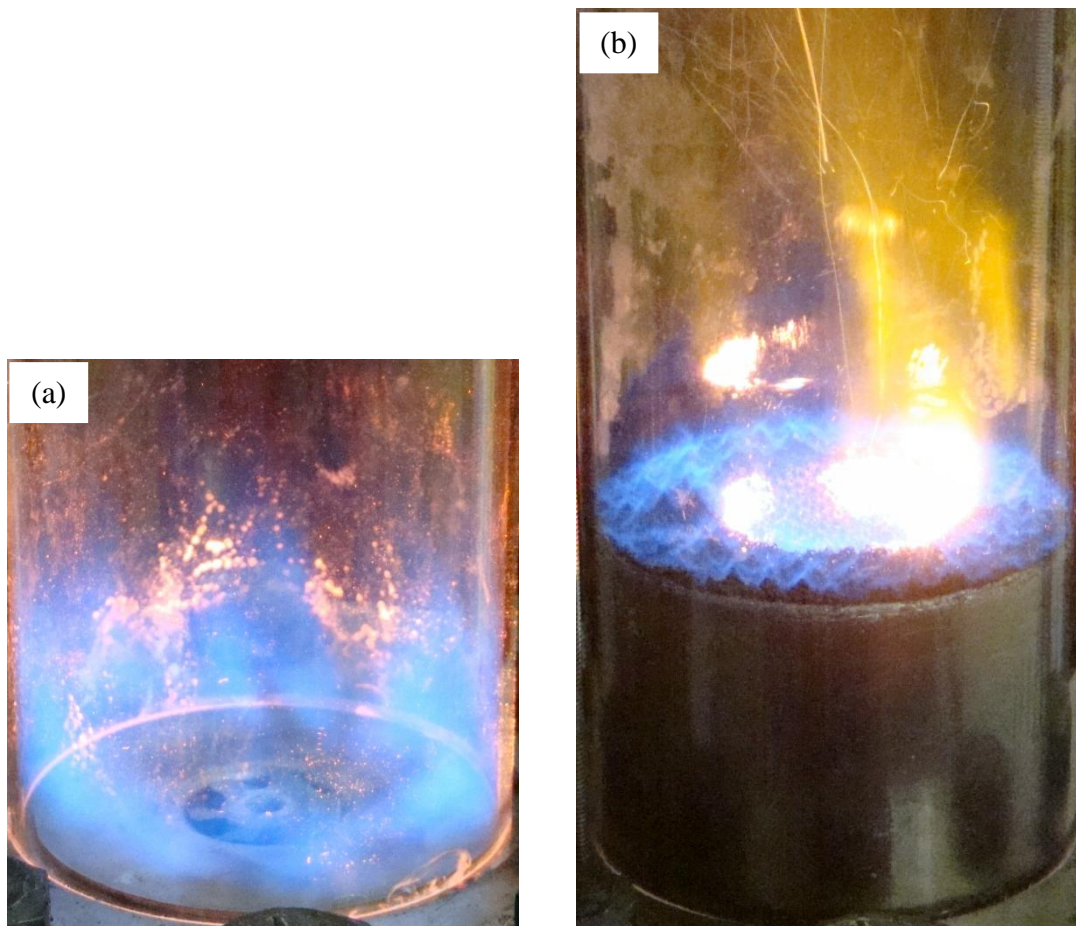


Figure 3.63. Results for  $T_{inlet} = 260^{\circ}\text{C}$ ,  $Q = 300$  SLPM,  $\phi = 0.75$  (a) Flame photograph without PIM, (b) Flame photograph with PIM, (c) Pressure drop measurements with and without PIM

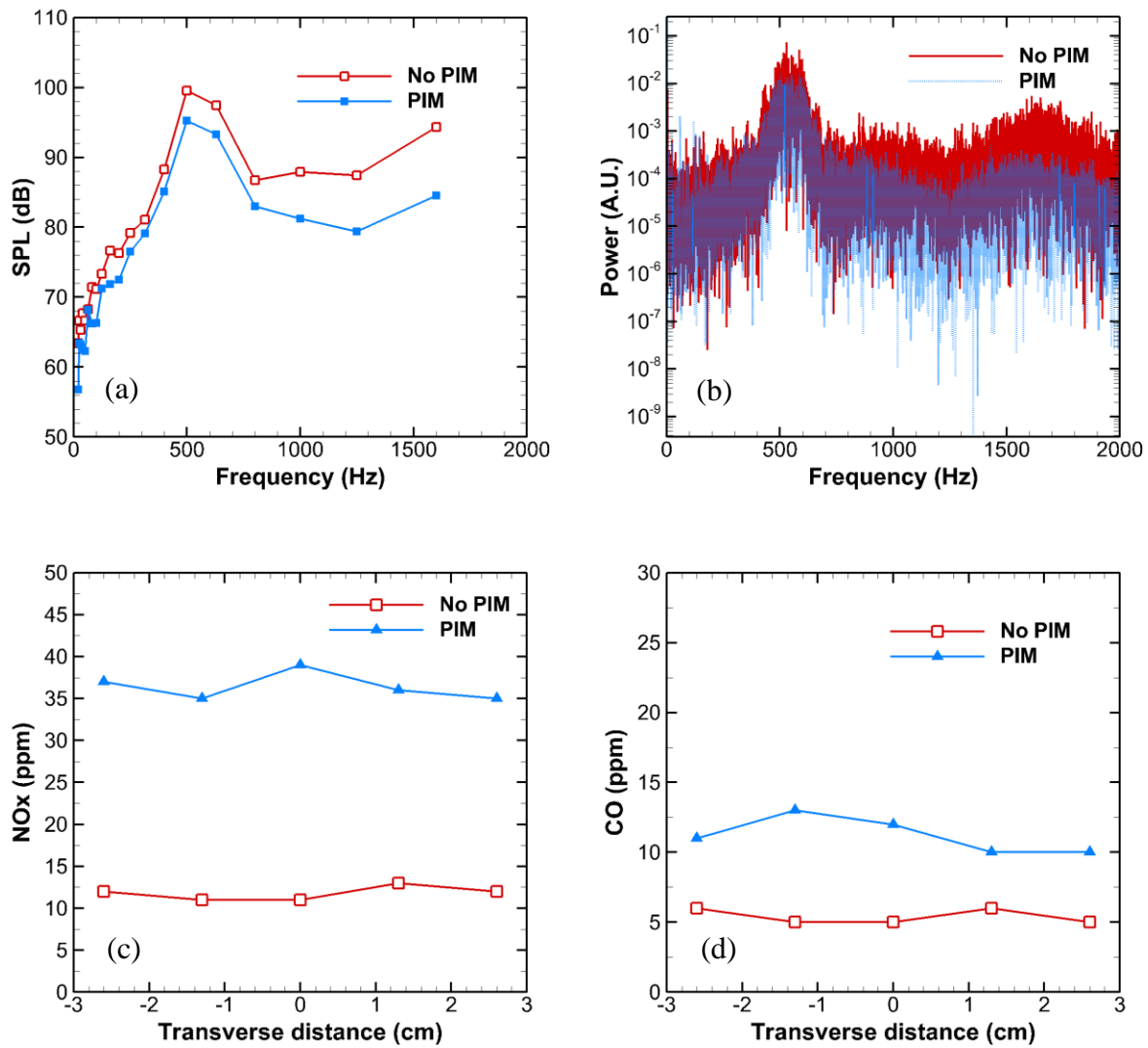


Figure 3.64. Results for  $T_{inlet} = 260^\circ\text{C}$ ,  $Q = 300$  SLPM,  $\phi = 0.75$  (a) SPL per 1/3 octave band, (b) Spectral power, (c) NOx emissions, (d) CO emissions

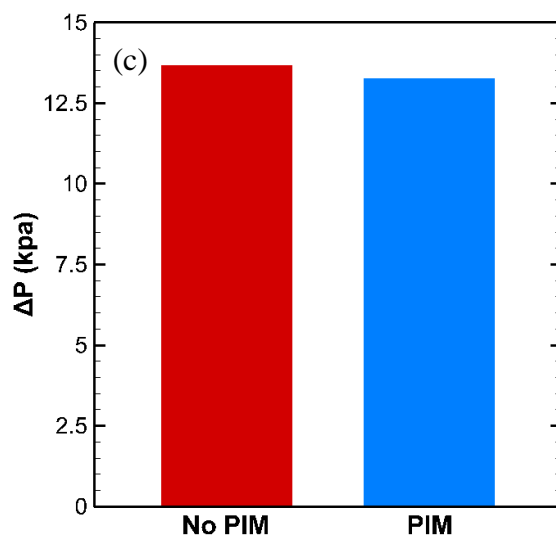
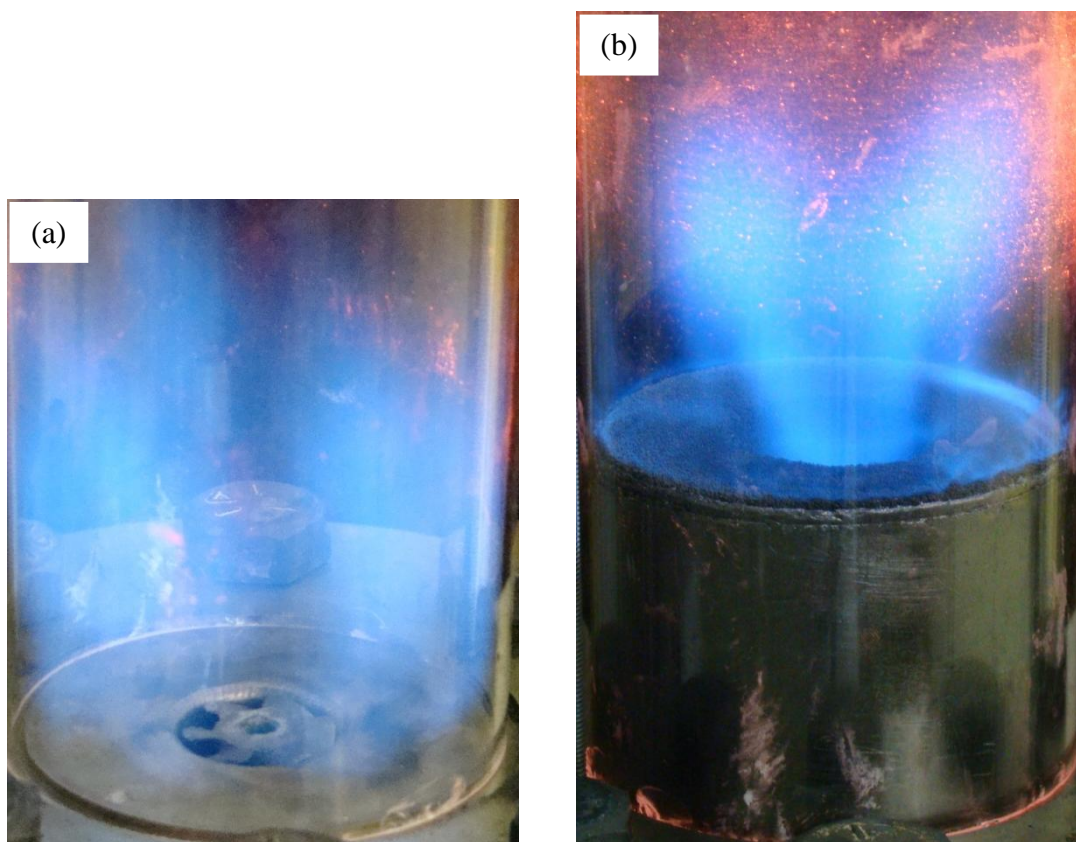


Figure 3.65. Results for  $T_{\text{inlet}} = 260^{\circ}\text{C}$ ,  $Q = 600$  SLPM,  $\phi = 0.60$  (a) Flame photograph without PIM, (b) Flame photograph with PIM, (c) Pressure drop measurements with and without PIM

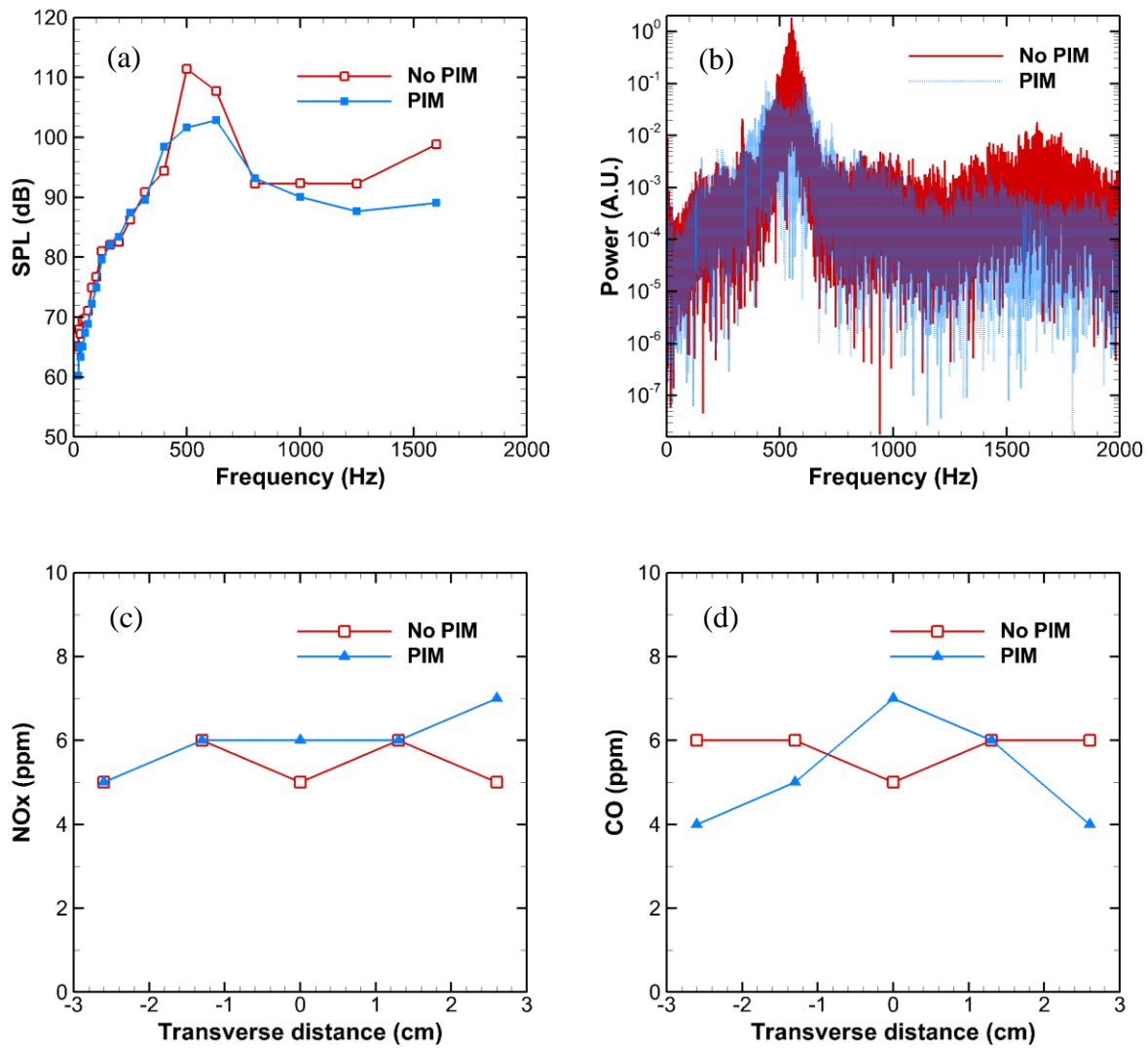


Figure 3.66. Results for  $T_{inlet} = 260^\circ\text{C}$ ,  $Q = 600$  SLPM,  $\phi = 0.60$  (a) SPL per 1/3 octave band, (b) Spectral power, (c) NOx emissions, (d) CO emissions

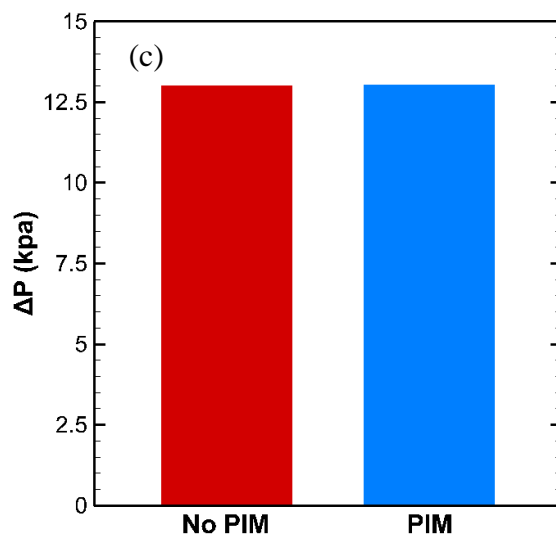
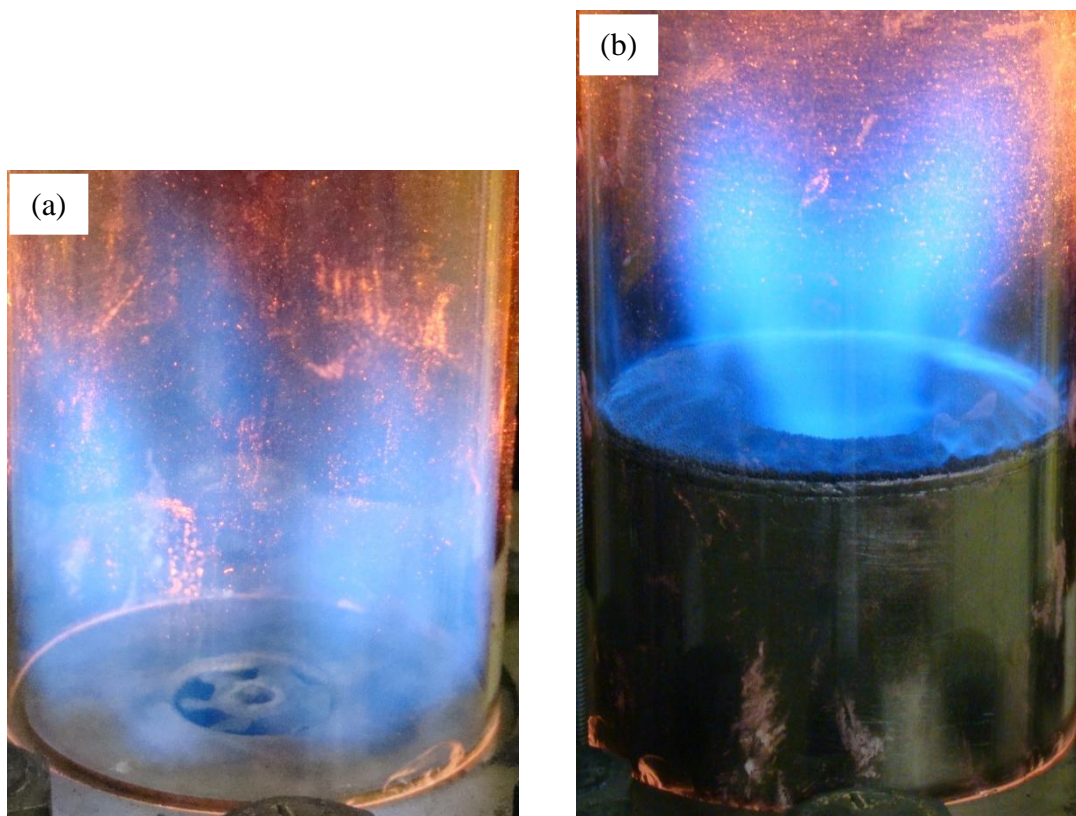


Figure 3.67. Results for  $T_{inlet} = 260^{\circ}C$ ,  $Q = 600$  SLPM,  $\phi = 0.65$  (a) Flame photograph without PIM, (b) Flame photograph with PIM, (c) Pressure drop measurements with and without PIM

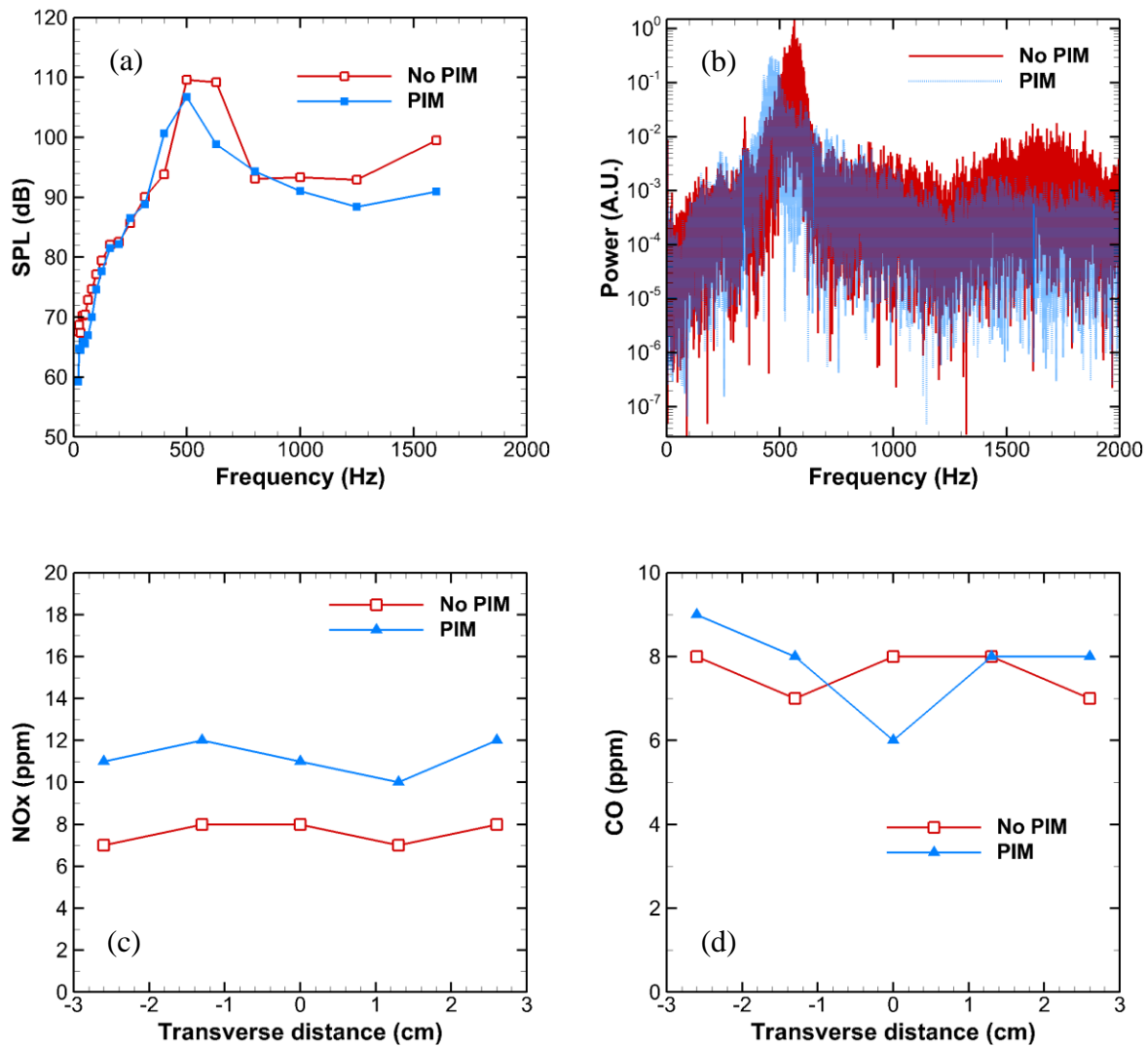


Figure 3.68. Results for  $T_{inlet} = 260^{\circ}\text{C}$ ,  $Q = 600$  SLPM,  $\phi = 0.65$  (a) SPL per 1/3 octave band, (b) Spectral power, (c) NOx emissions, (d) CO emissions

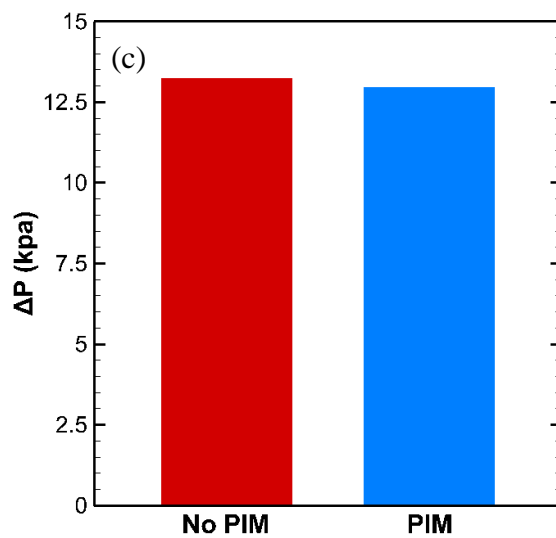
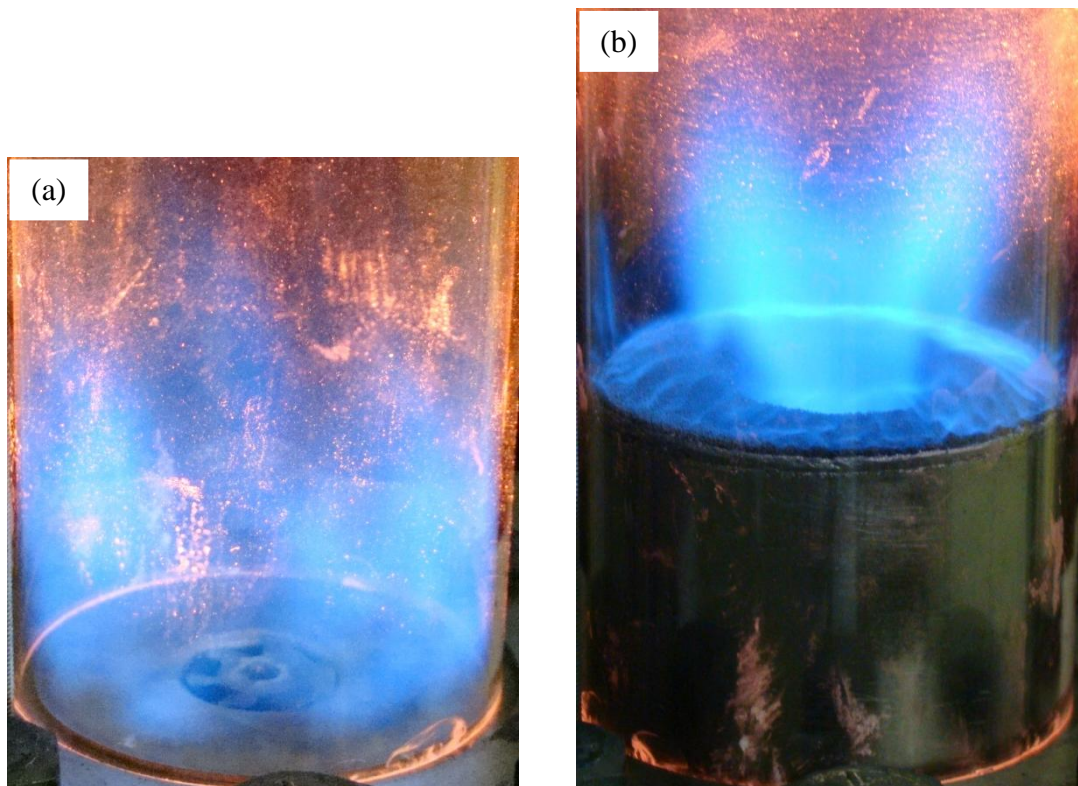


Figure 3.69. Results for  $T_{\text{inlet}} = 260^{\circ}\text{C}$ ,  $Q = 600$  SLPM,  $\phi = 0.70$  (a) Flame photograph without PIM, (b) Flame photograph with PIM, (c) Pressure drop measurements with and without PIM

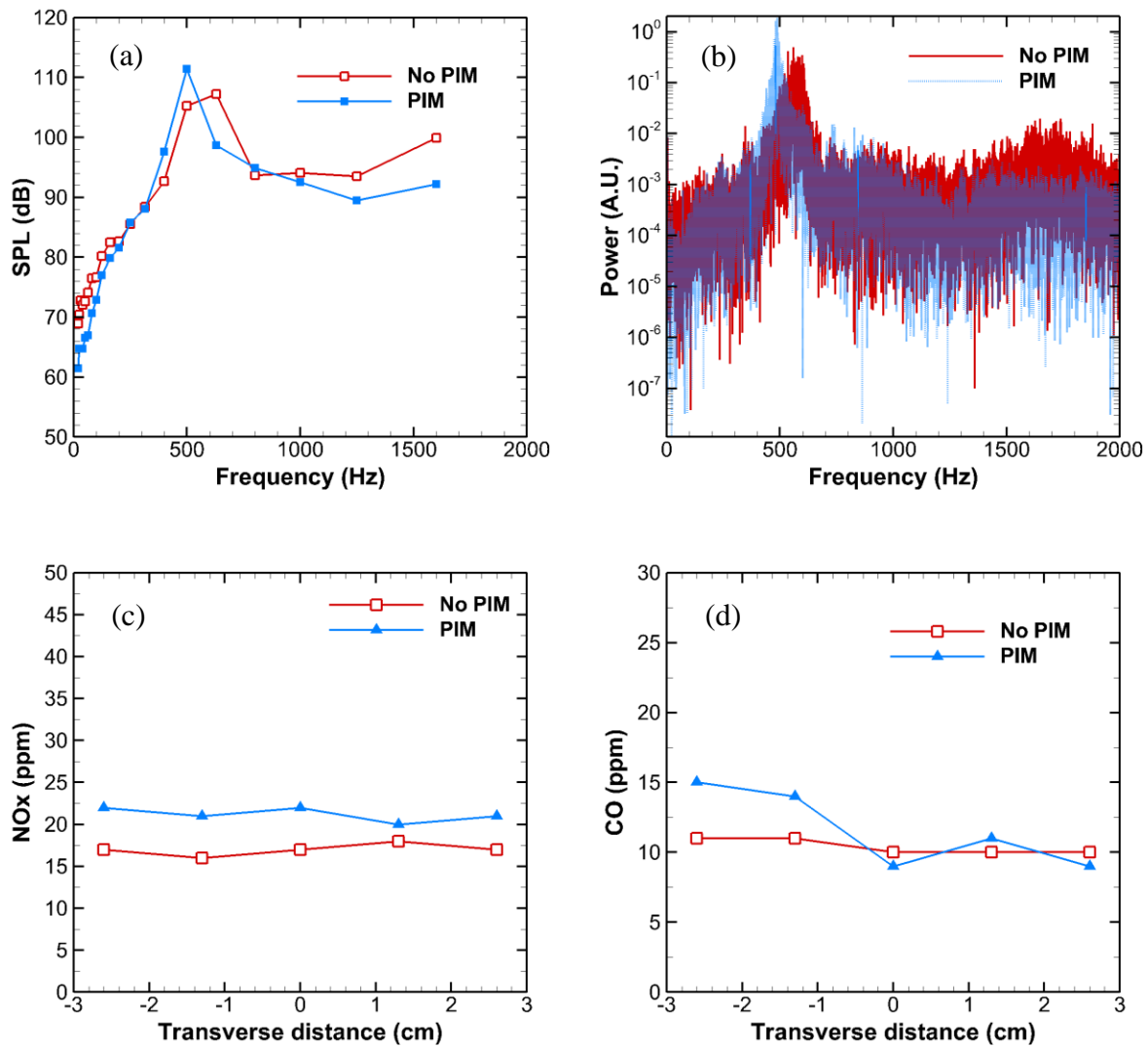


Figure 3.70. Results for  $T_{\text{inlet}} = 260^{\circ}\text{C}$ ,  $Q = 600$  SLPM,  $\phi = 0.70$  (a) SPL per 1/3 octave band, (b) Spectral power, (c) NOx emissions, (d) CO emissions

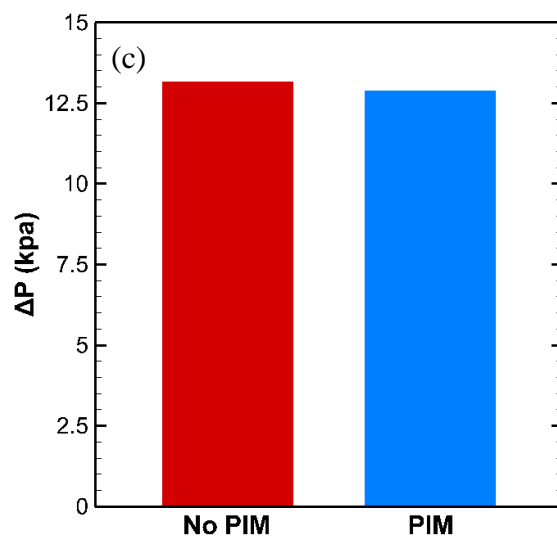
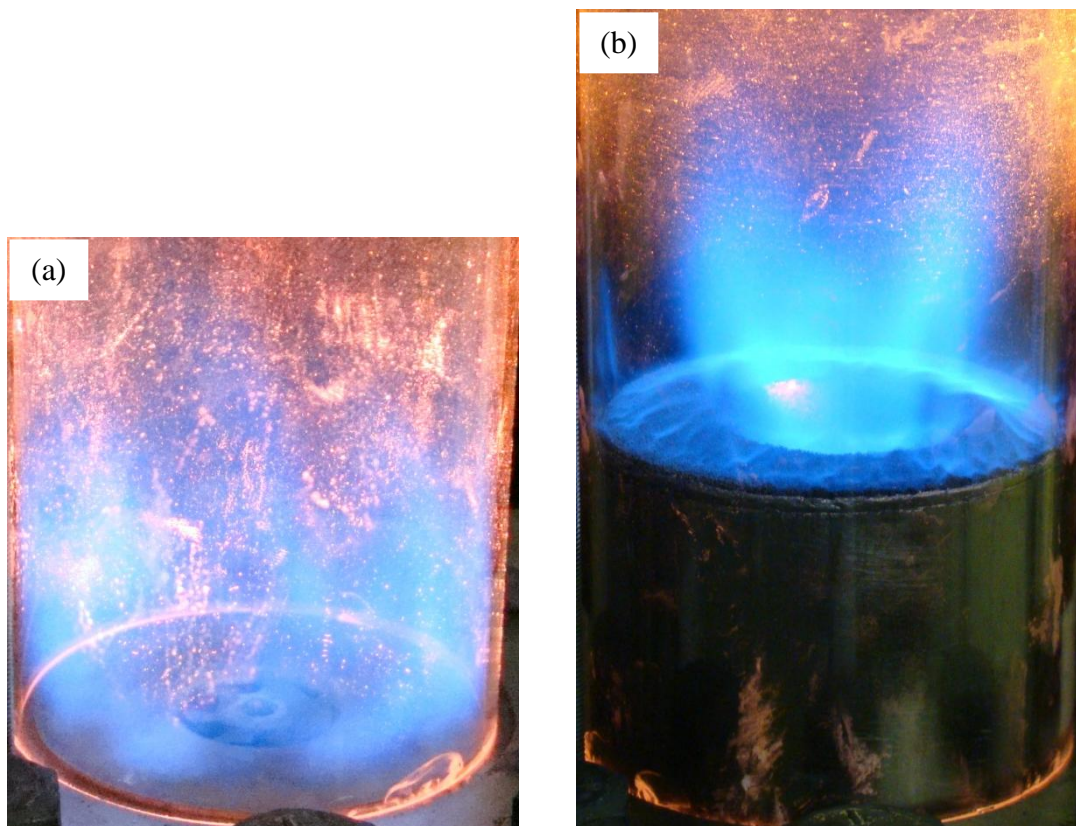


Figure 3.71. Results for  $T_{\text{inlet}} = 260^{\circ}\text{C}$ ,  $Q = 600$  SLPM,  $\phi = 0.75$  (a) Flame photograph without PIM, (b) Flame photograph with PIM, (c) Pressure drop measurements with and without PIM

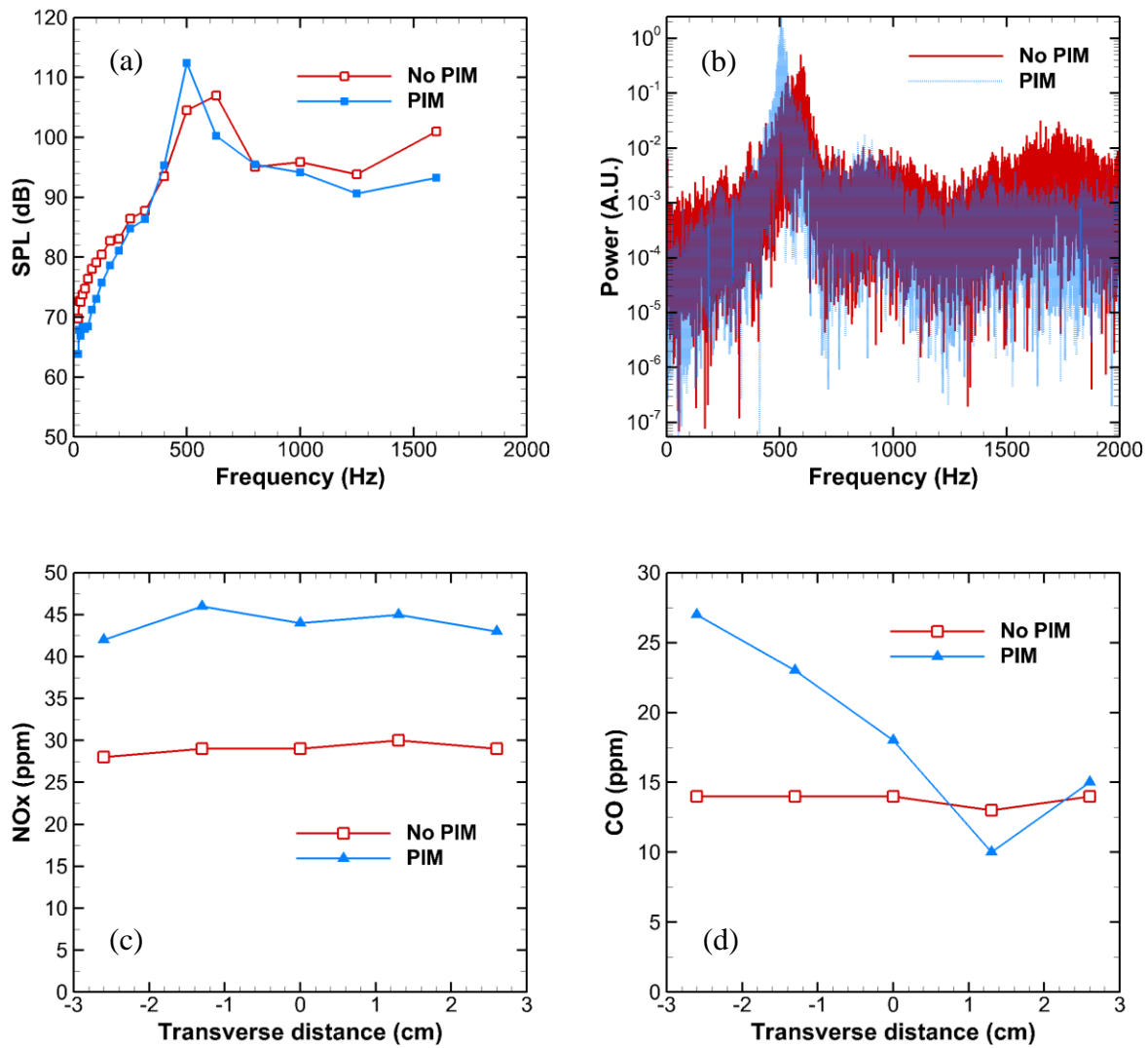


Figure 3.72. Results for  $T_{\text{inlet}} = 260^\circ\text{C}$ ,  $Q = 600$  SLPM,  $\phi = 0.75$  (a) SPL per 1/3 octave band, (b) Spectral power, (c) NOx emissions, (d) CO emissions

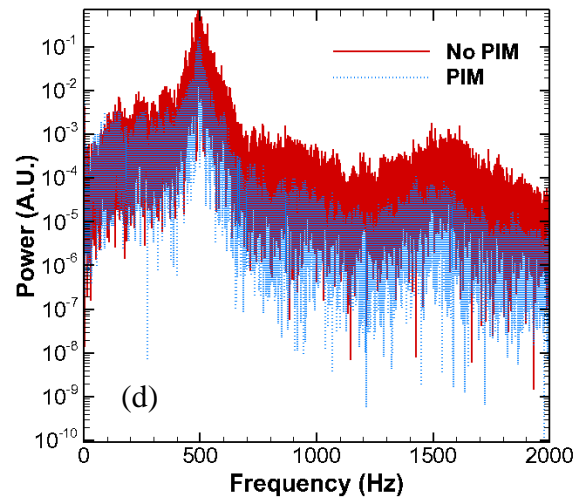
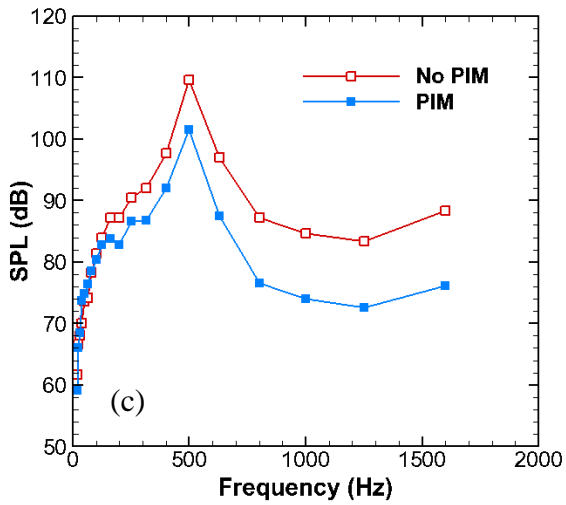


Figure 3.73. Results for flush mounted swirler,  $T_{inlet} = 21^{\circ}\text{C}$ ,  $Q = 600$  SLPM,  $\phi = 0.60$  (a) Flame photograph without PIM, (b) Flame photograph with PIM, (c) SPL per 1/3 octave band, (d) Spectral power

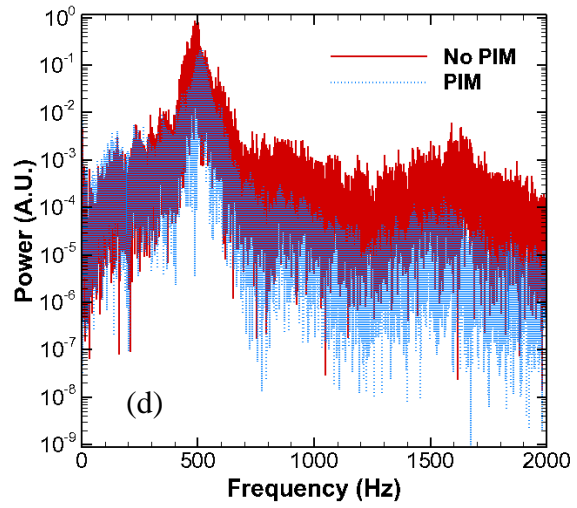
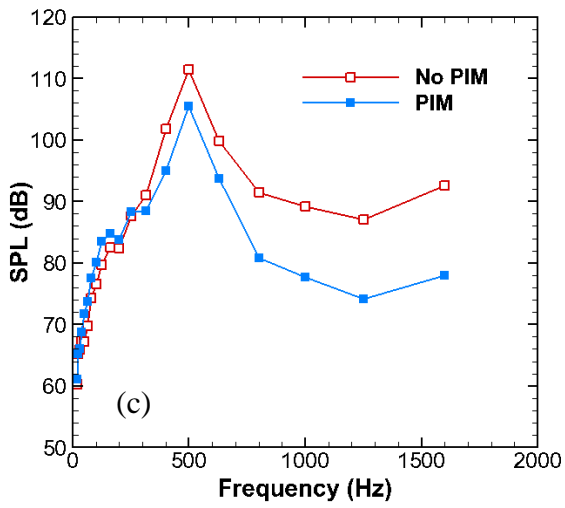


Figure 3.74. Results for flush mounted swirler,  $T_{inlet} = 21^{\circ}\text{C}$ ,  $Q = 600$  SLPM,  $\phi = 0.65$  (a) Flame photograph without PIM, (b) Flame photograph with PIM, (c) SPL per 1/3 octave band, (d) Spectral power

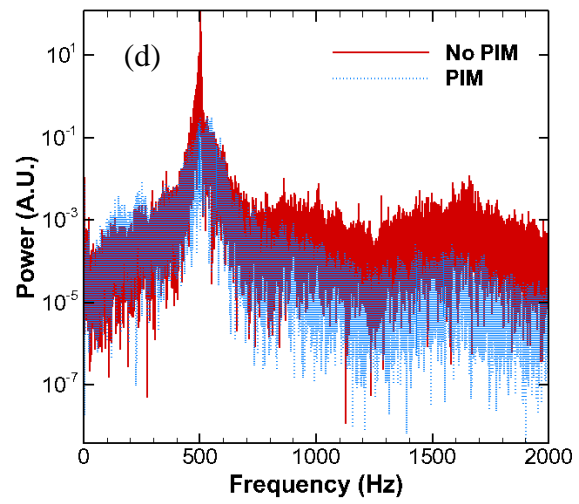
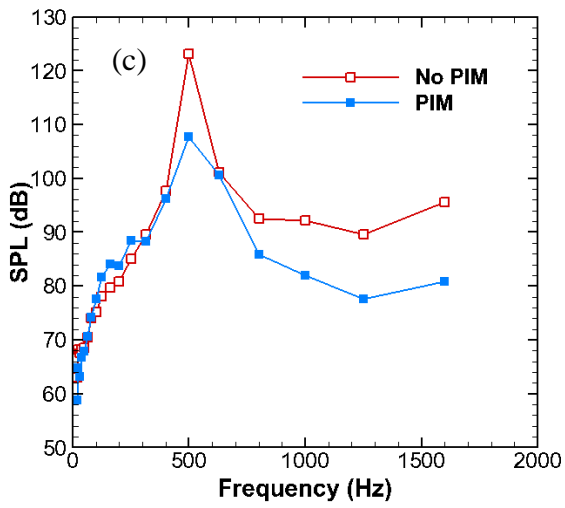


Figure 3.75. Results for flush mounted swirler,  $T_{inlet} = 21^{\circ}\text{C}$ ,  $Q = 600$  SLPM,  $\phi = 0.70$  (a) Flame photograph without PIM, (b) Flame photograph with PIM, (c) SPL per 1/3 octave band, (d) Spectral power

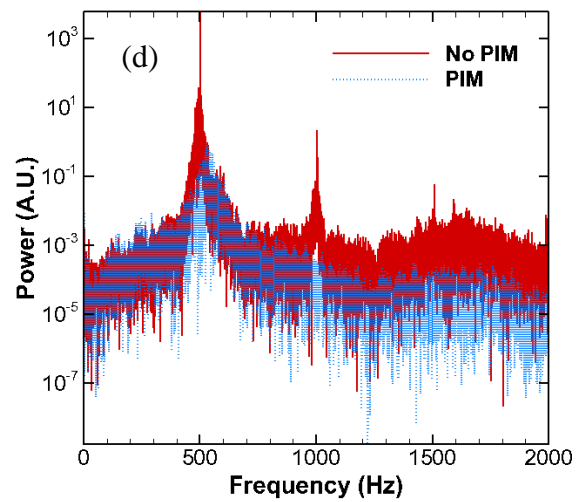
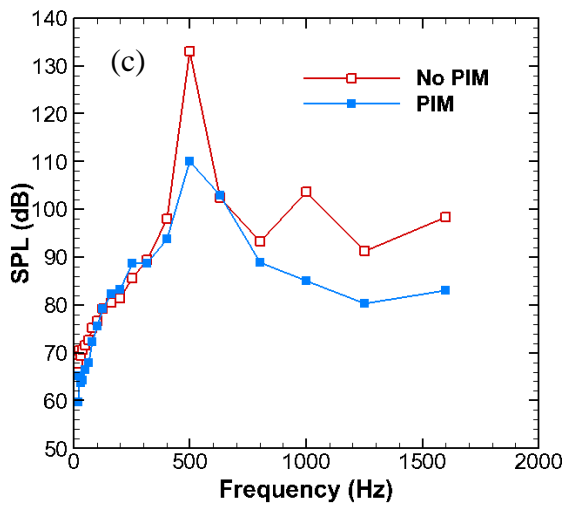


Figure 3.76. Results for flush mounted swirler,  $T_{inlet} = 21^\circ\text{C}$ ,  $Q = 600$  SLPM,  $\phi = 0.75$  (a) Flame photograph without PIM, (b) Flame photograph with PIM, (c) SPL per 1/3 octave band, (d) Spectral power

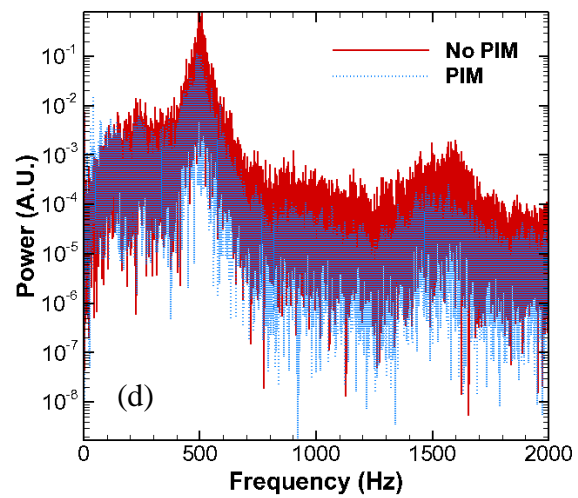
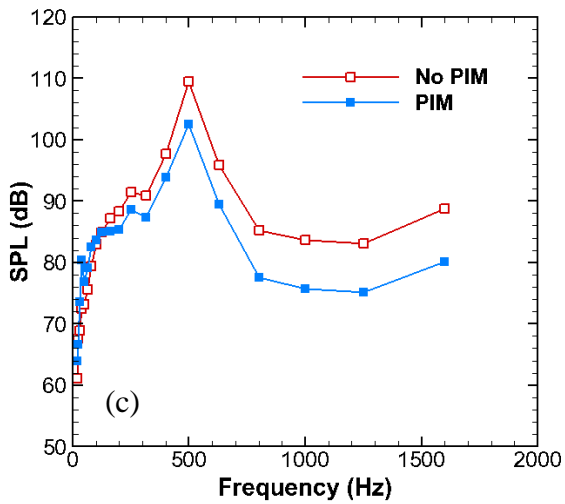
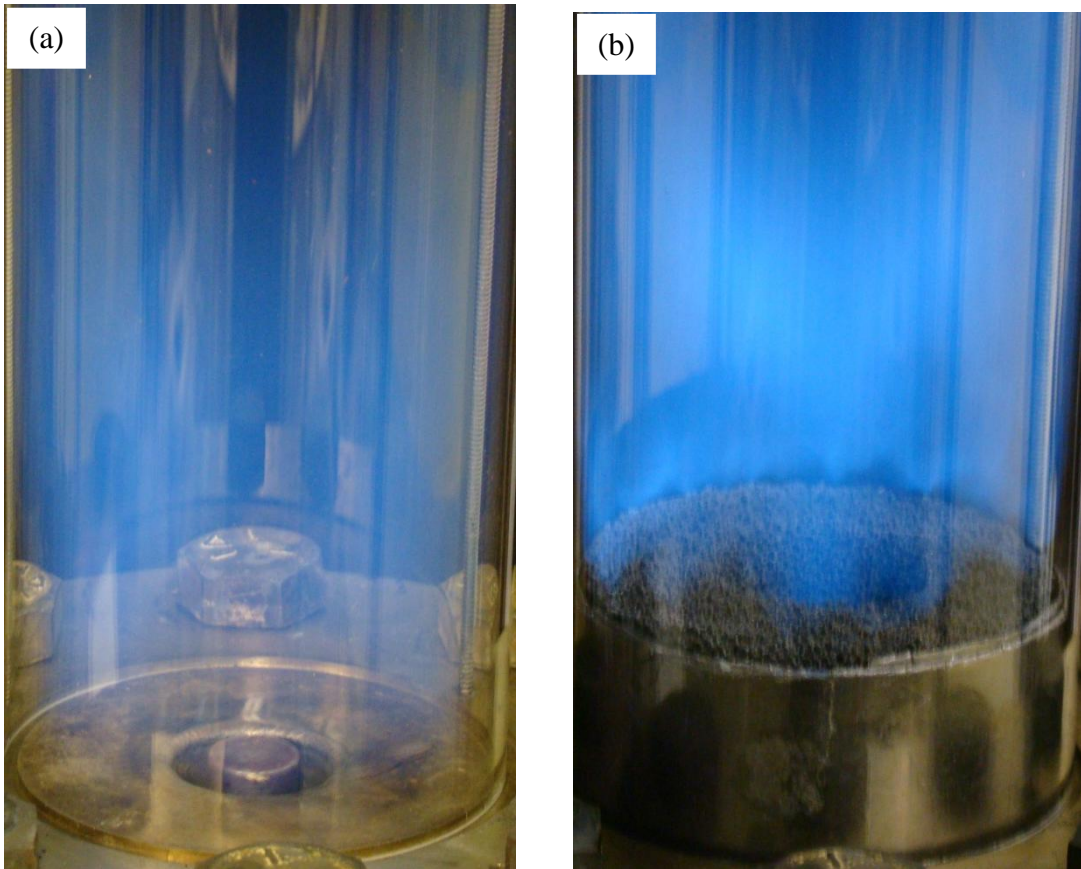


Figure 3.77. Results for recessed swirler,  $T_{inlet} = 21^{\circ}\text{C}$ ,  $Q = 600$  SLPM,  $\phi = 0.60$  (a) Flame photograph without PIM, (b) Flame photograph with PIM, (c) SPL per 1/3 octave band, (d) Spectral power

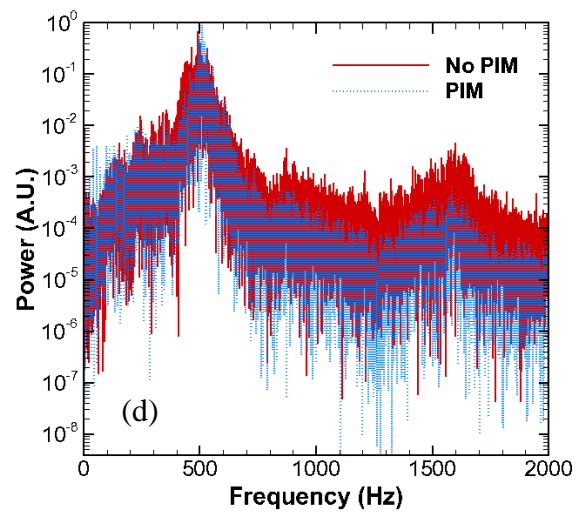
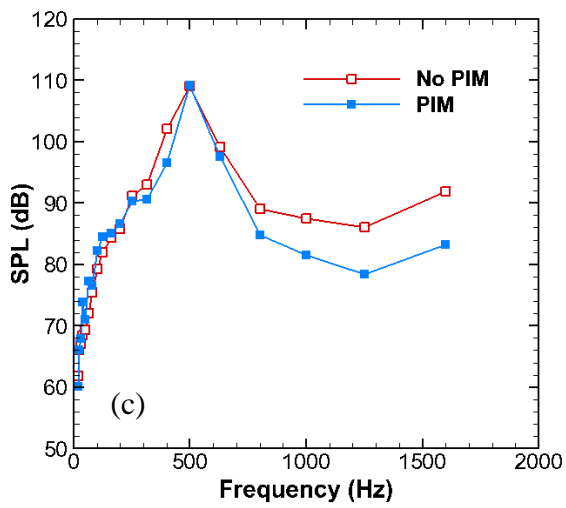


Figure 3.78. Results for recessed swirler,  $T_{inlet} = 21^{\circ}\text{C}$ ,  $Q = 600$  SLPM,  $\phi = 0.65$  (a) Flame photograph without PIM, (b) Flame photograph with PIM, (c) SPL per 1/3 octave band, (d) Spectral power

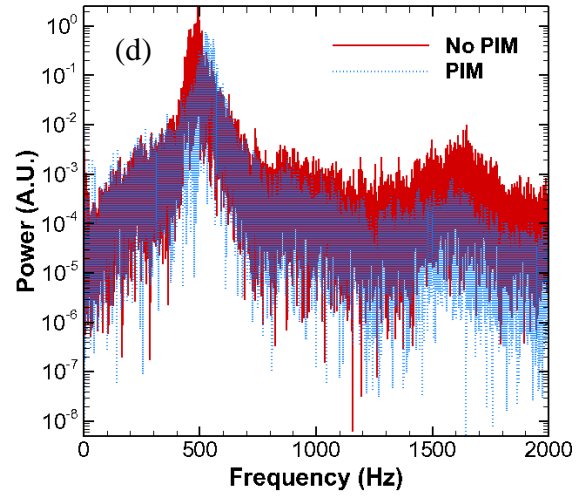
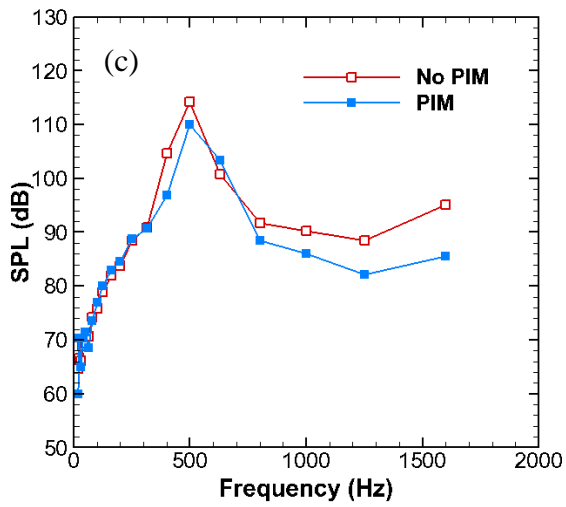


Figure 3.79. Results for recessed swirler,  $T_{inlet} = 21^{\circ}\text{C}$ ,  $Q = 600$  SLPM,  $\phi = 0.70$  (a) Flame photograph without PIM, (b) Flame photograph with PIM, (c) SPL per 1/3 octave band, (d) Spectral power

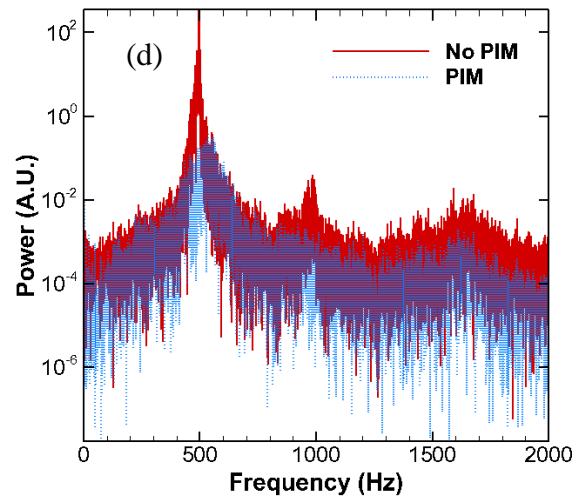
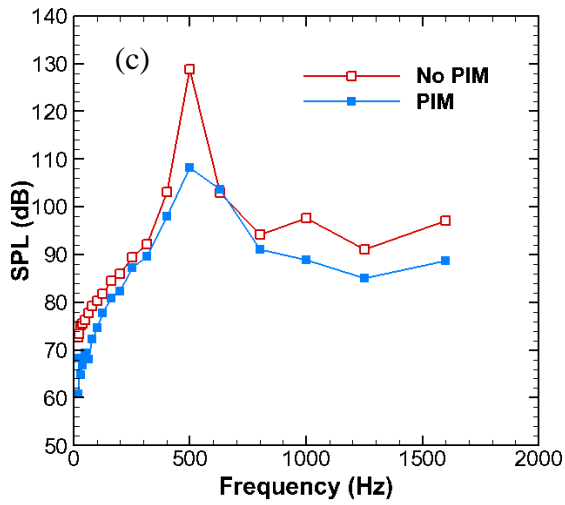
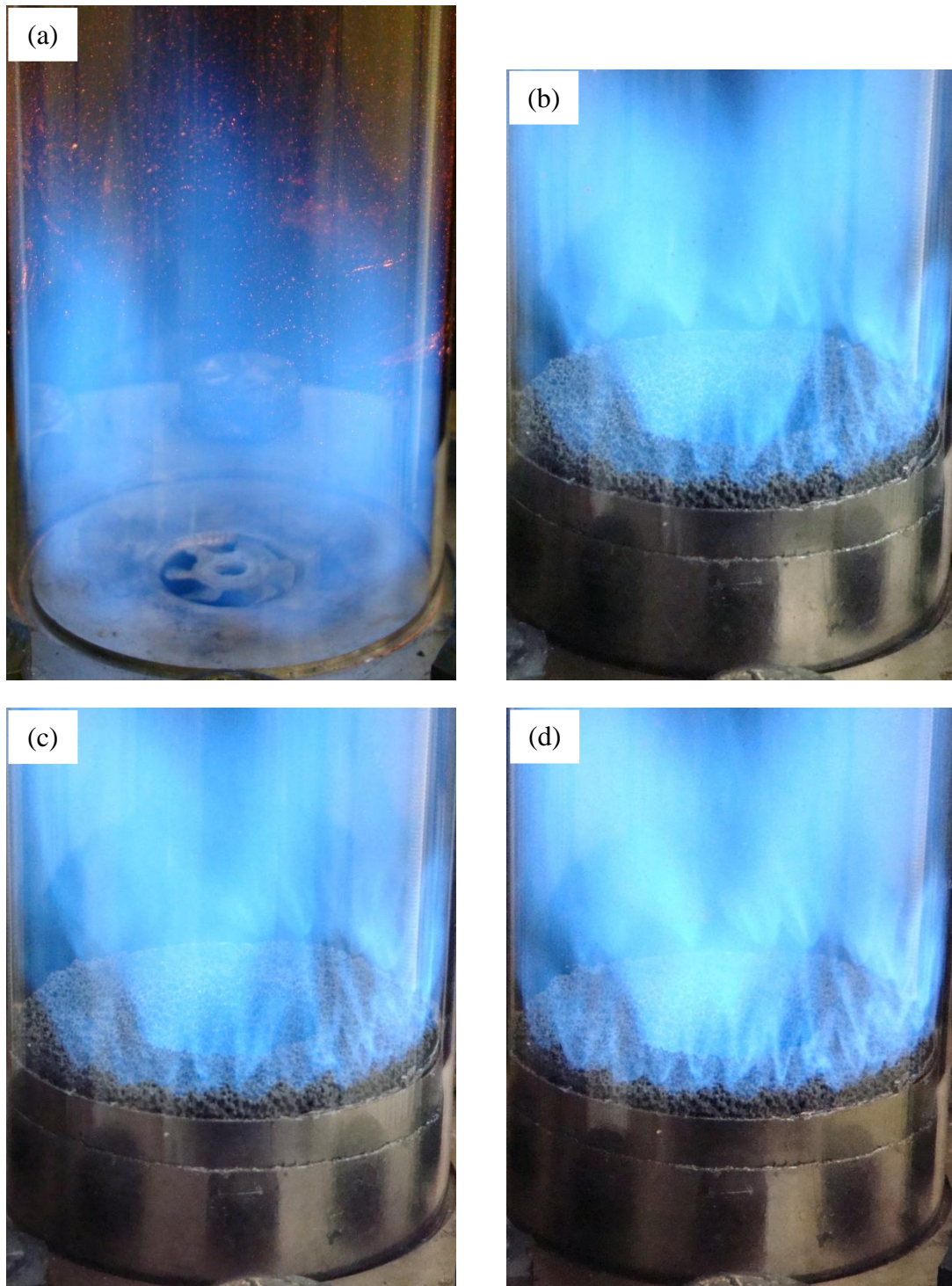


Figure 3.80. Results for recessed swirler,  $T_{inlet} = 21^{\circ}C$ ,  $Q = 600$  SLPM,  $\phi = 0.75$ (a) Flame photograph without PIM, (b) Flame photograph with PIM, (c) SPL per 1/3 octave band, (d) Spectral power



*Figure 3.81.* Flame photographs from endurance test,  $T_{\text{inlet}} = 21^{\circ}\text{C}$ ,  $Q = 600$  SLPM,  $\phi = 0.70$  (a) Baseline case without PIM (b) Immediately after ignition with PIM (c) 5 hours after ignition with PIM (d) 10 hours after ignition with PIM

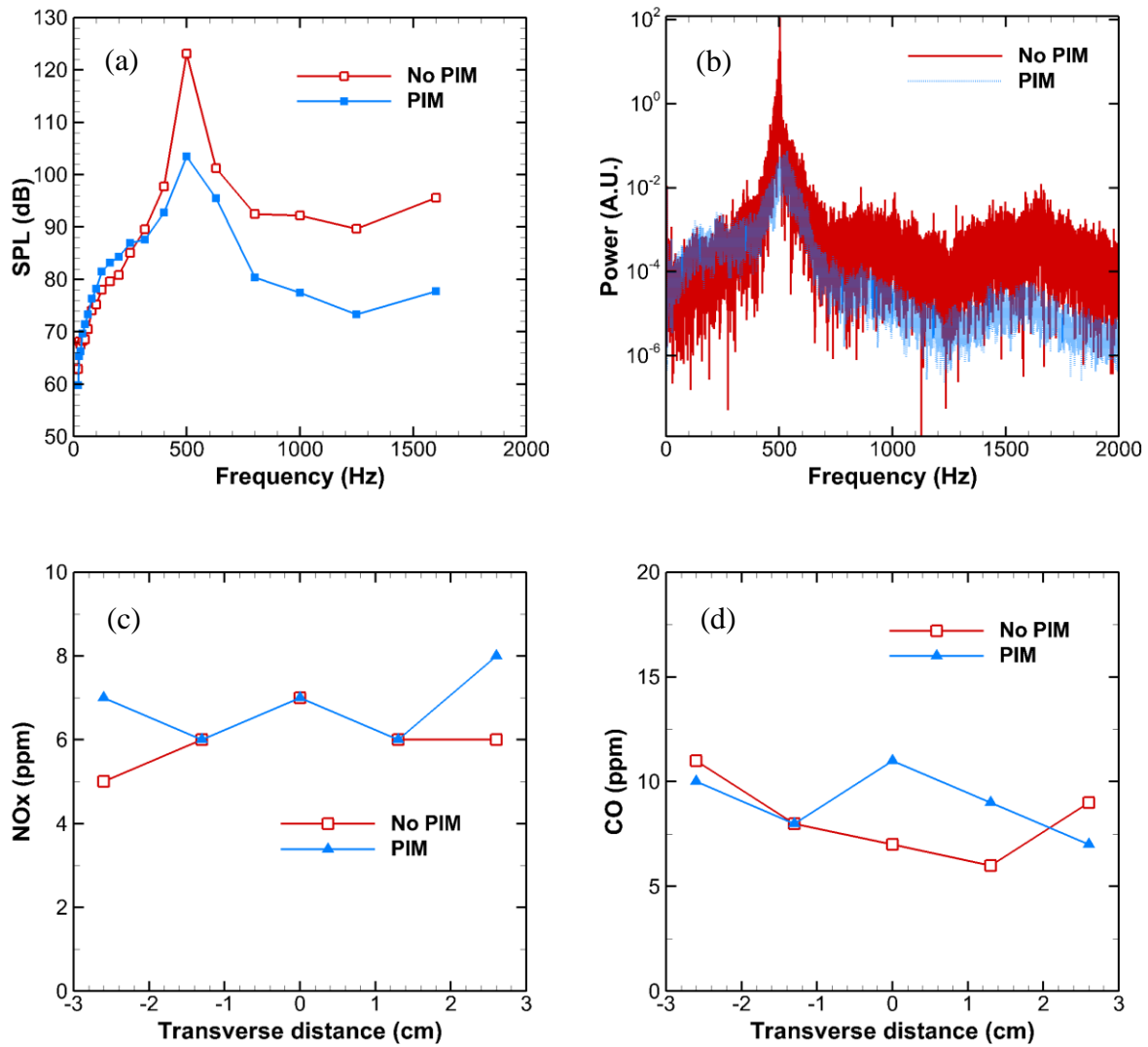


Figure 3.82. Results for endurance test immediately after ignition,  $T_{inlet} = 21^{\circ}\text{C}$ ,  $Q = 600$  SLPM,  $\phi = 0.70$  (a) SPL per 1/3 octave band, (b) Spectral power, (c) NOx emissions, (d) CO emissions

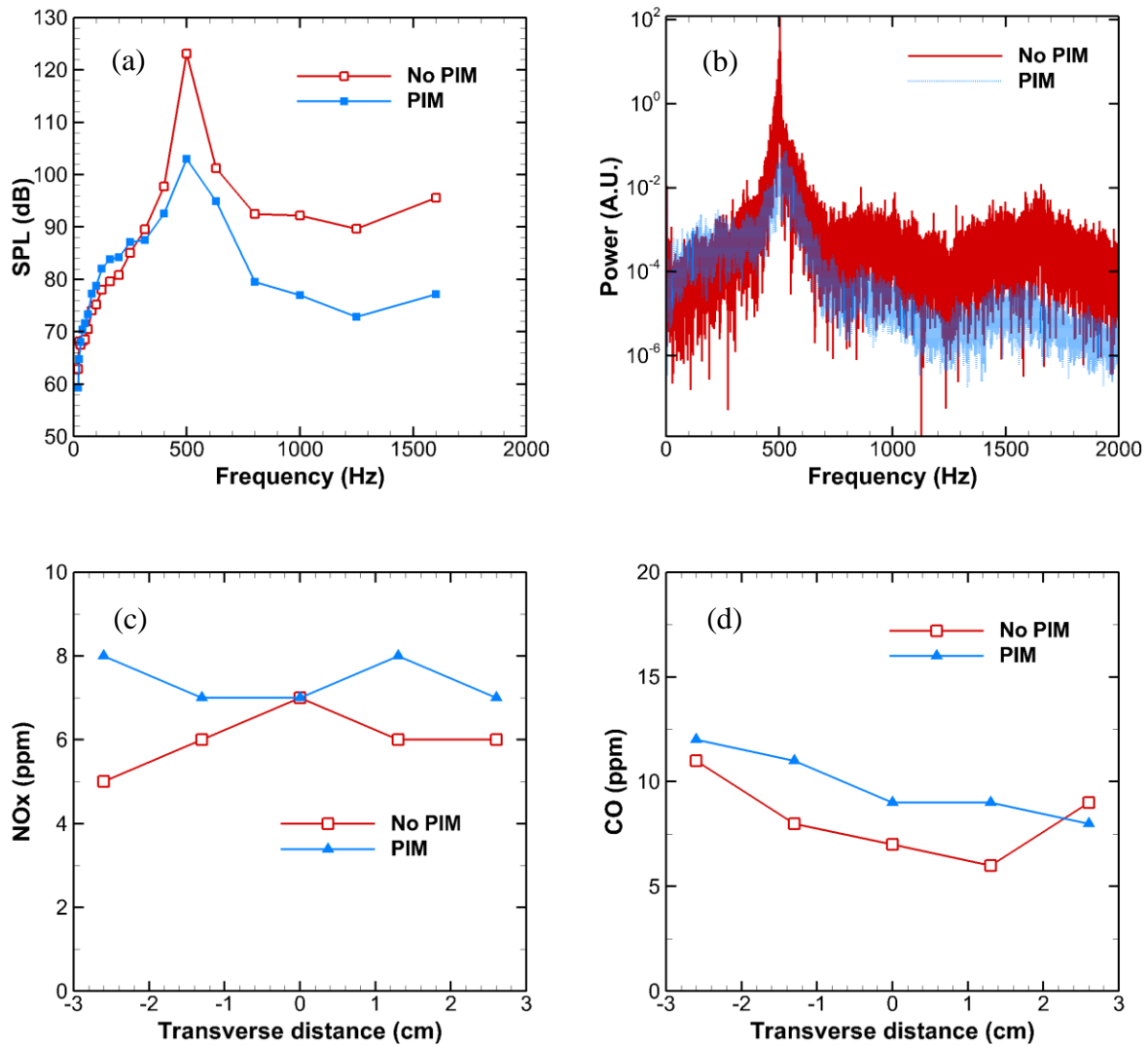


Figure 3.83. Results for endurance test 2 hours after ignition,  $T_{\text{inlet}} = 21^{\circ}\text{C}$ ,  $Q = 600$  SLPM,  $\phi = 0.70$  (a) SPL per 1/3 octave band, (b) Spectral power, (c) NOx emissions, (d) CO emissions

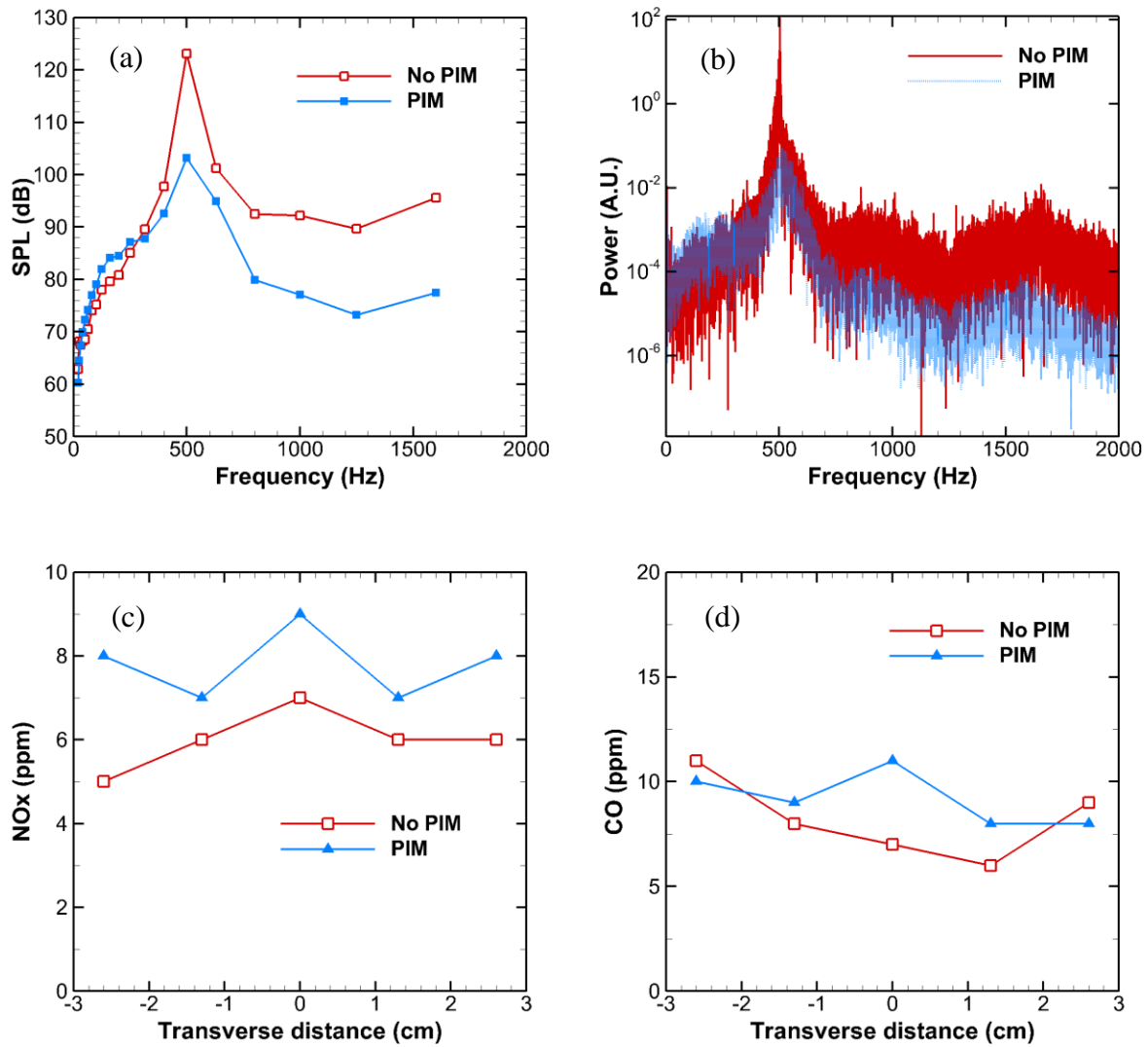


Figure 3.84. Results for endurance test 4 hours after ignition,  $T_{inlet} = 21^{\circ}\text{C}$ ,  $Q = 600$  SLPM,  $\phi = 0.70$  (a) SPL per 1/3 octave band, (b) Spectral power, (c) NOx emissions, (d) CO emissions

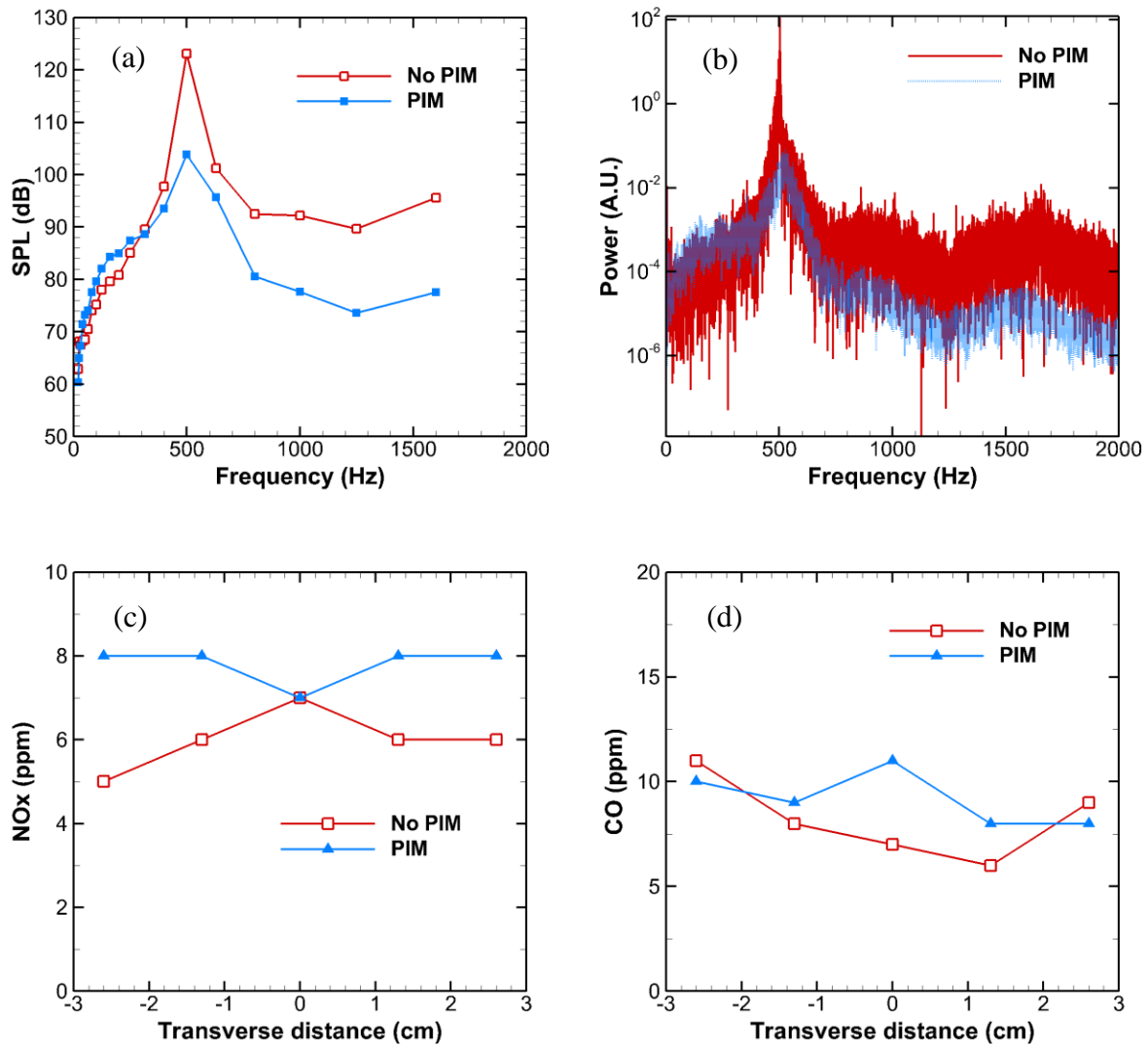


Figure 3.85. Results for endurance test 6 hours after ignition,  $T_{inlet} = 21^{\circ}\text{C}$ ,  $Q = 600$  SLPM,  $\phi = 0.70$  (a) SPL per 1/3 octave band, (b) Spectral power, (c) NOx emissions, (d) CO emissions

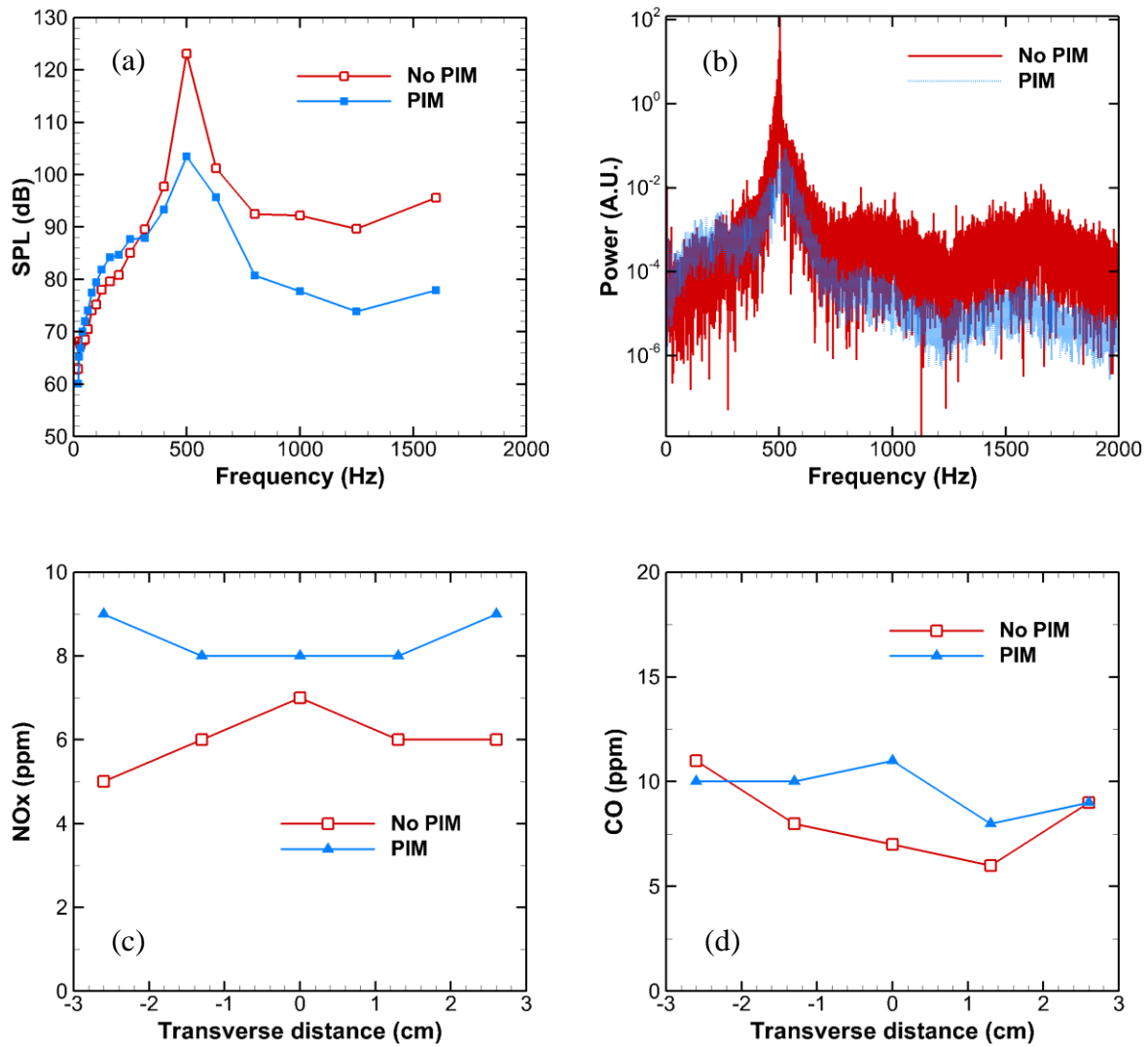


Figure 3.86. Results for endurance test 8 hours after ignition,  $T_{inlet} = 21^\circ\text{C}$ ,  $Q = 600$  SLPM,  $\phi = 0.70$  (a) SPL per 1/3 octave band, (b) Spectral power, (c) NOx emissions, (d) CO emissions

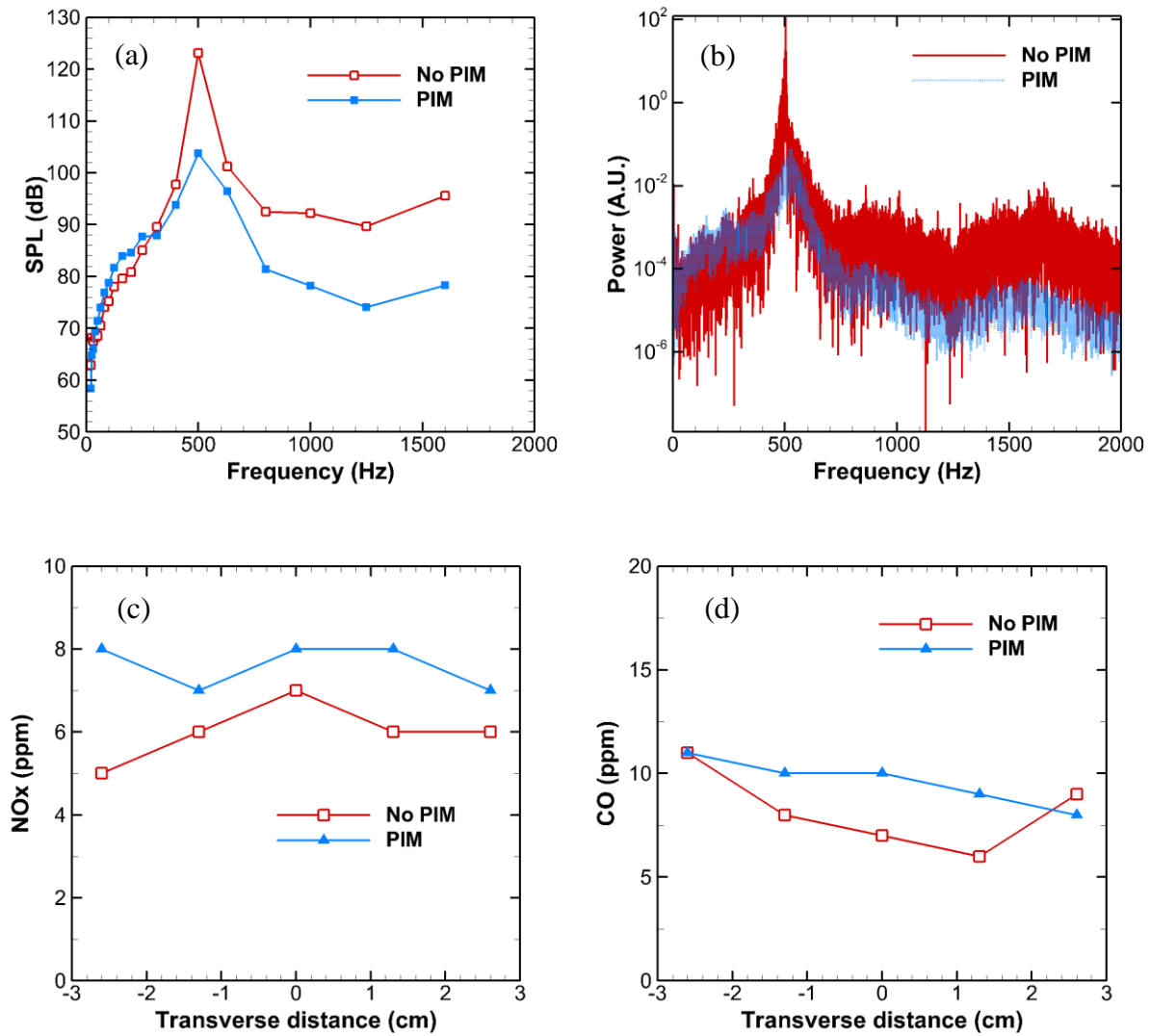


Figure 3.87. Results for endurance test 10 hours after ignition,  $T_{inlet} = 21^\circ\text{C}$ ,  $Q = 600$  SLPM,  $\phi = 0.70$  (a) SPL per 1/3 octave band, (b) Spectral power, (c) NOx emissions, (d) CO emissions

## CHAPTER 4

### CONCLUSIONS AND RECOMMENDATIONS

#### 4.1 Conclusions

The present study implements porous inert media in a LPM, swirl-stabilized combustor to suppress combustion noise and mitigate thermo-acoustic instability. The passive technique alters the combustor flow field to alleviate turbulent fluctuations while also attenuating acoustic waves. In this way, total sound pressure level is reduced and self-excited instabilities are eliminated.

A laboratory facility was developed to perform combustion experiments over a range of operating pressures with large air flow rates and high preheat temperatures. Design features and operating procedure of the facility are presented in detail. The experimental test rig was used to conduct an extensive set of combustion tests to analyze performance characteristics of the PIM at atmospheric pressure. Operating parameters such as air flow rate, air inlet temperature, and equivalence ratio were varied to observe effect on noise reduction. Mitigation of thermo-acoustic instability with PIM was examined by operating at conditions which exhibited instability without PIM. Effect of swirler geometry was investigated for different axial locations of the swirler within the premixer. Total SPL was quantified without and with PIM for each test case. An endurance test was performed in which the porous insert was subjected to continuous combustion for an extended period (10 hours) to observe any degradation in performance. Results from this study will be used as a baseline for future work at elevated pressures.

Main conclusions from the work presented in this thesis are:

- Significant reduction in broadband combustion noise was achieved with porous inert media assisted combustion in a lean-premixed, swirl-stabilized combustor. The findings of Sequera and Agrawal (2011) were maintained for a variety of operating conditions in an experimental test rig. Porous inert media is confirmed as a passive strategy to suppress combustion noise in gaseous combustion systems operating at a lean equivalence ratio. Additionally, no associated pressure drop penalty was incurred with the use of PIM.
- Porous inert media was proven to be extremely effective in eliminating large peaks in sound power and resulting combustion instability. Porous media eliminated instability for all cases where instability was present without PIM. In such cases, instability was shown to be the dominant source of overall sound pressure level. Thus, elimination of instability resulted in a drastic reduction of overall SPL.
- Surface combustion mode was achieved for all tests conducted in this study. While surface combustion does provide distribution of heat release rate, too much surface combustion can adversely affect NO<sub>x</sub> emissions by increasing local flame temperatures within the surface reaction zone. This effect necessitates an optimum PIM geometry to adequately distribute heat release rate while maintaining low levels of NO<sub>x</sub> emissions.
- Many central flames produced in this study were “lifted” and anchored to the downstream surface of the PIM rather than contained within the annular void. As a result, flow structure within the combustor was not modified in the manner originally prescribed by the technique. Even so, significant reduction in total sound pressure and instability is achieved. This observation confirms the ability of the PIM to attenuate

noise and flow fluctuations within the combustor. Increased flame length was observed with PIM, thereby increasing measured concentration of CO emissions. An optimum PIM geometry would enhance performance and decrease the overall flame length, eliminating the need for excess combustor length.

- Effect of swirler geometry on combustion noise and instability was identified in this study. Larger vane angle was shown to increase reduction in total sound pressure level as compared with the smaller angle used by Sequera and Agrawal, 2011. For some cases, SPL reduction with a recessed swirler was comparable to that with a flushed swirler. For other cases, the recessed configuration provided little, if any, reduction in broadband combustion noise. With either configuration, thermo-acoustic instability was completely eliminated.
- The porous inert media was shown to maintain performance over an extended operating time. For the duration of the 10 hour endurance test, no change in performance of the PIM was observed. During the test, no material deterioration was observed and emissions remained constant. It is reasonable to assume that the porous insert could be used for much longer periods without losing functionality.

#### 4.1 Recommendations

Recommendations for future research and improvements of current work are:

- Develop optimum PIM geometry and pore density such that the following criterion are met:
  - Increase PIM diffuser angle to reduce amount of surface combustion to minimize increase in NO<sub>x</sub> emissions.

- Modify swirler vane angle and/or PIM diffuser angle so that the central flame is anchored within the annular void.
  - Use appropriate pore density to avoid interior combustion at elevated air preheat temperatures.
- Further investigate decreased effectiveness of PIM to suppress broadband combustion noise at increased air inlet temperatures.
- Design and implement a more robust mechanism for securing the porous insert for testing with high reactant flow rates and large amounts of heat release.
- Conduct testing at elevated pressures to determine if PIM functionality is sustained in a high pressure environment, such as a gas turbine combustor.
- Implement combustion with PIM in a liquid fuel combustion system with sufficient atomization.

## REFERENCES

- Agrawal, A.K. & S. Vijaykant, (2010). Passive Noise Attenuation System. *U.S. Patent Application 20100059311*, The University of Alabama.
- Bussman, W. & Jayakaran, J. (2001). *Noise. The John Zink Combustion Handbook*. New York: CRC Press.
- Choi, G., Tanahashi, M., & Miyauchi, T. (2005). Control of Oscillating Combustion and Noise Based on Local Flame Structure. *Proceedings of the Combustion Institute*, 30, 1807-1814.
- Duchaine, P., Zimmer, L., & Schuller, T. (2009). Experimental Investigation of Mechanisms of Sound Production by Partially Premixed Flames. *Proceedings of the Combustion Institute*, 32, 1027-1034.
- Fernandez-Pello, A. C. (2002). Micropower Generation Using Combustion: Issues and Approaches. *Proceedings of the Combustion Institute*, 29, 883-899.
- Flemming, F., Olbrit, C., Wegner, B., Sadiki, A., Janicka, J., Bake, F., Michael, U., Lehmann, B., & Rohle, I. (2005). Analysis of Unsteady Motion with respect to Noise Sources in a Gas Turbine Combustor. *Flow, Turbulence, and Combustion*, 75, 3-27.
- Gupta, A.K., Lilley, D.G., & Syred, N. (1984). *Swirl Flows*. England: Abacus Press.
- Hirsch, C., Wasle, J., Winkler, A., & Sattelmayer, T. (2007) A Spectral Model for the Sound Pressure from Turbulent Premixed Combustion. *Proceedings of the Combustion Institute*, 31, 1435-1441.
- Howell, H.R., Hall, M. J., & Ellzey, J. L. (1996). Combustion of Hydrocarbon Fuels within Porous Inert Media. *Progress in Energy and Combustion Science*, 22, 121-145.
- Huang, Y. & Yang, V. (2009). Dynamics and Stability of Lean-Premixed Swirl-Stabilized Combustion. *Progress in Energy and Combustion Science*, 35, 293-364.
- Lee, J. G. & Santavicca, D. A. (2003) Experimental Diagnostics for the Study of Combustion Instabilities in Lean Premixed Combustors. *Journal of Propulsion and Power*, 19(5), 735-750.

- Lieuwen, T. C., & Yang, V. (2005). Combustion Instabilities in Gas Turbines. *Progress in AIAA*, 210.
- Marbach, T. & Agrawal, A.K. (2005). Experimental Study of Surface and Interior Combustion using Composite Porous Inert Media. *Journal of Engineering for Gas Turbines and Power*, 127, 307-313.
- Marbach, T. L., Sadasivuni, V., & Agrawal, A.K. (2007). Investigation of Miniature Combustor Using Porous Media Surface Stabilized Flame. *Combustion Science and Technology*, 179(9), 1901-1922.
- Noiray, N., Durox, D., Schuller, T., & Candel, S. (2009) Dynamic Phase Converter for Passive Control of Combustion Instabilities. *Proceedings of the Combustion Institute*, 32, 3163-3170.
- Putnam, A. (1971). *Combustion Driven Oscillations in Industry*. New York: Elsevier.
- Rajaram, R. Gray J., & Lieuwen, T. (2006). Premixed Combustion Noise Scaling: Total Power and Spectra. *AIAA Conference Paper 2006-2612*.
- Rayleigh, J.S.W. (1945). *The Theory of Sound, Vol. 2*. New York: Dover.
- Richards, G. A. & Straub, D.L. (2003) Passive Control of Combustion Dynamics in Stationary Gas Turbines. *Journal of Propulsion and Power*, 19(5), 795-810.
- Sequera, D. (2011). *Reduction of Combustion Noise and Instabilities using Porous Inert Material in a Swirl-Stabilized Burner*. (Doctoral Dissertation).
- Sequera, D. & Agrawal, A.K. (2009). Numerical Simulations of Swirl-Stabilized Combustion Coupled with Porous Inert Medium. *Proceedings of the 6<sup>th</sup> U.S. National Combustion Meeting*, Paper 11C3.
- Sequera, D. & Agrawal, A.K. (2011). Passive Control of Noise and Instability in a Swirl-Stabilized Combustor with the use of High-Strength Porous Insert. *Proceedings of ASME Turbo Expo*, Paper GT2011-46835.
- Schadow, K. C. & Gutmark, E. (1992). Combustion Instability Related to Vortex Shedding in Dump Combustors and their Passive Control. *Progress in Energy and Combustion Science*, 18, 117-132.
- Schadow, K. C., Gutmark, E., Wilson, K.J., & Smith, R. A. (1998). Multistep Dump Combustor Design to Reduce Combustion Instabilities. *AIAA/ASME/SAE/ASEE 24<sup>th</sup> Joint Propulsion Conference Paper 88-2854*.

- Schefer, R. W., Wicksall, D. M., & Agrawal, A. K. (2002). Combustion of Hydrogen-Enriched Methane in a Lean Premixed Swirl-Stabilized Burner. *Proceedings of the Combustion Institute*, 29(1), 843-851.
- Schwarz, A. & Janicka, J. (2009). *Combustion Noise*. Springer.
- Sreenivasan, K. R. & Raghun, S. (2000). The Control of Combustion Instability. *Current Science*, 79, 867-883.
- Steele, R. C., Cowell, L. H., Cannon S. M., & Smith, C. E. (2000). Passive Control of Combustion Instability in Lean Premixed Combustors. *Journal of Engineering for Gas Turbines and Power*, 122, 412-419.
- Strahle, W. (1978). Combustion Noise. *Progress in Energy and Combustion Science*, 4(3), 157-156.
- Trimis, D. & Durst F. (1996) Combustion in a Porous Medium – Advances and Applications. *Combustion Science and Technology*, 121, 153-168.
- Waitz, I.A. Gauba, G., & Tzeng, Y. S. (1998). Combustors for Micro-gas Turbine Engines. *Journal of Fluids Engineering*, 120, 109-117.
- Wicksall, D. M., Agrawal A. K., Schefer R.W., & Keller, J.O. (2005). Influence of Hydrogen Addition on Flow Structure in Enclosed Swirling Methane Flame. *Journal of Propulsion and Power*, 21, 16-24.
- Wicksall, D. M., Agrawal A. K., Schefer R.W., & Keller, J.O. (2005). The Interaction of Flame and Flow Field in a Lean Premixed Swirl-Stabilized Combustor Operated on H<sub>2</sub>/CH<sub>4</sub>/Air. *Proceedings of the Combustion Institute*, 30, 2875-2883.
- Zimont, V. (2000). Gas Premixed Combustion at High Turbulence. Turbulent Flame Closure Model Combustion Model. *Experimental Thermal and Fluid Science*, 21, 179-186.
- Zimont, V. L. & Lipatnikov, A.N. (1995). A Numerical Model of Premixed Turbulent Combustion of Gases. *Chemical Physics Report*, 14(7), 993-1025.
- Zimont, V., Polifke, W., Bettelini, M., & Weisenstein, W. (1998). An Efficient Computational Model for Premixed Turbulent Combustion at High Reynolds Numbers Based on Turbulent Flame Speed Closure. *Journal of Gas Turbine and Power*, 120, 526-532.

## APPENDIX A

### DETAILED DRAWINGS OF COMBUSTOR

The high pressure combustion chamber described in Chapter 2 is composed of a plenum base, a support pipe and flange, and an enclosure. The enclosure is outfitted with two rectangular ports designed to contain optical windows. The optical windows are held in place by rectangular flanges, which are bolted to the combustion chamber. Figure A.1 shows details of the plenum base plate. Figure A.2 shows details of the support pipe and connected flange. The threaded end of the support pipe is welded to the base plate to form the assembled plenum base, as illustrated in Figure A.3. Details of the high pressure enclosure are given in Figures A.4, A.5, and A.6. Threaded access ports are milled into the wall of the enclosure as shown in Figure A.7. Optical window ports are shown in Figure A.8 and window covers are shown in Figure A.9. Details of the optical windows are shown in Figure A.10.

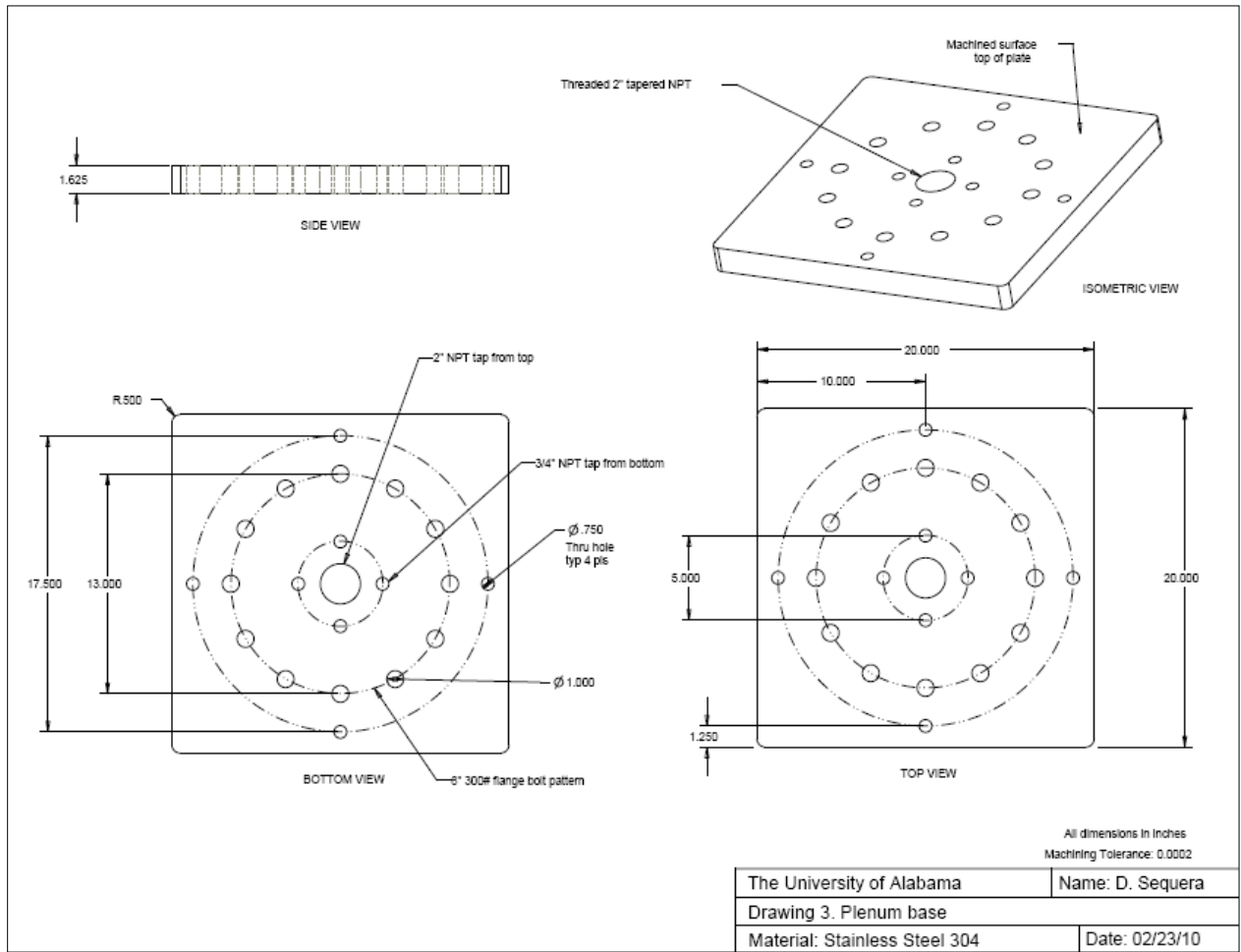


Figure A.1. Details of plenum base

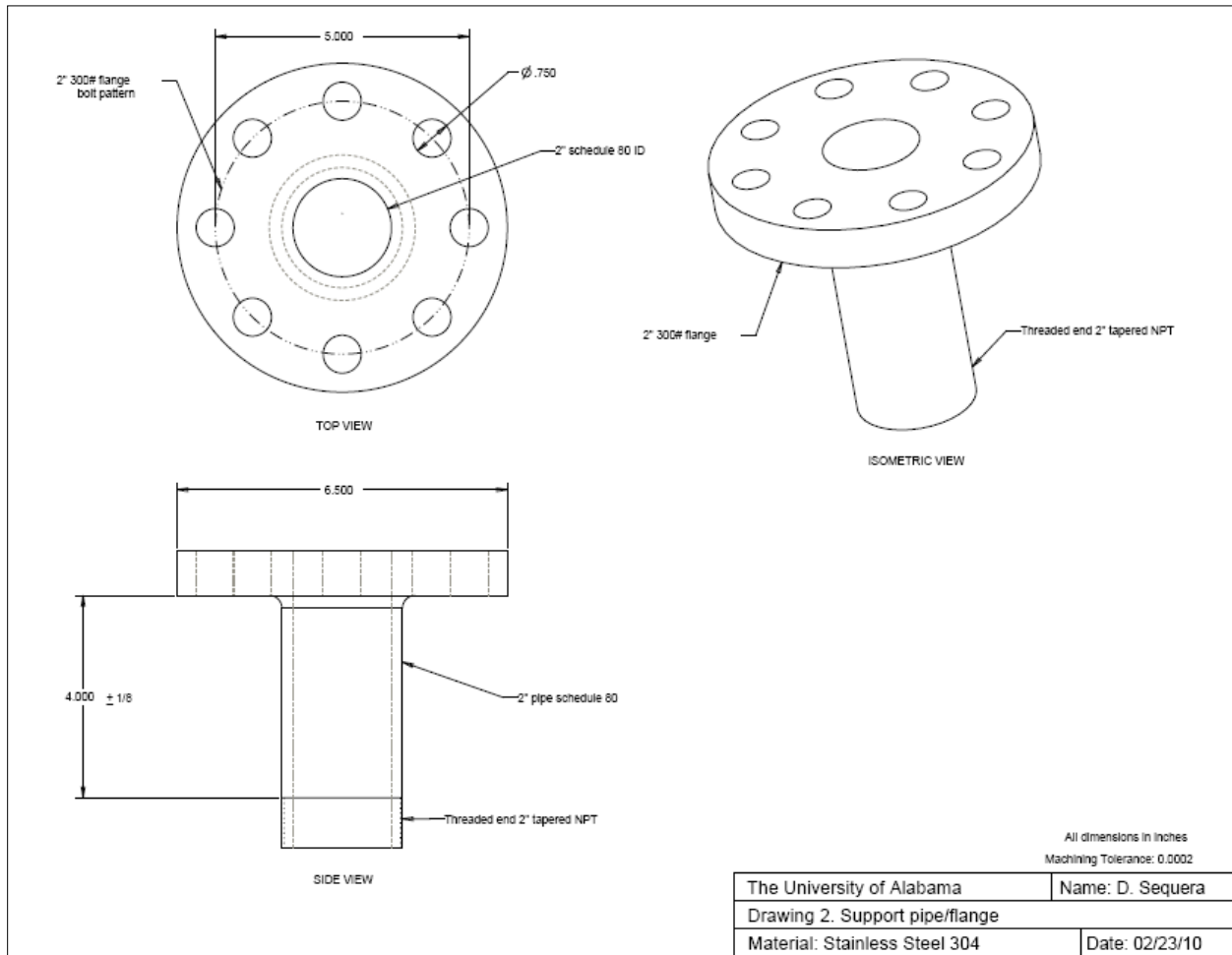


Figure A.2. Details of support pipe and flange

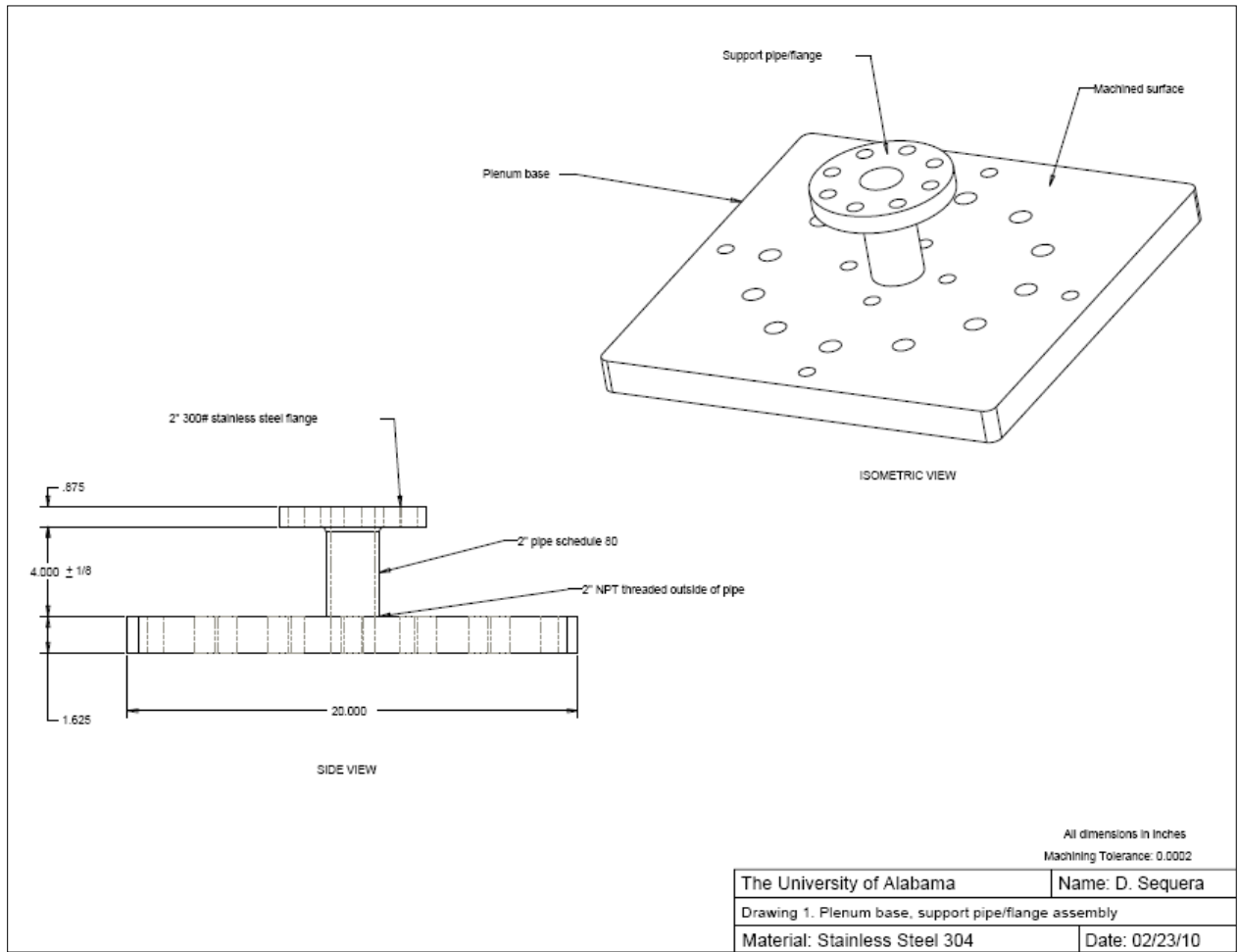


Figure A.3. Details of assembled plenum base

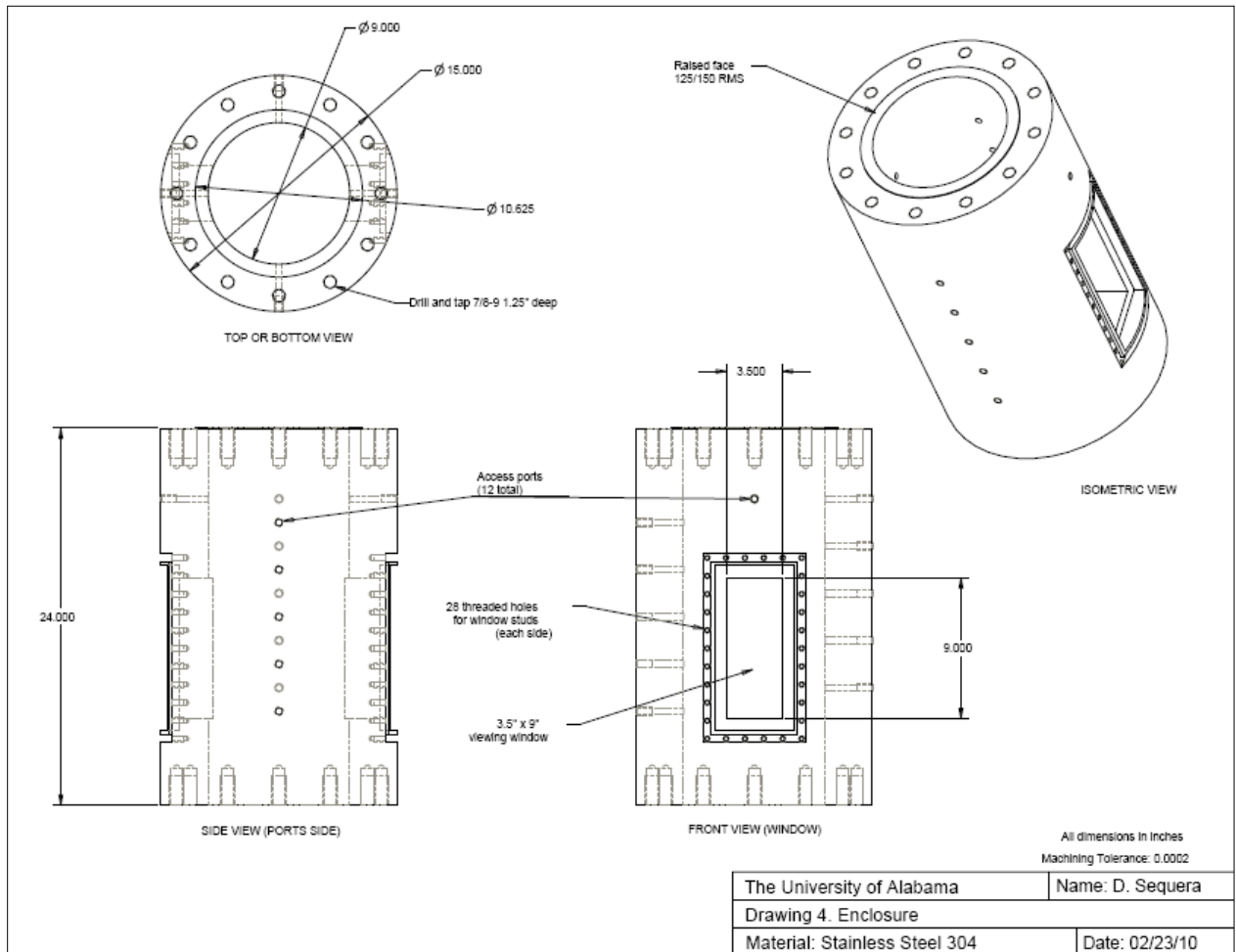


Figure A.4. Details of enclosure

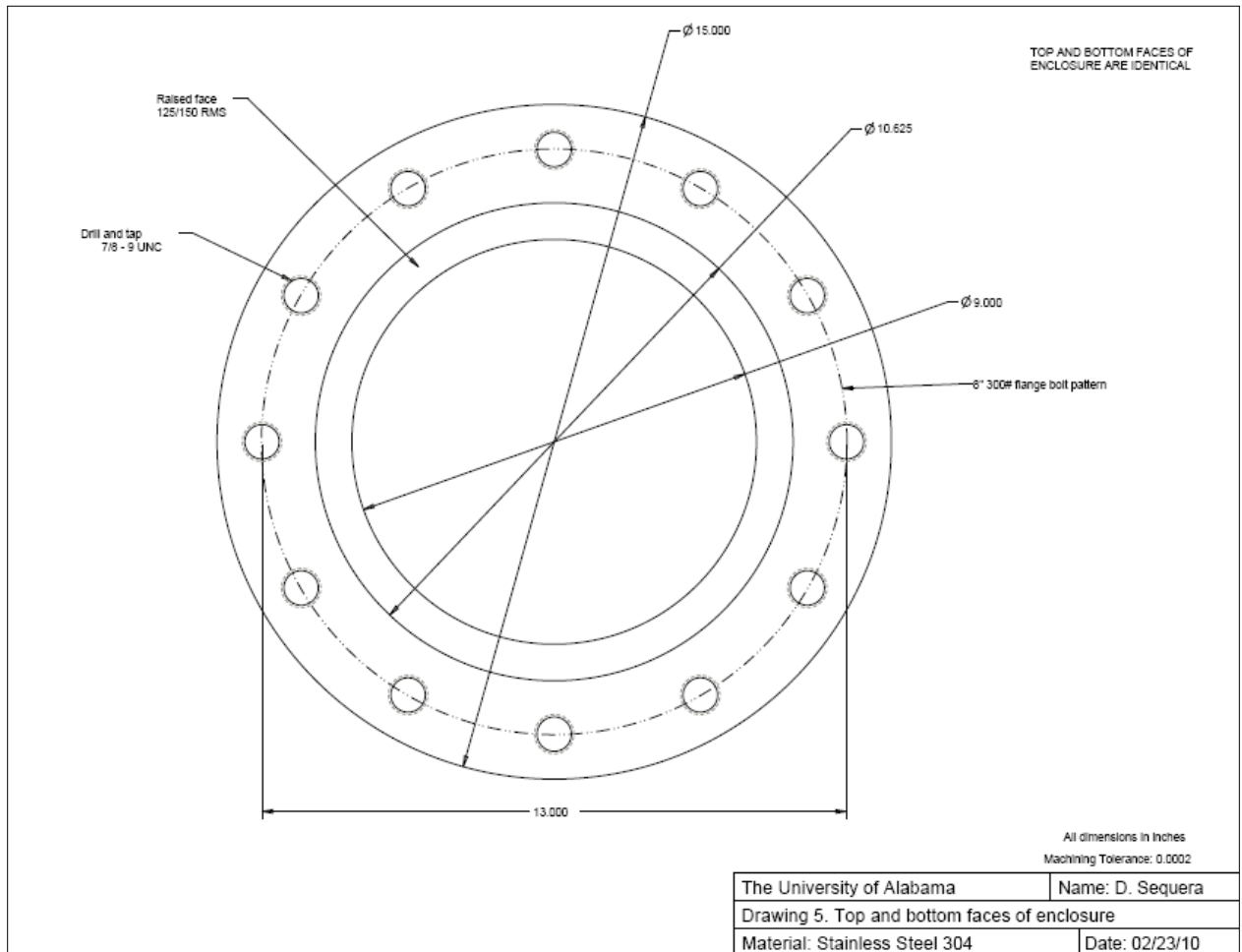


Figure A.5. Detail of faces of enclosure

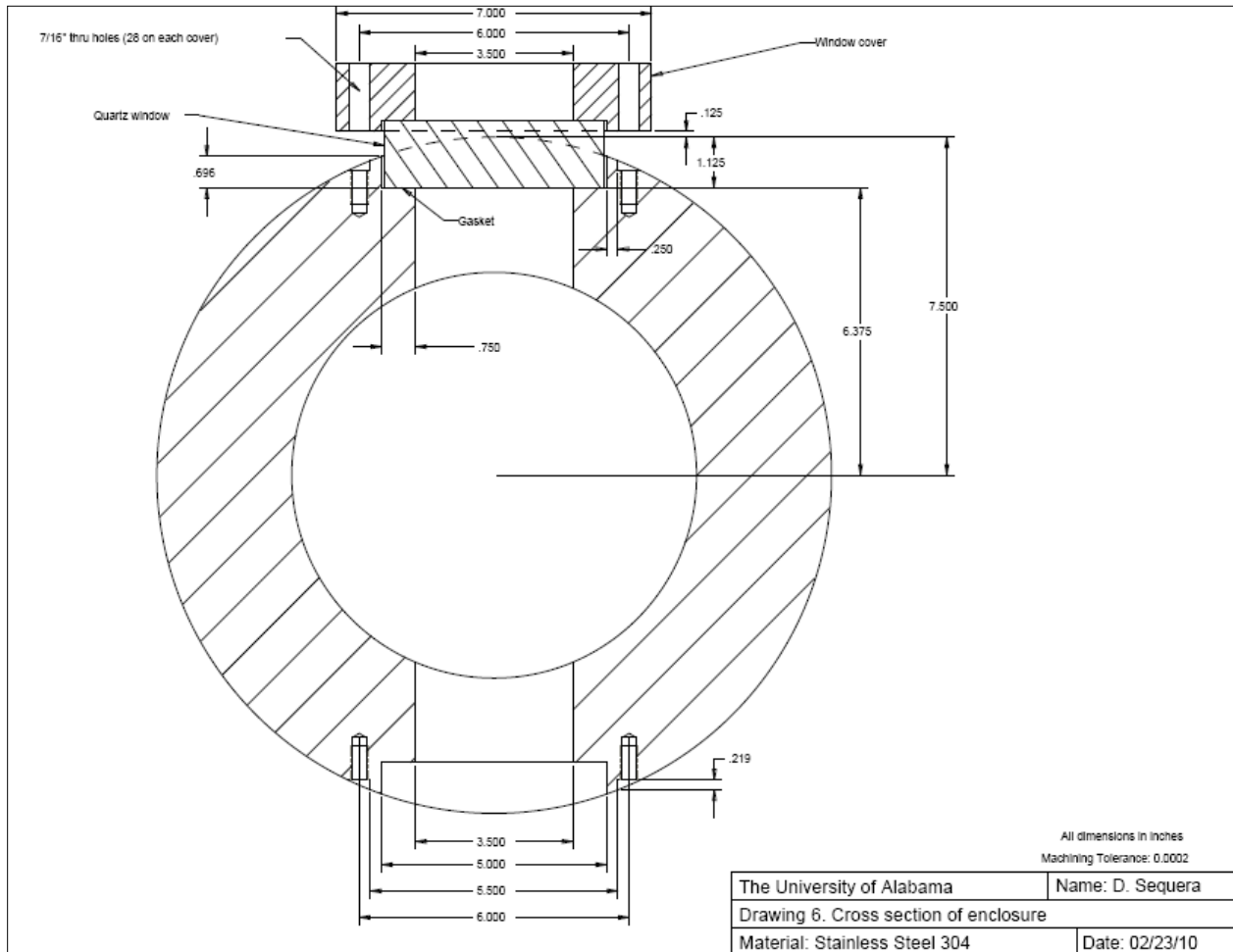


Figure A.6. Details of cross section of enclosure

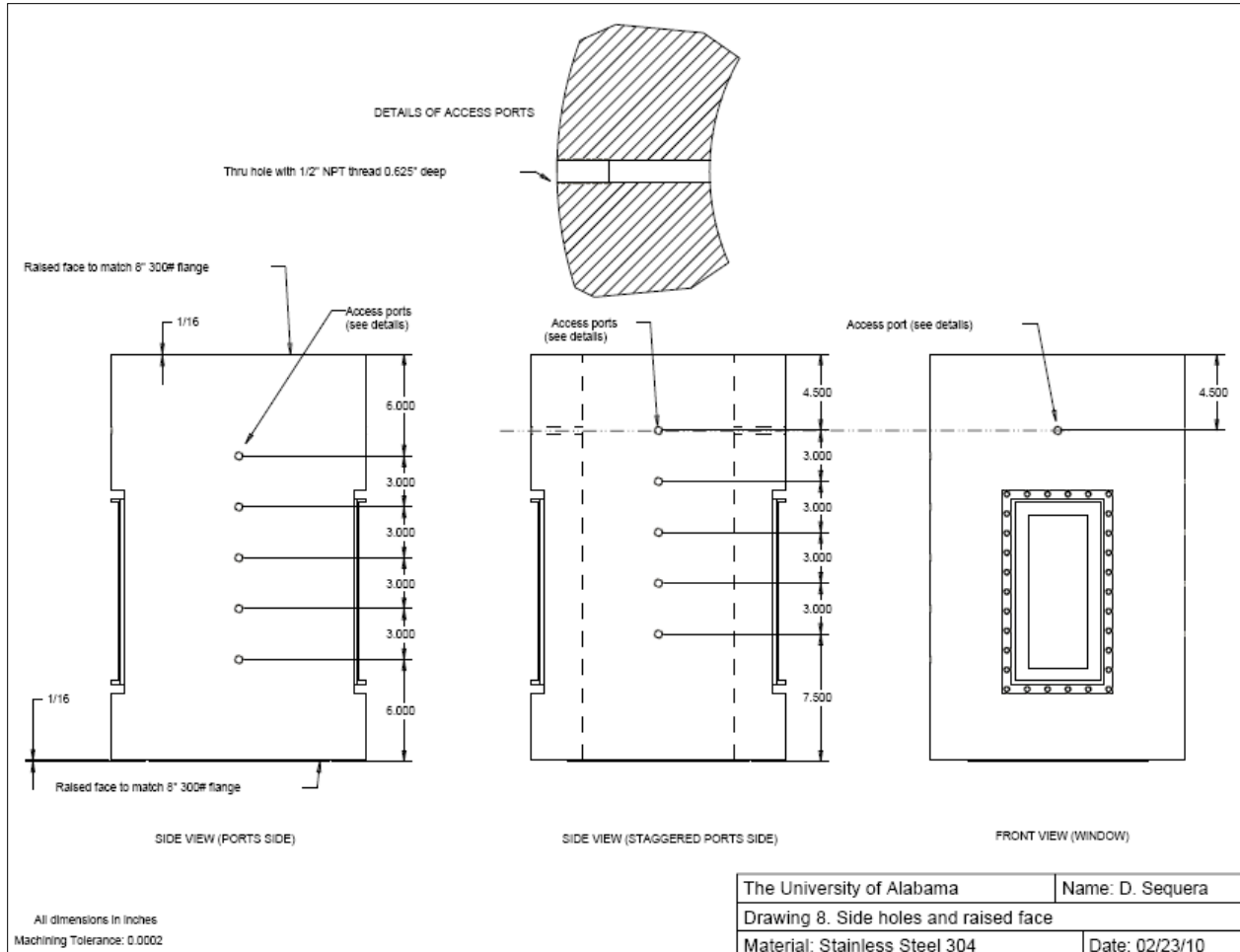


Figure A.7. Details of access ports on enclosure

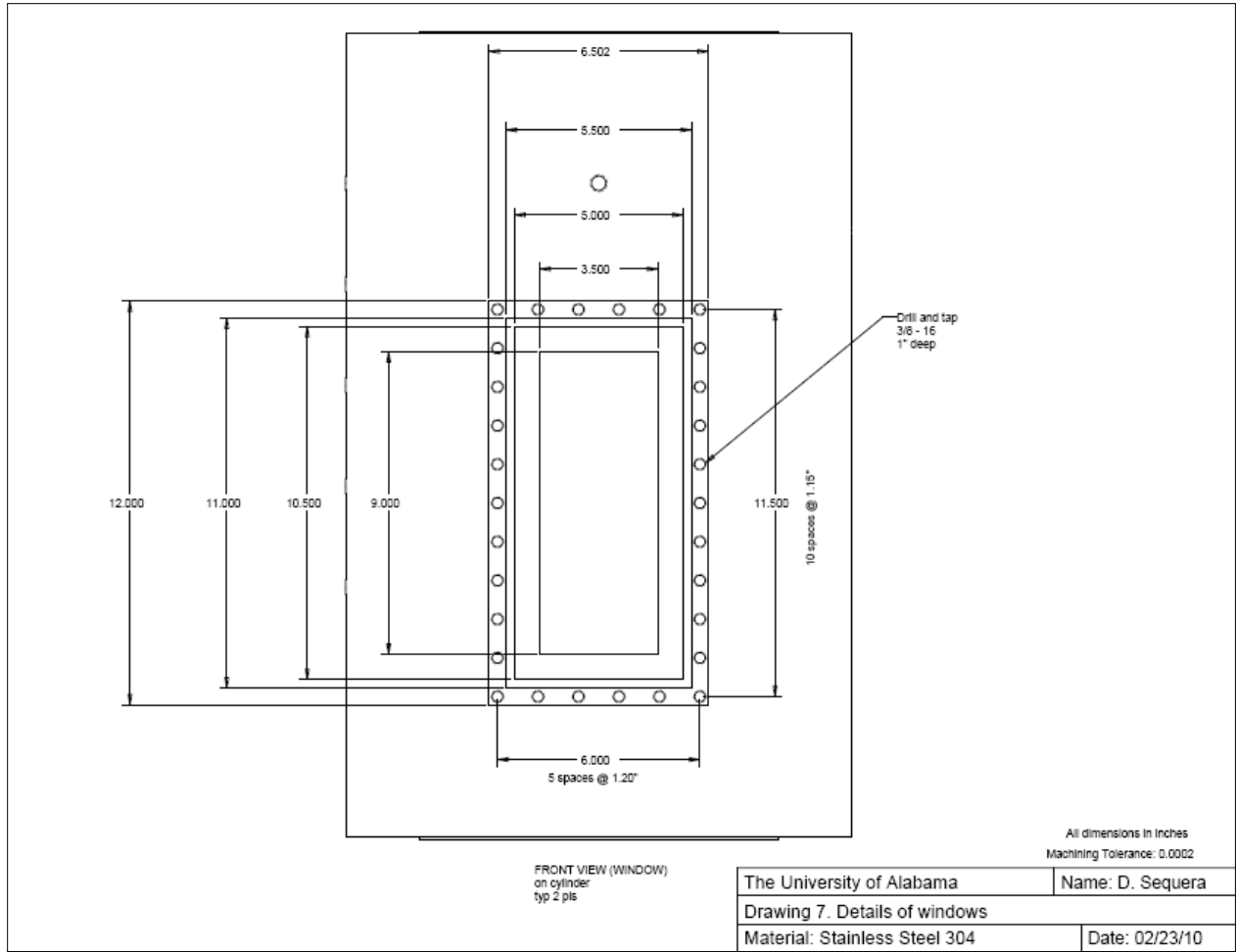


Figure A.8. Details of windows ports

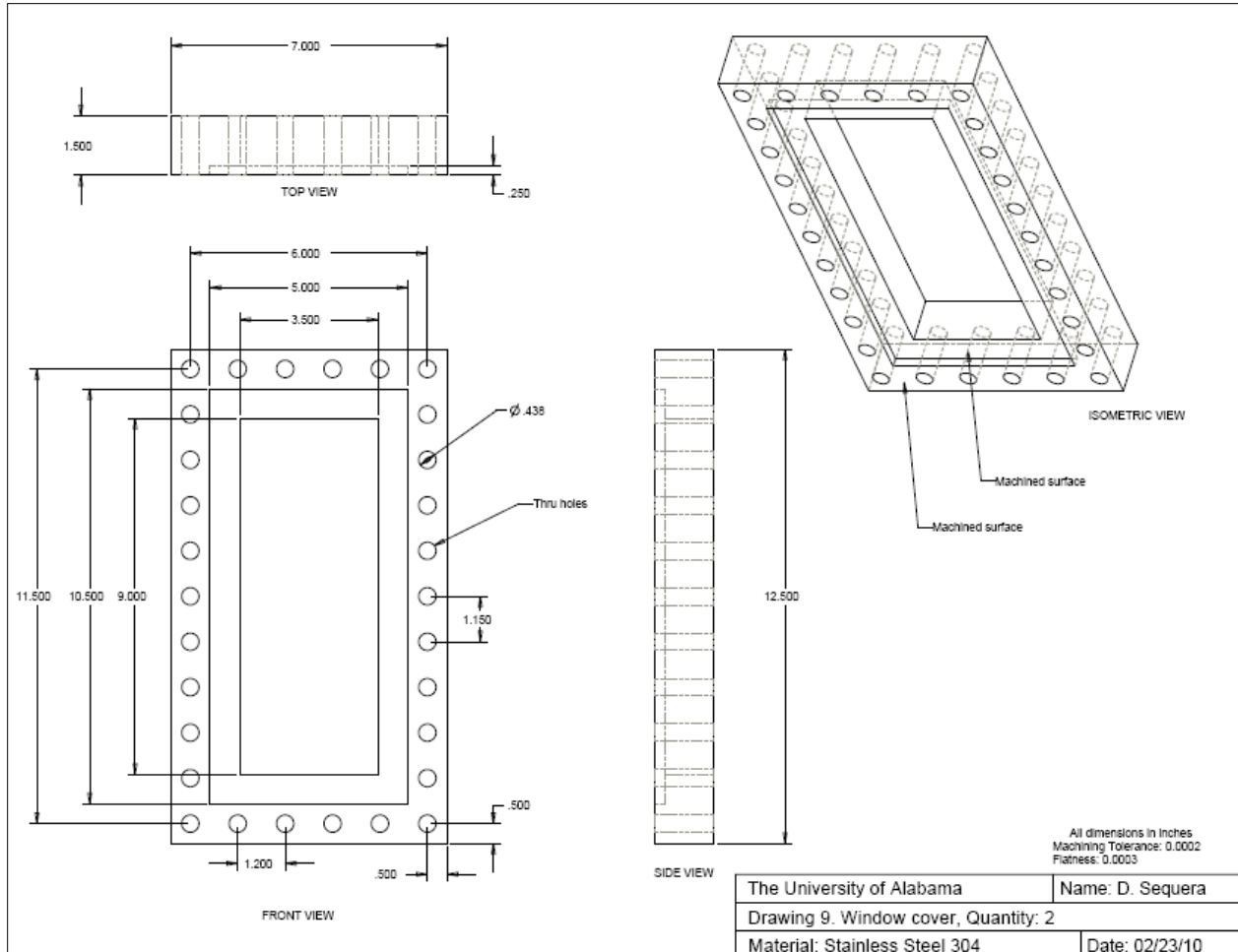


Figure A.9. Details of window covers

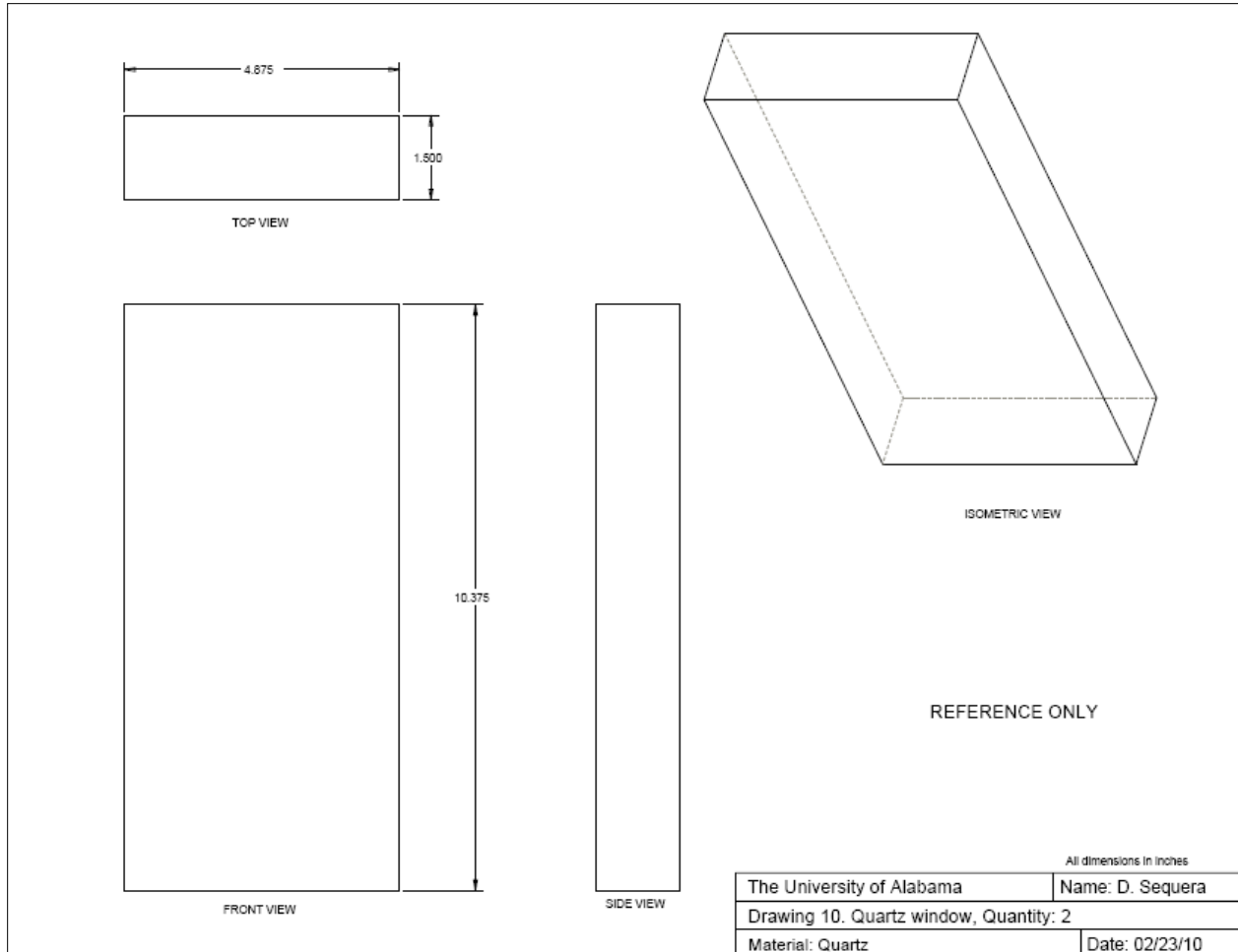
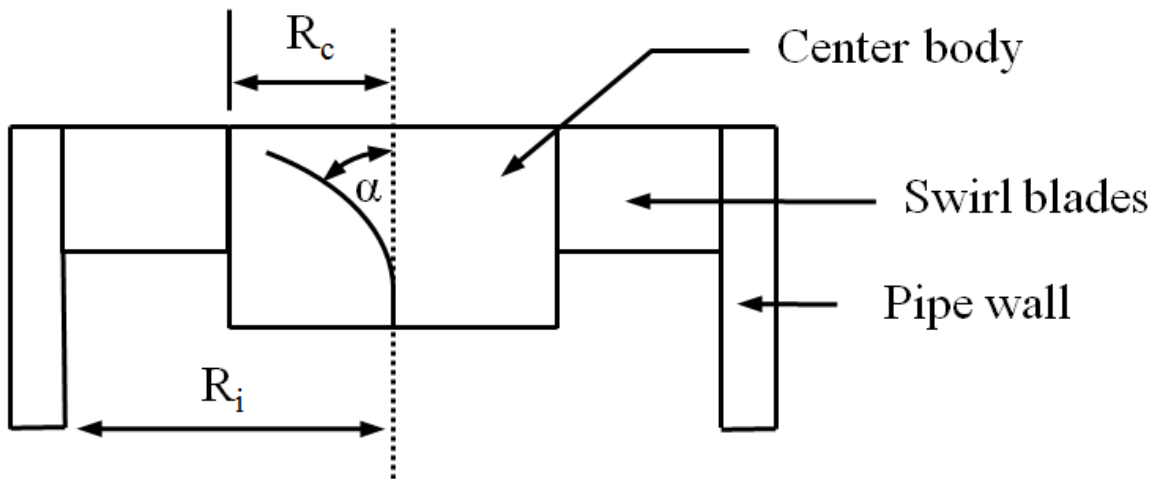


Figure A.10. Details of window

## APPENDIX B

### CALCULATION OF SWIRL NUMBER FOR FLOW SWIRLER

The flow swirler used for this study is depicted in Figure B.1.



*Figure B.1.* Schematic of flow swirler

The swirl number, S, is calculated in accordance with Johnson (reference needed) as:

$$S = \frac{2}{3} \tan \alpha \left( \frac{1 - R^3}{1 - R^2} \right) \quad (\text{B.1})$$

where  $\alpha$  is the vane angle with respect to the vertical axis and R is the effective radius defined by Johnson (need reference) as:

$$R = \frac{R_c}{R_i} \quad (\text{B.2})$$

where  $R_c$  is defined as the center body radius and  $R_i$  is defined as the total swirler radius.

For the flow swirler used in this study:

- $\alpha = 62^\circ$
- $R_c = 0.7 \text{ cm}$
- $R_i = 1.2 \text{ cm}$

which gives:

$$R = 0.58$$

and

$$S = 1.5$$

## APPENDIX C

### CALCULATION OF AIR FLOW RATE, EQUIVALENCE RATIO, AND REYNOLDS NUMBER

As described in Chapter 2, an LFE is used to measure flow rate for both cooling and combustion air. In accordance with manufacturer specifications, temperature, absolute pressure, and differential pressure measurements are made in order to determine flow rate through the LFE. Volumetric flow rate through the system is calculated as:

$$Q_{CFM} = [(B \times \Delta P) + (C \times \Delta P^2)] \times \frac{\mu_{std}}{\mu_f} \quad (C.1)$$

where  $Q_{CFM}$  is the actual volumetric flowrate (CFM), B and C are calibration constants provided by the manufacturer,  $\Delta P$  is differential pressure (in H<sub>2</sub>O),  $\mu_{std}$  is the viscosity of flowing gas at 20 °C (micropoise), and  $\mu_f$  is the viscosity of flowing gas at actual temperature (micropoise). The viscosity of the flowing gas is calculated using Sutherland's equation:

$$\mu_f = \frac{bT^{3/2}}{T + S} \quad (C.2)$$

where T is temperature, b and S are constants for air:

$$b = 14.58 \frac{\mu P}{K^{1/2}}$$

(C.3)

and

$$S = 110.4 K$$

(C.4)

The volumetric flow rate is converted from CFM to LPM using:

$$Q_{LPM} = Q_{CFM} \times 28.317 \frac{L}{ft^3}$$

(C.5)

Volumetric flow rate in LPM is converted to SLPM by:

$$Q_{SLPM} = Q_{LPM} \times \frac{\rho}{\rho_{SLPM}}$$

(C.6)

where  $\rho$  is the density of air at flowing temperature (g/l), and  $\rho_{SLPM}$  is air density at Standard Temperature and Pressure (STP) (g/l). Standard conditions are taken as  $T_{STD} = 0 \text{ }^\circ\text{C}$  and  $P_{STD} = 1 \text{ atm}$ .

$$\rho_{SLPM} = 1.276 \frac{g}{l}$$

(C.7)

Density of air at the flowing temperature is calculated by the Ideal Gas Law:

$$\rho = \frac{P_{abs}}{RT}$$

(C.8)

where  $P_{abs}$  is absolute air pressure (pa),  $R$  is the specific gas constant for air (J/kg-K), and  $T$  is temperature (K).

Equivalence ratio,  $\phi$ , is calculated for methane-air combustion as:

$$\phi = \frac{AF_{st}}{AF} \quad (C.9)$$

where  $AF_{st}$  is the mass based stoichiometric air to fuel ratio and  $AF$  is the mass based actual air to fuel ratio. For methane-air combustion:

$$AF_{st} = 17.19 \quad (C.10)$$

and

$$AF = \frac{\dot{m}_{air}}{\dot{m}_{CH_4}} = \frac{(\rho \times Q)_{air}}{(\rho \times Q)_{CH_4}} \quad (C.11)$$

Reynolds number is a dimensionless parameter which gives a measure of the ratio of internal to viscous forces for flow conditions. In this study, Reynolds number of incoming reactant flow is calculated for each case tested. For flow inside a pipe, Reynolds number is calculated by Equation C.12. Results are shown in Table C.1

$$Re = \frac{\rho U D}{\mu} \quad (C.12)$$

Table C.1

*Reynolds number of reactant flow inside premixer pipe*

| Q<br>(SLPM) | $\dot{m}$<br>(kg/min) | $T_{\text{inlet}}$<br>(°C) | $P_{\text{inlet}}$<br>(kPa) | $\rho$<br>(kg/m <sup>3</sup> ) | $\mu$<br>(Pa-s) | U<br>(m/s) | Re<br>(—) |
|-------------|-----------------------|----------------------------|-----------------------------|--------------------------------|-----------------|------------|-----------|
| 300         | 0.382                 | 21                         | 1.5                         | 1.22                           | 1.8E-05         | 16.4       | 11,755    |
|             |                       | 130                        | 2.5                         | 0.90                           | 2.3E-05         | 22.3       | 9,251     |
|             |                       | 260                        | 3.5                         | 0.68                           | 2.8E-05         | 29.2       | 7,626     |
| 600         | 0.764                 | 21                         | 6.5                         | 1.27                           | 1.8E-05         | 31.3       | 23,510    |
|             |                       | 130                        | 9.0                         | 0.95                           | 2.3E-05         | 41.9       | 18,501    |
|             |                       | 260                        | 13.0                        | 0.75                           | 2.8E-05         | 53.5       | 15,252    |
| 900         | 1.145                 | 21                         | 13.5                        | 1.36                           | 1.8E-05         | 44.0       | 35,234    |
|             |                       | 130                        | 16.5                        | 1.02                           | 2.3E-05         | 58.8       | 27,728    |
|             |                       | 260                        | 19.5                        | 0.79                           | 2.8E-05         | 75.9       | 22,858    |

## APPENDIX D

### SOUND PRESSURE LEVEL CALCULATION M-SCRIPT

As described in Chapter 2, a Matlab script code is used to calculate total SPL for sound measurements in this study. LabVIEW is used to perform an FFT of the scaled microphone voltage, which is subsequently fed into the script code to calculate SPL per frequency, SPL per one-third octave band, and total SPL. All sound pressure level calculations are based on a reference pressure of 20  $\mu\text{Pa}$ .

```
%Determine power per one-third octave frequency band
%%%%%%%%%%%%%%%%%%%%%%%%%%%%%%%%%%%%%%%%%%%%%%%%%%%%%%%%%%%%%%%%%%%%%%%%
j=1;
for i=91:113
band1(i)=Prms(i);          %generating array
end
P(j)=sum(band1);          %total power in frequency band and generating SPL array
j=j+1;
%%%%%%%%%%%%%%%%%%%%%%%%%%%%%%%%%%%%%%%%%%%%%%%%%%%%%%%%%%%%%%%%%%%%%%%%
for i=113:141
band2(i)=Prms(i);          %generating array
end
```

```

P(j)=sum(band2);      %total power in frequency band
j=j+1;
%%%%%%%%%%
for i=141:178
band3(i)=Prms(i);      %generating array
end
P(j)=sum(band3);      %total power in frequency band and generating SPL array
j=j+1;
%%%%%%%%%%
for i=178:226
band4(i)=Prms(i);      %generating array
end
P(j)=sum(band4);      %total power in frequency band and generating SPL array
j=j+1;
%%%%%%%%%%
for i=226:281
band5(i)=Prms(i);      %generating array
end
P(j)=sum(band5);      %total power in frequency band and generating SPL array
j=j+1;
%%%%%%%%%%
for i=281:356
band6(i)=Prms(i);      %generating array
end
P(j)=sum(band6);      %total power in frequency band and generating SPL array

```

```

j=j+1;
%%%%%%%%%%
for i=356:451
band7(i)=Prms(i);          %generating array
end
P(j)=sum(band7);         %total power in frequency band and generating SPL array
j=j+1;
%%%%%%%%%%
for i=451:561
band8(i)=Prms(i);          %generating array
end
P(j)=sum(band8);         %total power in frequency band and generating SPL array
j=j+1;
%%%%%%%%%%
for i=561:701
band9(i)=Prms(i);          %generating array
end
P(j)=sum(band9);         %total power in frequency band and generating SPL array
j=j+1;
%%%%%%%%%%
for i=701:901
band10(i)=Prms(i);          %generating array
end
P(j)=sum(band10);         %total power in frequency band and generating SPL array
j=j+1;

```

```

%%%%%%%%%%
for i=901:1121
band11(i)=Prms(i);          %generating array
end
P(j)=sum(band11);          %total power in frequency band and generating SPL array
j=j+1;
%%%%%%%%%%
for i=1121:1401
band12(i)=Prms(i);          %generating array
end
P(j)=sum(band12);          %total power in frequency band and generating SPL array
j=j+1;
%%%%%%%%%%
for i=1401:1776
band13(i)=Prms(i);          %generating array
end
P(j)=sum(band13);          %total power in frequency band and generating SPL array
j=j+1;
%%%%%%%%%%
for i=1776:2251
band14(i)=Prms(i);          %generating array
end
P(j)=sum(band14);          %total power in frequency band and generating SPL array
j=j+1;
%%%%%%%%%%

```

```

for i=2251:2801
band15(i)=Prms(i);          %generating array
end
P(j)=sum(band15);          %total power in frequency band and generating SPL array
j=j+1;
%%%%%%%%%%%%%%

for i=2801:3551
band16(i)=Prms(i);          %generating array
end
P(j)=sum(band16);          %total power in frequency band and generating SPL array
j=j+1;
%%%%%%%%%%%%%%

for i=3551:4501
band17(i)=Prms(i);          %generating array
end
P(j)=sum(band17);          %total power in frequency band and generating SPL array
j=j+1;
%%%%%%%%%%%%%%

for i=4501:5616
band18(i)=Prms(i);          %generating array
end
P(j)=sum(band18);          %total power in frequency band and generating SPL array
j=j+1;
%%%%%%%%%%%%%%

for i=5616:7066

```

```

band19(i)=Prms(i);          %generating array
end
P(j)=sum(band19);          %total power in frequency band and generating SPL array
j=j+1;
%%%%%%%%%%
for i=7066:8896
band20(i)=Prms(i);          %generating array
end
P(j)=sum(band20);          %total power in frequency band and generating SPL array
%%%%%%%%%%

%CALCULATION OF SOUND PRESSURE LEVEL PER ONE-THIRD OCTAVE BAND

Freq_band=[20 25 31.5 40 50 63 80 100 125 160 200 250 315 400 500 630 800 1000 1250
1600]; %Centers of frequency bands

SPL=10*log10(P/(4E-10));          %SPL per
1/3 octave band

%plot(Freq_band,SPL)

%CALCULATION OF SOUND PRESSURE LEVEL PER FREQUENCY

Freq=0:0.2:1999.8;          %Frequency range, by frequency resolution
dB_per_freq=10*log10(Prms/4E-10); %SPL at each frequency

```

%CALCULATION OF TOTAL dB

Rel\_power=10.^(SPL./10);                    %Converting dB to relative power to sum dB levels

Sum\_Rel\_power=sum(Rel\_power);

Total\_dB=10\*log10(Sum\_Rel\_power);

%CALCULATION OF dBA AND TOTAL dBA

%A-weighting correction factors:

A\_factor=[50.50 44.70 39.40 34.60 30.20 26.20 22.50 19.10 16.10 13.40 10.90 8.60 6.60 4.80  
3.20 1.90 0.80 0.0 -0.60 -1.00];

SPL\_dBA=SPL-A\_factor; %Sound pressure level in dBA

Rel\_power\_dBA=10.^(SPL\_dBA./10);                    %Converting dB to relative power to sum dB  
levels

Sum\_Rel\_power\_dBA=sum(Rel\_power\_dBA);

Total\_dBA=10\*log10(Sum\_Rel\_power\_dBA);

```
%%%%%%%%%%JET
NOISE%%%%%%%%%
```

```
%Determine power per one-third octave frequency band
```

```
%%%%%%%%%
```

```
Jj=1;
```

```
for Ji=91:113
```

```
bandJ1(Ji)=PrmsJ(Ji);          %generating array
```

```
end
```

```
PJ(Jj)=sum(bandJ1);          %total power in frequency band and generating SPL array
```

```
Jj=Jj+1;
```

```
%%%%%%%%%
```

```
for Ji=113:141
```

```
bandJ2(Ji)=PrmsJ(Ji);          %generating array
```

```
end
```

```
PJ(Jj)=sum(bandJ2);          %total power in frequency band
```

```
Jj=Jj+1;
```

```
%%%%%%%%%
```

```
for Ji=141:178
```

```
bandJ3(Ji)=PrmsJ(Ji);          %generating array
```

```
end
```

```

PJ(Jj)=sum(bandJ3);      %total power in frequency band and generating SPL array
Jj=Jj+1;
%%%%%%%%%%
for Ji=178:226
bandJ4(Ji)=PrmsJ(Ji);      %generating array
end
PJ(Jj)=sum(bandJ4);      %total power in frequency band and generating SPL array
Jj=Jj+1;
%%%%%%%%%%
for Ji=226:281
bandJ5(Ji)=PrmsJ(Ji);      %generating array
end
PJ(Jj)=sum(bandJ5);      %total power in frequency band and generating SPL array
Jj=Jj+1;
%%%%%%%%%%
for Ji=281:356
bandJ6(Ji)=PrmsJ(Ji);      %generating array
end
PJ(Jj)=sum(bandJ6);      %total power in frequency band and generating SPL array
Jj=Jj+1;
%%%%%%%%%%
for Ji=356:451
bandJ7(Ji)=PrmsJ(Ji);      %generating array
end
PJ(Jj)=sum(bandJ7);      %total power in frequency band and generating SPL array

```

```

Jj=Jj+1;
%%%%%%%%%%
for Ji=451:561
bandJ8(Ji)=PrmsJ(Ji);          %generating array
end
PJ(Jj)=sum(bandJ8);          %total power in frequency band and generating SPL array
Jj=Jj+1;
%%%%%%%%%%
for Ji=561:701
bandJ9(Ji)=PrmsJ(Ji);          %generating array
end
PJ(Jj)=sum(bandJ9);          %total power in frequency band and generating SPL array
Jj=Jj+1;
%%%%%%%%%%
for Ji=701:901
bandJ10(Ji)=PrmsJ(Ji);         %generating array
end
PJ(Jj)=sum(bandJ10);         %total power in frequency band and generating SPL array
Jj=Jj+1;
%%%%%%%%%%
for Ji=901:1121
bandJ11(Ji)=PrmsJ(Ji);         %generating array
end
PJ(Jj)=sum(bandJ11);         %total power in frequency band and generating SPL array
Jj=Jj+1;

```

```

%%%%%%%%%%
for Ji=1121:1401
bandJ12(Ji)=PrmsJ(Ji);          %generating array
end
PJ(Jj)=sum(bandJ12);          %total power in frequency band and generating SPL array
Jj=Jj+1;
%%%%%%%%%%
for Ji=1401:1776
bandJ13(Ji)=PrmsJ(Ji);          %generating array
end
PJ(Jj)=sum(bandJ13);          %total power in frequency band and generating SPL array
Jj=Jj+1;
%%%%%%%%%%
for Ji=1776:2251
bandJ14(Ji)=PrmsJ(Ji);          %generating array
end
PJ(Jj)=sum(bandJ14);          %total power in frequency band and generating SPL array
Jj=Jj+1;
%%%%%%%%%%
for Ji=2251:2801
bandJ15(Ji)=PrmsJ(Ji);          %generating array
end
PJ(Jj)=sum(bandJ15);          %total power in frequency band and generating SPL array
Jj=Jj+1;
%%%%%%%%%%

```

```

for Ji=2801:3551
bandJ16(Ji)=PrmsJ(Ji);          %generating array
end
PJ(Jj)=sum(bandJ16);          %total power in frequency band and generating SPL array
Jj=Jj+1;
%%%%%%%%%%%%%%

for Ji=3551:4501
bandJ17(Ji)=PrmsJ(Ji);          %generating array
end
PJ(Jj)=sum(bandJ17);          %total power in frequency band and generating SPL array
Jj=Jj+1;
%%%%%%%%%%%%%%

for Ji=4501:5616
bandJ18(Ji)=PrmsJ(Ji);          %generating array
end
PJ(Jj)=sum(bandJ18);          %total power in frequency band and generating SPL array
Jj=Jj+1;
%%%%%%%%%%%%%%

for Ji=5616:7066
bandJ19(Ji)=PrmsJ(Ji);          %generating array
end
PJ(Jj)=sum(bandJ19);          %total power in frequency band and generating SPL array
Jj=Jj+1;
%%%%%%%%%%%%%%

for Ji=7066:8896

```

```

bandJ20(Ji)=PrmsJ(Ji);          %generating array
end

PJ(Jj)=sum(bandJ20);          %total power in frequency band and generating SPL array
%%%

%CALCULATION OF SOUND PRESSURE LEVEL PER ONE-THIRD OCTAVE BAND

Freq_band_J=[20 25 31.5 40 50 63 80 100 125 160 200 250 315 400 500 630 800 1000 1250
1600];    %Centers of frequency bands

SPL_J=10*log10(PJ/(4E-10));          %SPL
per 1/3 octave band

%plot(Freq_band_J,SPL_J)

%CALCULATION OF SOUND PRESSURE LEVEL PER FREQUENCY

Freq_J=0:0.2:1999.8;          %Frequency range, by frequency resolution
%%%

dB_per_freq_J=10*log10(PrmsJ/4E-10);    %SPL at each frequency

%CALCULATION OF TOTAL dB

Rel_power_J=10.^(SPL_J./10);          %Converting dB to relative power to sum dB levels

```

```
Sum_Rel_power_J=sum(Rel_power_J);
```

```
Total_dB_J=10*log10(Sum_Rel_power_J);
```

```
%CALCULATION OF dBA AND TOTAL dBA
```

```
%A-weighting correction factors:
```

```
A_factor_J=[50.50 44.70 39.40 34.60 30.20 26.20 22.50 19.10 16.10 13.40 10.90 8.60 6.60 4.80  
3.20 1.90 0.80 0.00 -0.60 -1.00];
```

```
SPL_dBA_J=SPL_J-A_factor_J; %Sound pressure level in dBA
```

```
Rel_power_dBA_J=10.^(SPL_dBA_J./10); %Converting dB to relative power to sum  
dB levels
```

```
Sum_Rel_power_dBA_J=sum(Rel_power_dBA_J);
```

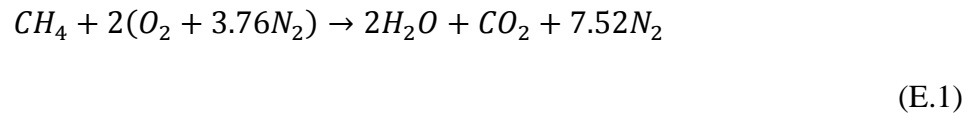
```
Total_dBA_J=10*log10(Sum_Rel_power_dBA_J)
```

## APPENDIX E

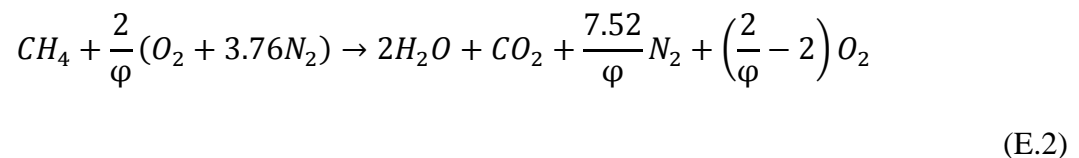
### SAMPLE CALCULATIONS OF O<sub>2</sub> AND CO<sub>2</sub> CONCENTRATIONS

For a given fuel type and equivalence ratio, resulting product concentrations of diatomic oxygen and carbon dioxide can be calculated. Similarly, measured concentrations of either product species can be used to calculate equivalence ratio of the reactant mixture. This process provides a cross-check to equivalence ratio calculated with measured fuel and air flow rates. The calculation is valid when assuming complete combustion and no dissociation. Accordingly, product species contain no minor species such as CO or NO<sub>x</sub>. This is an appropriate assumption since measured concentrations of CO and NO<sub>x</sub> are on the order of parts per million (ppm). Since product samples are passed through an ice bath, measured concentrations are calculated on a dry basis. Thus, no water vapor is present in the product gases.

For stoichiometric methane-air combustion:



For fuel lean combustion ( $0 < \phi < 1$ ):



Product concentrations of O<sub>2</sub> and CO<sub>2</sub> are calculated by:

$$\%O_2 = \frac{\left(\frac{2}{\phi} - 2\right)}{1 + \left(\frac{7.52}{\phi}\right) + \left(\frac{2}{\phi} - 2\right)} \times 100\% \quad (\text{E.3})$$

and

$$\%CO_2 = \frac{1}{1 + \left(\frac{7.52}{\phi}\right) + \left(\frac{2}{\phi} - 2\right)} \times 100\% \quad (\text{E.4})$$

For example, when  $\phi = 0.70$ :

$$\%O_2 = \frac{\left(\frac{2}{0.70} - 2\right)}{1 + \left(\frac{7.52}{0.70}\right) + \left(\frac{2}{0.70} - 2\right)} \times 100\% = 6.8\%$$

and

$$\%CO_2 = \frac{1}{1 + \left(\frac{7.52}{0.70}\right) + \left(\frac{2}{0.70} - 2\right)} \times 100\% = 7.9\%$$

Values calculated with Equations E.3 and E.4 compared with experimentally measured concentrations to ensure that the proper reactant mixture is being supplied to the combustor.

APPENDIX F  
UNCERTAINTY ANALYSIS

Experimental uncertainty analysis is performed for measurements made in this study. As outlined by Coleman and Steele (1999 need ref), systematic and random errors are computed for each measured quantity. Both errors are then used to calculate total uncertainty in the measured value.

Overall uncertainty of the measured result,  $U_r$ , is calculated as the square root of the sum of the squares of systematic and random uncertainties:

$$\mu_r = \sqrt{B_r^2 + P_r^2}$$

F.1

where  $B_r$  is the systematic uncertainty and  $P_r$  is the random uncertainty. Expressions for both quantities are given as:

$$B_r^2 = \sum \left( \frac{\partial r}{\partial X_i} \right)^2 B_{X_i}^2$$

F.2

$$P_r^2 = \sum \left( \frac{\partial r}{\partial X_i} \right)^2 P_{X_i}^2$$

F.3

The systematic error is provided for each instrument by the manufacturer calibration. Random uncertainty is calculated using a random sample of readings for the variable  $X_i$  and is given by the equation:

$$P_{X_i} = \frac{tS_X}{\sqrt{N}} \tag{F.4}$$

where  $t$  is the tabulated distribution for 95% confidence interval with  $N-1$  degrees of freedom,  $S_X$  is the standard deviation of the sampled dataset, and  $N$  is the number of samples. Standard deviation is defined as:

$$S_X = \left[ \frac{1}{N-1} \sum (X_i - \bar{X})^2 \right]^{1/2} \tag{F.5}$$

where the mean of the sample readings is calculated by:

$$\bar{X} = \frac{1}{N} \sum X_i \tag{F.6}$$

In this section, experimental uncertainty is calculated for air flow measured by the LFE, fuel flow measured by the mass flow controller, and resulting equivalence ratio. Sample calculations are presented for an air flow rate of 600 SLPM, a fuel flow rate of ## SLPM, and equivalence ratio of 0.70. The bias error for the LFE is specified as 0.72% of measured value. Bias error for the fuel mass flow controller is given as 0.5% of measured value plus 0.1% full scale. Thus for air flow,  $B_A = 4.3$  SLPM and for fuel flow,  $B_F = 0.7$  SLPM. Six random samples are taken for each measured quantity as shown in Table F.1. For five degrees of freedom at 95%

confidence,  $t = 2.571$ . Equation F.4 is used to calculate random uncertainties of  $P_A = 6.4$  SLPM and  $P_F = 0.1$  SLPM. Substituting into Equation F.1 gives  $\mu_A = \pm 7.7$  SLPM and  $\mu_F = \pm 0.7$  SLPM. Resulting uncertainties of air and fuel flow rate are used to obtain overall uncertainties in equivalence ratio.

Table F.1

*Random sample measurements for air and fuel flow rates*

| N                  | Air Flow (SLPM) | Fuel Flow (SLPM) |
|--------------------|-----------------|------------------|
| 1                  | 607.8           | 44.0             |
| 2                  | 598.1           | 44.1             |
| 3                  | 598.7           | 43.9             |
| 4                  | 606.2           | 43.8             |
| 5                  | 609.1           | 43.9             |
| 6                  | 596.5           | 43.8             |
| Mean               | 602.7           | 43.9             |
| Standard Deviation | 5.6             | 0.1              |

For methane-air combustion:

$$\varphi = 9.52 \left( \frac{F}{A} \right)$$

F.7

Uncertainty in equivalence ratio is obtained from Equations F.1, F.2 and F.3:

$$\mu_\varphi^2 = \left( \frac{\partial \varphi}{\partial A} \right)^2 \mu_A^2 + \left( \frac{\partial \varphi}{\partial F} \right)^2 \mu_F^2$$

F.8

where

$$\frac{\partial \phi}{\partial A} = -\frac{9.52}{A^2} = 2.64 \times 10^{-5}$$

F.9

and

$$\frac{\partial \phi}{\partial F} = \frac{9.52}{A} = 1.59 \times 10^{-2}$$

F.10

Thus, total uncertainty in equivalence ratio is  $\mu_\phi = \pm 0.01$

For the differential pressure transducer used to measure pressure drop across the swirler and

PIM, uncertainty data is provided from the manufacturer:

- Linearity =  $\pm 0.25\%$  full scale
- Hysteresis =  $\pm 0.10\%$  full scale
- Repeatability =  $\pm 0.05$  full scale

Thus, the total uncertainty in the differential pressure measurement is  $\mu_{\Delta P} = \pm 0.25\%$  full scale.

Since full scale pressure range is 6,895 Pa [2 psi]:

$$\mu_{\Delta P} = \frac{0.25}{100} \times FS = \frac{0.25}{100} \times 6,895 \text{ Pa} = \pm 20 \text{ Pa}$$

F.11

For sound pressure level measurement, total uncertainty is given by the manufacturer as:

$$\mu_{SPL} = \pm 0.2 \text{ dB}$$